Integrated Metabonomic Studies In Liver Biochemistry

A thesis submitted by

IVAN K. S. YAP

For the degree of Doctor of Philosophy of the University of London

Department of Biological Chemistry
Biomedical Sciences Division
Faculty of Life Sciences
Imperial College London

2005

To my family –

Mum, dad, Cathy, Winston, Eric and Nelson for your endless love and encouragement.
Without your support and believe, I would not be where I am today.
This thesis is dedicated to you.

Acknowledgments

I would like to express many thanks to my supervisors at Imperial College - Professor Jeremy K. Nicholson, Professor John C. Lindon and Dr. T. Andrew Clayton for their enthusiasm, ideas and guidance as well as for creating this project, Dr. T. Andrew Clayton who has kindly acted as a third, unofficial supervisor and for doing majority of the biofluid NMR work. I would also like to express thanks to my industrial supervisors Dr. Jeremy R. Everett of Pfizer Global Research and Development, Sandwich; not forgetting Dr. Gilles Hanton, M. Jean-Pierre Provost, Dr. Jean-Loic Le Net and M. Claude Charuel of Pfizer Global Research, Amboise Research Centre, France for their invaluable contributions and support in this project. I would also like to acknowledge Pfizer and Overseas Research Student Awards Scheme for their financial support.

I would like to thank all of the members of the Biological Chemistry group for their help and support over the past three years with various aspects of this project and outside the realm of postgraduate studies for their friendship and the kindness they have shown me. A special thank you to Dr. Huiru Tang and Dr. Yulan Wang for their invaluable time, patience, guidance and help in the area of metabonomics and NMR spectroscopy. I would also like to thank Dr. Olaf Beckonert and Dr. Olivier Cloarec for their help and advices on chemometrics and the application of pattern recognition software. A special thank you is reserved for all the great friends that I have made whilst at Imperial College especially Francois-Pierre, Toby, Alison, James, Alim, Dave, Dr. Manoj Mehta and Dr. Suzanne Drury. Thanks for keeping me sane!

Finally, I would like to thank my parents and my wife, Catherine, for their patience, encouragement, love, support and hope, as the Scottish author Samuel Smiles once wrote, "Hope is the companion of power and mother of success; for who so hopes strongly has within him the gift of miracles."

Statement of Originality

I certify that this thesis, and the research to which it refers, are the product of my own work, and that any ideas or quotations from the work of other people, published or otherwise, are fully acknowledged in accordance with the standard referencing practices of the discipline.

Abstract

NMR spectroscopy of tissue samples can be integrated with more conventional biofluid NMR spectroscopy to provide a comprehensive metabolic profile. The aim of this project is to integrate and interpret a combination of NMR and conventional toxicological data from urine, plasma and liver samples obtained over various time points during hepatotoxicity studies in the rat. The combined studies provided insights into the mechanisms and also sites of toxic damage. This integrated interrogation of the complex data sets also give a more holistic approach to the study of time-related toxic effects in the intact rat system and allow characterisation of key metabolic effects during toxic insult. High-resolution Magic Angle Spinning ^{1}H NMR spectroscopy has therefore been used to investigate the biochemical composition of rat liver tissue samples and the data integrated with the results of biofluid NMR spectroscopy, clinical chemistry and histopathology to provide a comprehensive and sequential view of altered metabolism and toxicity using allyl formate, chlorpromazine and thioacetamide as model hepatotoxicants in the first instance. The NMR data were analysed collectively using a combination of pattern recognition techniques to describe the integrated metabolic effects in the whole system. Chemometric methods based on principal components analysis and partial least squares analysis were used to identify key features and biochemical correlations between the data sets. In addition, time-dependent metabolic variations in the treated-animals were obtained by means of multivariate mean trajectory approach. ^{1}H MAS NMR of intact tissue provided a 'snap shot' of the endogenous perturbations in the organ at a particular time. In addition, ^{1}H NMR spectroscopy of the biofluids enabled sequential monitoring of the biochemical changes following treatment, reflecting the altered metabolism in the whole organism. The analysis identified toxin-induced changes in liver, plasma and urine metabolic profiles which are related to choline metabolism, glucose homeostasis and energy metabolism represented by changes in liver TMAO, glucose and lipid levels, changes in plasma glucose and lipid levels and changes in urinary TMAO and tricarboxylic acid cycle intermediates i.e. succinate, citrate and 2-oxoglutarate. These studies demonstrated the varied applications of NMR-based metabonomic techniques in toxicological studies and that the integrated metabonomic approach is a powerful method for investigating complex biological systems.

Table of Contents

Table of Figures

List of Tables

List of Abbreviations

γ-GGT	γ-glutamyltransferase
2-OG	2-oxoglutarate
3-HPMA	3-hydroxypropylmercapturic acid
5'NU	5' nucleotidase
ADH	Alcohol dehydrogenase
ADP	Adenosine diphosphate
ALAT	Alanine aminotransferase
ALB	Albumin
ALDH	Aldehyde dehydrogenase
ALP	Alkaline phosphatase
ANOVA	Analysis of variance
ASAT	Aspartate aminotransferase
ATP	Adenosine triphosphate
BILI	Bilirubin
CHOL	Cholesterol
CPMG	Carr-Purcell-Meiboom-Gill
CSA	Chemical shift anisotropy
DMA	Dimethylamine
DMG	Dimethylglycine
FAD	Flavin adenine dinucleotide
FDA	Food and drug administration
FID	Free induction decay
FMO	Flavin Monooxygenase
GAA	Guanidinoacetic acid
GLP	Good laboratory practice
GLUC	Glucose
GSH	Glutathione
GST	Glutathione-S-transferase
HCA	Hierarchical clustering analysis
HMQC	Heteronuclear Multiple Quantum Coherence
JRES	J-Resolved
KNN	K-nearest neighbour

LDL	Low density lipoproteins
MAS-NMR	Magic angle spinning nuclear magnetic resonance spectroscopy
MMA	Monomethylamine
MVDA	Multivariate data analysis
NAG	N-acetyl glycine
NLM	Non-linear mapping
NMR	Nuclear magnetic resonance spectroscopy
NOE	Nuclear Overhauser Effect
PAG	Phehylacetylglycine
PCA	Principal components analysis
PLS	Partial least squares
PLS-DA	Partial least squares discriminant analysis
ppm	Parts per million
PR	Pattern recognition
PROT	Protein
SIMCA	Soft independent modelling of classification analogy
STOCSY	Statistical total correlation spectroscopy
TAA	Thioacetamide
TAT	Tyrosine aminotransferase
TBA	Total bile acids
TCA	Tricarboxylic acid cycle
TMA	Trimethylamine
TMAO	Trimethylamine-N-oxide
TOCSY	Total correlation spectroscopy
TRIG	Triglycerides
VIP	Variable importance plot
VLDL	Very low density lipoproteins

Chapter 1. Introduction

1.1 Background

The use of medicines and drugs dates back in time as far as the first Egyptian dynasty of 3100 B.C. Discovery of the majority of these early drugs has been a trial-and-error process and serendipitous. The endeavour to optimize drug discovery and to rationalise the process has led to the concept of quantitative structure-activity relationships and brings about the progressive replacement of the highly serendipitous process to a process dominated by new technology. The process of bringing a new drug to market is very expensive and time consuming. It has been estimated that the cost to bring a drug to market successfully is now USD$800 million and takes about 10 to 15 years (DiMasi, 2001). The introduction of combinatorial chemistry and the setting up of library-based synthesis programmes has brought about the rapid generation and discovery of possible lead compounds and this therefore increases the pressure on the drug safety evaluation process. The knowledge of the toxicology of the drug candidate is vital in determining which candidate to be selected for development. However, complete toxicology testing for large numbers of lead compounds has proven to be both impractical (due to timescale) and costly. Therefore it is a prudent approach to reject unsuitable lead compounds in the early stage of development, and new ways of minimising such attrition are needed. The incorporation of screens that allow rational selection and optimisation of these molecules based on pivotal characteristics such as the way in which the candidate drug is metabolised (drug metabolism) or absorbed in *in-vitro* and *in-vivo* models coupled with pharmacological and preliminary toxicological data will enable identification of major metabolic imperfections in these molecules. These criteria will then form the basis for the decisions to advance one candidate into development over another (Ball and Borman 1998).

In-vivo toxicity testing is still regarded as the most comprehensive approach. The use of results from *in-vitro* testing is rather restricted. The use of *in-vitro* data for assessment and classification of toxicity is usually in the early stages of a toxicology study to screen out most toxic compounds e.g. an Ames test to determine if a chemical is a mutagen. This is

simply because the results generated in *in-vitro* studies do not mirror the total effects observed within standardized animal testing due to the complexity of living animals. *In-silico* toxicology, also known as computational toxicology involves the use of computer technology and informatics to analyse, model and estimate the chemical toxicity based on structure-activity relationships (Mathews *et al.* 2000). This technology can be used to estimate effective dose related to toxicological end point. However, the use of *in-silico* technology is limited by the current existing knowledge on toxicological data and can never provide a definitive toxicity assessment. The Food and Drug Administration (FDA) does not recognize the use of *in-silico* toxicological information in regulatory submissions. This is simply due to the fact that *in-silico* technology generates unreliable prediction of toxicity, poor coverage for FDA-regulated substances and incorrect logic with respect to FDA hazard identification practices (Mathews *et al.* 2000).

Disease biology is complex and drug development must be driven by insights into biological responses (Butcher *et al*. 2004). Understanding the relationships between genetic factors, the risks of developing major diseases and the molecular basis of drug efficacy and toxicity is a fundamental problem in modern biology (Nicholson *et al*. 2004). System biology approach aims to integrate multivariate 'omics-generated' biological data, to better describe and understand interactions in complex biological systems and ultimately to develop predictive models of human diseases (Nicholson *et al*. 2004, Butcher *et al*. 2004, Nicholson and Wilson 2003). The challenges of modelling mammalian biological complexities have been described recently by Nicholson *et al*. in a fascinating review (*Nat. Biotechnol.* 22, 1268 – 1274, October 2004). The relationships between 'endogenous' metabolic processes (coded in the genome and intrinsic to cellular function) and 'xenobiotic' (foreign compound) metabolism are poorly understood, especially with respect to environmental factors (Nicholson and Wilson 2003). Metabonomics as part of the 'omics trinity' (genomics, proteomics and metabonomics) promise to, at least partially, provide a means of modelling these interactions.

1.2 Overview of the project

The studies on which this project is based were split into two distinct phases. In phase one, four model hepatotoxins were individually dosed to rats. In phase two, four Pfizer compounds of known toxicity were individually dosed. However, only three of the phase one model hepatotoxins are presented in this thesis as one of the hepatotoxins, isoniazid, do not produce any liver toxicity. The overall aim was to use the phase one data to build models of hepatotoxicity, which would then be used in characterising any hepatotoxicity in the phase two compounds. All the studies were conducted on male Sprague-Dawley rats housed individually in metabolic cages. Majority of this project will focus on integrating the NMR-generated metabonomic data of both biofluids and liver tissues as well as histopathological and clinical chemistry data to give a global view on the effects of model hepatotoxins in mammalian system.

The highly complex and information-rich NMR spectra necessitate the use of computer-based pattern recognition data reduction and mapping techniques to assist in spectral interpretation. Chemometric methods based on principal components analysis and projections to latent structures by means of partial least squares analysis were used to identify key features and biochemical correlations between the data sets. In addition, time-dependent metabolic variations in the treated-animals were obtained by means of multivariate statistical batch processing and mean trajectory approaches. This enabled sequential monitoring of the biochemical changes following treatment, reflecting the altered metabolism in the whole organism.

The general layout of this thesis is outlined below in Figure 1.1.

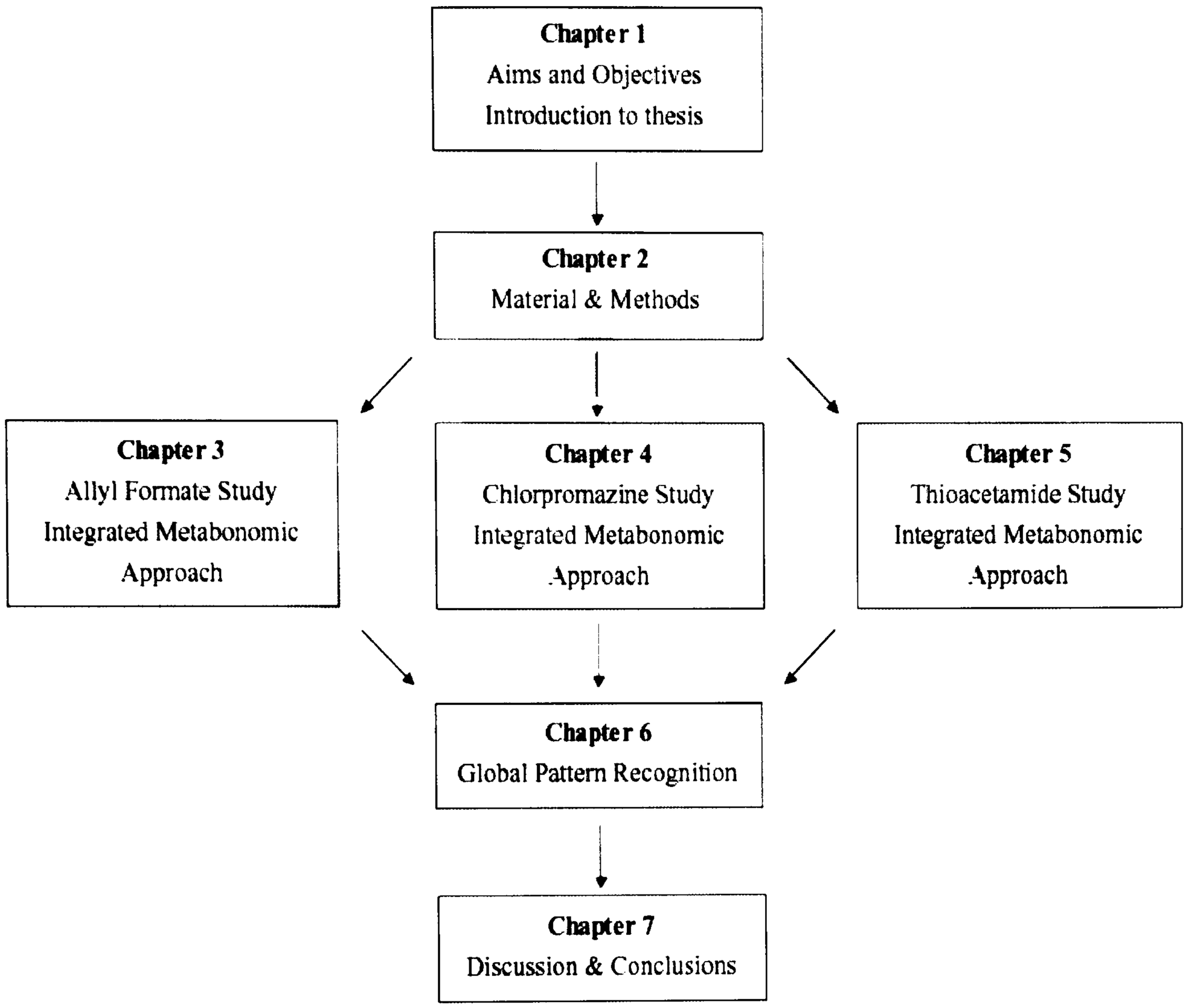

Figure 1.1 Thesis Structure.

1.3 Research Aims and objectives

The overall aim of this project was to investigate the use of Magic Angle Spinning Nuclear Magnetic Resonance (MAS-NMR) spectroscopy to identify hepatotoxin-induced changes in the liver of experimental animals and to integrate and correlate these changes with the corresponding NMR spectroscopic data generated from urine and blood plasma and with the findings of histopathology and clinical chemistry.

The specific objectives are:

1. To measure and analyse MAS-NMR spectra of liver tissue samples from rats dosed with a range of liver toxins acting by different mechanisms.

2. To compare and contrast the NMR results obtained from the liver tissue and biofluid samples.

3. To compare and contrast the spectroscopic and conventional toxicological data.

4. To integrate spectroscopic data from liver, blood plasma and urine samples to provide a more complete understanding of hepatotoxin-induced biochemical changes.

5. To develop chemometric models based on the MAS NMR spectra of liver tissue, which can be used for detecting and quantifying hepatoxicity of chemical compounds.

6. To identify metabolic biomarkers in liver tissue common to all hepatotoxins and those which allow distinction of the various types of hepatotoxic changes.

7. To improve the understanding of the mechanisms of action of hepatotoxic compounds.

1.4 The Liver

1.4.1 Structure and function

The liver (Fig. 1.2) is situated below the diaphragm in the abdominal cavity. It is the largest organ of the body representing about 2-3% of body weight in mammals. The liver is subdivided into two lobules, which consist of lobes. The primary cells in the liver are the hepatocytes and the Kupffer cells. The liver is a highly active, multi-functional organ, which plays a major role in maintaining homeostatic control in the body and controls of a multitude of metabolic activities essential for the regulation of blood composition. The liver performs a large variety of functions including excretory and detoxification functions, cholesterol metabolism, exocrine and endocrine functions, and digestive functions.

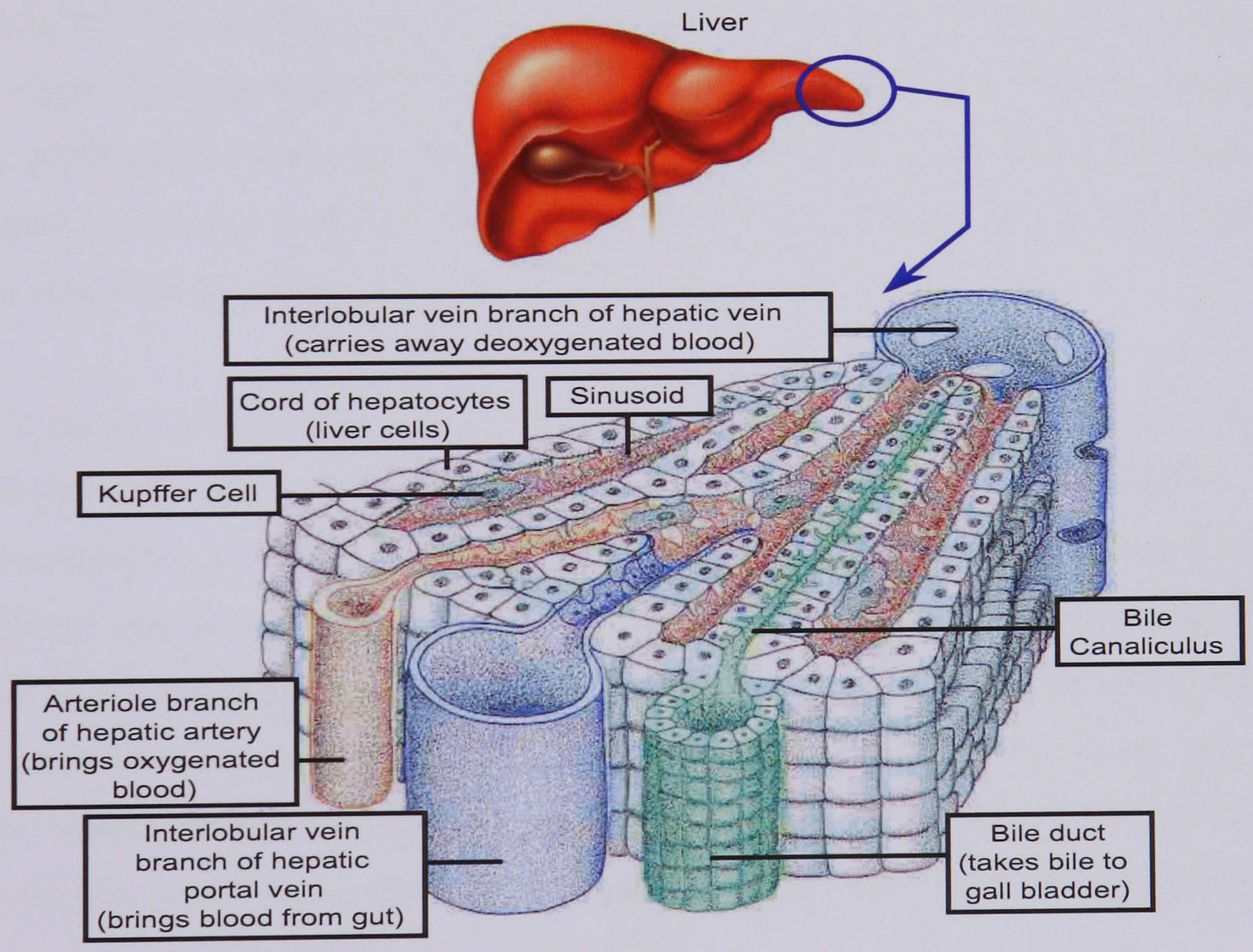

Figure 1.2 The liver and hepatic lobules (adapted from http://www.biologymad.com/master.html?http://www.biologymad.com/Kidneys/Kidneys.htm).

The liver is served by two blood supplies, with the hepatic portal vein supplying 75% of the hepatic blood, and the hepatic artery, which supplies the remainder. Venous blood from the intestine, stomach, pancreas and spleen converges into the portal vein thus supplying the liver with nutrients, and the hepatic artery supplies oxygenated blood to the liver. The structural unit of liver, the hepatic lobules, are hexagonal in shape. At the peripheries of the lobules are the portal triads consisting of a portal vein, a hepatic artery and a bile duct. The portal vein divides into branches of interlobular veins surrounding the hepatic lobules (Fig. 1.2). Blood passes through these vessels between the liver cells (sinusoids) to the centre of the lobule. The hepatic artery also branches and accompanies the portal veins between the lobules. Hepatic arterial blood enters the sinusoids in the liver where it mixes with the blood from the portal vein. Sinusoids are highly fenestrated vascular channels. They are lined with endothelial cells bounded by hepatocytes and Kupffer cells. The endothelial cells are flat, non-phagocytic cells, which remove lipoproteins, glycoproteins and sugars from the blood. The Kupffer cells are macrophages, which remove old blood cells from spaces in between the endothelial cells and hepatocytes. Blood flow through the sinusoids is emptied into the central vein in each lobule. These central veins coalesce to form hepatic veins, which leave the liver and empty into the vena cava.

The biliary system consists of channels and ducts that transfer bile from the liver to the small intestine. Bile is a product of hepatocytes. Hepatocytes are arranged in 'plates' surrounding the sinusoids. The basal part of adjacent hepatocytes is joined together to form canaliculi (the first channel in the biliary system). This is the intercellular space between the adjacent hepatocytes. Hepatocytes secrete bile into the canaliculi. Bile flows parallel to the sinusoids but in the opposite direction to the flow of blood. The bile drains into the bile ducts, which are lined with epithelial cells. The bile ducts are situated in close proximity to the end branches of both portal vein and hepatic artery. Small bile ducts merged into bigger ducts eventually forming the common bile duct.

The hepatic acini are the functional unit of the liver. The acinus consists of a unit bounded by two portal triads and a central vein. The hepatocytes in each acinus are divided into three concentric elliptical zones that correspond to the distance from the arterial blood

supply (Fig 1.3). There are metabolic differences in each zone as those hepatocytes closest to the arterioles, zone 1 or periportal region, are the best oxygenated followed by zone 2 or mediolobular region and finally zone 3 or centrilobular region. This arrangement also means that cells in the center of the acinus (zone 1) are the first to encounter and potentially absorb blood-borne toxins absorbed into portal blood from the small intestine. Consequently, a variety of pathological processes lead to lesions that reflect acinar structure i.e. periportal necrosis or centrilobular necrosis.

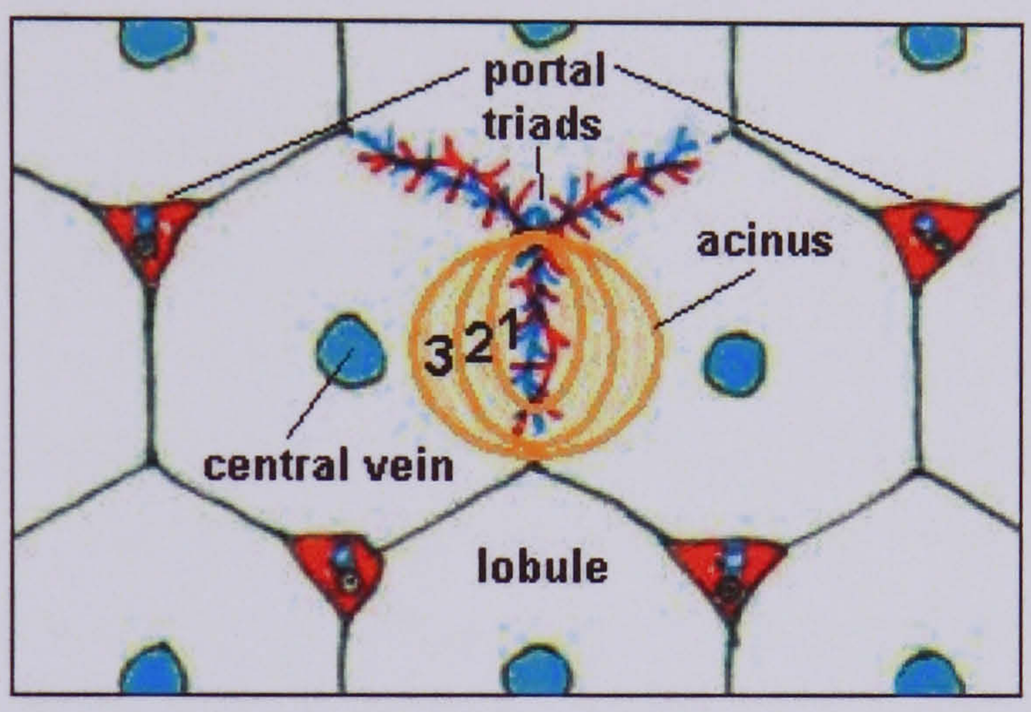

Figure 1.3 Hepatic acinus and hepatocytes (adapted from http://arbl.cvmbs.colostate.edu/hbooks/pathphys/digestion/liver/histo_acinus.html).

1.4.2 Carbohydrate Metabolism

The liver is capable of producing glycogen, the principal storage polysaccharide, by glycogenesis and of degrading the stored glycogen by glycogenolysis. An individual's metabolic status determines whether glycogen synthesis or glycogen degradation predominates. Liver glycogen is the only source for homeostatic control of the blood glucose level, since only the liver is equipped with the enzyme glucose-6-phosphatase that converts glucose-6-phosphate to glucose. In the liver, approximately 10% of the glucose of glycogen is available for immediate enzymatic release because of the highly branched glycogen structure (Kaplan and Pesce, 1989). Liver glycogen storage is dynamic in nature, functioning as a source of glucose for all parts of the body except muscle. Increased demand for glucose will normally be met by an increase in glycogenolysis. However,

gluconeogenesis enables a continued supply of glucose when the body's store of glycogen is depleted under strenuous conditions by producing glucose-6-phosphate from amino acids, lactate and glycerol.

1.4.3 Bile Formation

Bile acids are the major metabolic product of cholesterol. Bile acids synthesis from cholesterol is a multi-enzyme coordinated process (Palmeira and Rolo, 2004). In this pathway, the addition of hydroxyl groups, reduction of double bonds and the oxidation of the side chain, form a soluble end product from cholesterol. Hydroxylation is always on one side of the molecule resulting in an amphipathic molecule having a hydrophobic tail on one side and a hydrophilic tail on the other. However, different bile acids have varying degree of hydrophobicity and hydrophilicity determined by their physicochemical and biochemical properties (Palmeira and Rolo, 2004). The major bile acids in humans are cholic, chenodeoxycholic, lithocholic and deoxycholic acids. These four major bile acids differ only in the number and position of hydroxyl groups that are attached to the steroid nucleus with cholic acid having three hydroxyl groups, both chenodeoxycholic and deoxycholic acids having two hydroxyl groups and lithocholic acid has only one (Figure 1.4).

The bile acids which are synthesised within the hepatocytes are called primary bile acids i.e. cholic and chenodeoxycholic acids. These bile acids are further conjugated with glycine or taurine to form glycol- or tauro-conjugated bile acids, which are then secreted by the liver into the bile. Regulation of bile acids synthesis is determined by the amount of bile acids returned from the intestine to the liver. Biosynthesis decreases as more bile acids are reabsorbed (Montgomery *et al.* 1996). Bile acids biosynthesis is also controlled by the amount of cholesterol ingested. An increase in cholesterol consumption will lead to an increase in bile acids synthesis. Therefore, continuous conversion of cholesterol into bile acids in the liver is vital in preventing the body from having a cholesterol overload.

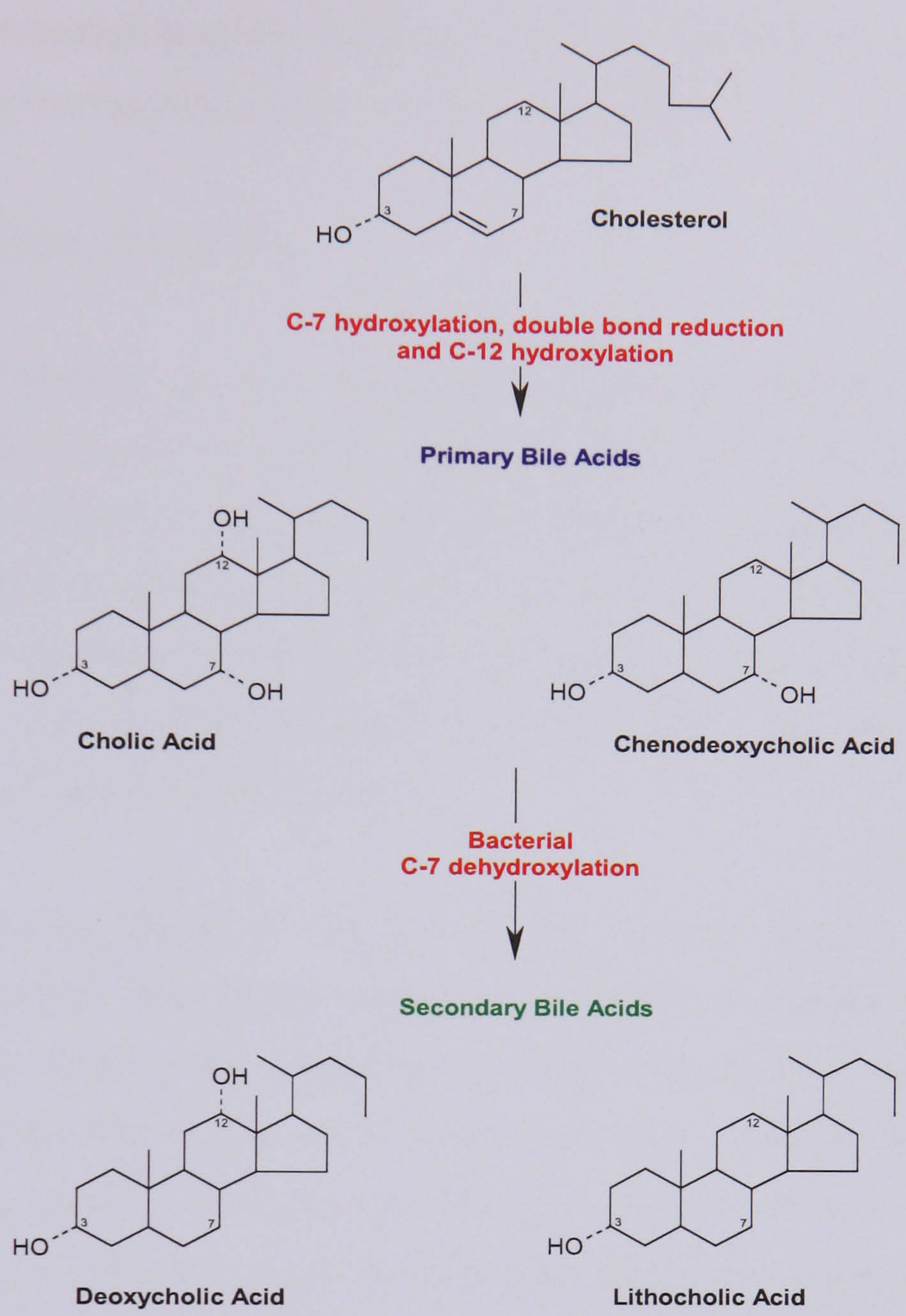

Figure 1.4 Schematics of bile acids synthesis (adapted from Montgomery *et al.* 1996).

Conjugated primary bile acids are either secreted by the liver directly into the duodenum via the common bile duct or stored temporarily in the gall bladder. Bile is secreted into the intestine to emulsify lipids, a process necessary for hydrolysis and absorption of dietary fat. Secretion of bile acids from the liver and the emptying of the gallbladder are controlled by the hormone hepatocrinin and cholecystokinin respectively. Deoxycholic and lithocholic acids are both secondary bile acids. They are formed through the action of intestinal bacterial enzymes on the primary bile acids in the intestine. The process involves the deconjugation of the primary bile acids followed by the C-7 dehydroxylation of the primary

bile acids by intestinal bacteria. Secondary bile acids are also conjugated with glycine or taurine to form corresponding glyco- and tauro-conjugates.

1.4.4 Enterohepatic Circulation

Although bile acids are secreted in large quantities into the intestine, only a small amount of the bile acids secreted are lost from the body. About 95% of bile acids secreted into the duodenum are reabsorbed back into the blood circulation through the ileum. The venous blood from ileum empties into the portal vein, which passes through the sinusoids to the liver. Here, the bile acids are extracted by the hepatocytes surrounding the sinusoids. These extracted bile acids are then resecreted into the canaliculi. The whole process is termed 'Enterohepatic Recirculation' (Figure 1.5).

Enterohepatic recirculation is the process by which a drug is reabsorbed in the gastrointestinal track after biliary excretion. A drug that is excreted in the bile enters the intestine after storage in the gallbladder. A major prerequisite for such a process is the conjugation of the drug by a phase II biotransformation in the liver and the excretion into the bile of the resulting conjugate (glucuronide, glycoside, sulfate). This conjugate may then be enzymatically hydrolyzed by intestinal microflora in the gastrointestinal track releasing the parent drug for reabsorbtion into the portal circulation. Biliary secretion and intestinal reabsorption may continue until the drug is ultimately eliminated from the body via renal or fecal excretion or other routes of disposition. Hence, enterohepatic circulation may result in unusually long persistence of drug in the body, and may influence such pharmacokinetic parameters as the drug half-life, the area under the plasma level versus time curve (AUC) and possibly estimates of bioavailability.

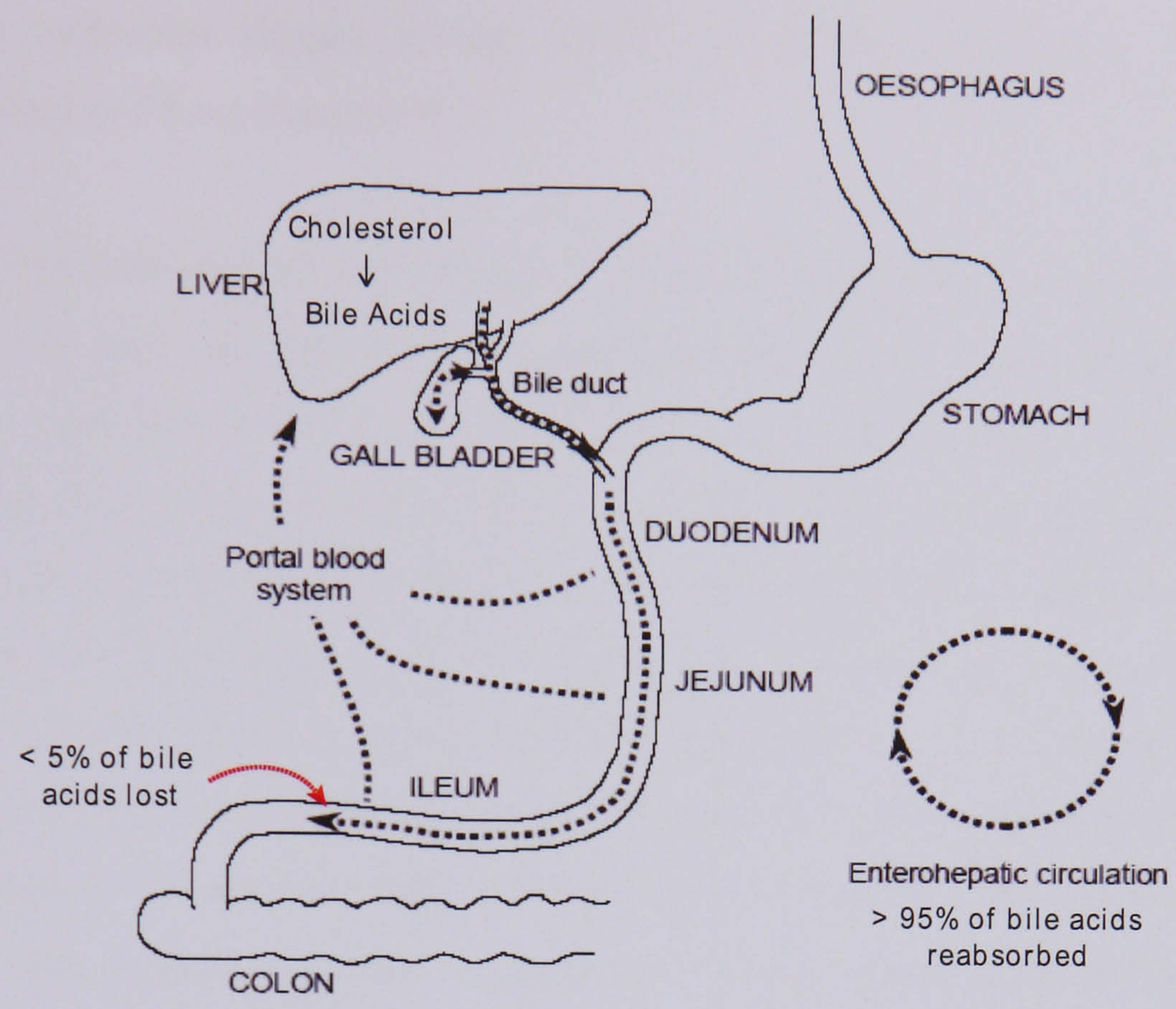

Figure 1.5 Enterohepatic Recirculation (adapted from Chan *et al.* 2004).

1.4.5 Metabolism and Detoxification

As the liver is one of the major points of entry to the tissues of the body, it is one of the primary sites of metabolism and elimination of most xenobiotics. The liver removes mostly water-insoluble drugs, which are bound to albumin, from the blood plasma. It then converts the water-insoluble drugs to a more water-soluble form, which may be excreted into bile and eliminated via the gastrointestinal tract. The process of enhancing the water solubility of xenobiotics is termed biotransformation. Biotransformation of xenobiotics is mostly accomplished by liver microsomes which contain a family of enzymes that oxidise various chemicals such as carcinogens, drugs and steroids. These microsomal systems are termed mixed-function oxidases consisting mainly of cytochrome P-450 mono-oxygenases and flavin-containing mono-oxygenases. Many of the biotransformation reactions such as epoxidation, hydroxylation, dehalogenation and oxidative deamination are catalysed by these mixed-function oxidases. Metabolism of xenobiotics by mixed-function oxidases is classed as *Phase 1* metabolism. Phase 1 metabolism normally involves the alteration of

foreign molecules simply by the addition of a functional group. These can then be conjugated in *Phase 2* metabolism.

Phase 2 metabolism involves mainly conjugation with readily available polar endogenous compounds such as glucuronic acid and sulphate, to the functional group present on the foreign molecule or those introduced by Phase 1 metabolism. This renders the whole molecule more polar and thus more water-soluble, facilitating excretion and reducing the likelihood of toxicity. Another important route of Phase 2 metabolism is glutathione conjugation. This is because it involves the removal of reactive intermediates. Glutathione is a tripeptide found in many mammalian tissues especially in the liver. It plays a major protective role in the body as it is a scavenger for reactive compounds of various types, combining at the reactive centre in the molecule therefore reducing the toxicity (Timbrell 2002). The sulphydryl group of glutathione acts as a nucleophile which either displaces another atom or attacks an electrophilic site. Consequently, glutathione may react either chemically or in enzyme-catalysed reactions with a variety of compounds which are either reactive or are electrophilic metabolites produced in Phase 1 reactions. The reactions may be catalysed by one of a group of glutathione transferases located in the soluble fraction of the cell. The resulting conjugate may be either excreted into the bile unchanged or metabolised further, via Phase 3 reactions, to yield an N-acetylcysteine conjugate. A detailed description of the underlying principles of biochemical toxicology has been extensively covered in numerous publications (Timbrell 2000, Gibson & Skett 1994)

1.5 Common Liver Diseases Associated with Drug Toxicity

The effects of hepatotoxins may be highly reproducible whereby upon a single exposure or repeated exposure to the hepatotoxin, the liver consistently shows signs of hepatic injury. Such toxins include chloroform, carbon tetrachloride, tetracycline, and anti cancer drugs. On the other hand, the effects of a hepatotoxin can be idiosyncratic whereby it produces a toxic response in only a tiny proportion (e.g. 1 in 10000) of animals or humans. Halothane is such an example where the damage could be due to the phenotypic susceptibility of a

particular animal. However, this project will focus on identification of reliable and consistent hepatotoxins.

Liver damage may arise from either single or repetitive exposure to hepatotoxins. The main types of acute liver damage that may occur are *necrosis* (cell death), *steatosis* (fatty liver) and *cholestasis* (obstruction of bile flow) leading to biliary damage. The term necrosis is used to describe the condition when irreversible damage occurs in cell beyond repair and cell death ensues. This is normally followed by a series of degenerative changes including hydrolysis of cellular components and protein denaturation (Timbrell 2003). Steatosis is defined as accumulation of fat, largely triglycerides, exceeding 5% of the liver weight (Sherlock & Dooley 2002). This is a common response to toxic compounds and is usually reversible. It is caused by failure of fat metabolism in the liver due to damage to the hepatocytes. The excess lipid may appear in the cell as small/large droplets thus producing characteristic yellowish liver. Cholestasis is defined as interference of bile flow or bile formation (Sherlock & Dooley 2002.). This can occur anywhere in the sinusoids, hepatocytes and the ampullae of Vater. For instance, if the sinusoidal membrane lining of the hepatocytes is destroyed, blockages of the ductules can occur due to debris from necrotic cells thus triggering cholestasis. Cholestasis can also result from errors in bile synthesis.

1.6 Application of ^{1}H NMR Spectroscopy to Metabolic Profiling

1.6.1 Metabolic Profiling and the Metabonomics Approach

Metabolic profiling provides a powerful new tool for gaining insight into functional biology. Xenobiotics cause perturbations of the concentration and fluxes of endogenous metabolites involved in the countless multifaceted catabolic and biosynthetic pathways existing in all living systems. The response of cells to toxic insult generally first entails an adjustment of the intra- and/or extra-cellular environment in order to maintain homeostatic control in their highly regulated environment. Metabolic regulations in response to pathophysiological and/or genetic stimuli can be expressed as a unique fingerprint of biochemical perturbations that is characteristic of the nature or site of toxic insult or disease processes.

Metabolic profiling can be divided into two distinct classes according to the level of biological organisation. Metabolomics, is defined as the study of the metabolite profiles in single cell systems (Nicholson *et al.* 1999, Nicholson *et al.* 2002) whilst metabonomics is defined as 'the quantitative measurement of the dynamic multiparametric metabolic response of living systems to pathophysiological stimuli or genetic modification' (Nicholson *et al.* 1999). As a result, metabonomics represents a full system biology approach to understanding the dynamics as well as organ-specific biochemical responses in response to pathophysiological stimuli and genetic modification.

A variety of spectroscopic methods can be used to acquire metabonomic data sets on complex biological samples. Nuclear Magnetic Resonance (NMR) spectroscopy has been instrumental in providing a snapshot of the level of numerous small molecules within a cell or a biofluid and how those levels change under different physiological, pharmacological and toxicological conditions. Additionally, NMR spectroscopy enables the study of molecular dynamics providing information such as molecular reorientation-correlation times and diffusion coefficients in solution and in intact tissues. It is complementary to gene expression (genomic) and proteomic studies. It is by far the most powerful method for

examining biofluids and essentially the only method capable of studying intact tissues providing comprehensive profile of metabolite signals without laborious sample preparation or derivatisation steps. Mass spectrometry can also be used to generate metabolic data, however, differences in the efficiency of ionisation can affect detectability and quantitation, and a prior separation stage such as HPLC is required as this can introduce additional variability. Nevertheless, mass spectrometry can be much more sensitive than NMR spectroscopy. Most metabonomic investigations have examined the biochemical effects of xenobiotics in animal models and the majority of these studies have employed high-resolution ^{1}H-NMR spectroscopy to characterise and quantify various metabolites in biofluids such as urine and plasma whilst Magic Angle Spinning (MAS) NMR spectroscopy has been used to analyse cells and tissues (Holmes *et al.* 1994, Robertson *et al.* 2000, Waters *et al.* 2001, Garrod *et al.* 2001, Nicholson *et al.* 2002). These methods are usually coupled with powerful pattern recognition (PR) and expert system methods to allow classification of the samples on the basis of the different fingerprints arising from the highly complex and information-rich high-resolution NMR spectra.

1.6.2 Principles of Nuclear Magnetic Resonance

Nuclear Magnetic Resonance (NMR) spectroscopy detects the way in which electromagnetic radiation interacts with the spin of atomic nuclei. The spin is characterised by a nuclear spin quantum number, I, that can take integer and half integer values. Those nuclei with $I = 0$ will have no spin and therefore are not observable by NMR. However, most elements i.e. ^{1}H, ^{13}C, and ^{31}P, have $I > 0$ and are therefore NMR-observable. All charged spinning nuclei have an angular momentum, J, which give rise to a magnetic moment, μ such that:

$$\mu = \gamma J$$

where γ is the magnetogyric ratio. The bigger the magnetogyric ratio the larger the magnetic moment of the nucleus. The magnetic moment is quantised and can only take certain values. When an external magnetic field, B_0 (measured in Tesla), is applied to

magnetic nuclei, the nuclei will precess at 2I + 1 possible orientations. Therefore, for a spin-1/2 nucleus like ^1H, this will generate two spin states in a magnetic field. The energy of these states can be characterised by the magnetic quantum number, m. The lower energy state corresponds to $m_\alpha = + ½$. This occurs when the lower energy state, precesses parallel with the applied magnetic field, B_0. The higher energy state corresponds to $m_\beta = - ½$. This occurs when the energy state precesses against B_0. This splitting of spin energy level into specific states is called the Zeeman effect. There is a tendency for the magnetic moments to align in the direction of B_0 because of the slightly lower energy state it is associated with, and the ratio of the populations (η) of the two states is given by the Boltzmann rule:

$$\eta\alpha/\eta\beta = e^{\Delta E/kT}$$

where ΔE is the energy difference between the spin states, k is Boltzmann's constant and T is the absolute temperature in Kelvin. When the force B_0 is applied to a nucleus, it causes the nuclei to precess at an angular frequency called the Larmor frequency. The angular frequency, ω_0, increases proportionally with B_0: $\omega_0 = \gamma B_0$, or in frequency terms: $\nu_0 = \gamma B_0/2\pi$. Given the linear relationship between B_0 and ΔE, the natural precession frequency can be expressed in frequency terms by Planck's relationship:

$$\Delta E = h\nu_0$$

where h is the Planck's constant ($6.626208 * 10^{-34}$ J S). Thus, as:

$$\Delta E = h\gamma B_0/2\pi$$

All different types of nuclei have a unique resonant frequency because of their different values for γ. When a second magnetic field, B_1, is applied at a radio frequency, the frequency matching that of the Larmor frequency of the nucleus causes the excess spins to move from the lower energy state to the higher energy state by a process called resonance.

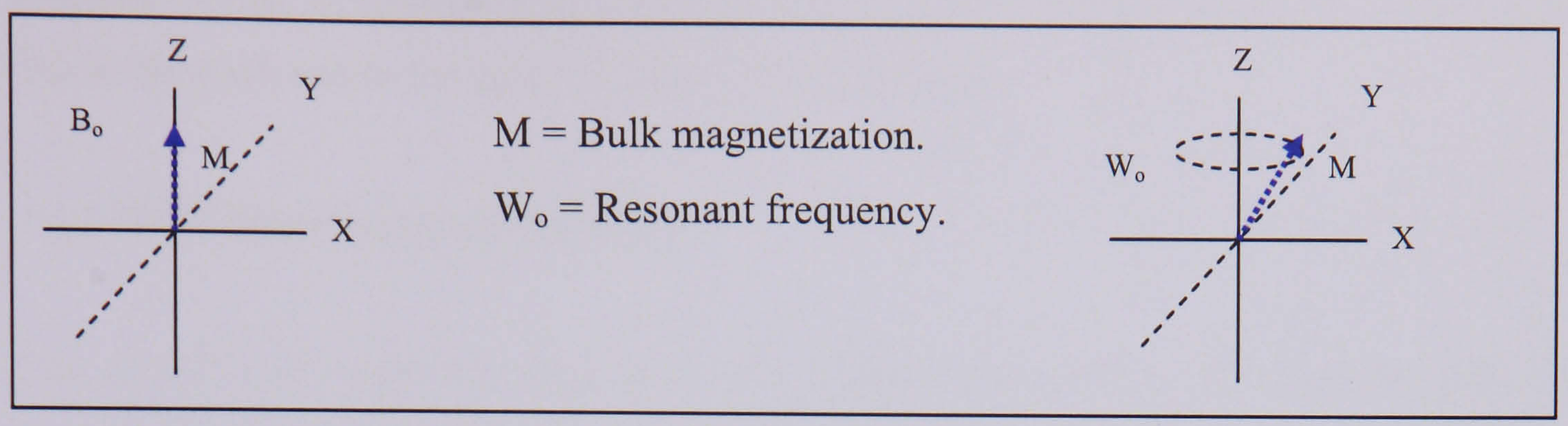

Figure 1.6 3D-Diagram of magnetization behaviour in magnetic field.

If the axis system is considered to rotate at the Larmor frequency then the magnetisation has a net value along the Z (B_0) axis as shown in Figure 1.6. Application of radiofrequency energy can then be regarded as tipping M into the XY plane. This is usually done by a short intense pulse along the X-axis. Sufficient energy to tip M to along the Y-axis equalises the populations of the two states, and is termed a 90° pulse. The magnetisation that precesses in the XY plane induces an oscillating current in a receiver coil and is the NMR signal. This magnetisation will return to equilibrium when the radio frequency pulse is turned off and thus the signal will decay. This signal is called a Free Induction Decay (FID) (Figure 1.7). To convert this to a normal frequency domain spectrum, Fourier transformation is used, usually by employing the Cooley-Tukey algorithm.

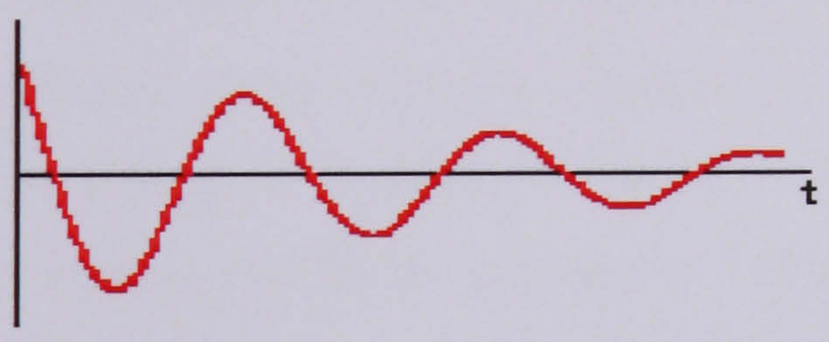

Figure 1.7 Free Induction Decay (FID).

Not all nuclei of the same type (e.g. ^1H) resonate at exactly the same frequency. The resonance frequency depends on the chemical environment, which leads to the phenomenon known as the chemical shift. Additionally, each peak can be split by an interaction called spin-spin coupling - an indirect interaction between magnetic nuclei mediated through the

chemical bonds. In addition peak areas are proportional to both the number of nuclei giving rise to the peak and to the concentration of the substance.

1.6.3 NMR Spectroscopy of Biofluids

One of the most important developments in NMR spectroscopy in the last 20 years has been the application of high-resolution ^{1}H NMR spectroscopy to the analysis of biofluids to investigate and understand numerous diseases and toxic processes. NMR spectroscopy enables the simultaneous detection of a wide range of low-molecular weight compounds within a biological matrix without sample preparation. Biofluids have diverse biological purposes and the composition of biofluids varies with their role and the functional integrity of the organ systems that are communicating with them and ultimately with the physiological status of the whole organism (Nicholson *et al.* 2002). A shift in the physiological status of a living organism in response to disease or xenobiotic exposure will result in subtle modifications in the biochemical composition of its intra- and extracellular fluids. These are often reflected in changes in the composition of other biofluids, such as urine and plasma as the organism tries to maintain homeostatic control.

Metabolic profiles of biofluids such as plasma, urine and cerebrospinal fluid reflect both normal variation and the pathophysiological impact of toxicity or disease on single or multiple organ systems. Therefore, each biofluid will yield a characteristic ^{1}H-NMR spectroscopic fingerprint, which characteristically mirrors their altered endogenous metabolic profile in response to changes in physiological status, toxic insult or disease progression. Plasma and urine are, by far, the most useful and widely used biofluids because they can be obtained in a non- or minimally invasive manner and therefore, are ideal for disease diagnosis and clinical-trial monitoring. Analysis of these biofluids provides an abundance of information on the nature and severity of single or multiple organ dysfunctions thus reflecting the vast array of biochemical processes taking place in key organs and tissues within the body.

NMR spectroscopy of biofluids has clear advantage over conventional analytical techniques as a wide range of metabolites can be detected simultaneously without the need to pre-select metabolites of interest in order to detect and quantify them. Its non-destructive nature and the fact that no- or relatively minimal sample preparation is required makes NMR spectroscopy an ideal technique to probe many cellular biochemical status in the fields of toxicology (Holmes *et al.* 1998), drug metabolism (Bales *et al.* 1988) and clinical investigation (Foxall *et al.* 1995). The pattern of endogenous metabolites in biofluids depends strongly on the type of toxin an animal is exposed to or the animal's disease state. Each toxic compound or disease produces characteristic changes in the concentration and pattern of endogenous metabolites in biofluids that provide information on the sites and/or basic mechanism of toxic or disease processes. Such changes, if detectable, offers a much greater diagnostic value rather than relying on a change in a single chemical entity. This is because it is very difficult to ascertain that a change in a single compound is a marker for the disease or organ dysfunction. Numerous studies on NMR spectroscopy of biofluids have been well documented and some examples are summarised in Table 1.1.

Table 1.1 Examples of NMR spectroscopy of biofluids.

Biofluid	Research Field	References
Bile	Toxicology	(Blackledge *et al.* 2002)
Blood	Inborn errors of metabolism	(Constantinou *et al.* 2004)
Cerebrospinal fluid	Neuropathy	(Ghauri *et al.* 1993)
Plasma	Toxicology	(Anthony *et al.* 1993)
Seminal fluid	Baseline biochemical composition	(Tomlins *et al.* 1998a)
Urine	Physiological variation	(Bollard *et al.* 2001)
Urine	Inborn errors of metabolism	(Holmes *et al.* 1994)
Urine	Pharmaceuticals	(Beckwith-Hall *et al.* 2002)
Urine	Toxicology	(Holmes *et al.* 1998)
Urine	Drug metabolism	(Bales *et al.* 1988)

1.6.4 ^{1}H NMR Spectroscopy of Blood Plasma

Blood makes up about 6% of total body weight in humans. It consists of cellular elements suspended in a complex fluid matrix of proteins, mainly albumin, glycoproteins, lipoproteins and immunoglobulins, together with a vast number of inorganic and low molecular weight organic solvents (Lindon *et al.* 2000). Blood is the vehicle of transportation, transporting oxygen, carbon dioxide, metabolic products and hormones. It is this function that makes possible the specialisation of structure and function that is characteristic of all but the lowest organisms. It is by means of circulating blood that the constancy of the internal environment is maintained. Consequently, the concentration of many blood constituents may vary as a result of diverse influences such as diet and metabolic demand. Additionally, disease processes or abnormalities in the body will lead to the perturbation of the constancy of the internal environment, which are often reflected to various extents in altered blood composition.

Various high-resolution ^{1}H NMR studies have been applied on the biochemistry of blood and its numerous cellular components and plasma (Lindon *et al.* 2000). The ^{1}H NMR spectra of blood plasma can provide a plethora of biochemical information on macromolecular structure and organisation, and on low molecular weight metabolites. The presence of proteins, lipids and lipoproteins in plasma give rise to highly overlapped and broad envelope of ^{1}H signals in NMR spectra which over shadow the resonances from low molecular weight metabolites. However, the complexity of single pulse ^{1}H NMR spectrum of blood plasma can be simplified by the use of spin-echo experiments that allow the signals from high molecular weight metabolites to be attenuated (Nicholson *et al.* 1995). The Carr-Purcell-Meiboom-Gill (CPMG) pulse sequence is an effective means of editing plasma ^{1}H NMR spectra according to their transverse (T_2) relaxation time, thus resulting in the elimination of broad signals from slowly tumbling high molecular weight species and the resultant spectra consist mainly of low molecular weight species, which cannot be resolved in the single pulse experiment.

1.6.5 ^{1}H NMR Spectroscopy of Urine

The kidneys play an important role in the maintenance of body homeostasis, effectively regulating body biochemistry. This is done through the excretion of unwanted organic and inorganic compounds thus maintaining constancy in the internal environment at the expense of variation in urine composition. Therefore, varying urine composition reflects the large number of biochemical processes which take place in the body. This offers a great diagnostic potential in NMR urine analysis. Urine composition is highly variable and complex both between species and within species due to variation in lifestyle, gender and age (Bollard *et al.* 2005, Lindon *et al.* 2000). The kidneys also have an endocrine function that is associated with ionic and water balance. The variable nature of urine composition also reflects the functionality of the kidneys, and physiological and biochemical status of the organisms (Nicholson and Wilson, 1989). It is possible to detect vast numbers of organic species using NMR spectroscopy since a wide range of organic acids and bases, low molecular weight proteins, simple sugars and polysaccharides as well as inorganic species such as Na^{+}, Ca^{2+}, HCO_3^{-} and phosphates are present together in urine (Lindon *et al.* 2000).

The physiological processes in all animals are modulated by biological rhythms. These processes includes excretory processes, consequently, the urinary composition of an animal may vary according the time it is collected. Changes in urinary composition according to diurnal variations can be observed using NMR-based metabonomic method as observed by Bollard *et al.* (2001). Therefore it is imperative that closely matched controls are obtained when studying toxicological or disease processes. Urinary composition also changes according to diet both in man and animals. For example, the consumption of shellfish and fish is associated with high levels of betaine and trimethylamine in urine (Nicholson and Wilson 1989). Thus it is critical to distinguish these dietary signatures from disease-related processes in clinical or toxicological studies.

1.7 Introduction to Magic Angle Spinning NMR

Tissue samples can provide complementary information to that obtained in biofluids. However, obtaining useful biochemical information from ^{1}H NMR measurements of intact tissues *in-vivo* can be difficult as the spectral quality is severely compromised by the utilisation of low magnetic fields (Lindon *et al.* 2004). In addition, heterogeneity of the sample usually gives rise to magnetic susceptibility differences causing magnetic field inhomogeneity. This combined with restricted molecular motions of molecules in tissues leads to low sensitivity and resolution. Consequently, NMR spectral analysis of tissues has relied largely on tissue extraction methods. This requires relatively large amounts of tissue sample and multiple extraction methods to extract both the lipophilic and lipophobic phases. Although it is possible to extract water and lipid soluble compounds by using extraction techniques, the extract composition usually reflects the solubility of the metabolites as well as the tissue compositions. In addition, extraction methods do not take into account the composition of cell membrane constituents as aqueous soluble metabolites may be encapsulated in lipid compartments thereby inhibiting their extraction. Such bilayer structures are usually associated with chemical and more importantly xenobiotic transport around the cell. Moreover, extraction techniques are destructive in nature. *In vivo* ^{1}H magnetic resonance spectroscopic (MRS) studies, on the other hand, uses low magnetic fields thus suffers from low sensitivity and spectral dispersion.

Magic Angle Spinning (MAS) was initially developed to study rigid solids mainly in ^{13}C NMR spectroscopy. ^{13}C is a very dilute nucleus therefore produces low sensitivity. To obtain high-resolution ^{13}C NMR spectra, three techniques were combined:

1. ^{1}H to ^{13}C spin cross polarisation to improve sensitivity
2. High power broadband decoupling of ^{1}H nuclei to remove heteronuclear dipolar coupling.

3. Magic Angle Spinning (MAS) to remove remaining residual dipolar coupling and ^{13}C chemical shift anisotropy.

However, the development of high resolution ^{1}H magic-angle-spinning (MAS) NMR and its application in the field of metabonomics within the past few years has had a significant impact on the ability to analyse intact tissues (Garrod *et al.* 1999). An advantage of high resolution MAS NMR is that it avoids time-consuming sample extraction processes by analyzing the tissue directly and it is possible to observe metabolites lost in extraction processes through MAS NMR.

1.7.1 Principles of Magic Angle Spinning NMR

Molecules in liquid phases undergo fast isotropic motion and thus the chemical shift and spin coupling values, which are orientation dependent, are simple isotropic averages of second rank tensors (Andrew and Szczesniak 1995). This effectively removes line-broadening effects from the spectrum. In anisotropic environments, a new interaction termed direct dipole-dipole coupling (with an isotropic average value of zero) can be manifested. Biological samples, especially tissues, do not behave as true solids because the molecules experience some mobility in the cell compartments. Therefore they exhibit intermediate behaviour between a rigid solid and isotropic liquid and the interactions, which cause line broadening in solids, are partially averaged out.

In MAS NMR spectroscopy, the tissue sample is placed in a zirconium rotor (Figure 1.8A) using a spacer. The use of a spacer enables analysis using smaller total sample size and thus easier adjustment of the shimming of the B_0 magnetic field to achieve homogeneity across the whole sample. This results in improved spectral quality. The rotor is placed into a magnet, tilted and rotated at an angle, β relative to the applied magnetic field, B_0. This causes a modulation of the anisotropic interactions by a factor of $3(\cos^2\beta\text{-}1)/2$. If β is chosen to be 54.7° (i.e. when $3\cos^2\beta\text{-}1 = 0$) then the average value of the anisotropic parameters goes to zero. 54.7° is also known as the magic angle (Figure 1.8B). The advantage of using semi solids is that the ^{1}H-^{1}H dipolar couplings are partially averaged by

the resulting restricted molecular motion thus resulting in moderate line broadening. MAS experimental conditions can be applied to improve resolution and produce spectra with narrow lines.

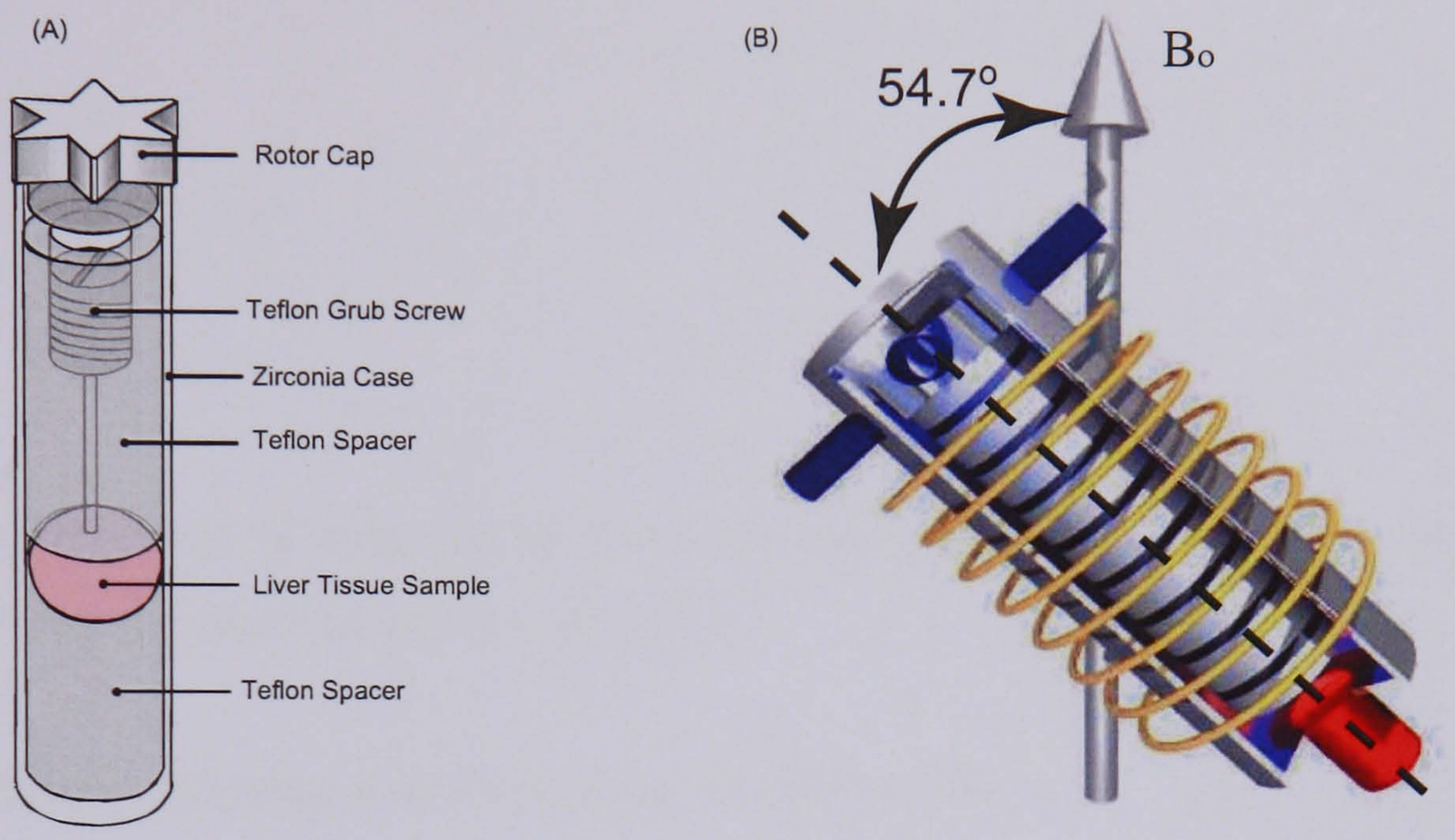

Figure 1.8 Schematic diagram of: (A) magic angle spinning rotor (adapted from Mehta 2004), and (B) Sample spinning at the magic angle ($\theta = 54.7°$).

In order for the MAS experiment to succeed, the spinning frequency must be greater than the value of the anisotropic broadening. Figure 1.9 shows the effects of spinning a sample at the magic angle on spectral resolution. However, the disadvantage of MAS-NMR is that it is time consuming where it is only possible to analyse about 10 samples per day as compared to solution state NMR, which can analyse more than 100 samples per day.

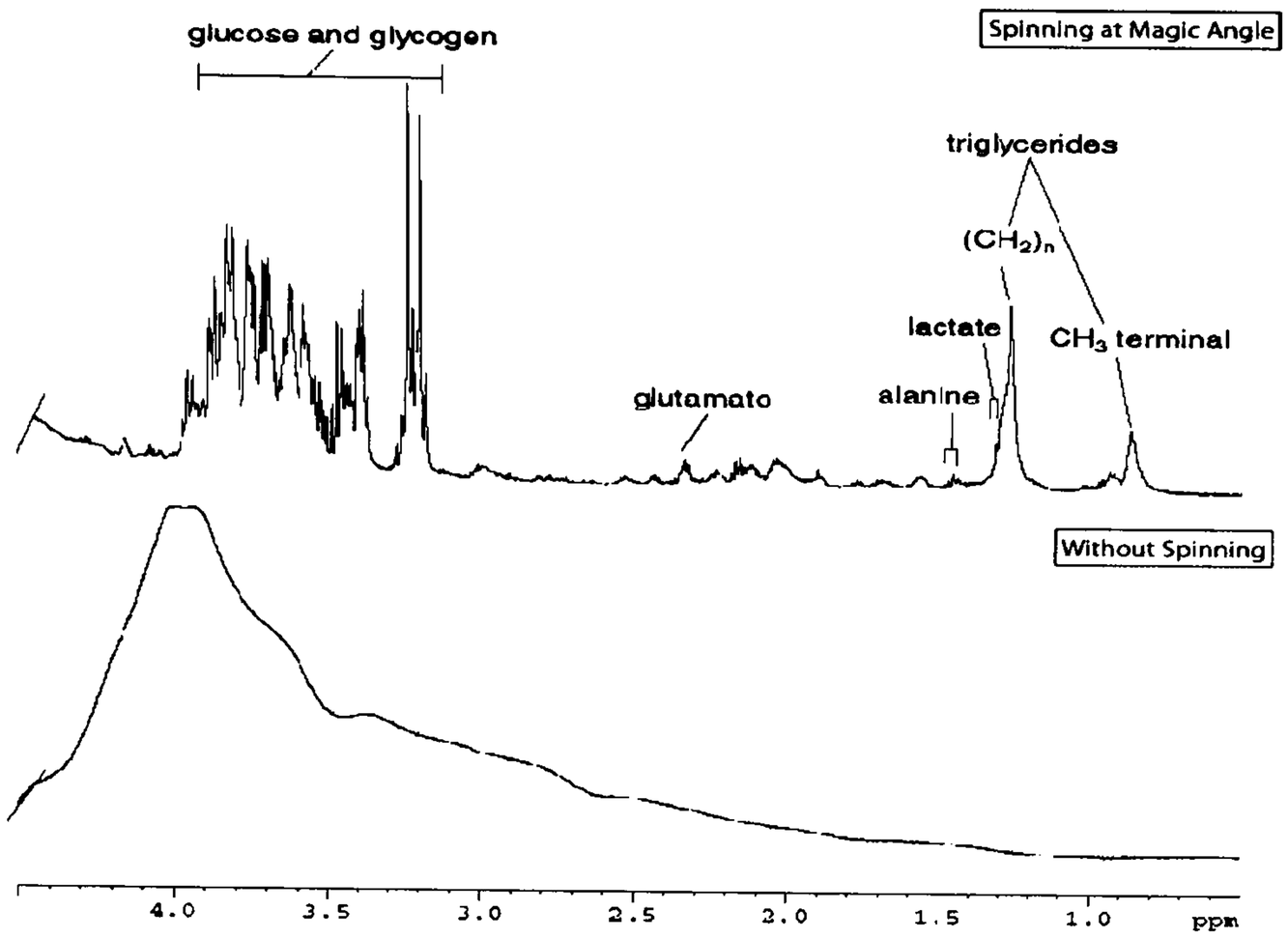

Figure 1.9 Effect of spinning at the magic angle on ^{1}H NMR spectral resolution in intact rat liver tissue (Bollard *et al.* 2000).

1.7.2 Factors Affecting Line Broadening in MAS NMR

1.7.2.1 Dipolar Coupling

Dipolar coupling (D) is an anisotropic effect. Dipolar coupling between two nuclei is usually the major contributor to line broadening effect in solids and semi-solids. Dipolar coupling between two nuclei A and B is given by the equation:

$$D_{AB} = \gamma_A \gamma_B r_{AB}^{-3} (3\cos^2\theta_{AB}-1)$$

Where, γ_A and γ_B are the magnetogyric moments of A and B, r is the internuclear distance and θ is the angle between the internuclear vector and the magnetic field, B_o. Dipole coupling is orientation dependent such that if the internuclear vector is parallel or perpendicular to B_o then the relative values will be +1 or –0.5 respectively. In solutions, the rapid isotropic motion averages the dipolar couplings to zero but the value of D at any one time will not be zero. These transient fluctuating interactions are an important source of spin relaxation giving rise to the Nuclear Overhauser Effect (NOE). In solids, the average of D is never zero. The D value between two hydrogens in a solid crystal can be as large as

20000 Hz. In a powder, the internuclear vector will experience a range of orientations from parallel to perpendicular to B_o thus resulting in a 'Pake doublet' broad line (Figure 1.10).

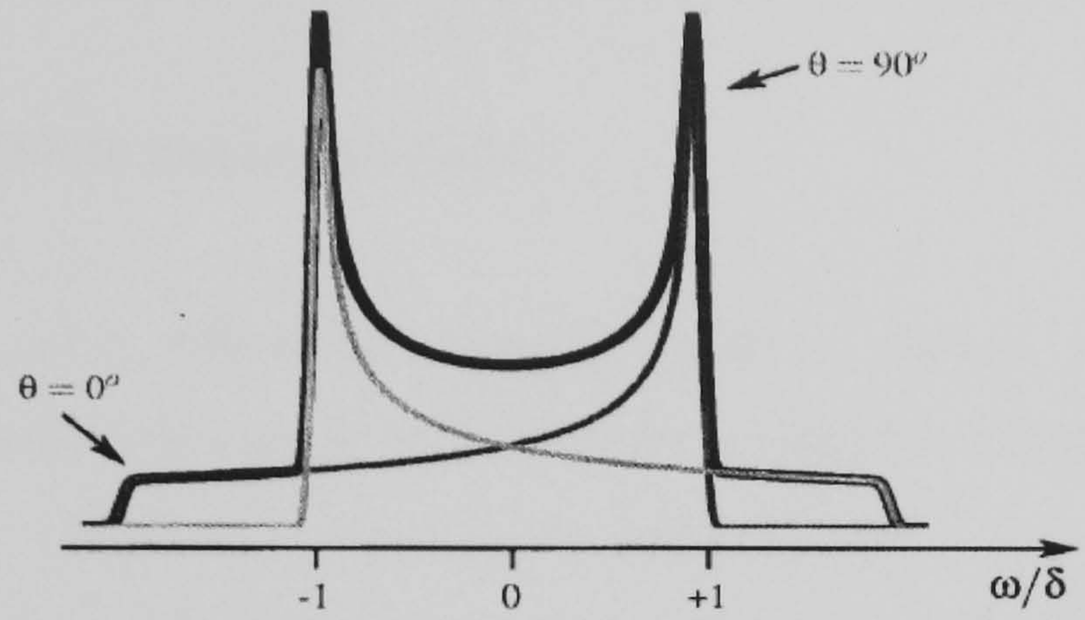

Figure 1.10 'Pake' doublet.

Therefore, to generate a sharp line, the molecule must tumble fast enough to produce an average isotropic motion, which will give a dipolar coupling of zero. Biological tissues do not behave as true solids instead they exhibit intermediate behaviour between true solid and liquid because of the restricted molecular mobility due to tissue compartmentalisation. Therefore some components will experience considerable molecular motion, which can be either faster or slower than the other albeit slower in general as compare to liquid. This will generate an anisotropic effect due to residual dipolar couplings thus resulting in line broadening. The dipolar couplings in tissues are usually ≤ 1 kHz.

1.7.2.2 Magnetic Susceptibility

Another major contributor to line broadening effects in semi-solids is anisotropy in magnetic susceptibility. Biological tissue i.e. liver samples are heterogeneous in nature, containing significant amounts of water, lipids, and other fluid components in different compartments. These samples suffer from anisotropy in magnetic susceptibility due to magnetic field inhomogeneity because components inside and outside a compartment will experience different magnetic fields leading to severe line broadening. Anisotropic magnetic susceptibility has a similar angular dependence to dipolar coupling. Therefore, magic angle spinning can be applied to circumvent the line broadening effect induced by

magnetic susceptibility anisotropy. Any differences in the isotropic value of the magnetic susceptibility due to different cellular environments for example will give rise to a chemical shift difference for a molecule, which is present in both compartments.

1.7.2.3 Chemical Shift Anisotropy (CSA)

Chemical shifts occur when the magnetic field is applied to the electron density surrounding a nucleus and thus shielding a nucleus. Chemical shifts in solids depend on the orientation of the molecule relative to the magnetic field, B_o, applied. It is direction dependent. In a liquid the movements of the molecules are fast enough to produce a rapid isotropic motion, which therefore averages the chemical shift to a single value. In solids these chemical shifts are not averaged to one value because of the way the molecules are held in a tethered conformation. However, this is not a serious problem in ^{1}H NMR spectroscopy because chemical shift anisotropies are small even before the motional averaging process.

1.7.3 Application of MAS NMR Spectroscopy in Tissues Analysis

Although MAS NMR method is time-consuming as compared to solution state NMR, it requires little or no sample preparation at all. In addition, the spectral information obtained has proven to be invaluable in the field of metabonomics. Recent advances in MAS instrumentation and probe technology, has made it possible to analyse very small biological tissue samples directly, ca 8 mg (Bollard *et al.* 2001), with little or no sample treatment required and an MAS NMR spectrum, comprising well-resolved sharp peaks, can be acquired in less than 10 minutes. The application of NMR in tissue analysis has revealed that there are enormous differences between the diseased and toxin-affected tissues, and those of healthy organ (Moka *et al.* 1998, Waters *et al.* 2002). The application of MAS NMR to study tissue compartmentalisation by Griffin *et al.* (2000a) has yielded vital information on not only tissue compartmentalisation but on molecular dynamics as well which would have otherwise been very difficult to obtain. ^{1}H MAS NMR spectroscopy enables a holistic analysis of tissues, providing a link between biofluid and histopathology

and an insight into the actual mechanisms of toxicity at a molecular level (Lindon *et al.* 2004)

The various pulse sequences, spectral editing and 2-dimensional techniques used in normal fluid NMR can also be applied in MAS NMR and this make MAS NMR a very versatile method for tissue analysis. The principle of spectral editing is based largely on the spin properties of both macromolecules and small molecules, whereby the limited translational motion and longer rotational correlation times experienced by macromolecules entail a shorter T_2 (transverse) relaxation time and smaller diffusion coefficient compared to those of smaller molecules (Johnson Jr. 1999, Wang *et al.* 2003). Spectral editing utilising T_2 relaxation time is termed T_2-edited spectroscopy (Stejskal and Tanner 1965). One of the most common T_2-edited spectroscopy methods used is the Carr-Purcell-Meiboom-Gill spin-echo pulse-sequence, which is very effective in removing broad signals from slowly tumbling macromolecules. Conversely, it is also possible to attenuate signals from smaller molecules with fast molecular diffusion coefficient to produce a spectrum of only macromolecules and slow-moving molecules and this is termed diffusion-edited spectroscopy. Molecular diffusion can cause NMR signal intensity changes when pulse field gradient are applied during the NMR experiment (Stejskal and Tanner 1965). Diffusion-edited spectroscopy has been successfully applied to study lipoproteins in blood plasma (Liu *et al.* 1996). Therefore it is noteworthy that by utilising both transverse relaxation and molecular diffusion coefficients the characterisation of biomolecules in complex biological matrix such as tissues can be improved.

The NMR methods are extended by 2-dimensional spectroscopy. The use of J-Resolved NMR, where the spin-coupled multiplets are rotated at 90 ° to the chemical shift axis to reduce spectral overlap also causes exclusion of broad peaks, which are normally associated with macromolecules and more resolved signals can be obtained for the endogenous metabolites of interest. This technique is based on the spin-echo technique and works well because most small metabolite signals have long T_2 relaxation times. The use of ^1H - ^1H MAS Total Correlation Spectroscopy NMR (MAS TOCSY NMR), where information on protons, which are close together in chemical bond terms, can be obtained.

This is highly useful for biomarker identification (Moka *et al.* 1998). High resolution MAS NMR offers a way for the first time to simultaneously investigate all the different components of the cell. It provides very informative data for studying lipid profiles particularly for long-term effects of lipophilic xenobiotics (Griffin *et al.* 2000a). The application of the ^{1}H - ^{13}C Heteronuclear Multiple Quantum Coherence (HMQC) technique, where values of hydrogen and carbon chemical shifts in CH_n groups of metabolites can be determined, provides information on small molecules, cytosolic components, and macromolecular and supramolecular bodies i.e. lipid moieties (Moka *et al.* 1998). The application of MAS NMR spectroscopy on various biological samples has been well documented. Some examples are listed in Table 1.2.

Table 1.2 Examples of MAS NMR spectroscopy of tissues.

Tissue Sample Type	Field of Research	References
Adipocyte tissue	Oncology	(Millis *et al.* 1999)
Brain tissue	Oncology	(Griffin *et al.* 2003a)
Breast tissue	Oncology	(Cheng *et al.* 1998)
Cardiac tissue	Genetic disorders	(Griffin *et al.* 2001)
Cardiac tissue	Biochemical composition	(Bollard *et al.* 2003)
Endometrial cell	Oncology	(Griffin *et al.* 2003b)
Liver tissue	Biochemical composition	(Bollard *et al.* 2000)
Liver tissue	Toxicology	(Wang *et al.* 2003)
Neuronal and glial cells	Neurology	(Griffin *et al.* 2002)
Prostate tissue	Oncology	(Tomlins *et al.* 1998b)
Renal tissue	Biochemical composition	(Waters *et al.*, 2000)
Renal tissue	Oncology	(Tate *et al.* 2000)
Renal tissue	Toxicology	(Garrod *et al.* 2001)
Testicular tissue	Biochemical composition	(Griffin *et al.* 2000a)

1.8 Introduction to Multivariate Data Analysis

Modern analytical methods such as NMR spectroscopy and chromatography generate large data sets where large numbers of variables are measured over large numbers of specimens. These multivariate data sets require specialised techniques, which can handle, interpret and predict the data sets in order to identify and display structure within the chemical data, and extract chemical information. Multivariate data analysis (MVDA) is the analysis of data with many observed variables as well as the study of systems with many important types of variation (Martens and Martens 2001). MVDA belongs to a family of statistical techniques that are designed to handle complex multivariate data.

1.8.1 Pattern Recognition

Pattern recognition (PR) methods are often used to identify significant "patterns" within complex multiparametric data sets. It is a common phrase used to define data analysis methods that can be used to generate scientific hypotheses as well as testing the hypotheses by ways of reducing the many parameters mathematically (Nicholson *et al.* 1999). The aim of pattern recognition is to identify the intrinsic patterns or clustering behaviour in a set of measurements so as to categorise an object or predict the origin of an object; and to explain the relationship between the observations within each class in complex data sets. It is also used to reduce the dimensionality of complex data sets thus facilitating the visualisation of inherent patterns in a data set.

NMR spectra of tissues and biofluids are highly complex, containing thousands of overlapping resonances within a small chemical shift range (10 ppm). This can make it difficult to extract meaningful biochemical information from the NMR spectra. Therefore, computer-based pattern recognition (PR) and expert systems have been used to enable interpretation of the complex multivariate NMR spectral data. Pattern recognition on NMR spectra enables classification of samples as being normal or abnormal, classifying target-organ toxicity and the site and mechanism of action within the organ, identifying potential biomarkers of toxicity and evaluating the time course of the effect i.e. the onset, evolution and regression of toxicity (Nicholson *et al.* 2002)

Pattern recognition methods can be either 'unsupervised' or 'supervised'. In the 'unsupervised' approach, the inherent clustering behaviour of a set of samples is established without prior knowledge of classes. The most commonly used 'unsupervised' pattern recognition approaches are Principal Components Analysis (PCA) (Van Der Greef *et al.* 1983, Wold 1978, 1987), Non-Linear Mapping (NLM) (Kakuso and Mizoguchi, 1983, Van Der Greef *et al.* 1983) and Hierarchical Clustering Analysis (HCA) (Chtioui *et al.* 1996, Beckonert *et al.* 2003). 'Supervised' approaches, however, rely on prior knowledge of classes. This approach attempts to determine the characteristic or distinguishing features of pre-specified groups. The commonly used 'supervised' methods are Partial Least Squares regression (PLS) (Gerlach *et al.* 1979), Soft Independent Modelling of Classification Analogy (SIMCA) (Blomquist *et al.* 1979, Wold *et al.* 1981) and K-Nearest Neighbour (KNN) (Van Der Greef *et al.* 1983, Kakuso and Mizoguchi 1983, Beckonert *et al.* 2003). Preliminary analysis often involves the use of 'unsupervised' pattern recognition methods such as PCA to establish the site- and/or mechanisms-related metabolic responses. This is followed by more sophisticated 'supervised' algorithms, which can be applied to the data using the knowledge on sample class to optimise the differentiation between classes. This enables the extraction of information relating to biomarkers of toxicity or recovery, which will further the understanding of the mechanisms of toxicity.

1.8.2 Data Reduction and Pre-processing of NMR spectra

Prior to pattern recognition, the highly complex high-resolution ^{1}H NMR spectral region (δ 0.02 - δ 9.0) can be digitised into integrated regions (typically 250 sequential spectral regions of 0.04 ppm width for urine and plasma samples, and 830 sequential spectral regions of 0.01 ppm for tissue samples). The 0.04 ppm bucket width was chosen for urine samples in order to account for variations in the pH-dependent chemical shift species i.e. citrate. Certain spectral regions carry no real diagnostic or conflicting biochemical information. Typically the spectral region between (δ 4.5 and δ 6.0), where residual water and urea protons resonate, are usually removed to eliminate variations in water suppression and the urea signal due to partial cross saturation via proton solvent-exchange. Water peak

suppression is carried out due to the dynamic range problem with water in comparison with other metabolites. Small variations in water suppression can lead to classification problems. Partial cross saturation of urea and water will occur thus the urea signal can be affected by variation in water suppression.

Variation in data not related to differences between treatment groups confounds any method of analysis. These variations cannot be removed even with careful experimentation and thus must be treated and minimised by normalization to make comparisons made on the data set as sensitive as possible by ensuring the variation remaining within the data set is related to the phenomenon of interest. Normalisation is very important when analyzing tissues and biofluids because the former suffers from variation in tissue weights and the latter suffers from concentration differences and differences in osmolarity. The reduced spectral data are normally normalized to constant total spectral area. Each spectral integral is standardized to the sum of the absolute value for all the spectral integrals.

Scaling is an essential step of pre-processing in the analysis of spectral data in order to optimize information recovery. There are a variety of scaling methods that are used to scale spectral descriptors. The commonly used scaling techniques are mean centering, unit variance (auto scaling) and Pareto. In mean centering, the average value of each variable is calculated and subtracted from the data. This improves model interpretability when the variables are aligned together (Figure 1.11). Mean centering highlights the variations in high concentration signals in the spectra. It is used when the measurement units for variables are in the same scale of magnitude i.e. spectroscopic units. With unit variance scaling, each variables range is divided by its standard deviation to give all the variables an equal variance. Thus, by converting all variables to a comparable footing, no variable will dominate over another because of its numerical range. Through unit variance scaling, both variables with larger and lower ranges will have the same variance although the mean values remained different. Therefore, small variations in the levels of low concentration signal in the spectra will be detected. Unit variance scaling is effective when variables have different units of measurement and are not directly comparable. However, unit variance scaling has the tendency to make analyses more susceptible to the influence of artefacts. In

Pareto scaling, each variable is given a numerical variance that is equal to its initial standard deviation. Thus, Pareto scaling is intermediate between mean centering and unit variance (Eriksson *et al.* 2001)

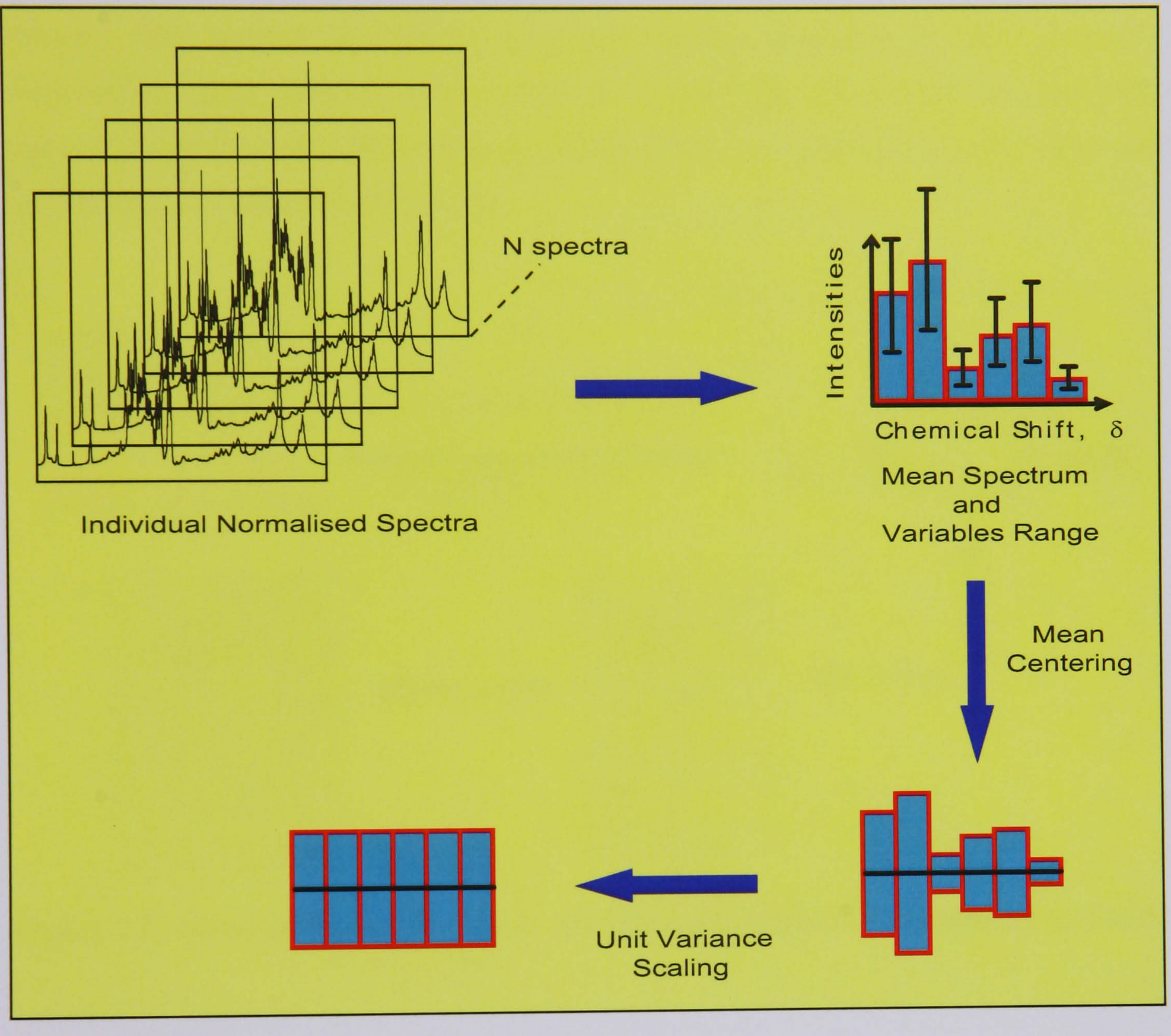

Figure 1.11 Schematic representation of mean centering & unit variance (adapted from Eriksson *et al.* 2001).

The strategy for metabonomic analysis is shown in Figure 1.12. The spectra are obtained and processed (A), primary data reduction is carried out by the removal of all the redundant signals, normalisation of spectral data, application of appropriate scaling, and digitization of the one dimensional spectrum into a series of typically 250-1000 integrated regions (B). Primary data analysis is used to map the samples according to their biochemical composition, using methods such as PCA (C). Each class of samples is then modeled separately and class boundaries and confidence limits are calculated to construct a model for prediction of independent data (D).

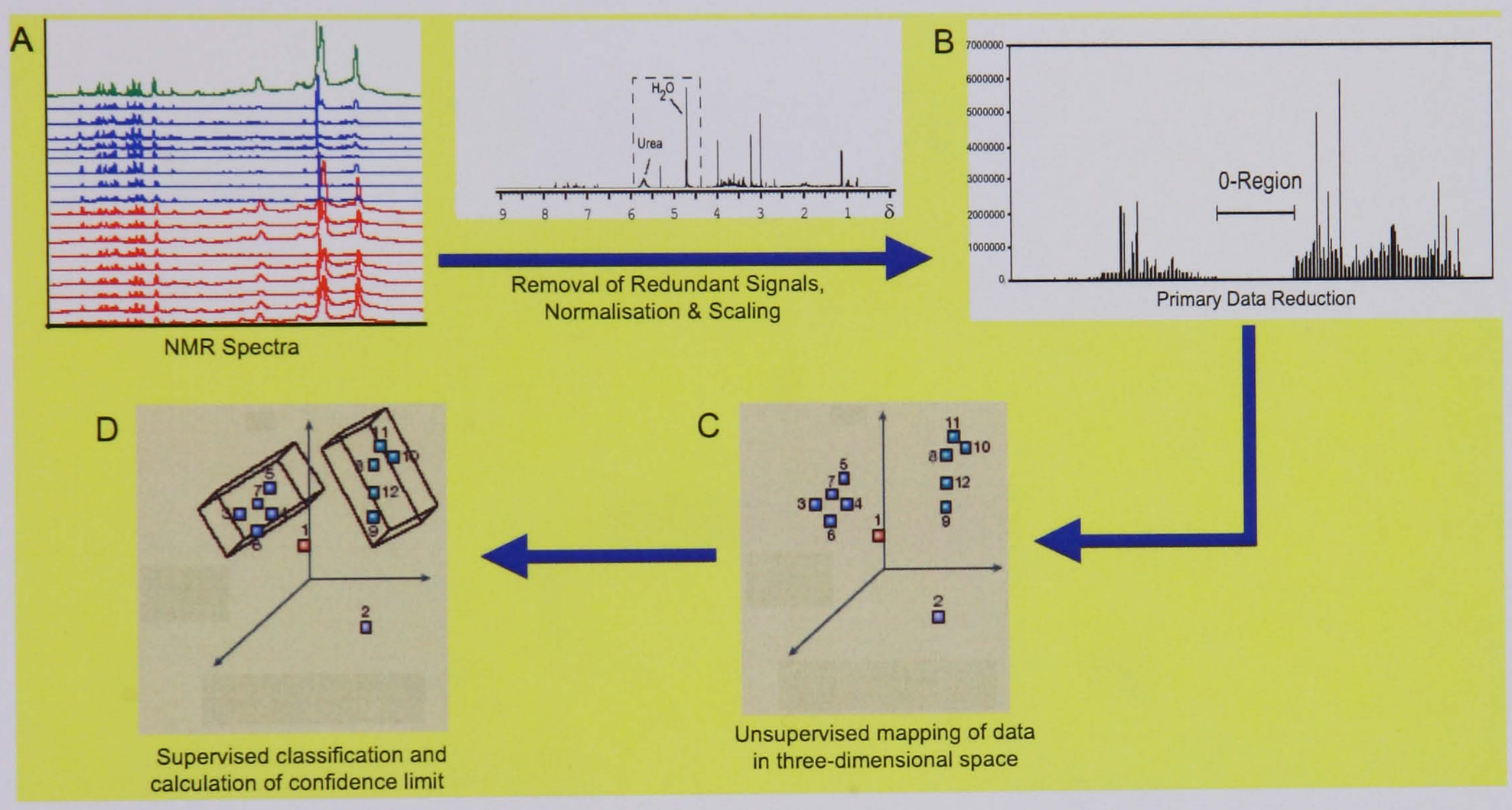

Figure 1.12 Strategy for metabonomic analysis (adapted from Nicholson *et al.* 2002).

1.8.3 Principal Components Analysis (PCA)

PCA is regarded as the 'mother of all multivariate methods' (Martens and Martens 2001). It is employed to represent highly complex multivariate data i.e. NMR spectra as a low-dimensional plane to obtain an overview of the data for trends and patterns that are dominating the data set as well as relationships between observations and variables, grouping observations, time trends and outliers (Eriksson *et al.*, 2001). As mentioned above, PCA is an unsupervised approach with no *a priori* assumptions being made about the sample classes.

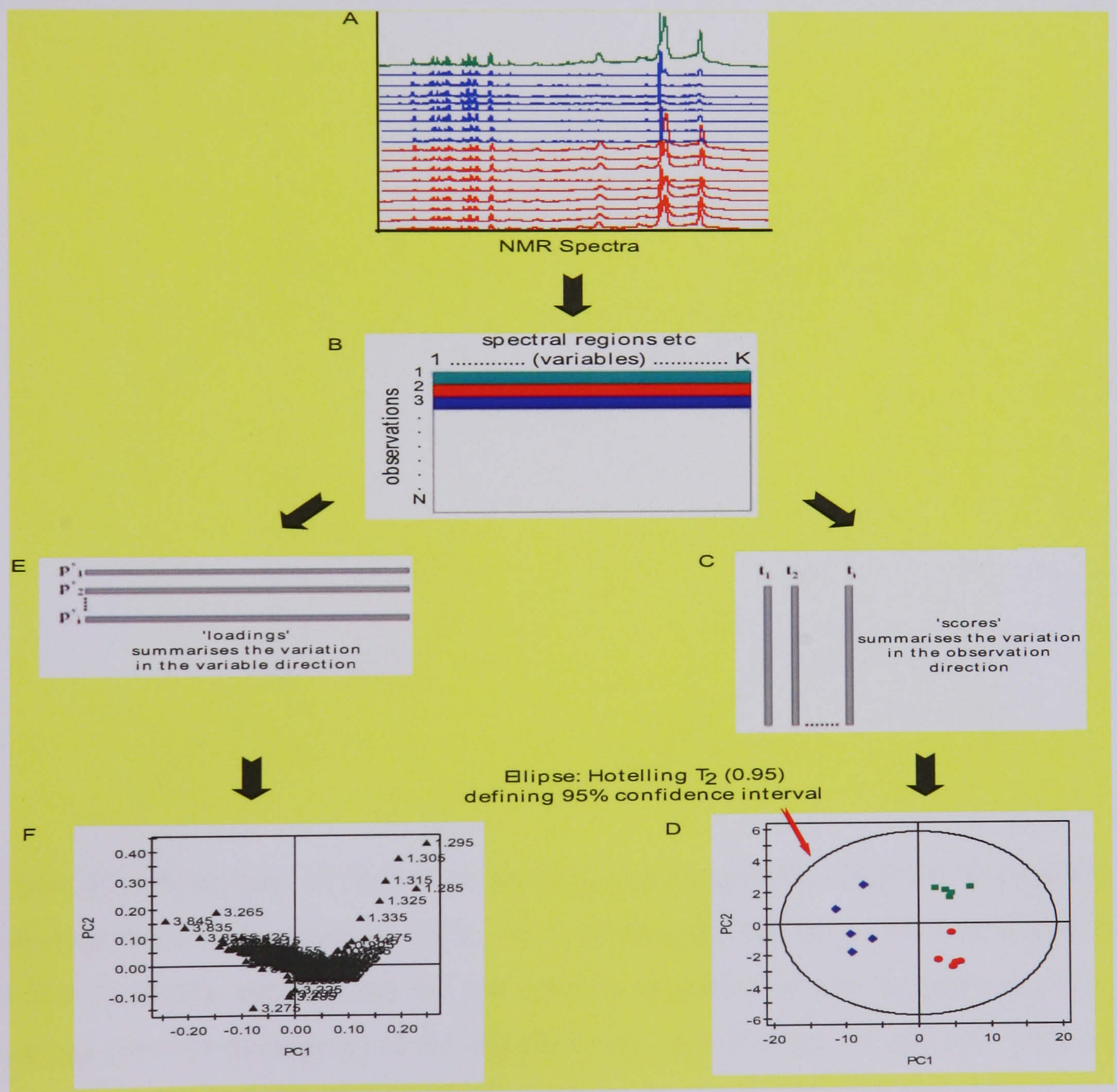

Figure 1.13 Principal Component Analysis Sequential Diagram.

Statistically, PCA enables projection of data vectors in an *n* dimensional hyperplane (where *n* is typically 2 or 3), with as much of the variance explained as possible within the dimensions. It reduces the dimensionality of the initial data set (Figure 1.13A) according to its main variation in order to obtain an overview of the data. In an X-matrix (Figure 1.13B) with N-observations (e.g. NMR spectra) and K-variables i.e. the number of integral values for peaks per spectrum, a K-dimensions space is constructed (Figure 1.14A) with each variable representing a coordinate axis plotted in this K-dimensional space (Figure 1.14B). The effect of mean centering basically moves the origin of the co-ordinate system so that its origin now coincides with the average of the cluster of observations (Figure 1.14 C and D).

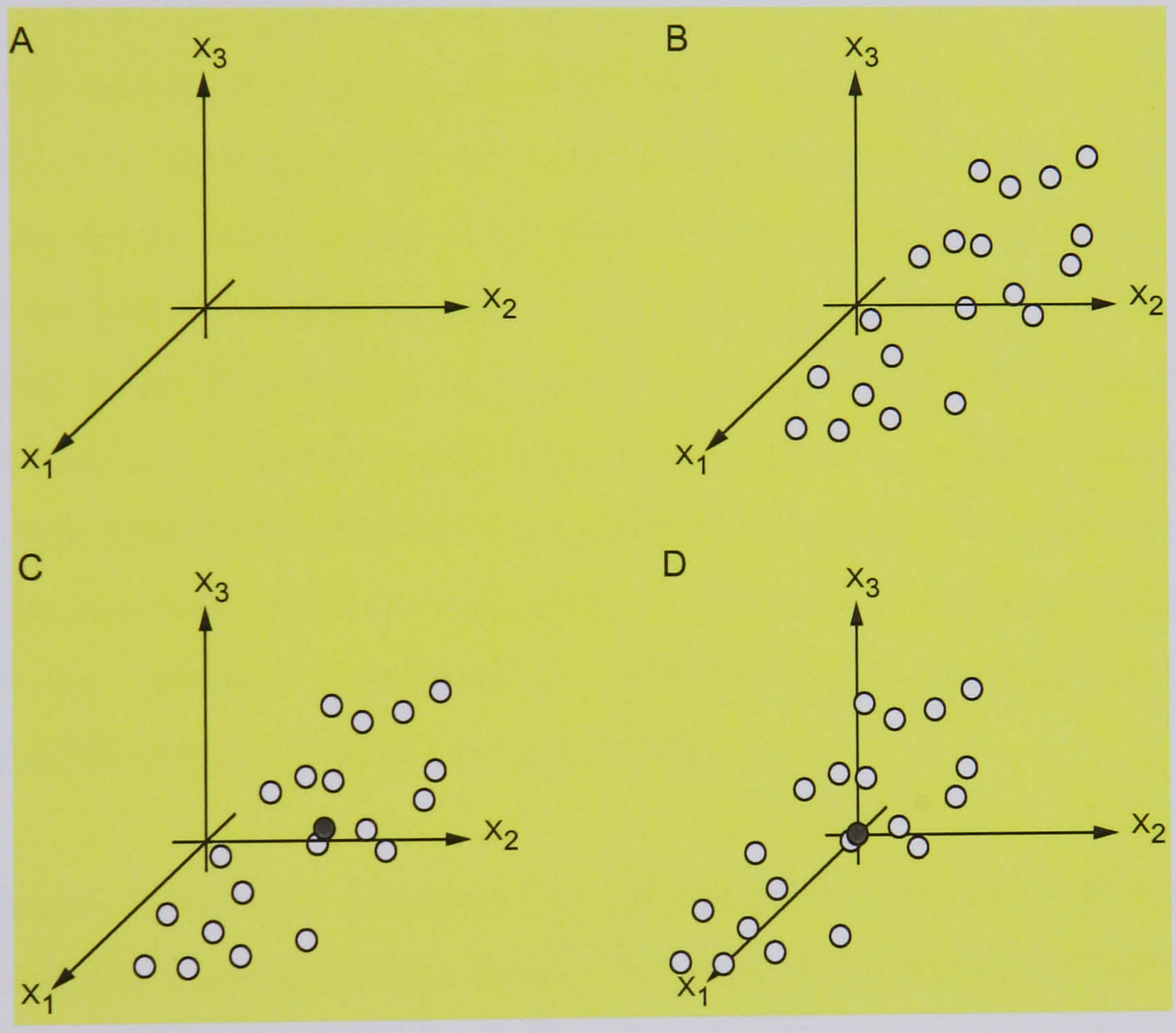

Figure 1.14 Principles of K-dimensional hyperspace and the effects of mean centering (adapted from Eriksson *et al.* 2001). (A) A K-dimensional space. (B) The observations in the X-matrix represented by the swarm of points in the hyperspace. (C) The average point (● dark grey) in the middle of the swarm of points. (D) The origin of the co-ordinates is moved to the centroid.

PCA finds planes in the K-dimensional space that best approximate the data in a least square sense. Each component is expressed as combinations of the response variables, and explains the dispersion structure in the data set; hence they are called Principal Components (PCs). The first PC is a linear combination of the original input variables with appropriate weighting coefficients and contains the maximum variance in the data set. The second PC is another linear combination of the variables that is orthogonal to the first PC and explains the next highest variance in the data set. Successive PCs are orthogonal and will therefore explain less of the data variance until the PCs only consist of the data noise.

In order to get the new scores (t) (Figure 1.13C), each N-observation must be projected onto the plane and the axes are described by the relevant PC. Scores plot (Figure 1.13D), which is a 2- or 3- dimensional PC map, can be constructed to visualise information in the data set. The scores plot enables investigation of any inherent clustering behaviour of samples in the data set. Variables, which are correlated to each other and variables, which are influential in the PCs, can be investigated by the principal component loadings. The loadings (Figure 1.13 E and F) describe the orientation of the original variables in the PC plane therefore reveals the variables contributing to the scores plot. It provides information regarding the variables which are responsible for the pattern observed in the scores plot, and details the variable's correlations to each other. The loadings also describe the importance of the original variables to the respective PC.

In PCA models, there exists a fundamental difference between how well a model fits the data and its ability to predict other samples. The quantitative measure of how well a model can fit the data is linked to the amount of variation within the data set that can be explained by the model. This is given by the parameter R^2. The problem with trying to fit a model well is that with sufficiently many components in the model, R^2 can be made arbitrarily close to the optimal value of one, thus, the model is said to be over-fitted. However, this is not the case for the prediction ability Q^2. Q^2 is a measure of how accurately the X data can be predicted either by using the existing data set or by using an independent validation set of observation set. The addition of many latent variables may introduce components, which are uncorrelated with the patterns within the data set therefore reducing the predictive

ability of the model. Consequently, the number of PCs selected for a model is aimed at maximising both the Q^2 and R^2 values.

1.8.4 Projection to Latent Structures by means of Partial Least Squares (PLS)

PLS is designed to relate two data matrices, X and Y, with each other by means of a linear multivariate model. It is a regression extension of PCA. It provides a means to model X and Y data matrices as well as to identify input and process variables (X) that are responsible for the change in the output variables Y with the aim of maximizing the correlation between X and Y. These models of X and Y spaces attempt to approximate the best variation in the point swarms of the X and Y spaces thus giving a geometric interpretations similar to that of PCA. However, PLS models of X and Y spaces share an inner relation such that the scores of X space can be related to the Y space thus maximizing the covariance between the scores. The first PLS component through the point swarms of the X and Y spaces provide a maximum correlation between each components whilst maintaining good approximation of each space. Successive components are orthogonal to preceding components.

PLS-Discriminant Analysis (PLS-DA) emphasise more on class separation to ensure maximal separation between pre-defined classes is achieved. The method involves the rotation of the projection of latent variables. Latent variables are formed as the linear combination of all the original variables in the X matrix in such a way that most of the association with the Y variables can be explained together with the variation in X (Lee *et al.* 2003). Unlike PCA or PLS, the Y matrix of PLS-DA consists of a set of dummy variables, which are set up to describe the class membership of each observation in the X matrix. These dummy variables comprises a series of ones and zeros set in columns such that observations for a set class, B, will have a value of one and the others zero. The quantitative measure of the discriminatory power for each chemical descriptor in a PLS-DA model can be obtained from a Variable Importance Plot (VIP). The higher the numerical value for a variable in the VIP plot, the strongest its discriminatory ability in the X-matrix. However, it is important to note that discriminative techniques like PLS-DA, have a

tendency to over fit when variables out number samples. Therefore, it is very important to validate the models.

Chapter 2: Materials and Methodology

2.1 Introduction

2.2.1 Outline of toxicity study design

All animal studies were conducted in accordance to the requirements of the relevant national legislation and local guidelines. The studies were carried out at Pfizer, Centre de Recherche, Amboise, France. Male Sprague-Dawley rats (250 g, Charles River, St. Germainsur-l' Abresle, France) were acclimatised in individual metabolic cages with free access to water and standard rodent diet (diet A04C, Usine d'Alimentation Rationelle, Villemoisson-sur-Orge, France). Compounds and control treatments were administered on day 1 by intraperitoneal injection with the dosages and animal numbers shown in Table 2.1. All treatments were single dose with a constant volume of administration with each study.

2.2.2 Sampling, pathology and clinical chemistry analyses

Using CO_2, five animals of each treatment group were euthanased post-dosing at day 2 and the remainder at day 8. Prior to euthanasia, individual pre- and post-dose urine samples were collected into ice-cooled vessels containing 0.1 ml of a 100 mg/ml solution of sodium azide for 7 h daily with an additional overnight urine collection on the day of dosing. Urinary volumes were measured by gravimetry. Individual blood samples were taken under isoflurane anaesthesia from the orbital sinus, immediately prior to euthanasia. These were collected into vials containing lithium heparin as anticoagulant and the plasma obtained by centrifugation. A summary of the sampling regime is show in Table 2.2 and Table 2.3.

Table 2.1: Summary of animal studies.

Study Number	Compound	Study Group	Dose of toxin administered (mg/kg)	Animal Number	Euthanased	
					Day 2	Day 8
98053	Saline	Control	0	1-10	6-10	1-5
	Allyl Formate in saline	Low Dose	25	101-110	106-110	101-105
		High Dose	75	201-210	206-210	201-205
	Chlorpromazine in saline	Low Dose	30	301-310	306-310	301-305
		High Dose	60	401-410	406-410	401-405
99057	Saline	Control	0	1-10	6-10	1-5
	Thioacetamide in saline	Low Dose	50	301-310	306-310	301-305
		High Dose	200	401-410	406-410	401-405

Table 2.2 Sampling regime for animal study 98053

		Study Day										
		Pre-dose		Post-dose								
		-2	*-1*	*1*	*1*	*2*	*3*	*4*	*5*	*6*	*7*	*8*
GROUP	*Urine Collection period (hrs)*	0-7	0-7	0-7	0-7	0-7	0-7	0-7	0-7	0-7	0-7	-
	Late euthanased group (Day 8)	**BU**	**U**	**U**	**U**	**U**	**U**	**U**	**U**	**U**	**U**	**BL P**
	Early euthanased group (Day 2)	**BU**	**U**	**U**	**U**	**BL P**						

B = blood, U = urine, L = liver, and P = pathology

Table 2.3 Sampling regime for animal study 99057.

		Study Day											
		Pre-dose			Post-dose								
		-3	*-2*	*-1*	*1*	*1*	*2*	*3*	*4*	*5*	*6*	*7*	*8*
GROUP	*Urine Collection period (hrs)*	0-7	0-7	0-7	0-7	0-7	0-7	0-7	0-7	0-7	0-7	0-7	-
	Late euthanased group (Day 8)	**BU**	**U**	**U**	**U**	**U**	**U**	**U**	**U**	**U**	**U**	**U**	**BL P**
	Early euthanased group (Day 2)	**BU**	**U**	**U**	**U**	**U**	**BL P**						

B = blood, U = urine, L = liver, and P = pathology

2.2.3 Necropsy and pathology

Necropsy was carried out immediately after euthanasia. The liver was weighed and duplicate samples of the left liver lobe were immediately snap-frozen in liquid nitrogen and stored at -70°C for subsequent NMR analysis. Liver samples were embedded in paraffin wax, sectioned (4-6 μm) and stained with hematoxylin and eosin for histopathological assessment. Selected liver samples were also stained with Oil Red O and according to the periodic acid-Schiff method.

2.2.4 Clinical chemistry

Clinical chemistry was carried on a Monarch 200 centrifugal analyser (Instrumentation Laboratory, Warrington, UK) in Study 98053 and on AU600 multiparametric analyser (Olympus, Hamburg, Germany) in Study 99057. The plasma parameters urea, glucose (GLUC), total bile acids (TBA), total cholesterol (CHOL), triglycerides (TRIG), albumin (ALB), total protein (PROT), bilirubin (BILI), alkaline phosphatase (ALP), aspartate aminotransferase (ASAT), alanine aminotransferase (ALAT), 5' nucleotidase (5NT), and γ-glutamyltransferase (GGT) were measured. The albumin/globulin (A/G) ratio was

calculated as albumin/(total protein-albumin). For each parameter, analysis of variance was performed on rank-transformed data. When the analysis of variance was significant at the 5% level, pair-wise comparisons were made for each treated group versus controls. Additionally, principal component analysis (PCA) was performed on the day 2 clinical chemistry data, unit variance (UV) scaling was being used to scale each variable prior to PCA in order to give equal weight to each variable.

2.2.5 Samples analysed by NMR

In the first toxicology study (Study 98053), every urine, plasma and liver samples was analysed by NMR. Based on the findings on the first study, selected samples were analysed in all subsequent studies (urine samples from Day -1, Day +1 (0-7 hr), Day +2, Day +3 and Day +7; Day -3 and Day +2 plasma samples; Day -3 and Day +2 liver samples were selected for analysis). The majority of the urine and plasma NMR data were collected by T. A. Clayton as part of his PhD thesis (Clayton 2001) whilst the liver NMR data were collected and all NMR data analyses were carried out by I. K. S. Yap.

2.2.6 Liver sample preparation and ^{1}H MAS NMR analysis

The liver tissue samples were analysed by ^{1}H MAS NMR spectroscopy at 400.13 MHz using a Bruker AV-400 spectrometer equipped with a high-resolution magic-angle-spinning (HR MAS) probe head with a field gradient coil at the magic angle. Each sample (approx. 20 mg) was rinsed in saline/D_2O and placed in a 4 mm zirconium oxide rotor (Bruker Biospin, Rheinstetten, Germany), using a proprietary insert to make a spherical sample chamber. The samples were spun at 4000 Hz. To minimise sample degradation, the NMR spectra were acquired at an external temperature of 276 K measured by a Bruker VTU 3000 temperature control unit. Typically, 512 transients were collected into 16K data points using a spectral width of 8 kHz and a standard 1D pulse sequence for solvent presaturation suppression (RD-90°-t1-90°-tm-90°-acquire data, where RD is a relaxation delay) with an irradiation at the water frequency during RD (2 s) and the mixing time, tm, of 100ms. The

chemical shifts were referenced to the H1 anomeric proton resonance of α-glucose (δ 5.233).

Additionally, water suppressed spin-echo CPMG spectra were acquired using the pulse sequence: RD-90°-$(\tau$-180°-$\tau)_n$-acquire free induction decay, with a spin-spin relaxation delay, $2n\tau$, of 200 ms. This experiment reduces the spectral contribution from the resonances of large molecules such as lipids, proteins, and other less mobile membrane components, thus producing a clearer spectrum of resonances from low molecular weight components of the tissue.

Small molecules have fast molecular diffusion coefficients and this was used in a further diffusion editing pulse sequence to enable observation of larger slow-moving molecules selectively. Diffusion edited ^{1}H NMR spectra with water suppression were acquired using the bipolar-pair-longitudinal-eddy-current pulse sequence: RD-90°-G_1-τ-180°-G_2-τ-90°-Δ-90°-G_3-τ-180°-G_4-τ-90°-T_e-90°-acquire free induction decay (Wu et al. 1995), where G is the pulse field gradient, τ is the time between bipolar gradients, Δ is the diffusion time and T_e is an eddy current delay. A sine-shaped gradient strength of 19 G/cm with gradient pulse length of 5 ms was used, followed by a 300 μs delay for eddy current decay. A diffusion time of 80 ms and delay T_e of 5 ms were used.

J-Resolved (JRES) NMR spectra provide information on chemical shift and coupling constant only presented in a 2-dimensional matrix. In this project, 2-dimensional JRES ^{1}H NMR spectra were acquired to provide confirmation on spectral assignments. 2K data points with 40 increments and 40 scans per increment were collected using spectral widths of 4.2 kHz in the F2 dimension and 50 Hz in the F1 dimension.

It was found that the spin-echo spectra revealed a pattern of changes in the liver that was similar to that observed in the standard water-suppressed NMR spectra. Therefore, only the standard 1D pulse sequence spectra will be use for this thesis.

2.2.7 Urine sample preparation and ^1H NMR analysis

Urine samples were prepared by mixing 200 µl phosphate buffer (81:19 v/v mixture of 0.2 M Na_2HPO_4 and 0.2 M NaH_2PO_4; pH 7.4) with 400 µl urine. The urine-buffer mixture was left to stand for 10 min at room temperature and then centrifuged at 13 000 rpm for 10 min and the clear supernatant (500 µl) was pipetted into a 5 mm NMR tube together with 50 µl of a TSP (3-trimethylsilyl-1-[2,2,3,3,-$^2H_4$] propionate)/D_2O solution giving a final TSP concentration of 0.1 mM in the prepared sample. The urine samples were analysed at 303 K by ^1H NMR spectroscopy at 600.13 MHz using a Bruker AMX-600 spectrometer. Typically, 64 transients were collected into 64K data points using the standard 1D pulse sequence with solvent presaturation suppression as given above and an irradiation at the water frequency during RD (3 s) and the mixing time, tm, of 100ms.

2.2.8 Plasma sample preparation and ^1H NMR analysis

Plasma samples, were prepared by mixing 150 ml plasma with 350 ml saline (0.9% w/v NaCl in a mixture of 10% v/v D_2O and 90% v/v H_2O). The plasma samples were analysed at 310 K by ^1H NMR spectroscopy at 600.13 MHz using a Bruker AMX-600 spectrometer measured by a Bruker temperature control unit. Typically, 64 transients were collected into 64K data points using the standard 1D pulse sequence with solvent presaturation suppression given above. A spectral width of 10 kHz and an acquisition time per scan of 3.28 s were used. The water suppression irradiation was applied during RD (3 s) and the mixing time, tm, of 100ms; and the chemical shift scale of the spectra was referenced to the H1 anomeric proton resonance of α-glucose.

In addition to the standard 1D spectra for the blood plasma samples, standard Carr-Purcell-Meiboom-Gill (CPMG) spin-echo spectra were also acquired for 128 transients using the pulse sequence (RD-90°-(τ-180°-τ) n-acquire) with a spin-spin relaxation delay, 2nτ, of 87.8 ms. The CPMG spectrum attenuates resonances from substances with short T_2 relaxation times, comprising high molecular weight compounds, motionally restricted species and those undergoing chemical exchange. Visual inspection of the spectra obtained from the blood plasma samples revealed that the CPMG spin-echo spectra were clearer in

highlighting the biochemical information within the plasma samples than the standard ^{1}H NMR spectra.

2.2.9 Data reduction and pre-processing of ^{1}H NMR spectral data

Fourier transformed ^{1}H NMR spectra were manually phased, baseline-corrected and referenced using standard XWINNMR software (Bruker Biospin, Rheinstetten, Germany). For MAS NMR data, the spectral region of δ 0.2-9.0 was reduced to 828 regions each 0.01 ppm wide and the signal within each region integrated using an in-house written routine (MATLAB 6.5, Natick, MA, USA). The region of δ 4.5 - 5.0 was removed to eliminate any effects of imperfect water suppression. Each integral region was normalised prior to pattern recognition to give a total integration value of 1000 for each spectrum. For biofluid NMR data, the spectra over the range of δ 0.2 - 9.0 were segmented as above to 181 regions each 0.04-ppm wide and the total signal intensity in each region was computed. The region δ 4.0-6.0 was removed to eliminate variations in the suppressed water signal. Each integral region was normalized prior to pattern recognition to give a total integration value for each spectrum. These were then exported to SIMCA-P (version 10.5, Umetrics AB, Umeå, Sweden) software where all subsequent data analysis was carried out. The data presented in this thesis were mean-centred prior to pattern recognition analysis. NMR spectral assignments were based on the literature (Beckwith-Hall *et al.* 2003; Bollard *et al.* 2000; Fan 1996; Garrod *et al.* 1999; Lindon *et al.* 1999; Nicholson *et al.* 1995) with confirmation by examination of the JRES spectra where necessary.

PCA and PLS-DA analysis were performed on all standard 1D MAS NMR spectra of Day 2 liver samples. Additionally, PCA was also performed on all standard 1D MAS NMR spectra of Day 8 allyl formate and chlorpromazine liver samples. The data was mean-centered prior to modelling. In the scores plot, the data points are labelled and colour-coded so as to identify the treatment (e.g. C for control, LD for low dose and HD for high dose) and animal number. For the loadings plot, the data points are labelled according to the bucket or spectral segment that they represent. These buckets were always of 0.01 ppm so that each variable is a representation of the spectral chemical shift.

PCA and PLS-DA analysis were also performed on all CPMG spin-echo spectra of Day 2 plasma samples. The data was mean-centered prior to modelling. In the scores plot, the data points are labelled and colour-coded so as to identify the treatment (e.g. C for control, LD for low dose and HD for high dose) and animal number. For the loadings plot, the data points are labelled according to the bucket or spectral segment that they represent and ending with the letter P (designating plasma). These buckets were always of 0.04 ppm.

Prior to concatenating the data, each segmented spectral region of the reduced and normalised plasma 1D spin-echo NMR data was labelled with its segment number and ending with the letter P (designating plasma) as above. These were then concatenated with the standard 1D MAS NMR tissue data and exported into SIMCA-P software in which pattern recognition analysis was carried out. For the subsequent unsupervised (PCA) and supervised methods (PLS, PLS-DA), mean centre scaling was used to extract variables from both tissue and plasma NMR data that contributed to the variation observed in the scores plot. In the scores plot, the data points are labelled and colour-coded so as to identify the treatment (e.g. C for control, LD for low dose and HD for high dose) and animal number.

Urine NMR data was not concatenated with the tissue or plasma NMR data, because they were obtained from different animals and at different time points. PCA and mean trajectory analysis were performed on all the control and high dose standard ^{1}H NMR spectra of urine samples collected over five time points (predose, Day +1 (0-7h), Day +2, Day +3, and Day +7). The data were mean-centered prior to modelling. In the PCA scores plot, the data points are labelled and colour-coded so as to identify the treatment (e.g. C for control and HD for high dose) and animal number. For the loadings plot, the data points are labelled according to the bucket or spectral segment that they represent. These buckets were always of 0.04 ppm.

2.2.10 Quantitation of NMR data

Quantitation in NMR spectroscopy involves the measurement of the areas of NMR signals in order to obtain numerical values that reflects the concentration of the corresponding molecules in the observed sample (Van Hecke and Van Huffel 2001). In the context of biomedical research, the concentrations of the individual molecules in a biological sample are of interest, and NMR spectroscopy is a unique non-invasive analytical technique providing both an interpretable biochemical signature of the compounds present in a mixture and also their concentrations. However, quantitation in MAS NMR is more complex than in biofluids and the observed spectral changes may not be fully representative of sample compartment.

Over the years, substantial effort has been devoted in the search for accurate quantitative MAS NMR methods. Metz *et al.* (1996) used cross polarisation-magic angle spinning NMR experiments using linear ramp cross polarisation amplitudes to improve NMR signals for quantitation of N-t-Boc-alanine. However, the method is only ideal for samples where the proton spin lattice relaxation time is longer than the cross polarisation time constant. Elliot *et al.* (1999) used principal component analysis to quantify NMR spectral data sets. They found that the use of PCA is limited to NMR signals that can be spectrally isolated. PCA was also found not to be able to quantify individual peaks that are overlapped (Stoyanova and Brown 2001). Cheng *et al.* (2001) evaluated the use of MAS NMR to measure the spermine level in human prostate tissue using tissue water signals obtained from spectra without water presaturation as an internal standard. They found that the spermine level measured by NMR correlated with the volume percentage of normal prostatic epithelial cells measured by histopathology.

In the present studies, the normal approach was to normalise each spectrum to constant total area and to observe relative changes in pattern recognition investigation. However, the use of silicone rubber as an internal standard to quantify MAS spectral data has also been investigated in this project. Silicon rubber is used as an internal standard to measure the metabolite concentrations in both control and dosed liver samples. The mass of each liver

sample (M_L) and silicon rubber (M_S) was obtained prior to NMR analysis. The silicone rubber is embedded into the liver sample and placed in a 4 mm zirconium oxide rotor filled with saline/D_2O, using a proprietary insert to make a spherical sample chamber. The samples were spun at 5000 Hz. High-resolution ^1H NMR spectra were acquired on a Bruker DRX 600 Spectrometer (Bruker Biospin, Rheinstetten, Germany) operating at 600.13 MHz at an external temperature of 283K. Typically, 256 transients were collected into 32K data points using a spectral width of 7.2 kHz and a standard 1D pulse sequence for solvent presaturation suppression (as above) with RD (2 s) and the mixing time, tm, of 100ms was used. The integrals of all the peak of interest were obtained including the integrals of silicon peak. These were then divided by their respective masses i.e. integrals of peak of interest/mass of liver and integrals of silicon peak/mass of silicon. Therefore, the ratio (integrals of peak of interest/mass of liver)/(integrals of silicon peak/mass of silicon) will give a measure of liver metabolite concentration.

In plasma quantitation, relative measure of plasma metabolite concentrations were obtained using the formula '(integrals of peak of interest/integrals of peak of α-glucose H1) X (clinical chemistry glucose value)'. This essentially uses the clinical chemistry glucose values to scale the NMR spectra appropriately. This method assumes that the plasma ratio of α:β glucose anomers is constant at 36:64 (Morrison and Boyd, 1992).

Urine quantitation poses special problems because the experimenter has no control over when and what the rats urinate therefore what is excreted during a certain collection period may not be representative of what is passed to the bladder during that period. Moreover, some of the dosed compound i.e. chlorpromazine may caused reduce drinking which will produce small volume of highly concentrated urine. Thus there would be significant excretion error. Because of this, the changes in the excretion of endogenous urinary metabolites were measured relative to other endogenous urinary metabolite, in this case, creatinine. Creatinine is widely accepted as an internal standard for urinary quantitation. A correction was made for any pre-dose differences between control and treated groups. The levels of liver, plasma and urinary metabolites from the treated animals were compared with those from control animals sampled at the same time-point.

2.2.11 Reporting of quantitative results and univariate statistical analysis

The average value for the treated groups were ratioed against the average value of the control groups to obtain the quantitative data such as the concentration of plasma components measured by clinical chemistry, NMR, and urinary concentration ratio. The following conventions were used to report the ratios obtained:

↑↑: the average value for the treated groups was > 10 times the control average.
↑: the average value for the treated group was 1-10 times the control average.
↓: the average value for the treated group was 1-10 times less than the control average.
↓↓: the average value for the treated group was > 10 times less than the control average.

Univariate statistical analyses were performed to the clinical chemistry and NMR data for each day and study separately. Analyses of variance (ANOVA) performed on rank transformed data were used to compare groups. When the analysis of variance was significant at the 5% level, pair-wise comparisons were made for each treated group versus controls. All tests were two-tailed tests performed at the 5% confidence level.

The following conventions were used to report the ratios for treated/control:

*: designates significant difference at 95% confidence level.
**: designates significant difference at 99% confidence level.
***: designates significant difference at 99.9% confidence level.
NS designates no significant difference found at 95% confidence level.

Chapter 3: Integrated Allyl Formate Studies

3.1 Background: Metabolism and hepatotoxicity of allyl formate

Rees and Tarlow (1967) investigated the hepatotoxicity of allyl formate in rats. They suggested that the conversion of allyl formate to allyl alcohol and subsequently to toxic acrolein is the basis underlying the hepatotoxicity of allyl formate. From their study, they found necrosis in the periportal region of the liver lobule. This localised effect is believed to be due mainly to the localisation of the enzyme alcohol dehydrogenase (ADH), which is required for the conversion of allyl alcohol to acrolein. Rees and Tarlow also found acrolein to inhibit protein synthesis and to inhibit mitochondrial respiration and that acrolein and glutathione (GSH), at equimolar amounts, could react rapidly to near completion forming stable adducts without the presence of enzymes.

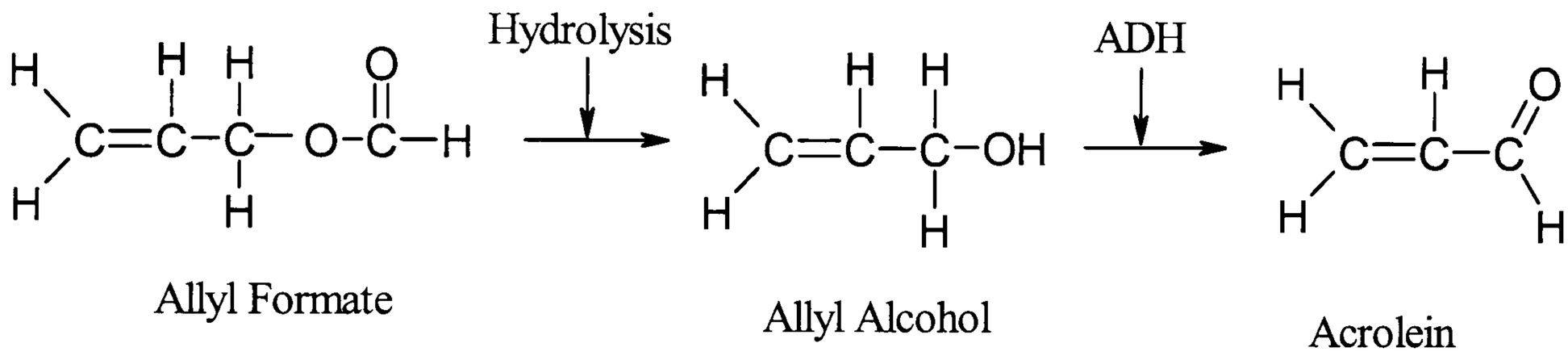

Figure 3.1 Conversion of allyl formate to toxic acrolein.

Kaye (1973) found evidence of mercapturic acid formation in rats administered with allyl alcohol or acrolein and Alarcon (1976) showed the presence of 3-hydroxypropyl mercapturic acid in urine from rats dosed with acrolein. Later, Sanduja *et al.* (1989) investigated the use of 3-hydroxypropylmercapturic acid (3-HPMA) as a biological marker of exposure to allylic and related compounds. They found that from 13 mg/kg of acrolein administered to rats, the amount of the mercapturic acid excreted in urine (0-24 hours after dosing) accounts for 79% of the dose. Chasseaud (1979) confirmed that αβ-unsaturated compounds activated by electron-withdrawing substituents attached to the α-carbon will react with GSH through the addition of the nucleophile, GS^-, to the β-carbon of the αβ-double bond. Such reactions can proceed rapidly without the presence of enzyme although

they may also be catalysed by glutathione-S-transferases. Following experiments in isolated rat hepatocytes incubated with allyl alcohol, Ohno *et al.* (1985) suggested the formation of a 1:1 ratio adduct between allyl alcohol-derived acrolein and glutathione with the adduct being further metabolised in a Phase 3 biotransformation. The addition of GSH to acrolein would be followed by the removal of the glutamyl group via γ-glutamyltranspeptidase, removal of the glycine group via the enzyme cysteinyl glycinase to form S-(2-formylethyl) cysteine, and acetylation of the amino group of cysteine by N-acetyl transferases coupled by acetyl CoA to form N-acetyl-S-(2-formylethyl) cysteine. N-acetyl-S-(2-formylethyl) cysteine would then be either reduced to form S-(3-hydroxypropyl) mercapturic acid (3-HPMA) or oxidised to form S-(2-carboxyethyl) mercapturic acid. This is summarised in Figure 3.2.

Zitting and Heinonen (1980) found a reduction in the GSH level in isolated rat hepatocytes incubated with acrolein. Hepatocytes treated with 0.025-0.25 mM acrolein showed a decrease in the GSH level, which recovered as the cells recovered. However, at 0.5 mM acrolein, the hepatocytes were depleted in GSH and were incapable of synthesising replacement GSH. At acrolein concentrations of 0.25-0.5 mM, lipid peroxidation impaired the membrane integrity of the hepatocytes. They also reported that acrolein is highly reactive and can react easily with sulphydryl groups in the biological system including glutathione-S-transferase. Thus, they concluded that extensive GSH decrease leads progressively to an increase in lipid peroxidation, cell membrane instability and finally cell lysis.

Jaeschke *et al.* (1987) investigated the role of acrolein in allyl alcohol-induced lipid peroxidation and liver cell damage in mice. Their results showed that after administration of allyl alcohol (64mg/kg), complete loss of hepatic glutathione was observed within the first 15 minutes, which then led to massive lipid peroxidation. This is confirmed by the observed 40-45% loss of polyunsaturated fatty acids (arachidonic and docosahexaenoic acids) in liver lipids. They also found that both *in vivo* inhibition of alcohol dehydrogenase by pyrazole, or induction of aldehyde dehydrogenase prevented allyl alcohol-induced glutathione depletion and the subsequent lipid peroxidation and liver cell damage.

Furthermore, the inhibition of aldehyde dehydrogenase by cyanamide caused the normally sub-toxic dose of allyl alcohol (35mg/kg) to be highly toxic. Their results suggested that the direct oxidation of acrolein to acrylic acid is an important detoxification pathway in mouse liver especially when the glutathione levels are low. They also reported that enhanced hepatic glutathione levels *in vivo* protected the cells from damaging allyl alcohol effects and that the depletion of liver glutathione itself induced marginal lipid peroxidation and no liver cell damage. Therefore, they concluded that depletion of liver glutathione levels is an important factor in acrolein toxicity but is not sufficient to initiate lipid peroxidation *in vitro* itself. They also found that the presence of the ferric ion chelator, desferoxamine methanesulphonate, prevented allyl alcohol-induced lipid peroxidation and liver cell damage *in vivo*. This suggested the importance of iron in the mechanism of cell damage by allyl alcohol. Iron plays an important role lipid peroxidation. In the presence of certain transition metal ions e.g. iron ions, hydroxyl radicals can be formed through either the Haber-Weiss reaction or the Fenton reaction, and this can cause lipid peroxidation and cell injury. This suggested that allyl alcohol causes GSH depletion and also induced iron-mediated lipid peroxidation, which leads to liver cell damage. Mitchell and Petersen (1987) investigated the inhibition of rat liver enzyme aldehyde dehydrogenase (ALDH). They found that acrolein is a potent inhibitor of rat ALDH in particular the mitochondrial and cytosolic ALDH. Both irreversible and reversible non-competitive inhibition was observed after incubation of the mitochondrial and cytosolic fraction with 30 μM acrolein and a significant inhibition observed at acrolein concentration of ≥ 50 μM. Inhibition of ALDH caused an increase in aldehydes thus leading to the potentiation of their toxicities.

Miccadei *et al.* (1988a and 1988b) investigated the effects of the toxins allyl alcohol, dinitrofluorobenzene and diethyl maleate, and the abrupt depletion of glutathione in cultured hepatocytes. Besides the conjugation of electrophilic compounds with or without catalysis by glutathione-S-transferases, glutathione has various other functions such as translocation of amino acids across cell membranes, maintenance of sulphydryl groups, and the catabolism of peroxides via glutathione peroxidases. It also destroys free radicals. Partially reduced oxygen species are produced continuously by electron transport carriers in the mitochondria or through the action of cytoplasmic oxidases of aerobic cells. Depletion

of glutathione or inhibition of the reduced glutathione-oxidised glutathione (GSH-GSSG) redox cycle sensitises the cell to an imposed oxidative stress due to the accumulating oxygen species. Miccadei *et al.* (1988a and 1988b) investigated the effect of glutathione depletion in relation to endogenous stress and their results showed that acrolein produces an abrupt glutathione depletion, which is then followed by lipid peroxidation and cell death. They suggested that the oxidative cell injury is caused by the inability to detoxify endogenous hydrogen peroxide and that the resulting iron-dependent formation of potent oxidising agent accounts for the hepatotoxicity of allyl alcohol better than covalent binding of acrolein to cellular macromolecules.

Ferrali *et al.* (1989), investigated allyl alcohol-induced haemolysis and its relation to iron release and lipid peroxidation. They reported that acrolein is a powerful electrophile, which will react spontaneously with nucleophiles such as sulphydryl groups, thus leading to a decrease in GSH and that acrolein is toxic not only to liver cells but also other cell types i.e. renal epithelial cells and pancreatic acinar cells. They found that haemolysis occurred in *ca.* 50% of allyl-alcohol treated mice and proceeded to investigate whether lipid peroxidation occurs in the membranes of the erythrocytes. They reported a rapid decrease in hepatic SH groups upon administration of allyl alcohol. This is then followed by development of lipid peroxidation and liver necrosis. Haemolysis occurred due to a decrease in the erythrocyte GSH level, which led to lipid peroxidation and membrane structure instability. Acrolein induces the release of iron from iron complexes in erythrocytes and this free iron is able to undergo a redox reaction with molecular oxygen thereby generating oxygen-derived free radicals such as the hydroxyl radicals. Hydroxyl radicals are highly reactive and will react with lipids thus promoting lipid peroxidation. This in turn leads to an increase in free chelatable iron.

Adams and Klaidman (1993) investigated acrolein-induced oxygen radical formation. The found that acrolein and the GSH adduct of acrolein, glutathionylpropionaldehyde (GS-propionaldehyde) can induce oxygen radical formation leading to lipid peroxidation thus suggesting an alternative mechanism for the cause of oxidative stress under conditions of depleted GSH. GS-propionaldehyde was found to be very reactive with ALDH and

xanthine oxidase to produce superoxide and acroleinyl radicals. It was found that acrolein was oxidised to superoxide and acroleinyl radicals through the action of xanthine oxidase whereas acrolein was oxidised to form superoxide radicals only through the action of ALDH. The study revealed that GS-propionaldehyde is a toxic metabolite of acrolein and is a more potent stimulator of oxygen radical formation than acrolein.

3.1.1 Study Details

Study number 98053 carried out at Pfizer, Centre de Recherche, Amboise, France.

Study Number	**Compound**	**Study Group**	**Dose of toxin administered (mg/kg)**	**Animal Number**	**Euthanased**	
					Day 2	**Day 8**
98053	Saline	Control	0	1-10	6-10	1-5
	Allyl Formate in saline	Low Dose	25	101-110	106-110	101-105
		High Dose	75	201-210	206-210	201-205

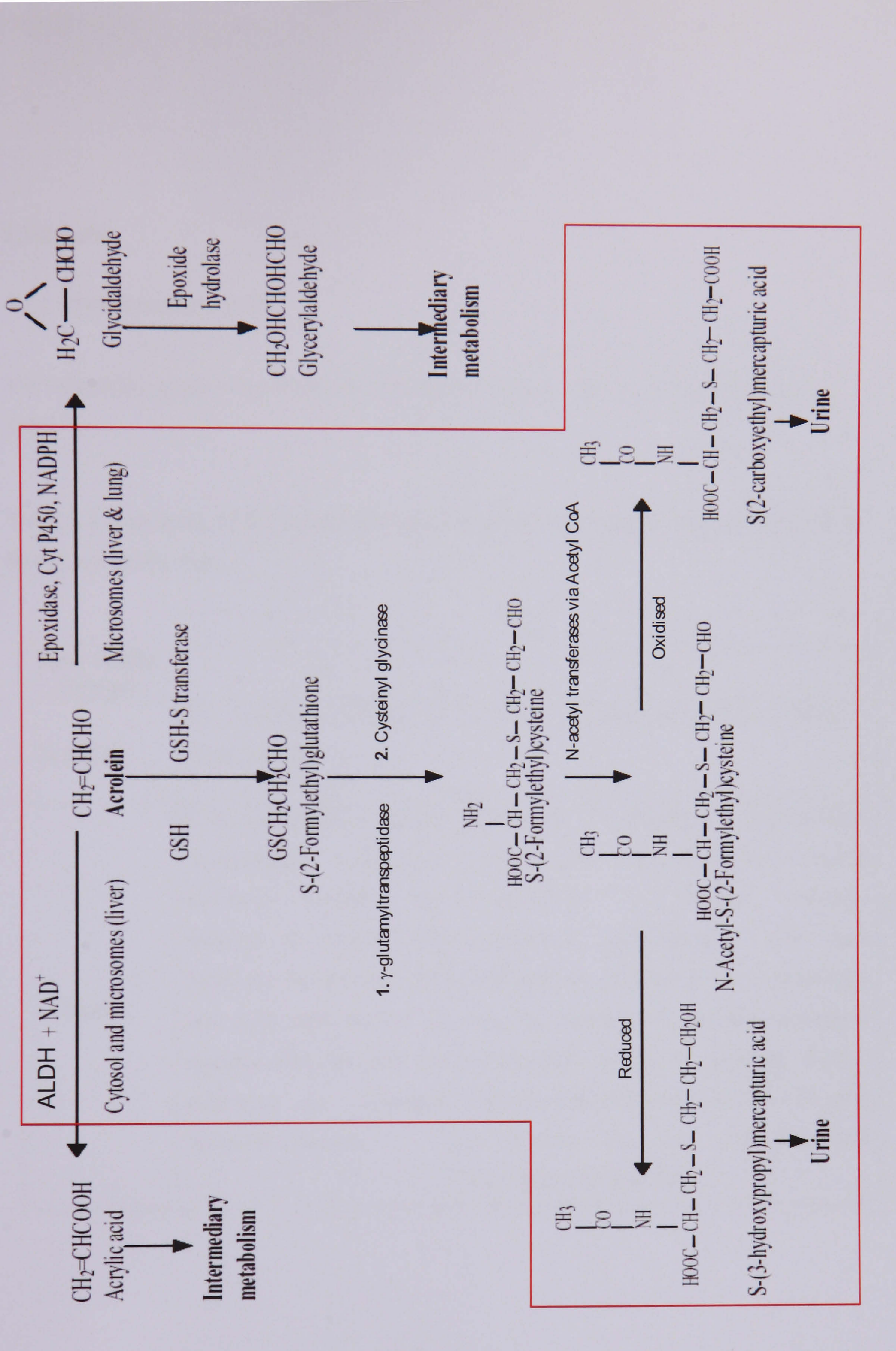

Figure 3.2 Metabolism of acrolein. Main pathway in red box (adapted from World Health Organisation).

3.2 Results

3.2.1 Histopathology results

The histopathological observations for allyl formate-dosed rats are summarised below in Table 3.1.

Table 3.1 Summary of the histopathological changes observed in allyl formate-dosed Sprague-Dawley rats.

	Day	
Dose of allyl formate	**2**	**8**
25 mg/kg	No significant differences from controls.	No significant differences from controls.
75 mg/kg	Periportal to diffuse lobular haemorrhagic coagulative necrosis. Necrosis was minimal in animal 208; moderate in animals 207 and 210; and marked in animals 206 and 209. No evidence of glycogen depletion detected.	Multifocal chronic post-necrotic inflammation characterised by variable combinations of fibrosis, necrosis, granulomas, mineralisation bile duct proliferation, infiltration of macrophages and the presence of variably vacuolated hepatocytes in the surrounding tissues. Changes were minimal in animal 204; mild in animals 202, 203, and 205; and moderate in animal 201.

3.2.2 Clinical chemistry results

The clinical chemistry data indicated minimal changes in the low dose animals on both Day 2 and Day 8. Clear signs of liver toxicity were observed in the high dose animals on Day 2. The Day 8 clinical chemistry data of the high dose showed minimal effects indicating recovery. Details of the clinical chemistry findings are summarised in Table 3.2.

Table 3.2 Summary of the plasma changes observed by clinical chemistry in allyl formate-dosed Sprague-Dawley rats.

	Day	
Dose of allyl formate	**2**	**8**
25 mg/kg	Triglycerides: ↓ (33%, *).	No group differences were found although γ-glutamyltransferase (GGT), bilirubin and triglycerides were elevated in animal 101.
75 mg/kg	Variable liver necrosis and cholestatic damage: ASAT: ↑↑ (***) ALAT: ↑↑ (***) TBA: ↑↑ (***) GGT: ↑ (***) Triglycerides: ↓ (54%, ***). Albumin: ↓ (19%, **) TP: ↓ (14%, ***). 3 out of 5 animals (animals 206, 207 & 209) showed an increase in bilirubin.	No group differences were found. TBA remained elevated in animals 201 and 204. Animal 202 showed unusually low creatinine.

3.2.2.1. Principal Component Analysis of Day 2 Plasma Chemistry Data

PCA scores and loadings plots for the first two components of the control/allyl formate Day 2 clinical chemistry data are shown in Figure 3.3. In the scores plot, the data points are colour-coded and labelled so as to identify the treatment (e.g. **black** for control, **red** for low dose and **blue** for high dose) and animal number.

The scores plot shown in Figure 3.3A shows separation between the low dose group and the controls along the second principal component. The corresponding loadings plot (Figure 3.3B) shows that decreases in plasma triglycerides and total plasma cholesterol and increases in bile acids and the albumin/globulin ratio are major contributors to this separation.

Figure 3.3C shows separation between the high dose group and the controls along the first principal component. An important feature observed in the corresponding loadings plot (Figure 3.3D) along the first principal component is the generalised increase in both aminotransferases, ALAT and ASAT, which are indicative of hepatocellular damage in the high dose animals. The loadings plot also shows that the high dose of allyl formate caused increases in 5-nucleotidase, γ-glutamyl transferase, bilirubin and bile acids, which are markers of hepatobiliary damage (Handler *et al.* 1997). Amongst other things, the loadings plot also indicates decreases in plasma triglycerides, in the albumin/globulin ratio and in total plasma proteins as the contributors to the separation between the high dose animals and the control animals. The decrease in the albumin/globulin ratio in the high dose animals is in contrast to the low dose animals which showed an increase in the albumin/globulin ratio.

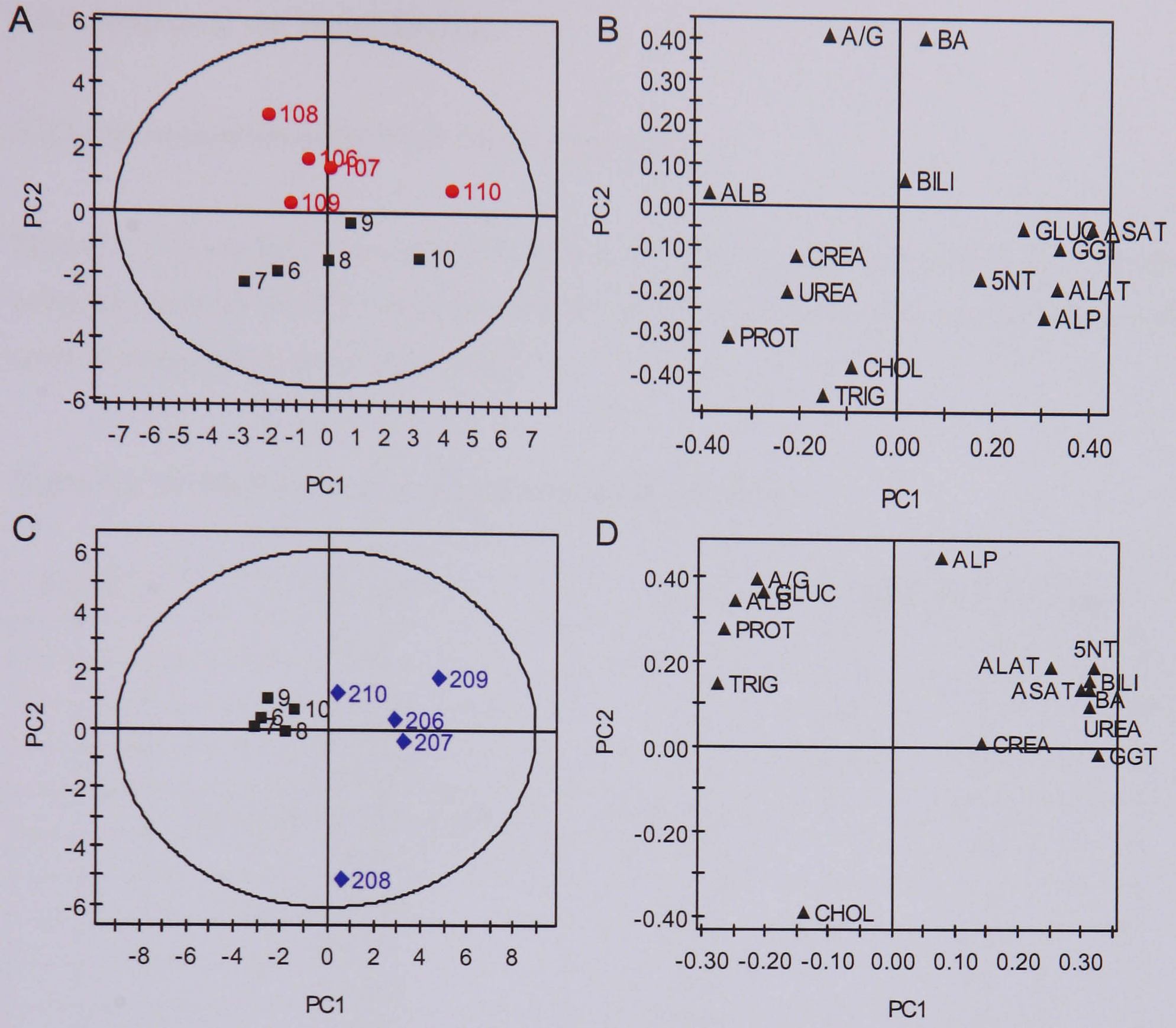

Figure 3.3 (A) Scores plot from PCA of control and low dose AF Day 2 clinical chemistry data, and (B) corresponding loadings plot. (C) Scores plot from PCA of control and high dose AF Day 2 clinical chemistry data, and (D) corresponding loadings plot. Key: TBA = total bile acids, CHOL = total plasma cholesterol, PROT = total plasma protein, TRIG = triglycerides, GLUC = glucose, ALB = albumin, A/G = albumin/globulin ratio, BILI = bilirubin, ALP = alkaline phosphatase, ASAT = aspartate aminotransferase, ALAT = alanine aminotransferase, 5NT = 5' nucleotidase, GGT = γ-glutamyltransferase.

3.2.3 Analysis of the Tissue Spectra

3.2.3.1 Examination of ^{1}H MAS NMR tissue spectra

Figure 3.4 shows the dose-dependent effects of allyl formate hepatotoxicity as visualised using standard 1D ^{1}H MAS NMR spectra of intact Day 2 rat liver. The corresponding NMR spectral assignments are listed in Table 3.3.

Table 3.3 ^{1}H NMR resonance assignments for liver tissue.

Peak No.	Molecule	Assignment	1H chemical shift (ppm)
1	Valine	**CH_3**	1.04
2	Lactate	**CH_3**	1.33
3	Acetate	**CH_3**	1.95
4	Glutamine	**CH_2**	2.39
5	Glucose/glycogen/α-H amino acids	**Ring protons/α-CH**	3.35-4.00
6	Lactate	**CH**	4.13
7	β-Glucose	**C_1H**	4.64
8	Glycogen	**CH**	4.65
9	α-Glucose	**C_1H**	5.23
10	Glycogen	**CH**	5.38-5.45
11	Alanine	**CH_3**	1.48
12	Lipids	$CH{=}CH\text{-}\mathbf{CH_2}\text{-}CH_2$	2.07
13	Glutamate	**CH**	2.15
14	Choline/phosphocholine	$N^{+}(\mathbf{CH_3})_3$	3.22
15	TMAO	**CH_3**	3.27
	Taurine	**$CH_2SO_3^-$**	3.25
16	Lipids	**CH_3**-(CH_2)n	0.90
17	Lipids	CH_3-(**CH_2**)n	1.29
18	Lipids	$CO\text{-}CH_2\text{-}\mathbf{CH_2}$	1.61
19	Lipids	$CO\text{-}\mathbf{CH_2}\text{-}CH_2$	2.25
20	Lipids	$=CH\text{-}\mathbf{CH_2}\text{-}CH=$	2.78
21	Lipids	**-CH=CH-**	5.30-5.35

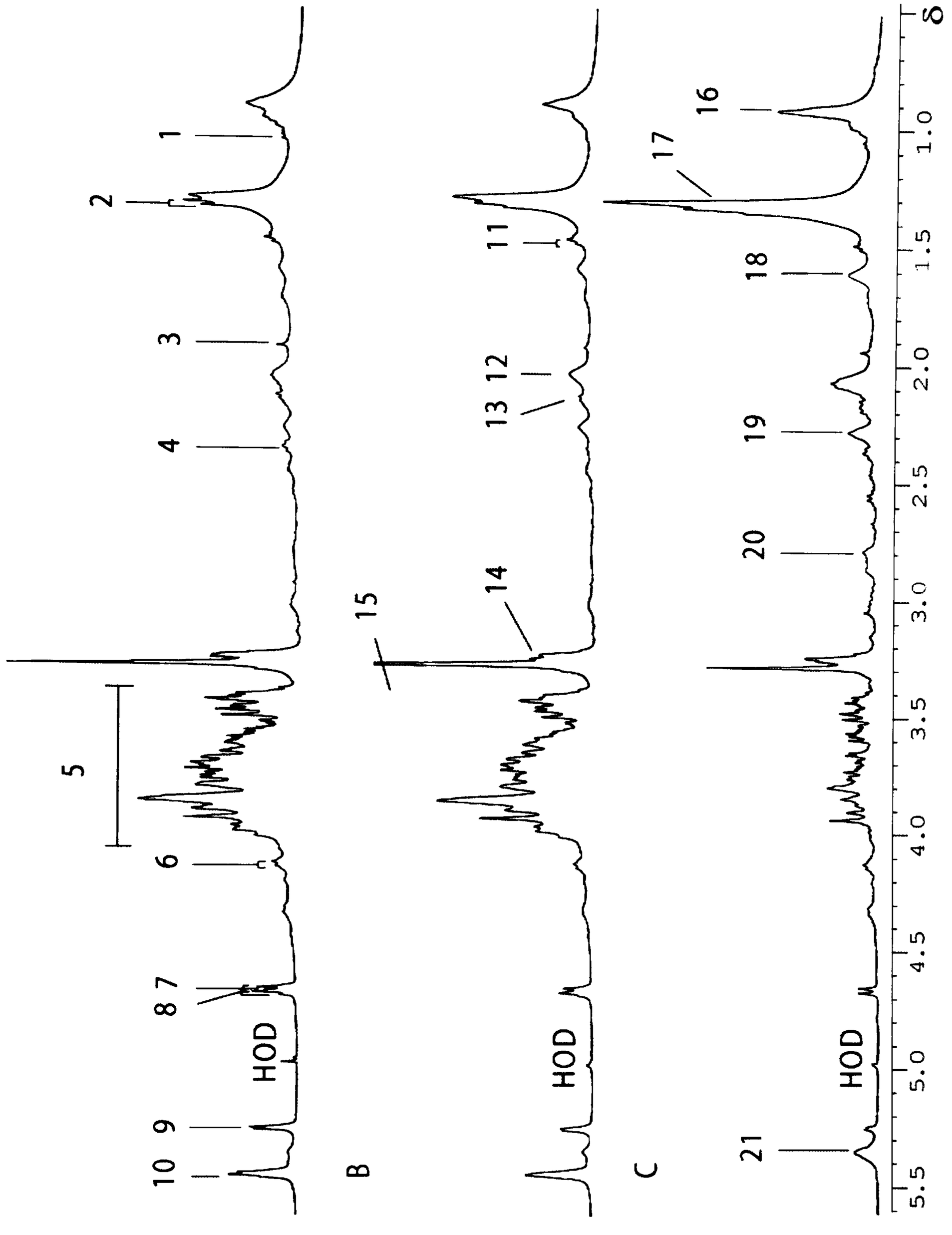

Figure 3.4 Dose-dependent effects of allyl formate hepatotoxicity as visualised using standard 1D ^{1}H MAS NMR spectra of intact Day 2 rat liver. A. Control liver. Liver from an animal administered: (B) Low-dose allyl formate and (C) High-dose allyl formate.

Visual inspection of the standard 1D spectrum of Day 2 control rat liver (Figure 3.4A) shows that it contains broader signals from large molecule such as lipids and sharper signals from small molecules such as lactate, glucose, trimethylamine N-oxide (TMAO) and taurine. Administration of the low dose of allyl formate appears to have relatively little effect on the rat liver (Figure 3.4B) with increases in TMAO and some increase in lipids. However, the administration of the high dose of allyl formate appears to have severe effects on the rat liver (Figure 3.4C). The liver lipids content, in particular the CH_2 and CH_3 moeties, increases drastically as compared to that of controls. In addition, depletion of liver glucose and glycogen levels are also observed in the high dose animals. Additionally, visual inspection of the high dose Day 2 MAS NMR spectra revealed that the extent of the lipid changes correlated with the extent of necrosis identified by histopathology, with animals 206 and 209 experiencing severe necrosis showing the biggest increase in the lipid moeties; and animals 207, 208 and 210 experiencing mild to moderate necrosis showing small to intermediate increase in the lipid moeties. The Day 8 MAS NMR spectra indicated minimal effects. Details of the MAS NMR observations for allyl formate-dosed rats are summarised below in Table 3.4 and the changes reported were quantified according to the method described in Chapter 2.

Table 3.4 Summary of the liver tissue changes observed by MAS NMR in allyl formate-dosed Sprague-Dawley rats.

Dose of allyl formate	Day	
	2	8
Low dose (25 mg/kg)	Changes were generally minimal. TMAO: ↑ (NS); All animals showed a slight relative increase in TMAO at δ3.27 except animal 106. Animal 110 also showed a relative decrease in glycogen signal at δ3.80.	There were minimal differences from controls.
High dose (75 mg/kg)	A similar pattern appeared on all spectra obtained, with: Lipids: ↑* Glucose (between δ 3.40 and δ 4.00): ↓* Glycogen (δ3.80 and δ5.42): ↓* TMAO: ↓*	The spectrum for animal 203 showed slightly elevated lipids. In the other animals there was occasionally a minor relative increase in the signal at δ3.27, compared to controls.

3.2.3.2 Principal Component Analysis of Day 2 Liver NMR Data

Principal component analysis of the control/low dose Day 2 data set revealed some dose-related structure to the variation in the data. Some separation between the low dose animals and control animals can be observed in the scores plot on the second principal components (Figure 3.5A). In addition, control animal, C6, is situated away from the rest of the controls along the first principal component. The corresponding loadings plot (Figure 3.5B) identifies the NMR spectral regions that are responsible for separation seen in the scores plot in Figure 3.5A. An increase in liver TMAO was identified as the major contributor to the separation between the dosed and control animals. The loadings plot also revealed a lower lipids content in control animal, C6, which contributed to its separation. Spectral inspection confirmed that animal C6 had a lower liver lipids content as compared to the rest of the control animals.

Figure 3.5C is a scores plot for the first two components of the control/high dose Day 2 data set. There is very clear treatment-related variation in the data set, which is described mainly by the first principal component. The corresponding loadings plot (Figure 3.5D) indicates increases in the regions attributed to lipids, and decreases in the regions attributed to glucose, glycogen and TMAO as the major contributors for the separation between the high dose animals and control animals along the first principal component. The second principal component loadings plot also showed the extent of lipid increase which correlated with the histopathological findings with animals 206 and 209 showing marked necrosis furthest from the rest of the high dose animals which showed mild to moderate necrosis.

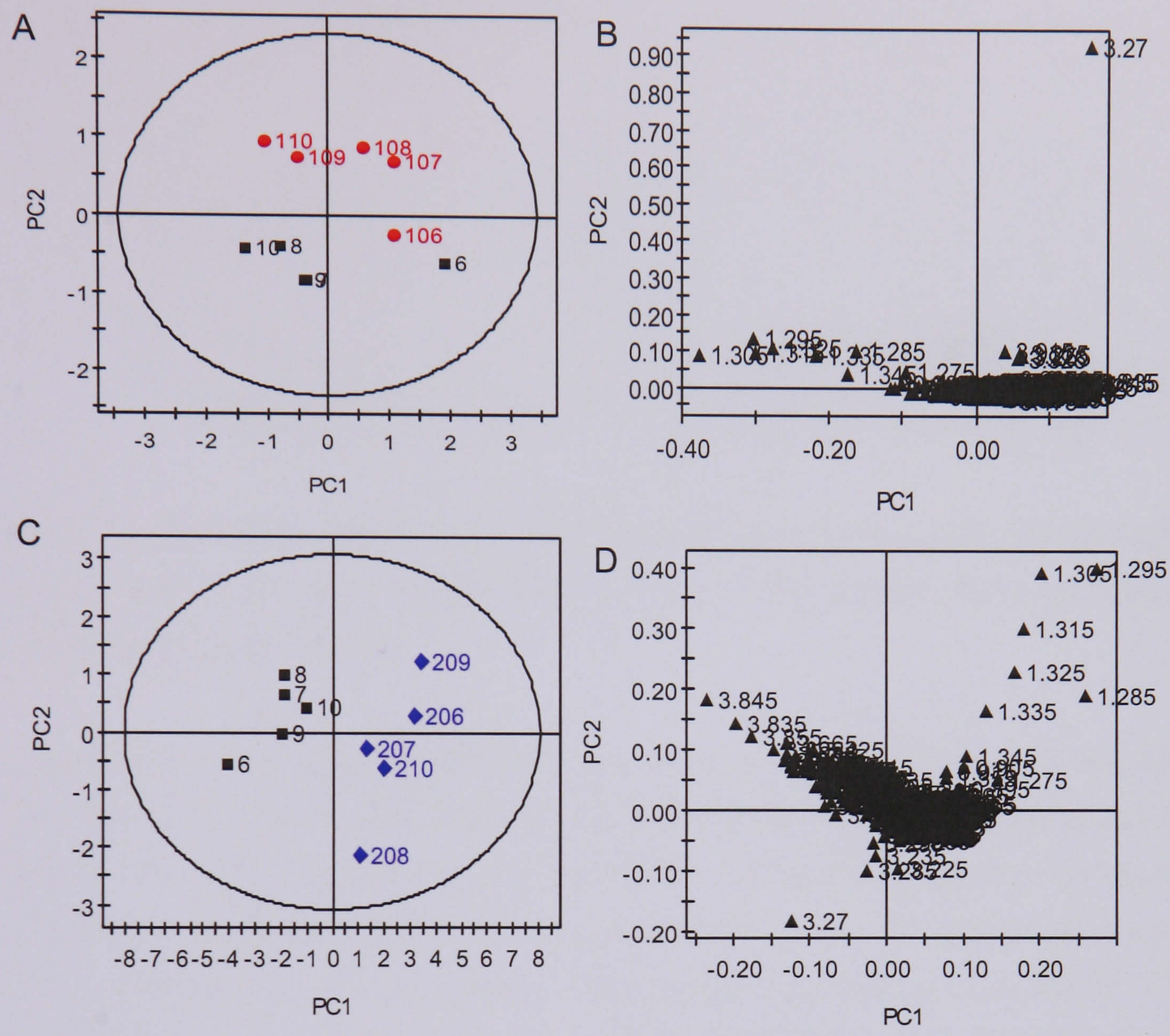

Figure 3.5 (A) PCA scores plot of the ^{1}H MAS NMR spectra of allyl formate-dosed liver samples from Day 2 low-dose versus control groups, and (B) the corresponding loadings plot. (C) PCA scores plot of the ^{1}H MAS NMR spectra of allyl formate-dosed liver samples from Day 2 high-dose versus control groups and (D) the corresponding loadings plot.

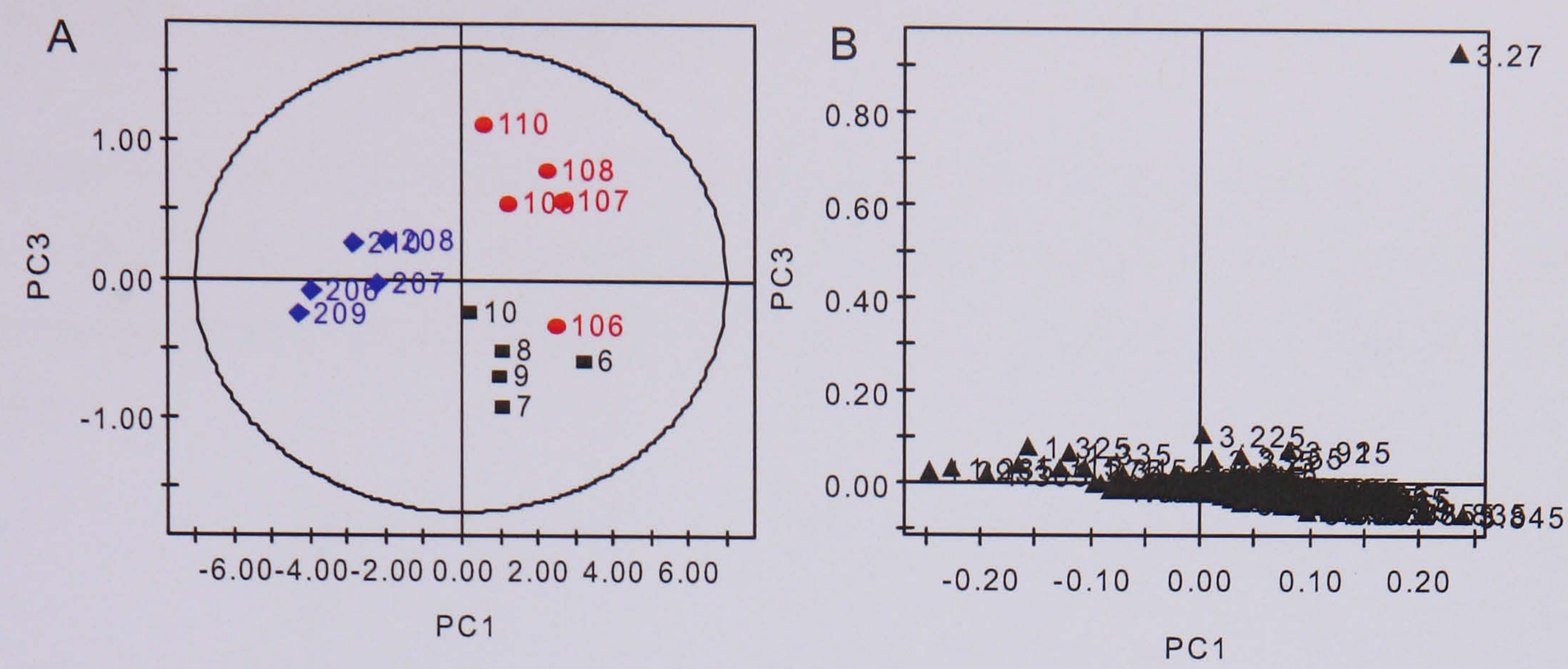

Figure 3.6 (A) Scores plot (PC1 vs. PC 3) from PCA of the standard ^{1}H MAS NMR spectra from all the liver samples taken on Day 2 allyl formate study, and (B) the corresponding loadings plot.

A scores plot of the first and third components from a PCA of all the Day 2 liver MAS NMR spectra for this study (Figure 3.6A) showed separation between the dosed groups and controls. The first component describes the variation between the high dose animals and control/low dose animals, whereas the third component describes the variation between the low dose animals and control animals. The corresponding loadings plot (Figure 3.6B) shows that allyl formate-induced increase in lipids, and decreases in glucose and glycogen are the major contributors to the separation along the first principal component, whereas an allyl formate-induced increase in TMAO is the major contributor to the separation along the third principal component.

3.2.3.3 PLS – Discriminant Analysis (PLS-DA) of Day 2 Liver NMR Data

In order to improve the information recovered from the liver MAS NMR data, a PLS-DA model was constructed, where the samples were classified assigned to one of three mutually orthogonal classes with **control** being class 1, **low dose** being class 2 and **high dose** being class 3.

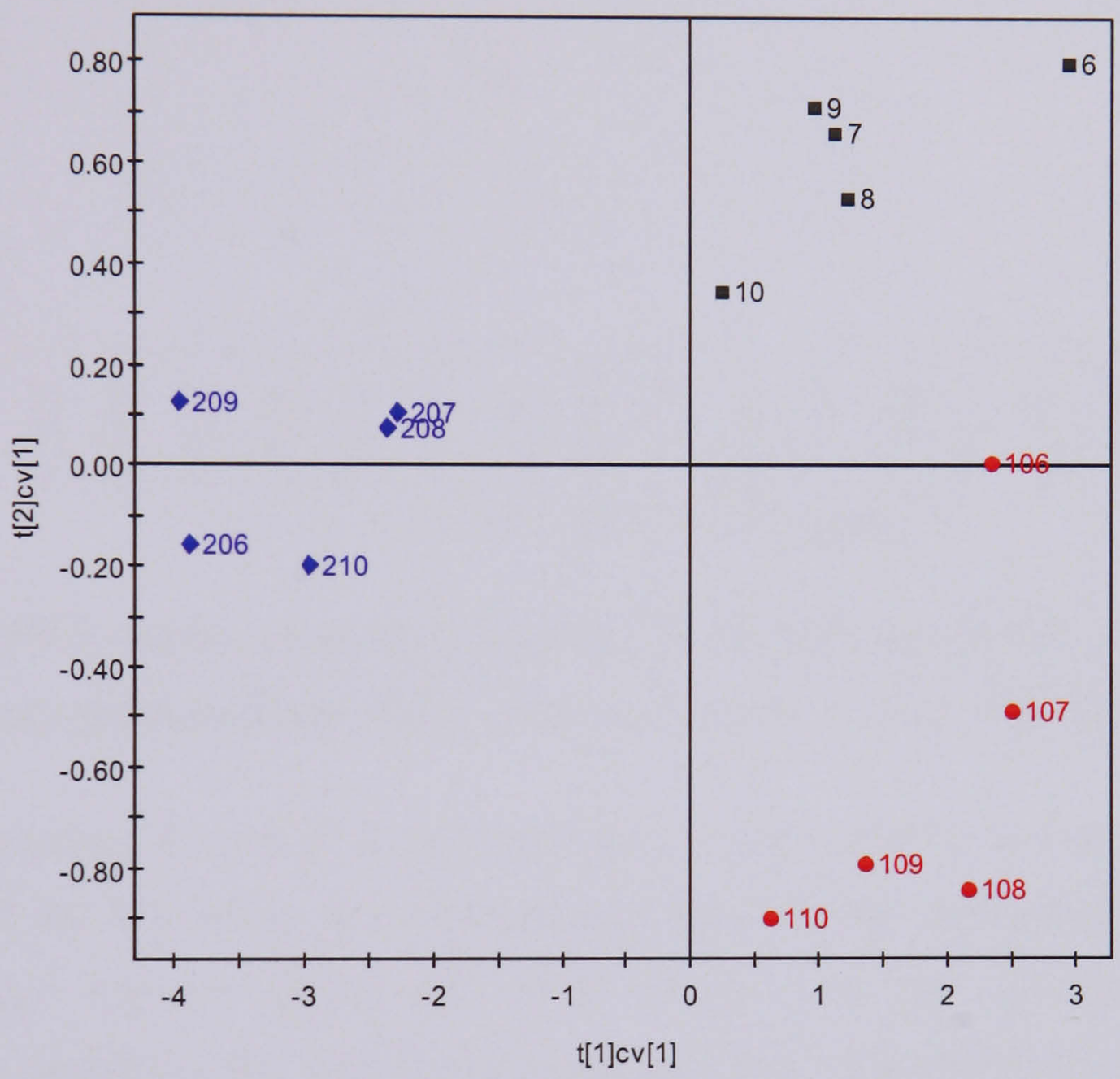

Figure 3.7 PLS-DA cross validated scores plot of the standard ^{1}H MAS NMR spectra of the Day 2 allyl formate study.

The resultant PLS-DA X-matrix cross validated scores plot of the first two components (Figure 3.7) shows distinct segregation of the three sample classes. The cluster of control animals is situated on the upper right quadrant of the plot. The low dose animals are separated from the control animals along PLS component two whereas the high dose animals are separated from the control/low dose animals along PLS component one.

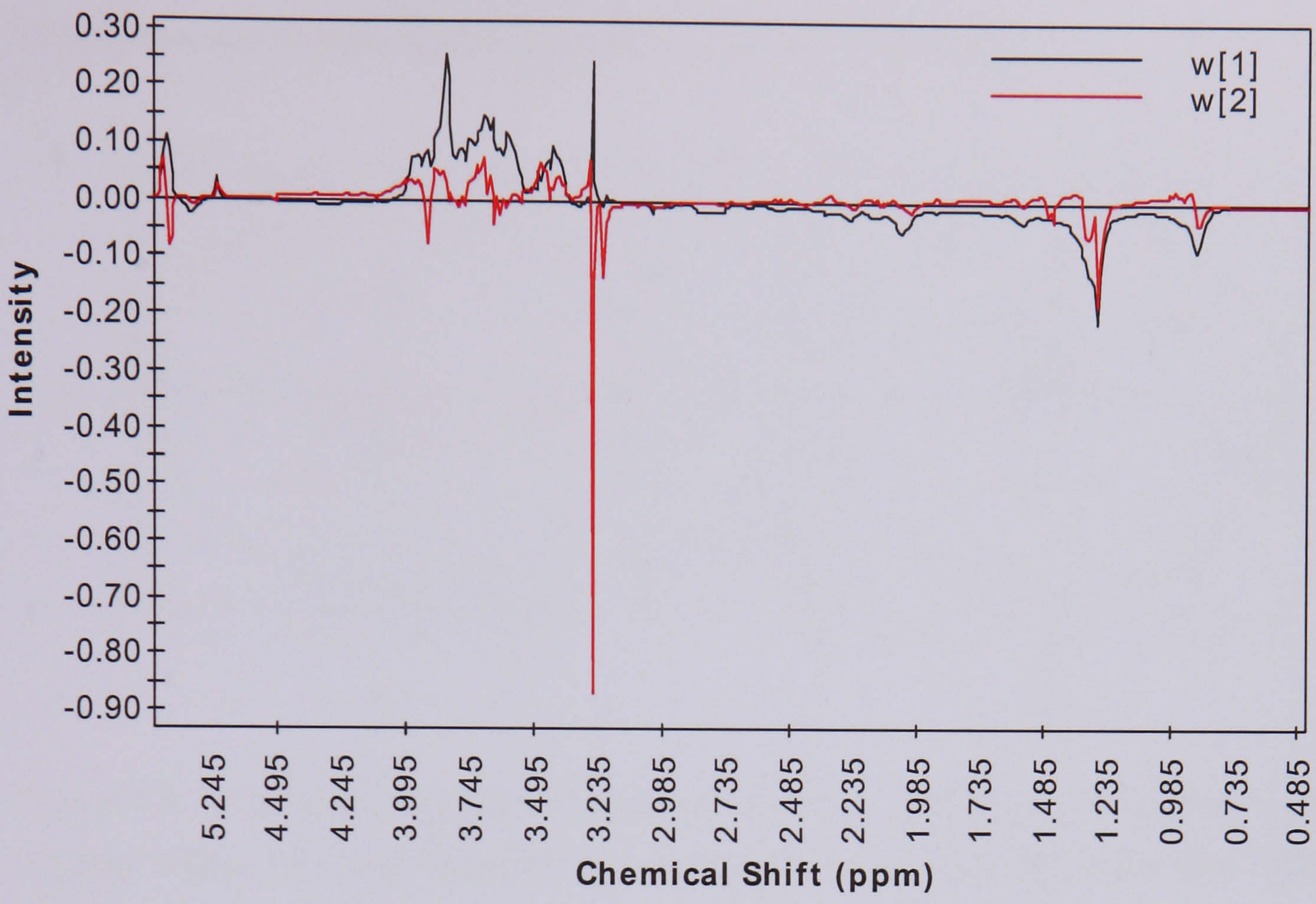

Figure 3.8 PLS weights from the standard ^{1}H MAS NMR spectra of the Day 2 allyl formate study tissue samples (W[1] = PLS component 1, W[2] = PLS component 2).

The corresponding X-block PLS loadings (Figure 3.8) are presented in line plots where the direction of the line along the intensity axis indicates the metabolites influencing the discrimination between control and dosed groups. The plot indicates that the first component, describing the variation between high dose and control/low dose animals, is due to elevated and altered liver lipid profiles and decreases in liver glucose and glycogen levels in the high dose animals. The second component, describing the variation between the low dose and control animals, is due to elevated liver TMAO level as well as some increase in the liver lipid in the low dose animals. The observations made from both PLS-DA scores and loadings plots confirmed the findings made by inspection of the ^{1}H MAS NMR spectra (Table 3.4) and from the corresponding PCA.

3.2.3.4 Principal Component Analysis of Day 8 Liver NMR Data

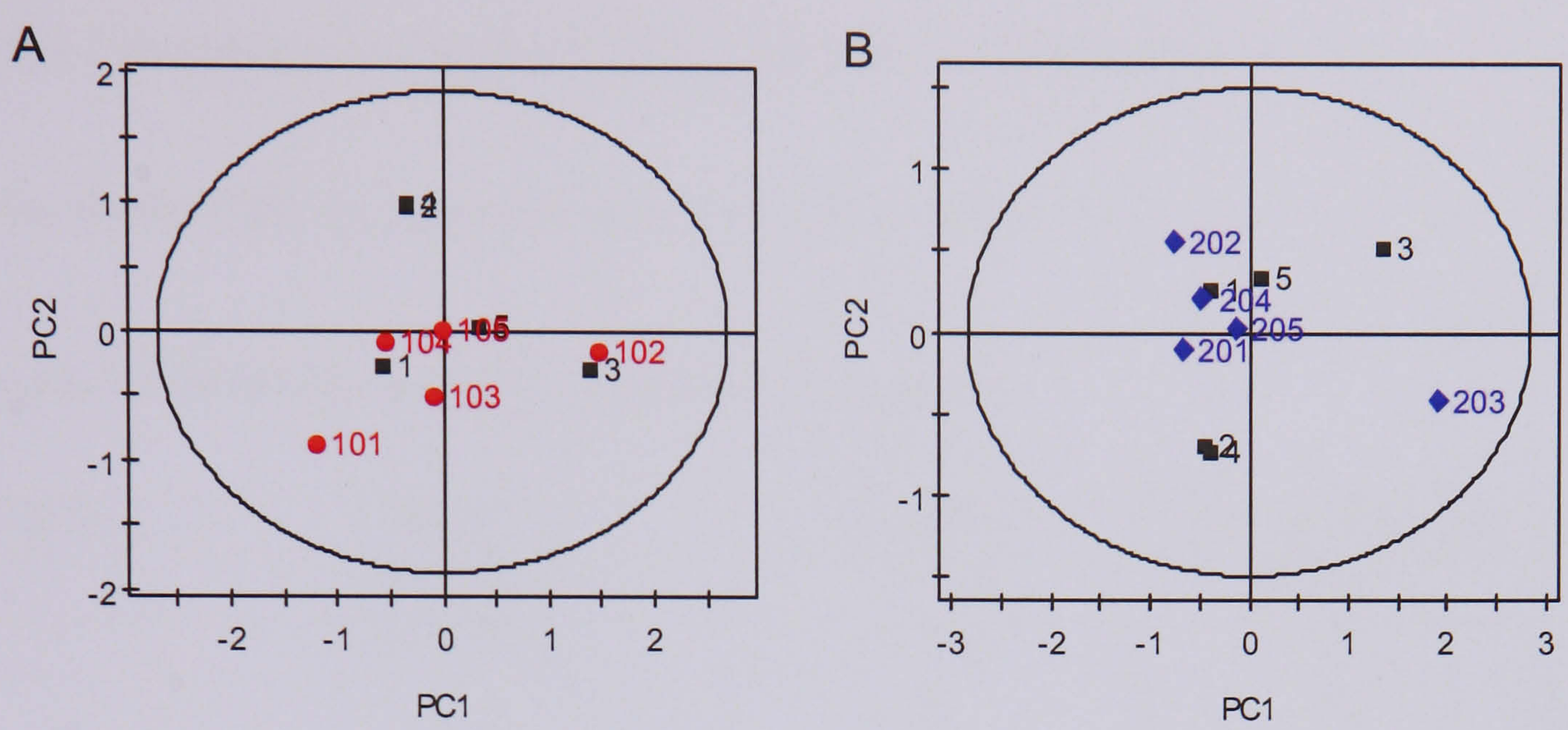

Figure 3.9 PCA scores plot of the standard ^{1}H MAS NMR spectra of Day 8 allyl formate study. (A) Low dose versus Control data set, and (B) High dose versus Control data set.

The PCA scores of plot of the allyl formate Day 8 tissue samples (Figure 3.9 A and B) indicated no clear separation between the dosed and control groups. This indicates recovery by Day 8 compared to Day 2.

3.2.4 Analysis of the Plasma Spectra

3.2.4.1 Examination of plasma CPMG spin-echo ^{1}H NMR spectra

The plasma NMR spectral assignments are listed in Table 3.5.

Table 3.5 ^{1}H NMR resonance assignments for plasma.

Peak No.	Molecule	Assignment	^{1}H chemical shift (ppm)
1	Lipids (LDL)	$-CH_2-\mathbf{CH_3}$	0.84
2	Lipids (VLDL)	$CH_2-\mathbf{CH_3}$	0.87
3	Valine	$\mathbf{CH_3}$	0.97
		$\mathbf{CH_3}$	1.02
4	3-D-hydroxybutyrate	$\mathbf{CH_3}$	1.20
5	Lipids (VLDL)	$-(\mathbf{CH_2})n$	1.29
6	Lactate	$\mathbf{CH_3}$	1.33
7	Alanine	$\mathbf{CH_3}$	1.46
8	Acetate	$\mathbf{CH_3}$	1.91
9	Acetoacetate	$\mathbf{CH_3}$	2.22
10	Glutamine	$\mathbf{CH_2}$	2.41
11	Citrate	$\mathbf{CH_2}$	2.52
		$\mathbf{CH_2}$	2.69
12	Choline	$N^+(\mathbf{CH_3})_3$	3.21
13	Glucose/Amino acids resonances	**Ring protons/α-CH**	3.35-4.00
14	Lactate	**CH**	4.10
15	α-Glucose	$\mathbf{C_1H}$	5.23
16	Isoleucine	$\mathbf{CH_3}$	0.93
17	Leucine	$\mathbf{CH_3}$	0.95
18	Isoleucine	$\mathbf{CH_3}$	1.00
19	Threonine	$\mathbf{CH_3}$	1.31
20	N-acetyl glycoproteins	NHCO $\mathbf{CH_3}$	2.04
21	Pyruvate	$\mathbf{CH_2}$	2.36
22	Creatine	$\mathbf{CH_3}$	3.04
23	TMAO	$\mathbf{CH_3}$	3.26
24	Creatine	$\mathbf{CH_2}$	3.93
25	Lipids	**-CH=CH-**	5.30

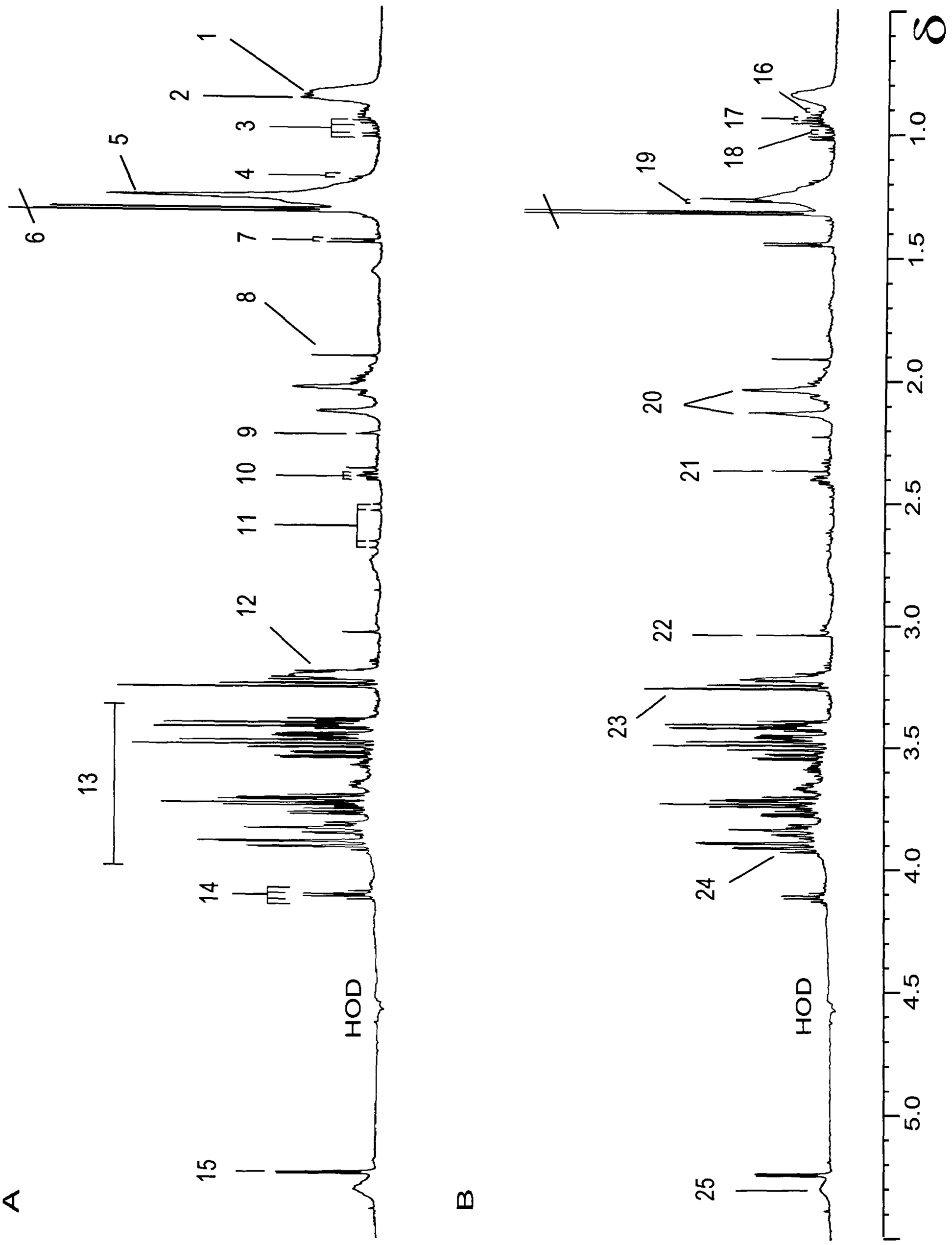

Figure 3.10 Effects of allyl formate (75 mg/kg) as visualised using CPMG spin-echo ^{1}H NMR spectra of Day 2 rat plasma. A. Control plasma. B. High-dose allyl formate.

Inspection of the Day 2 plasma CPMG spin-echo spectra revealed little change between the low dose and control animals. Figure 3.10 shows the effects of high dose allyl formate as visualised using CPMG spin-echo spectra of Day 2 plasma samples. The corresponding NMR spectral assignments are listed in Table 3.5. The most prominent change, observed in the high dose animals is a clear decrease in lipids especially the CH_2 and CH_3 moeties. Additionally, detailed inspection of the spectral data reveals more subtle biochemical variation between the spectral profiles of the high dose animals and control animals, with allyl formate-induced increases in creatine and tyrosine, and some changes in the glucose profiles. The Day 8 CPMG spin-echo spectra of the plasma samples indicate minimal effects. Details of the plasma NMR observations for allyl formate-dosed rats are summarised below in Table 3.6 and the changes reported being quantified according to the method described in Chapter 2.

Table 3.6 Summary of the plasma changes as observed in CPMG spin-echo NMR spectra of allyl formate-dosed rats.

Dose of allyl formate	Day	
	2	8
25 mg/kg	Visually, there were no clear differences from controls. VLDL/LDL: ↓ (NS). Total lipids: ↓ (27%, NS).	No observed differences from controls
75 mg/kg	Clear changes from controls were observed by visual inspection. Creatine: ↑ ** Tyrosine: ↑ **. Tyrosine was increased in animal, nos. 206, 207, 209 and 210. No increase was observed in animal 208. N-acetyl glycoprotein: ↑ * VLDL/LDL: ↓ **. Total lipids: ↓ (41%, NS).	Approximately the same as controls.

3.2.4.2 Principal Component Analysis of Day 2 Plasma NMR Data

An initial principal components analysis of the data set revealed some dose related structure to the variation in the data. Figure 3.11 shows the scores and loadings plots of the first two principal components of the PCA models between the allyl formate-treated animals and the controls.

The PCA scores plot of the control/low dose data set (Figure 3.11A) indicates differences in the metabolic profiles of the allyl formate-treated and control animals. Although there is a certain degree of overlap between the two groups the model gives a starting point from which further analysis may be carried out. In this case, the first principal component describes the variation between the two groups of animals. The corresponding loadings plot (Figure 3.11B) reveals the changes in the lipid moeties (VLDL, CH_2 and LDL, CH_3) that are the major contributors to the separation along the first principal component. The scores plot also revealed that control animal C7 is separated from the rest of the control animals along the second principal component. The corresponding loadings plot indicated that decreases in plasma lactate and choline are the contributors to the separation. Inspection of the CPMG spin-echo NMR spectrum of animal C7 indicated lower levels of choline and lactate as detected by PCA; and broad water peak, which contributed to spectral artefact (3.96P) shown in the loadings plot.

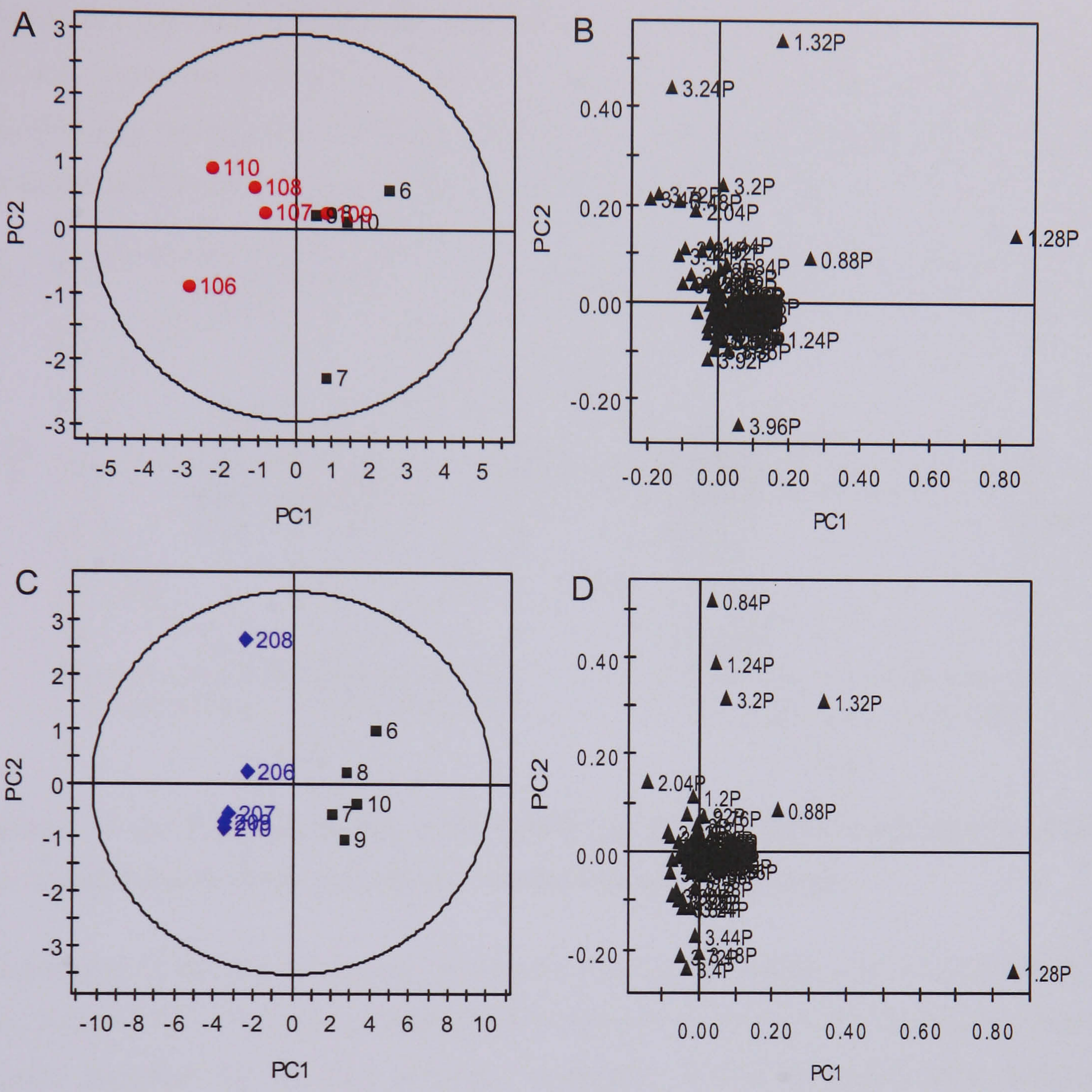

Figure 3.11 (A) PCA scores plot of the CPMG spin-echo NMR spectra of allyl formate-dosed plasma samples from Day 2 low-dose versus control groups, and (B) the corresponding loadings plot. (C) PCA scores plot of the CPMG spin-echo NMR spectra of allyl formate-dosed plasma samples from Day 2 high-dose versus control groups and (D) the corresponding loadings plot.

Figure 3.11C is a scores plot for the first two components of the high dose Day 2 plasma data set. There is very clear separation between the high dose animals and control animals in the first principal component. The corresponding loadings plot (Figure 3.11D) indicates that decreases in the regions attributed to lipids are the major contributors to the separation

between the high dose animals and control animals. Additionally, variability within the high dose group can be seen in the score plot along the second principal component. The corresponding loadings plot indicated that differences in the levels of plasma LDL, creatine and lactate contributed to the variability within the high dose animals.

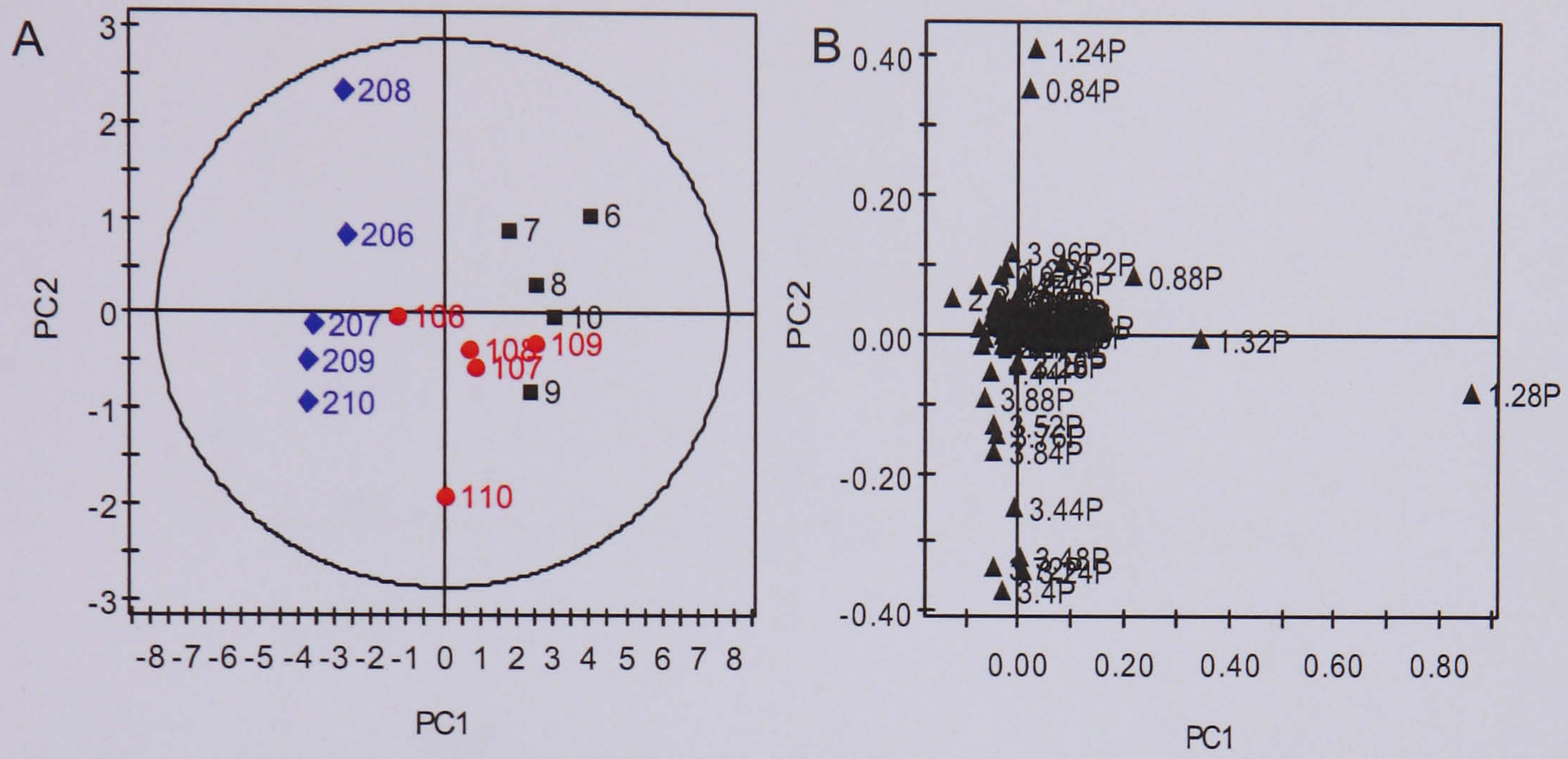

Figure 3.12 (A) PCA scores plot of the CPMG spin-echo NMR plasma spectra of the Day 2 allyl formate study, and (B) the corresponding loadings plot.

A scores plot of the first two components from a PCA of the combined Day 2 plasma NMR data (Figure 3.12A) showed clear separation between the high dose animals and the control animals described by the first principal component. Partial separation also occurred between the low dose animals and control animals along the first principal component. The corresponding loadings plot (Figure 3.12B) shows that allyl formate-induced decrease in lipids (VLDL) is the major contributor to the separation along the first principal component. Increases in plasma glucose as well as decreases in plasma lipids (LDL) contributed to the separation along the second principal component.

3.2.4.3 PLS – Discriminant Analysis (PLS-DA) of Day 2 Plasma NMR Data

The Day 2 plasma NMR data were also analysed using the PLS-DA approach to further refine the information recovery.

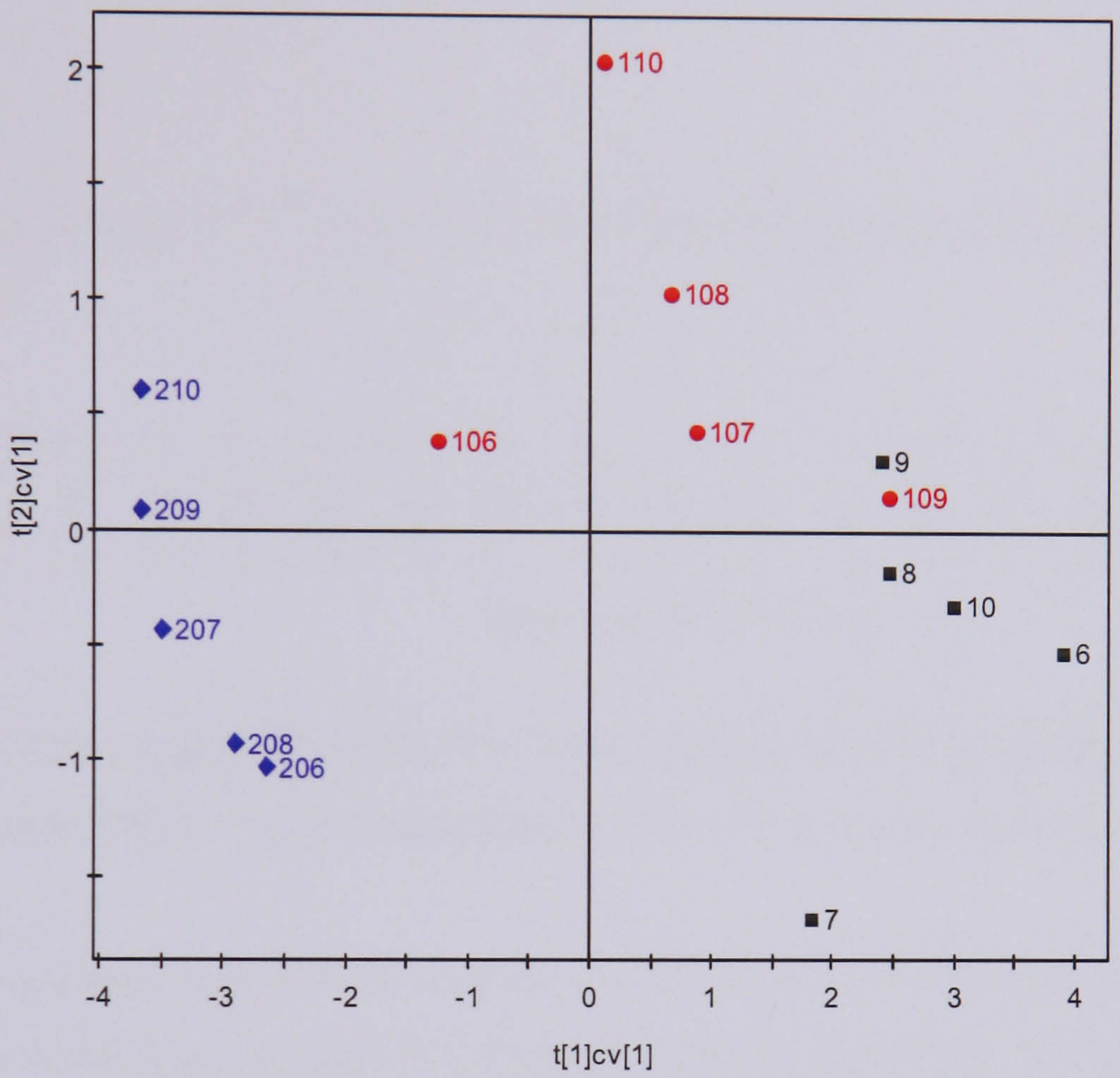

Figure 3.13 PLS-DA cross validated scores plot of the CPMG spin-echo NMR spectra of the Day 2 allyl formate study plasma samples.

The X matrix cross validated scores plot of the first two components (Figure 3.13) shows separation between each of the groups. The control group is situated on the lower right quadrant, with the low dose group (upper right quadrant) partially separated from the control group along the second PLS component. The high dose group is to the left of the plot separated from the control and low dose groups along the first PLS component. The score plot also revealed that control animal C7 is separated from the rest of the controls along the second PLS component.

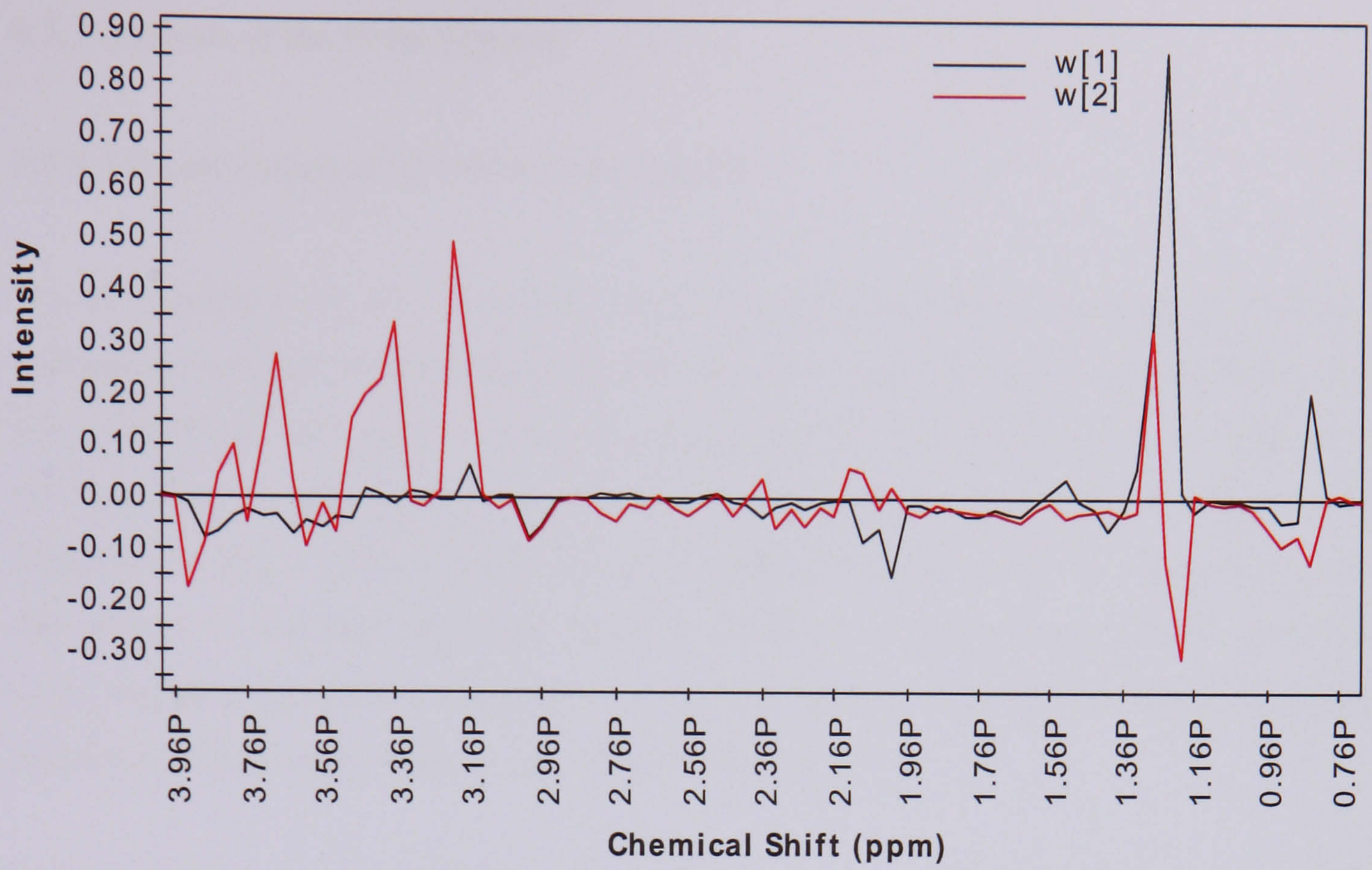

Figure 3.14 PLS weights from the ^{1}H CPMG spectra of the Day 2 allyl formate study plasma samples (W[1] = PLS component 1, W[2] = PLS component 2).

The corresponding X block PLS loadings plot (Figure 3.14) indicates that the first PLS component, describing the general variation between high dose and control/low dose animals, is due to a decrease plasma lipids and increases in plasma glycoprotein and creatine. The second PLS component, describing the variation between low dose and control animals, is due to increases in the plasma glucose and choline levels as well as some decrease in the plasma lipids. The loadings plot also indicated that reduced levels of plasma choline and glucose contributed to the separation of control animal C7 from the rest of the controls.

3.2.5 Analysis of the Urine Spectra

3.2.5.1 Examination of ^{1}H NMR urine spectra

Visual inspection of the low dose urine spectra revealed no substantial changes in endogenous urinary metabolites (data not shown). However, 3-hydroxypropylmercapturic acid (3-HPMA), an N-acetyl cysteine conjugate derived from allyl formate, was detected in the Day 1 (0-7 h post-dose) urine sample from each allyl formate-dosed rat and was also found in the Day 1 (7-24 h post-dose) urine samples obtained from the high dose animals. The effects of the high dose allyl formate treatment on endogenous urinary metabolites were assessed, as follows, using only the group euthanised at Day 8, which provided a sequence of daily urine samples covering the whole study.

Figure 3.15 shows a series of standard ^{1}H NMR urine spectra covering predose and various time points following the administration of high dose allyl formate. The high dose of allyl formate induced marked changes in the endogenous urinary metabolite profiles. The dominant changes included increases in creatine, taurine and phenylacetylglycine (PAG) and decreases in succinate, citrate, 2-oxoglutarate, TMAO and hippurate, which lasted up to Day 3 with maximal abnormality being observed in the Day 2 samples. In addition, the urine spectrum of animal 202 showed presence of short chain fatty acids i.e. propionate (δ1.08 and δ2.18), butyrate (δ0.9 and δ1.58) and lactate (δ1.32) on Day 2. The ^{1}H NMR spectra indicated recovery to normality by Day 7 post-dosing. Details of the urine NMR observations for allyl formate-dosed rats are summarised below in Table 3.7 and the changes reported were quantified according to the method described in Chapter 2.

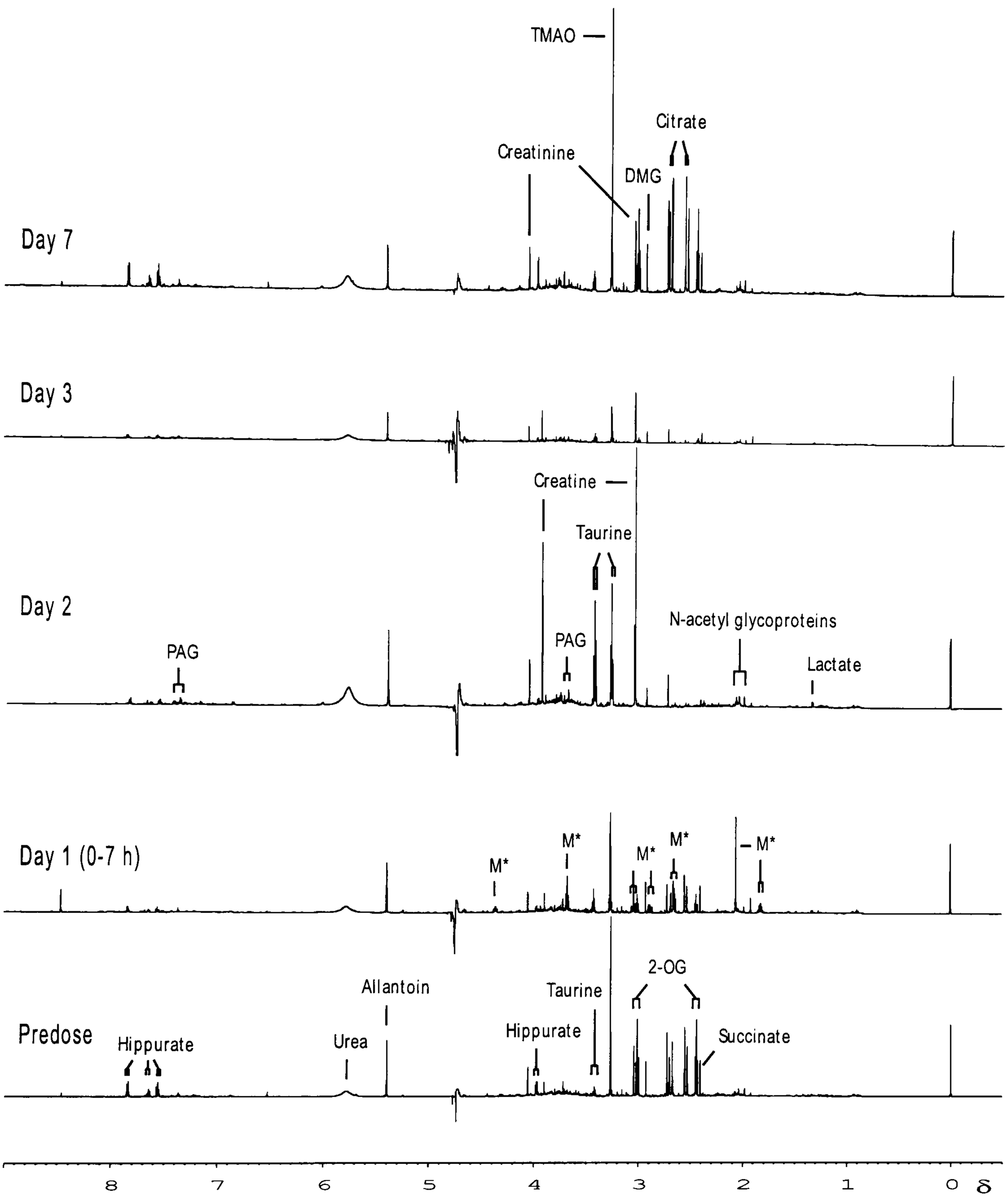

Figure 3.15 Series of standard ^{1}H NMR spectra of urine at predose and various time points following the administration of AF (75 mg/kg). Key: Metabolite of AF (M*), 2-oxoglutarate (2-OG), phenylacetylglycine (PAG), dimethylglycine (DMG).

Table 3.7 Summary of the urinary changes observed by NMR in allyl formate-dosed rats.

Dose of Allyl Formate	
25 mg/kg	**75 mg/kg**
3-HPMA present in the day 1 (0-1 hrs) samples.	3-HPMA present in both the day 1 (0-7 hrs) and day 1 (7-24 hrs) samples.
No substantial changes in the endogenous metabolites.	Marked changes in the endogenous metabolites were detected on various days. On Day 2 the changes were assessed as follows: Creatine: ↑ ** Taurine: ↑ (NS) 2-OG: ↓ ** Citrate: ↓ ** Phenylacetylglycine: ↑ (NS) Hippurate: ↓ (NS) TMAO: ↓ **

3.2.5.2 Principal Component Analysis of Urine NMR Data

Figure 3.16 shows a series of PCA scores plots of the first two principal components for the high dose allyl formate-treated animals and the controls. The scores plot of the pre-dose urine samples showed partial separation between the two groups. Animals 203, 204 and 205 are separated from the rest of the animals along the first principal component and control animal 4 is separated from the rest of the controls along the second principal component. The series of PCA scores plot highlighted that the endogenous biochemical differences between the two groups increased post-dose reaching a maximum at Day 2. However, separation between high dose animals and control animals on Day 1(0-7h) was mainly due to the presence of allyl formate metabolite, 3-HPMA. Additionally, the Day 1(0-7h) scores plot also shows animal 203 separated from the rest of the high dose animals along the second principal component. The Day 2 PCA scores plot shows clear differences between the high dose and control animals. The scores plot also indicated big variation within the high dose animals, which could reflect individual susceptibility to the high dose of allyl formate. The PCA scores plot of Day 3 urine samples shows partial separation between the two groups. In addition high dose animals 202 and 203 appear to be less affected than animals 201, 204 and 205 on Day 2 and recover faster than the rest of the high dose animals, being situated within the control group on Day 3. Finally, the scores plot of Day 7 shows some separation indicating partial recovery. These observations confirm that there are biochemical changes between the groups upon administration of high dose allyl formate that is becoming more prominent with increasing time until a time maxima of Day 2 before gradual recovery from the toxic insult on Day 3 onwards.

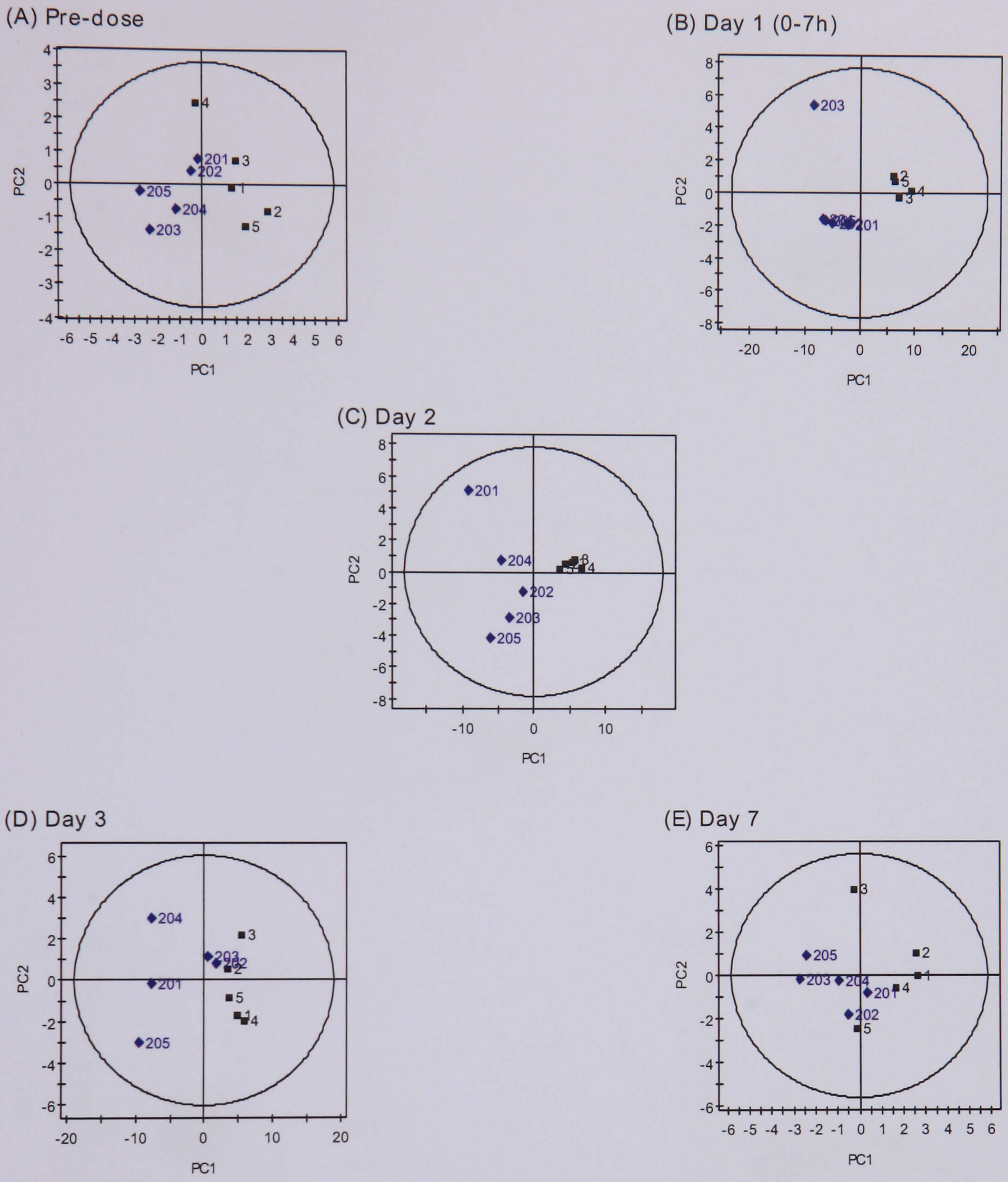

Figure 3.16 A series of PCA scores plots of the first two components to investigate time related metabolic differences associated with the effects of high dose allyl formate in the animals.

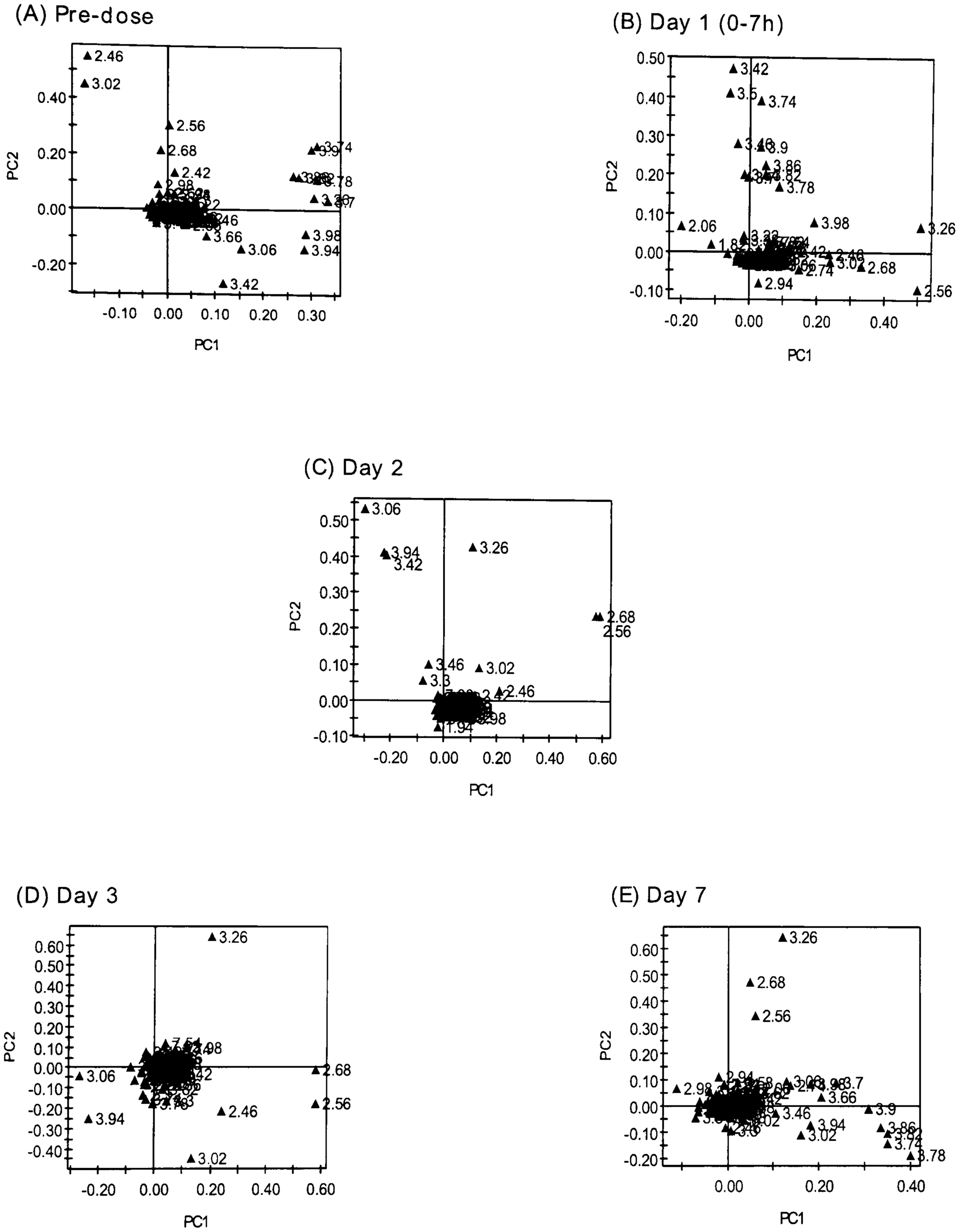

Figure 3.17 A series of corresponding PCA loadings plots of the first two components to investigate time related metabolic differences associated with the effects of high dose allyl formate in the animals.

Figure 3.17 shows a series of PCA loadings plots of the first two principal components of the high dose allyl formate-treated animals and the controls. The loadings plot for the pre-dose data indicated that high dose animals 203, 204 and 205 have lower urinary glucose and creatine as compare to the rest of the animals. Careful inspection of the urinary NMR data confirmed that high dose animals 203, 204 and 205 have lower levels of urinary glucose and creatine. In addition, control animal 4 showed higher level of urinary 2-oxoglutarate as compared to the rest of the animals, which contributed to the separation along the second principal component. Overall the loadings plots show that the trends seen in the PCA scores plots (Figure 3.16) were attributed to relative changes in the urinary endogenous metabolites, with the exception of Day 1 (0-7h). The loadings plot for Day 1 (0-7h) indicates changes in the endogenous metabolites i.e. decreases in urinary citrate, TMAO and 2-oxoglutarate as well as the appearance of N-acetyl cysteine conjugate of allyl formate, 3-hydroxypropylmercapturic acid (3-HPMA). High dose animal 203 was separated from the rest of the high dose animals due to higher urinary taurine level. The loadings plot for Day 2 shows that decreases in succinate, citrate, 2-oxoglutarate, TMAO and hippurate as well as increases in phenylacetylglycine (PAG), taurine and creatine are the major contributors to the separation along the first principal component. These changes can be seen clearly in the series of urinary NMR spectra (Figure 3.15). In addition, variation in the severity of changes of the endogenous metabolites contributed to the variation within the high dose animals along the second principal component. The loadings plot indicated that variation in the concentration of the endogenous metabolites such as creatine, citrate, TMAO and taurine contributed to the variation within the high dose animals. These changes could be due to inter-animal variability and susceptibility to allyl formate. The loadings plot for Day 3 indicated increases in urinary PAG, taurine and creatine as well as decreases in urinary citrate, TMAO, hippurate and 2-OG contributed to the separation along the first principal component. The loadings plot also shows that variation in urinary TMAO level contributed to the variation within the three most affected high dose animals (animals 201, 204, 205). The loadings plot for Day 7 shows the levels of endogenous metabolites returning to equilibrium. However, the loadings plot indicated that control animal C3 has a higher level of urinary TMAO and citrate as compare to the rest of the controls.

3.2.5.3 PCA Mean Trajectory of Urine NMR Data

PCA mean trajectory was performed using the ^{1}H NMR spectra of urine sample for all high dose animals over five time points as above to extract time-related metabolic changes in rat urine samples in response to xenobiotic insult. PCA mean trajectory was carry as described in chapter 2.

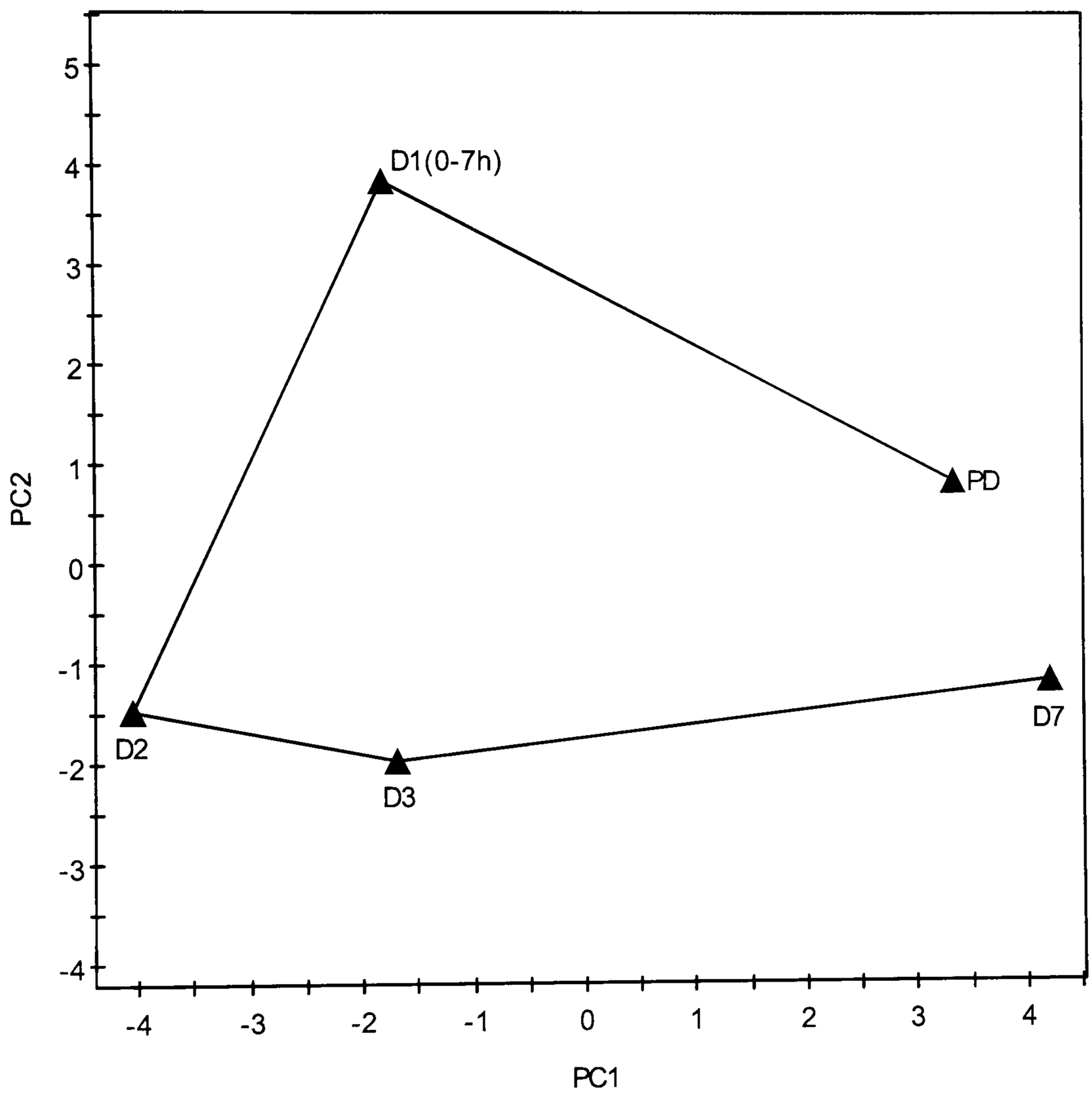

Figure 3.18 PCA mean metabolic trajectory plot mapping the average position of standard ^{1}H NMR high dose allyl formate urine spectra over five time points.

A PCA mean trajectory plot (Figure 3.18) was constructed from the complete data-reduced ^{1}H NMR spectra, excluding the region of water and urea (δ 4.0-6.0). The first two PCs described 93.2% of the total variance in X. The modelled metabolic evolution comprised three distinct phases. In phase one, corresponding to movement to the Day 1 (0-7h) time point, the trajectory of the urine sample coordinates moved away from the pre-dose (PD) position along the first component corresponding to the appearance of the mercapturic acid, 3-HPMA as well as some decreases in urinary citrate, TMAO and 2-oxoglutarate. Thereafter in phase two, corresponding to movement to the Day 2 time point, the trajectory changes direction moving away from the origin along the second component corresponding to the disappearance of 3-HPMA from the urine with a concomitant decrease in endogenous metabolites 2-oxoglutarate, TMAO, citrate, succinate, hippurate and an increase in urinary PAG, creatine, and taurine levels with the changes reaching maximal level on Day 2. Finally in phase three, corresponding to movement to Day 3 and Day 7 time points, the trajectory returned towards the starting point along the first component corresponding to increases in 2-oxoglutarate, citrate, succinate hippurate and decreases in creatine, TMAO and taurine to control levels indicating recovery.

3.2.6 Pattern Recognition Analysis of Concatenated Liver and Plasma NMR Data

3.2.6.1 Principal Component Analysis (PCA)

For the first time, PCA was performed on concatenated liver and plasma NMR data and Figure 3.19 shows the resulting scores and loadings plots. The scores plot for the low dose and control animals (Figure 3.19A) shows partial separation between the two groups with all but one of the low dose animals separated from the controls. The first principal component describes the variation between low dose animals and control animals with animal C6 showing relatively low liver lipids levels located away from the rest of the controls. The loadings plot (Figure 3.19B) indicates that decreases in plasma lipids (δ1.28 and δ0.88) and an increase in liver TMAO signal (δ 3.27) are the contributors to this separation along the first principal component, with the change in the plasma lipids at δ1.28 being the dominant factor.

A PCA scores plot of the high dose Day 2 liver and plasma data (Figure 3.19C) revealed clear separation between the high dose and control groups along principal component one. The corresponding loadings plot (Figure 3.19D) revealed that decreases in plasma lipids, liver glucose (δ3.30 - δ 4.00) and glycogen (δ5.42 and δ3.84) as well as increases in liver lipid signals (δ1.28 and δ0.90), plasma N-acetylglycoprotein (δ2.04), creatine (δ3.04 and δ3.92), choline, glucose and amino acids regions are the contributors to the separation along the first principal component. Again, the change in the plasma lipids at δ1.28 is the dominant factor contributing to this separation. The PCA model, however, failed to detect changes in tyrosine as observed in the plasma ^{1}H NMR spectra.

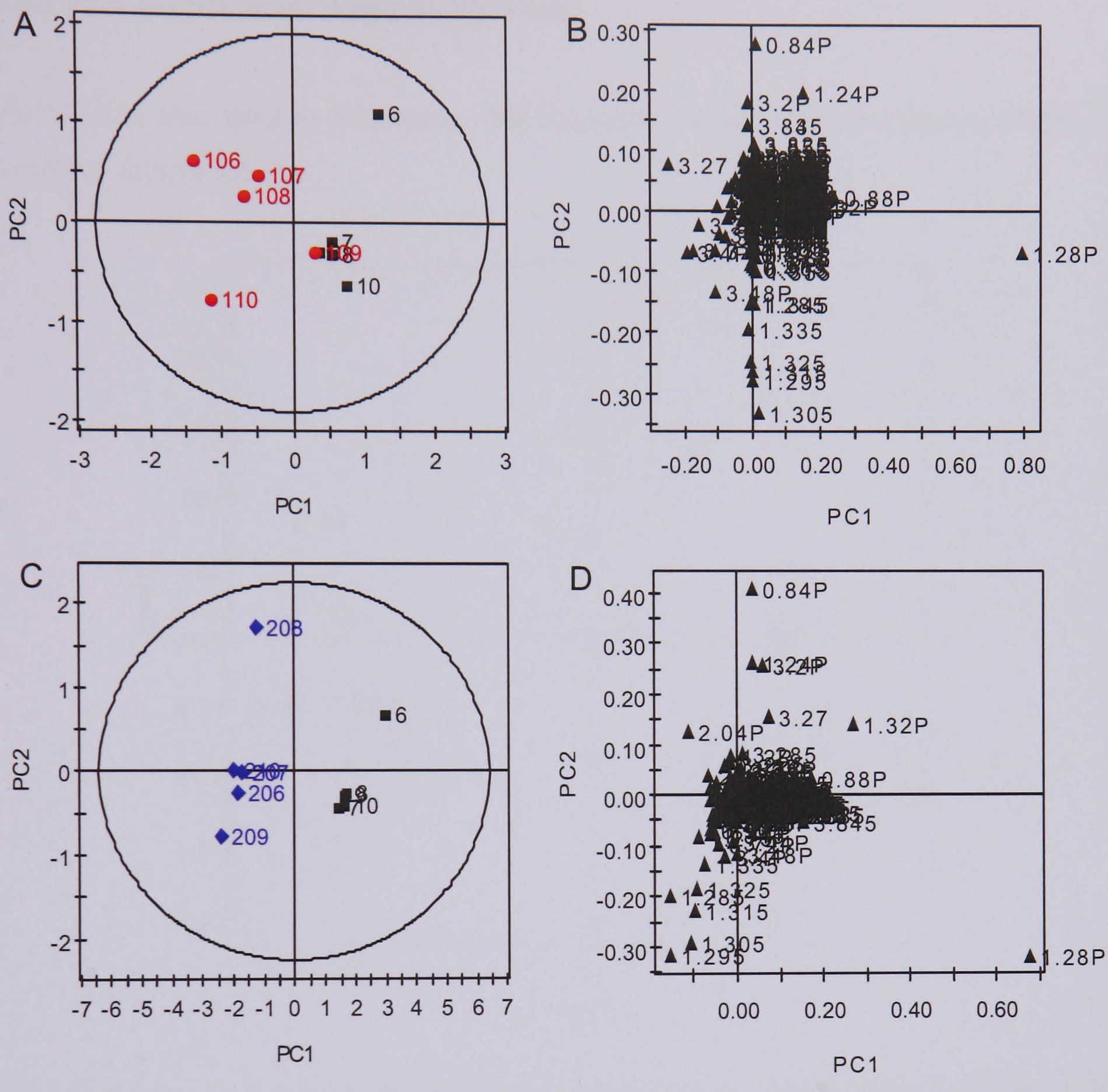

Figure 3.19 Concatenated PCA models for the first two components of the Day 2 standard 1D NMR spectra of allyl formate-dosed liver and CPMG spin-echo plasma NMR spectra. (A) Low-dose vs. control data and the corresponding loadings plot (B). (C) High-dose vs. control data and the corresponding loadings plot (D).

3.2.6.2 PLS-Discriminant Analysis (PLS-DA)

PLS-DA was also used to determine which variables in the liver and plasma NMR data predict the sample classes.

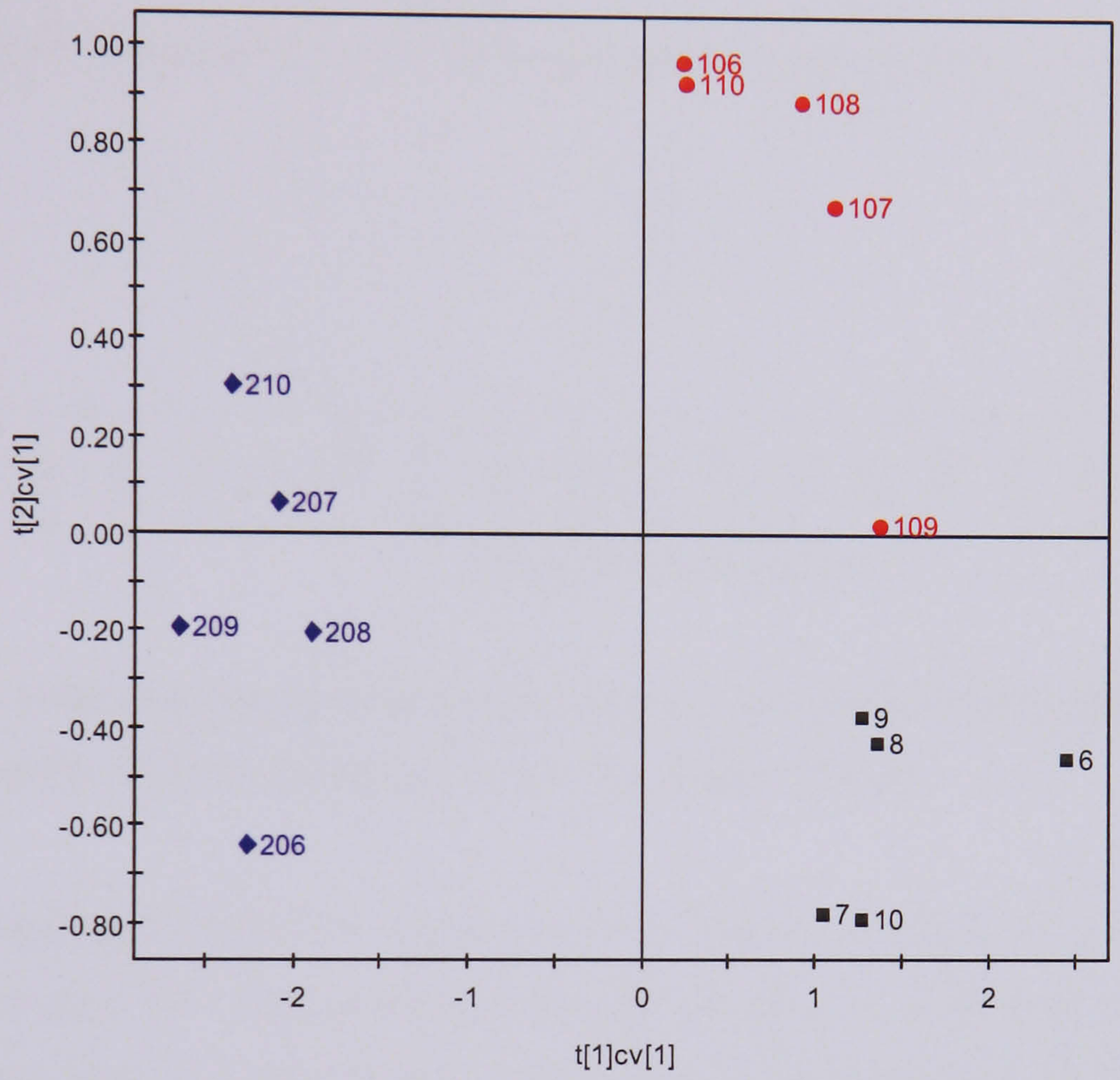

Figure 3.20 PLS-DA cross validated scores plot of standard ^{1}H NMR spectra of allyl formate Day 2 liver tissue and CPMG spin-echo NMR of Day 2 plasma samples.

By treating the NMR data as the X matrix and dosage groups as the Y matrix, the cross validated scores plot of the first two components (Figure 3.20) revealed clear separation between the controls and the dosed groups particularly between the low dose and control groups. The high dose animals are separated from the control and low dose animals along the first PLS component. The low dose animals are distinguished from the high dose and control animals along the second PLS component. The low dose animals are also partially separated from the high dose animals along the second PLS component.

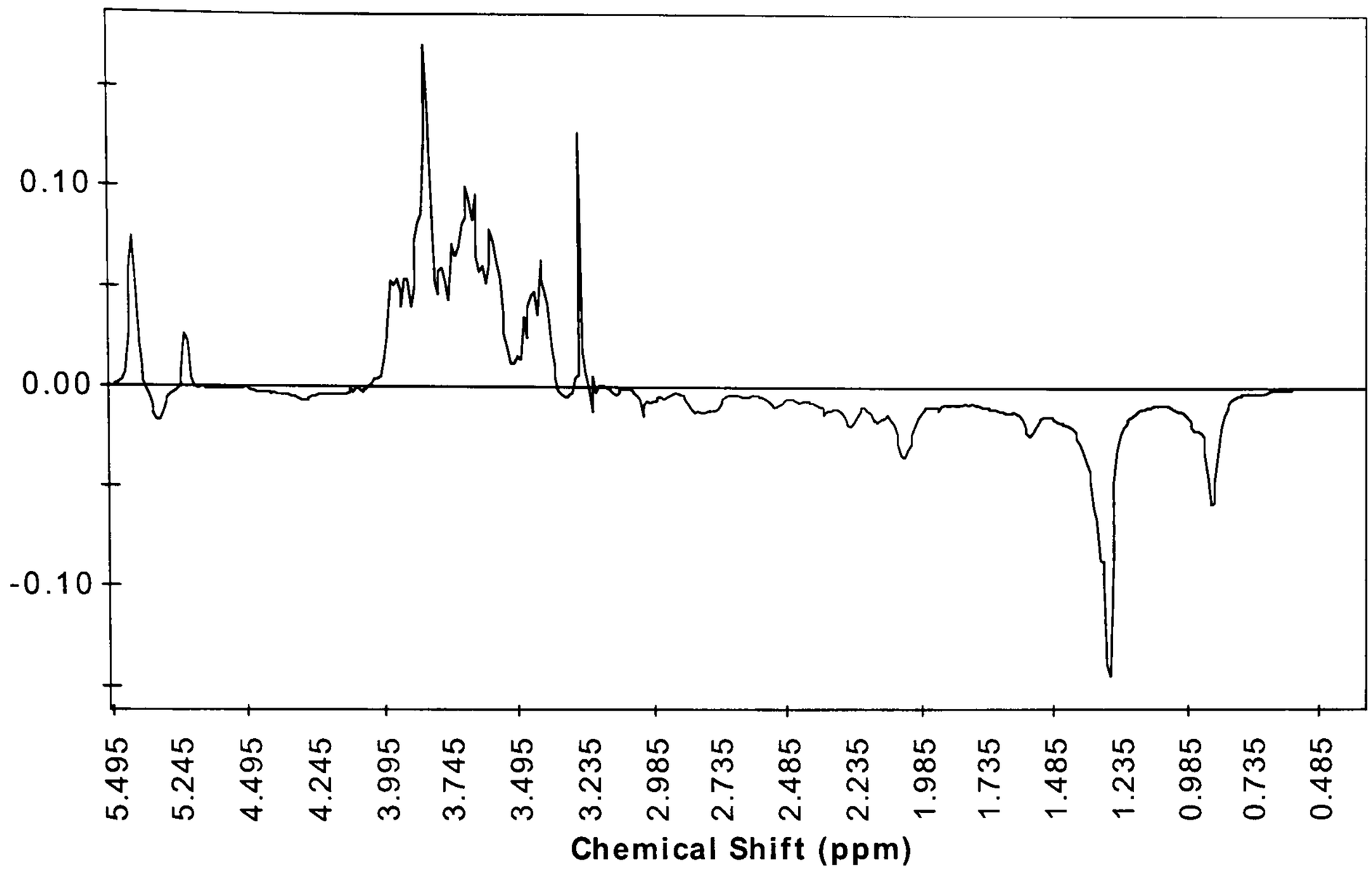

Figure 3.21 First component PLS weight (W[1]) from the PLS-DA model attributed to the standard 1D ^{1}H MAS NMR spectra of Day 2 liver tissues.

The corresponding X block first component PLS loadings attributed to the liver tissue data is shown in Figure 3.21. The plot shows the general effects of dosing on liver tissue along the first component. It indicates that animals dosed with high dose allyl formate exhibit elevated lipids and lower levels of carbohydrates and glycogen storage as well as TMAO. These changes contributed to the separation between the high dose animals and rest of the animals.

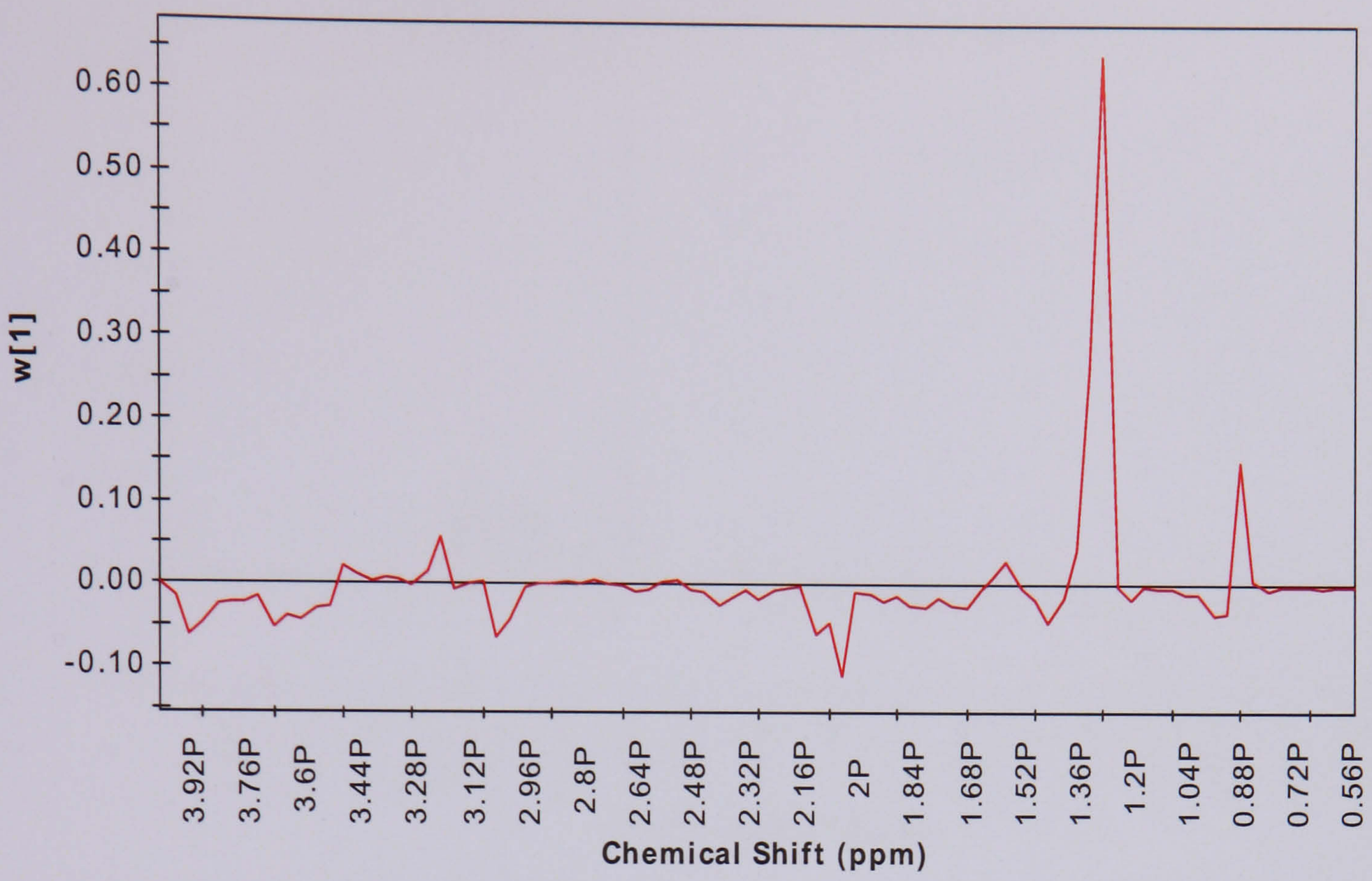

Figure 3.22 First component PLS weight (W[1]) from the PLS-DA model attributed to the CPMG spin-echo NMR data of Day 2 plasma samples.

The corresponding X block first component PLS loadings attributed to the plasma data is shown in Figure 3.22. This plot shows changes in the plasma profile that contributed to the separation along the first component of the PLS-DA scores plot in Figure 3.20. The plot indicates a decrease in plasma lipids is the major contributor to the separation between the high dose animals and the rest of the animals. Additionally, increases in plasma N-acetyl glycoprotein and creatine also contributed to the separation along the first component.

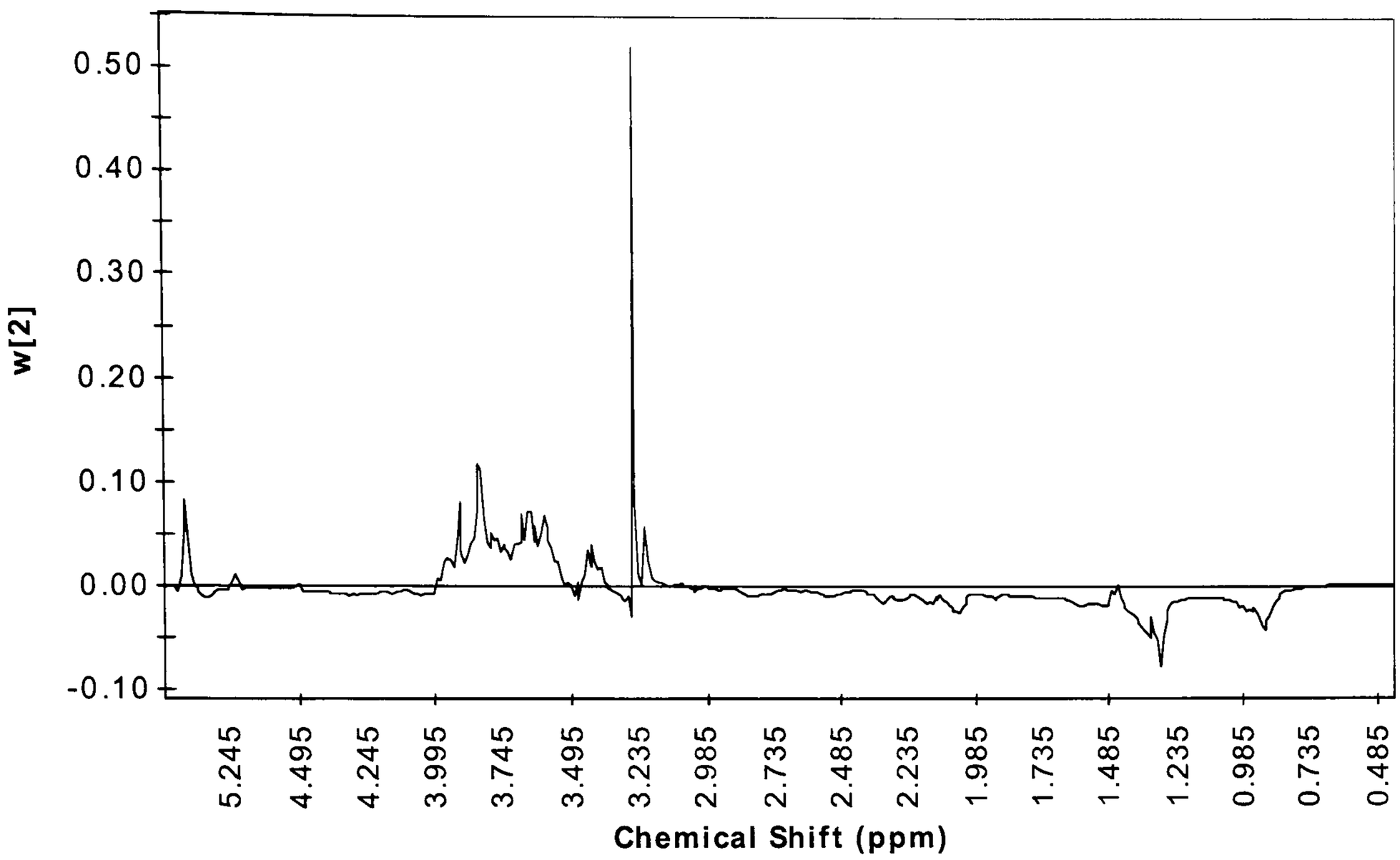

Figure 3.23 Second component PLS weight (W[2]) from the PLS-DA model attributed to the ^{1}H MAS NMR data of Day 2 liver tissues.

The corresponding X block second component PLS loadings attributed to the liver tissue data are shown in Figure 3.23. The plot shows the general effects of dosing on liver tissue along the second component. It indicates that animals given the low dose of allyl formate exhibit some decrease in lipids and higher levels of TMAO, carbohydrates and glycogen relative to controls. The loadings plot also showed variation within the high dose animals that is mainly due to changes in liver TMAO level.

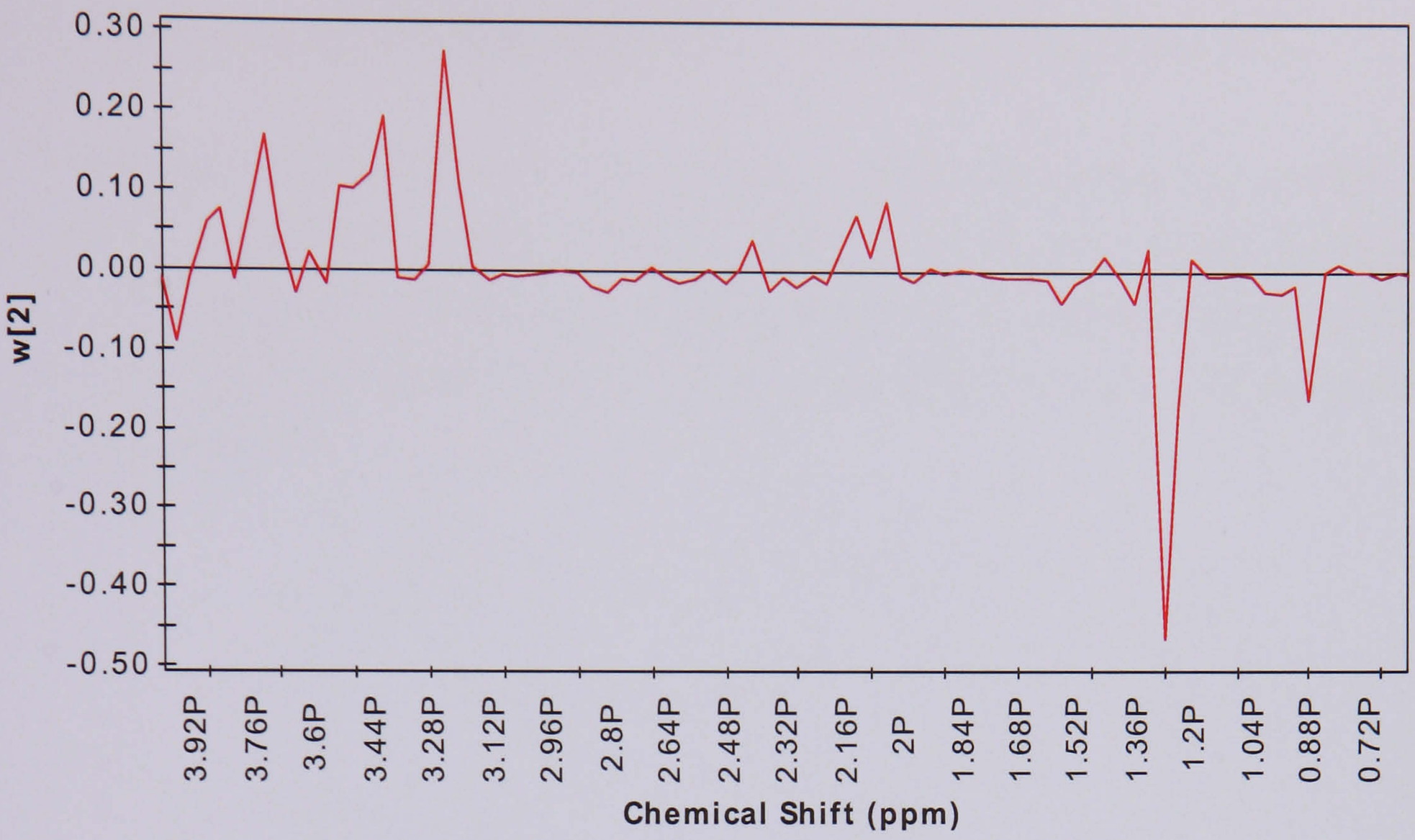

Figure 3.24 Second component PLS weight (W[2]) from the PLS-DA model attributed to the CPMG spin-echo NMR data of Day 2 plasma samples.

The corresponding X block second component PLS loadings attributed to the plasma data is shown in Figure 3.24. This plot shows changes in the plasma profile that contributed to the separation along the second component of the PLS-DA scores plot in Figure 3.20. The plot indicates that a decrease in plasma lipids and increase in plasma choline and glucose levels are the major contributors to the separation between the low dose animals and control animals.

3.2.6.3 Partial Least Square Projection to Latent Structures Approach (PLS)

Having established that there were intrinsic differences between groups, the two NMR data matrices were analyzed against each other using PLS to try and improve classification between groups. This approach also enabled determination of plasma NMR features that correlated with the liver MAS NMR biomarkers. The NMR data were mean centre-scaled prior to modelling.

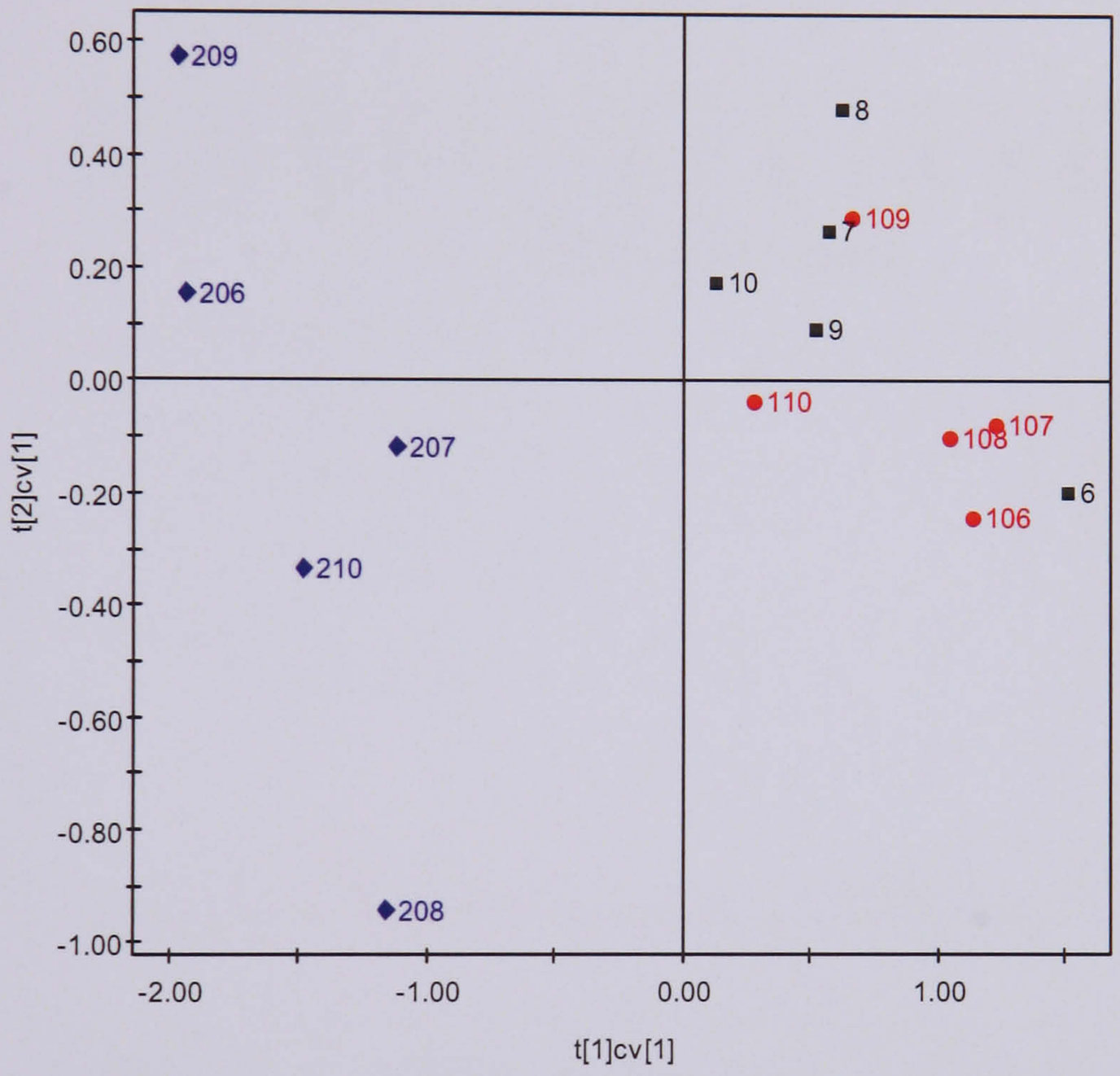

Figure 3.25 PLS cross validated scores plot of standard ^{1}H NMR spectra of allyl formate Day 2 liver tissue and CPMG spin-echo NMR data of Day 2 plasma samples.

By treating liver NMR data as the X matrix and plasma NMR data as the Y matrix, the cross validated scores plot (Figure 3.25) revealed clear separation between the high dose animals and the rest of the animals along the first PLS component. However, no separation occurs between the low dose and control groups.

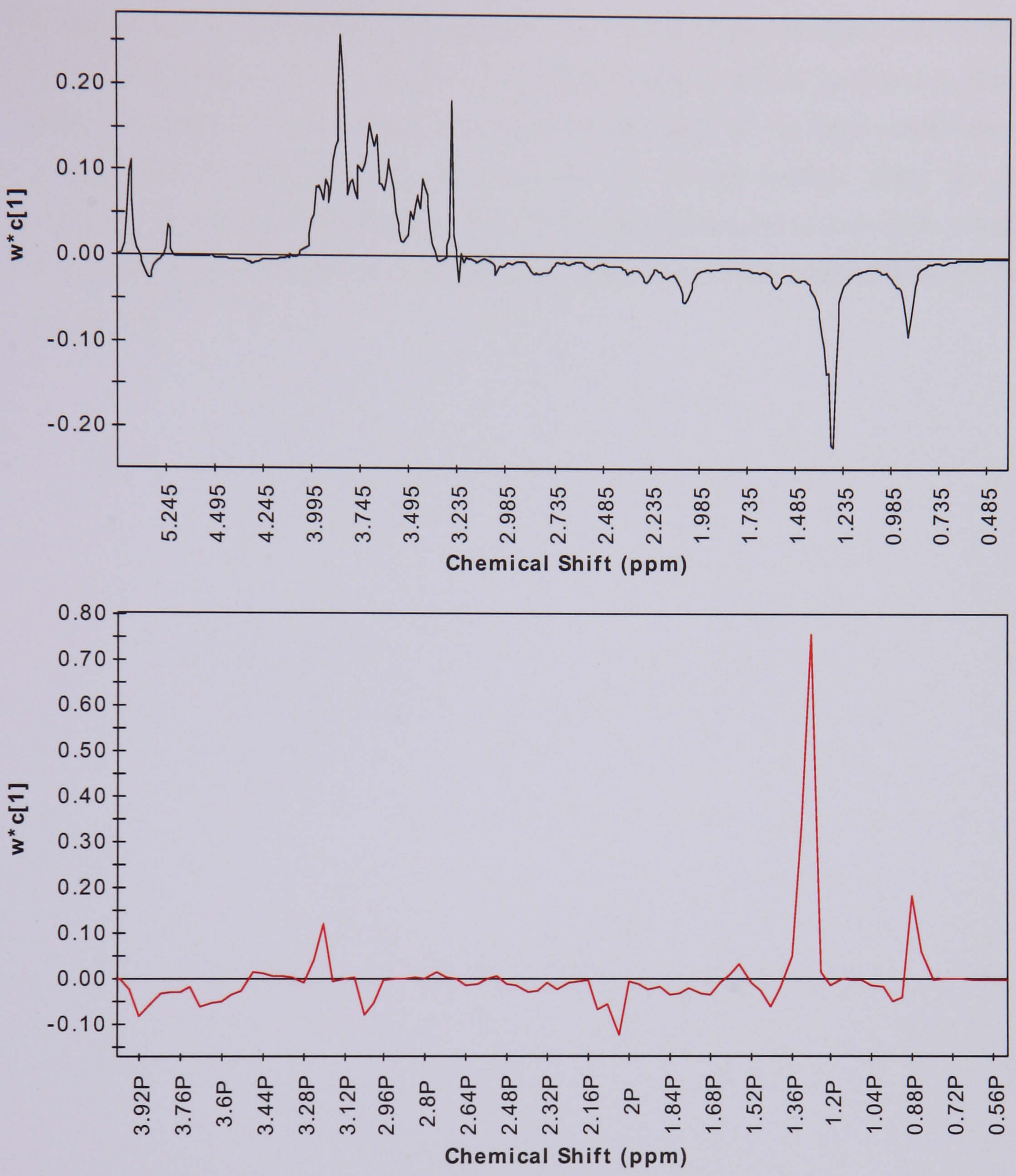

Figure 3.26 First component PLS weight (W*[1]) from the PLS model attributed to (A) ^{1}H MAS NMR data of Day 2 liver tissues (—), and (B) CPMG spin-echo NMR data of Day 2 plasma samples (—).

The corresponding PLS loadings plot (Figure 3.26) revealed that increases in liver lipids signals and decreases in liver carbohydrates and glycogen as well as increases in plasma creatine, N-acetyl glycoproteins and decreases in plasma lipids are the major contributors to the separation between the high dose animals and control animals along the first component. In addition, the loadings plot also indicated that increase in liver lipids is linked to a decrease in plasma lipids indicating possible reduction in lipid transport from the liver to the plasma.

3.3 Discussion

3.3.1 Effects of Allyl Formate on rat liver

At the high dose, allyl formate induced variable degrees of hepatocellular necrosis as revealed by the histopathological data The observed decreases in liver glycogen and glucose suggest increased energy demand within the liver and ATP-depletion by allyl alcohol has been confirmed in periportal regions of isolated perfused rat livers by Belinsky *et al.* (1986) and in isolated rat hepatocytes by Farghali *et al.* (1992). This increased demand for ATP is likely to arise through damage to the mitochondria, which are normally the major source of ATP, since allyl formate is also known to inhibit mitochondrial respiration (Rees and Tarlow 1967) and allyl alcohol can cause the collapse of mitochondrial membrane potentials in-vitro (Pang *et al.* 1997). With impairment of mitochondrial ATP-production, glycolysis would be expected to enable some ATP production as glucose is converted to lactate in the cytosol and glycogenolysis would increase the supply of glucose for this process.

To be observable by ^{1}H MAS NMR the lipid species must be in a mobile state and deposition of lipid droplets within the cell is the most likely candidate for the observed increases in lipid signals. Typically such lipid pools are found in cases of fatty liver and consist of a variety of compounds derived from fatty acids especially triglycerides. There are various reasons why liver triglycerides might increase with allyl formate-induced damage.

1. Normally, fatty acid metabolism is under strict homeostatic control and is responsive to physiological demands, with fatty acids being synthesised when carbohydrates and ATP are readily available and degraded through the fatty acid cycle. The latter cycle involves reaction of ATP with fatty acid as an activation step to form fatty acid-ADP anhydride. This is followed by β-oxidation to form acetyl CoA, which will then enters the citric acid cycle and ultimately form ATP. The periportal region is a major site of fatty acid oxidation and severe and prolonged

impairment of β-oxidation in the mitochondria is known to cause steatosis and, in some severe cases, liver failure and death (Fromenty and Pessayre, 1995). Thus, mitochondrial impairment could lead to fatty liver through impairment of fatty acid oxidation.

2. Secondly, the transport of triglycerides out of the liver requires apolipoprotein and could be decreased through impaired protein synthesis or through protein degradation. For example after dosing with ethionine or hydrazine, impaired apolipoprotein synthesis leads to reduced transport of triglycerides out of the liver (Waterfield *et al.* 1998; Waterfield *et al.* 1997). After dosing with allyl formate, impaired protein synthesis could arise simply through ATP-depletion but *in vitro* study has also shown that acrolein undergoes extensive carbonylation reactions with proteins (Burcham and Fontaine 2001) and that cysteine residues in proteins react readily with acrolein (Esterbauer *et al.* 1975). Thus, either ATP depletion or the presence of acrolein might lead to fatty liver by impairing the transport of triglycerides out of the liver.

3. Additionally, Lin *et al.* (1996) demonstrated that an increase in the intracellular bile acids concentration also inhibits the secretion of VLDL-associated triglycerides from hepatocytes as well as the secretion of the apolipoprotein associated with transport of VLDL namely apoB-100. Allyl formate causes some biliary damage and the plasma clinical chemistry results in our current study indicated an increase in total bile acids (TBA). Thus, bile acids could have an inhibitory effect on triglyceride secretion leading to accumulation of triglycerides in the liver.

The loss of glutathione is likely to be a key factor in the liver damage induced by allyl formate. GSH will be depleted by direct addition to acrolein and when GSH is depleted, acrolein will be free to attack other compounds and sites. However, our results do not appear to provide evidence for the lipid peroxidation reported by other worker (Adams and Klaidman 1993) and which has been suggested as a factor of allyl formate toxicity by Ferrali *et al.* (1989). The highly variable responses to allyl formate dosing are unexplained

but indicate inter-animal variation in the metabolism of allyl formate or in defensive capabilities.

The MAS NMR also showed a decrease in liver TMAO level in the high dose allyl formate animals. Increased phospholipids could lead to a decrease in TMAO levels, but the MAS NMR data did not show any such increase in liver phospholipids which would suggests the absence of phospholipidosis. The decrease in TMAO could then be related to a decrease in the level of the flavin monooxygenase (FMO) enzyme, which catalyse the oxidation of trimethylamine (TMA) to TMAO. The activity of FMO is highly dependent on NADPH (Ziegler 1990, Baker *et al.* 1963, Wu *et al.* 1986). At a pH of 7.4 and temperature of 41 °C, NADPH was found to have a short half-life of 6 ½ hrs (Wu *et al.* 1986) and acrolein has been shown to inhibit protein synthesis (Burcham and Fontaine 2001, Esterbauer *et al.* 1975).

3.3.2 Effects of Allyl Formate on blood plasma and urine

The effects of allyl formate on blood plasma are characterised by increases in aspartate and alanine aminotransferases, which are indicative of hepatocellular damage and increases in 5' nucleotidase, γ-glutamyl transferase and bile acids, which are specific markers of hepatobiliary dysfunction. Allyl formate also caused increases in creatine and tyrosine and a reduction in lipids and the VLDL/LDL ratio. In the urine, increases in taurine and creatine were observed together with the presence of 3-hydroxymercapturic acid (3-HPMA) (Clayton *et al.* 2003). Additionally, there were urinary decreases in citrate, 2-oxoglutarate, PAG and TMAO.

The reduction in the ratio of VLDL/LDL could be because of reduced lipid secretion from liver. The urinary taurine increases could arise from impaired hepatic protein synthesis with cysteine being diverted in consequence, from protein synthesis to taurine synthesis (Waterfield *et al.* 1991). The tyrosine increase in plasma also suggests protein degradation or impaired protein synthesis within the liver where, tyrosine is normally converted to p-hydroxyphenylpyruvate through the action of tyrosine-amino-transferase (TAT) which is an

unusually short-lived enzyme (t½ = 2 ½ hours). Allyl formate-induced protein degradation or impaired protein synthesis could rapidly lead to TAT depletion and consequent increases in tyrosine in the liver and blood.

The allyl formate-induced increases in urinary creatine may be related to increased cysteine biosynthesis from methionine as postulated by Clayton *et al.* (2003a). Cysteine is used to synthesise GSH, taurine and proteins. During this biosynthesis, S-adenosylmethionine donates a methyl group to the methyl acceptor, guanidinoacetic acid (GAA). The methylated-GAA is then converted to creatine, which enters the blood for use in peripheral tissues or excretion. The presence of 3-HPMA is supportive of the reaction of acrolein with glutathione (Sanduja *et al.* 1989). Decreases in urinary citrate, and 2-oxoglutarate are indicative of disruption in the tricarboxylic acid (TCA) cycle.

3.3.3 Comparison of Information Obtained from Different Sources

The use of high resolution ^{1}H MAS NMR spectroscopy to study intact liver tissues, which provides the essential link between the metabolite profiles obtained from biofluid NMR and the structural progression of the lesion observed by histopathological technique. The integrated approach wherein conventional toxicological data and multiple types of NMR data are analysed collectively, proved useful in describing allyl formate-induced toxicity in rats. Table 3.8 shows the summary of the effects of allyl formate in rats. Overall, the NMR findings are consistent with the clinical chemistry findings as well as the histopathology, which showed some allyl formate-induced effects in low dose animals and clear allyl formate-induced effects of variable severity in high dose animals with near total recovery by the end of the study. The Day 8 standard ^{1}H NMR spectra showed minimal effect and this was reflected in the PCA plots. This suggests that recovery was largely complete by Day 8. This is consistent with the histopathology and clinical chemistry findings. The Day 2 plasma NMR data showed clear increases in plasma tyrosine level in all high dose animals. The degree of change in plasma tyrosine level correlated with the variable severity of the hepatocellular necrosis observed in this group of animals as shown in Table 3.9. Thus plasma tyrosine could be a marker for liver necrosis as suggested by Kawamura-

Yasui *et al.* (1999) and Shaw and Lieber (1983), but might be partially related to ATP depletion and impaired protein synthesis.

Additionally, the Day 2 plasma NMR data also showed increase in plasma creatine. Increase in plasma creatine level normally leads to increase in urinary creatine level, which is evident in the current study. However, the increased plasma creatine does not correlate with the extent of necrosis detected in histopathology as shown in Table 3.10. Clayton *et al.* (2003a & 2003b) suggested that creatine is synthesised as a by-product of cysteine synthesis with cysteine in turn being required for the synthesis of taurine, glutathione and proteins. Therefore, if the increase in creatine is a symptom of defensive processes then the amount of the increase would not be expected to show a simple relationship to the amount of damage caused.

Table 3.8 Summary of the effects of allyl formate.

Dose of Allyl formate	Histopathology	Clinical Chemistry	Liver NMR	Plasma NMR	Urine NMR
25 mg/kg	No significant differences from controls.	Slight decrease in triglycerides.	Minimal change	Minimal change	Appearance of 3-HPMA.
75 mg/kg	Periportal to diffuse lobular haemorrhagic coagulative necrosis with various degree of severity.	Triglycerides: ↓ (***) ASAT: ↑↑ (***) ALAT: ↑↑ (***) TBA: ↑↑ (***) GGT: ↑ (***) Albumin: ↓ (**) TP: ↓ (***)	TMAO: ↓ (*) Glucose: ↓ (*) Glycogen: ↓ (*) Lipids: ↑ (*)	Creatine: ↑ (**) VLDL/LDL: ↓ (**) Total lipids: ↓ (NS) Tyrosine: ↑ (**) NAG: ↑ (*)	TMAO: ↓ (**) Creatine: ↑ (**) Taurine: ↑ (NS) 2-OG: ↓ (**) Citrate: ↓ (**) Hippurate: ↓ (NS) PAG: ↑ (NS)

Key: ASAT = aspartate aminotransferase, ALAT = alanine aminotransferase, TBA = total bile acids, GGT = γ-glutamyltransferase, TP = total plasma protein, TMAO = trimethylamine-N-oxide, NAG = N-acetyl glycoprotein, VLDL = very low density lipoprotein, LDL = low density lipoprotein, 3-HPMA = 3-hydroxypropylmercapturic acid, 2-OG = 2-oxoglutarate, PAG = phenylacetylglycine.

Table 3.9 Plasma tyrosine in relation to the extent of liver necrosis.

Animal Number	Concentration of Day 2 plasma Tyrosine (multiple of average control level)	Extent of Liver Necrosis Detected by Histopathology at Day 2
206	2.4 x control average	Marked
209	2.4 x control average	Marked
207	1.9 x control average	Moderate
210	1.9 x control average	Moderate
208	1.3 x control average	Minimal

Table 3.10 Plasma creatine in relation to the extent of liver necrosis.

Animal Number	Concentration of Day 2 Plasma creatine (multiple of average control level)	Extent of Liver Necrosis Detected by Histopathology at Day 2
206	3.4 x control average	Marked
209	3.4 x control average	Marked
207	3.5 x control average	Moderate
210	1.7 x control average	Moderate
208	2.5 x control average	Minimal

The Day 2 plasma NMR data also revealed variable decreases in plasma lipids but again, these changes did not correlate to the extent of necrosis observed by histopathology. Analysis of the LDL and VLDL moieties of the plasma NMR data showed decreases in both LDL and VLDL in the low dose animals. In the high dose animals, however, decrease in plasma VLDL is bigger in magnitude as compare to that of LDL (Table 3.11).

Table 3.11 Changes in Day 2 plasma LDL and VLDL levels.

Allyl formate dose group	**Decrease in Day 2 plasma LDL (NMR data, %)**	**Decrease in Day 2 plasma VLDL (NMR data, %)**
LD	16.8	26.9
HD	2.7	41.5

The integrated metabonomic analysis of liver and plasma NMR data enabled simultaneous study and extraction of information embedded in these two biomatrices and the use of PLS analysis on liver and plasma data provided insights into the changes in the liver which correlated with the changes in the plasma. The data presented by the PLS plots (Figure 3.24 and 3.25) showed an increase in liver triglycerides that correlated to a decrease in plasma lipids, which could indicate reduced lipid transport from the liver to the plasma.

The urinary decreases in TCA cycle intermediates such as citrate and 2-oxoglutarate suggest mitochondrial dysfunction (Antti *et al.* 2002). The urine NMR data also showed increases in urinary creatine and taurine, which are indicative of hepatotoxicity (Waterfield *et al.* 1993a). At both dose levels, NMR spectroscopy of the urine data also revealed the presence of 3-hydroxypropyl mercapturic acid in the post-dose urine, which is consistent with the metabolism of allyl formate to toxic acrolein and the formation of a glutathione conjugate (Rees and Tarlow 1967, Kaye 1973, Alarcon 1976).

Goodwin *et al.* (1994) reported that phenylacetic acid and benzoic acid are metabolic precursors of PAG (phenylacetylglycine) and hippurate (benzoylglycine) respectively. Both these aromatic acids are normally detoxified via conjugation with glycine. Hence the observed reduction in urinary hippurate may be explained by insufficient glycine for the conjugation of benzoic acid, which has been channelled into PAG production instead. PAG has been proposed as a putative biomarker for phospholipidosis (Espina *et al.* 2001). Phenylacetyl-CoA, derived from phenylacetic acid, conjugates with glycine to give rise to observed PAG in urine. β-Oxidation of free phenyl-substituted fatty acids derived from excess lipids may also be one possible source of phenylacetic acid or it might be derived from metabolism of phenylalanine as proposed by Nicholls *et al.* (2000).

The decrease in urinary TMAO level could be related to the decrease in liver TMAO level. There are three sources of methylamines: diet, bacterial synthesis and endogenous synthesis (Smith *et al.* 1994). Choline, a quartenary amine, is a precursor of phosphatidylcholine (a phospholipid), of betaine, of TMAO and of glycine (Figure 3.27). Changes in the level of TMAO could be directly related to the diet. The major route of biosynthesis of TMAO derives from the degradation of dietary choline which is metabolised to trimethylamine (TMA) by the enzymes of the gut microflora. Several strains of gut bacteria have been shown to decompose choline to TMA (Smith *et al.* 1994, Zhang *et al.* 1999). TMA is normally oxidised by the activity of the flavin monooxygenase system in the liver to TMAO, which is then excreted in the urine (Smith *et al.* 1994, Gut and Conney 1993, Zhang *et al.* 1999). Allyl formate-induced disruption in protein synthesis and protein function may reduce the formation of TMAO from trimethylamine via flavin monooxygenase. However, increased biosynthesis of phospholipids could also reduce the formation of TMAO and at the high dose of allyl formate, increased in urinary phehylacetylglycine (PAG) was observed, which Nicholls *et al.* (2000) have suggested may be a marker of phospholipidosis. If an increase in urinary PAG is due to increased phospholipids synthesis, it could lead to a decrease in TMAO by diversion of the choline utilisation. However, the Day 2 MAS NMR data showed no increase in liver phospholipids indicating that phospholipidosis did not occur in the liver. TMAO change might also reflect a disturbance of the gut microflora. Disruption of gut microflora, which there is some

evidence for with presence of short chain fatty acids in the urine of some high dose rats, will lead to decrease TMA and TMAO formation.

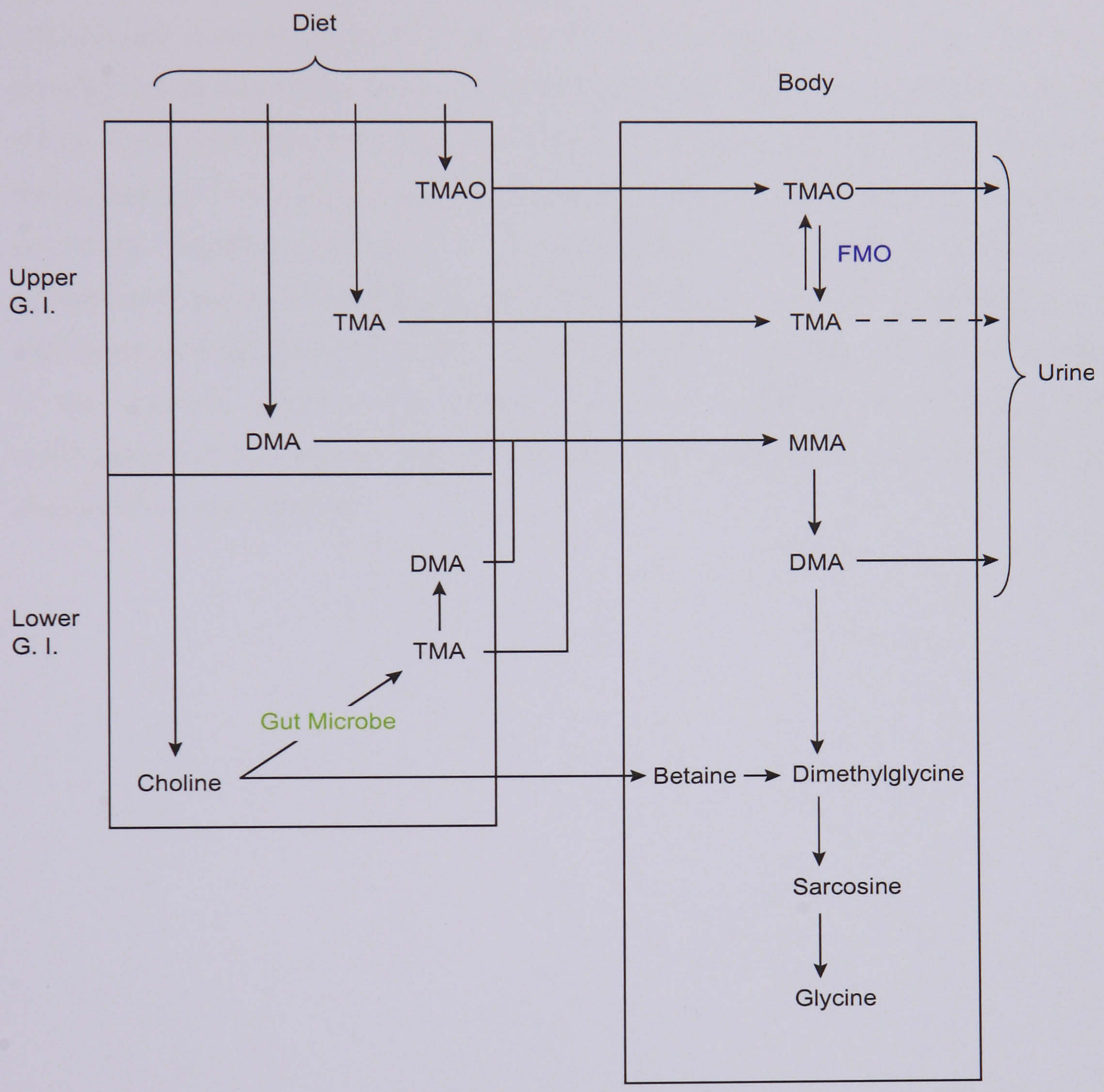

Figure 3.27 Metabolism and excretion of methylamines (adapted from Smith *et al.* 1994).

3.3.4 Summary

^{1}H NMR spectroscopy of liver and biofluids coupled with multivariate data analysis and conventional clinical chemistry has enabled an integrated study of biochemical perturbations in liver tissue, blood plasma and urine following treatment with allyl formate of rats. These have been compared to the degree of liver damage observed by conventional histopathology. The main biochemical effects observed in the liver in this study appear to be energy depletion, inhibition of protein synthesis and disruption of fatty acid metabolism/transport. The depletion of hepatic ATP is likely to be due to acrolein-induced mitochondrial damage and the consequent disruption in protein synthesis could be the cause of the observed lipidosis. The urinary excretion of 3-HPMA indicated the likely involvement of conjugation with glutathione as a route for the detoxification and elimination of allyl formate.

Chapter 4: Integrated Chlorpromazine Studies

4.1 Background: Metabolism and hepatotoxicity of chlorpromazine

Chlorpromazine is a phenothiazine compound used as an antipsychotic drug. It was first introduced in the early 1950s (Yeung *et al.* 1993). Phenothiazines are dopamine-D_2 antagonists. They are also thought to act as α_2-adrenegic, muscarinic cholinergic and histamine H_1 blockers. Phenothiazines are designed to cross the blood-brain barrier and chlorpromazine is a cationic amphiphilic drug soluble in both hydrophobic and hydrophilic solvents. Like most amphiphilic cations, chlorpromazine is able to change the composition of glycerophospholipids in the plasma membrane by affecting enzymes involved in phospholipid metabolism (Underhaug, 2001). Chlorpromazine has been reported to inhibit choline phosphate cytidylyl transferase, a regulatory enzyme for the synthesis of phosphatidylcholine (Underhaug, 2001). Chlorpromazine is extensively metabolised to numerous Phase 1 and Phase 2 metabolites (Figure 4.1). Otton *et al.* (1982) found that aromatic hydroxylation at the 7-position is the major reaction in human microsomes. One study detected 75 chlorpromazine metabolites in blood, urine and faeces with 34 being matched to synthetic standards (Jorgensen, 1986). A battery of chlorpromazine metabolic pathways was identified involving N-oxidation, hydroxylation, N-demethylation, and S-oxidation (Boehme & Strobel, 1998).

Dube *et al.* (1972) in their study of a single high dose (50 mg/kg) administration of chlorpromazine to adult male albino rats, found that chlorpromazine increased the activity of liver enzymes tyrosine-amino-transaminase (TAT), tryptophan pyrrolase and threonine dehydrase. They also found that administration of an inhibitor of RNA synthesis, Actinomycin D, inhibits the effect of chlorpromazine on the three liver enzymes. Knodell (1975) investigated the effect of chlorpromazine on bilirubin metabolism and biliary secretion in rats. Chlorpromazine was administered acutely and chronically and it was found that acute administration of chlorpromazine at 25 mg/kg increases bilirubin output and the level of plasma haemoglobin was elevated as well. Animals treated chronically also showed the same response. Knodell postulated that damage to hepatocytes or changes in the ability of the liver to conjugate bilirubin, might result in bilirubin accumulation. Increase in

plasma haemoglobin in acute treatment indicated an increase in bilirubin output, which is mainly due to haemolysis as chlorpromazine was able to change the osmotic pressure of erythrocytes. Chlorpromazine enhances hepatic heme synthesis by inducing haemolysis. The change in bilirubin conjugation is due to a chlorpromazine-induced defect in intrinsic hepatic function. It was further explained that the increase in unconjugated bilirubin and monoconjugated bilirubin, which are less soluble in bile than diconjugated bilirubin, may lead to the formation of biliary sludge or precipitation of bilirubin in the canaliculi. This would produce cholestatic lesion or initiate an inflammatory or immunological response leading to cholestasis. The increase in γ-azopigment, characteristic of biliary obstruction in rat and human, is consistent with the cholestatic nature of hepatic dysfunction associated with chlorpromazine.

Carey *et al.* (1976) studied the physicochemical interactions of chlorpromazine hydrochloride with biliary lipids *in vitro*. They reported that at pH values below the apparent pK of 7.4, chlorpromazine acts as a water-soluble cationic detergent. They found that chlorpromazine was able to form 1:1 salt complexes with bile salts at bile salt concentrations above their critical micellar concentrations. They also found that by mixing phosphatidylcholine with bile salts, precipitation was inhibited. Therefore, they postulated that because bile-water flow is determined by canalicular bile-salt secretion, the formation of complexes and precipitation of bile salts by chlorpromazine and its metabolites might be related physicochemically to the chlorpromazine-induced reversible bile secretory failure.

Tjioe *et al.* (1972) reported that chlorpromazine exerts various inhibitory effects on mitochondria. They also reported that 7,8-dihydroxychlorpromazine and 7,8-dioxochlorpromazine, metabolites of chlorpromazine, inhibit both calcium and oxygen uptake in isolated brain mitochondria. Abernathy *et al.* (1977) studied the effects of chlorpromazine and its metabolites on isolated hepatocytes. The study revealed that chlorpromazine at a concentration of $9 * 10^{-5}$ M or greater caused leakage of aspartate aminotransferase from the hepatocytes. The results also showed that mono- and didesmethylated-chlorpromazine were 3 and 6 times more potent than chlorpromazine respectively; and hydroxylation at positions 7 or 8 gives rise to metabolites, which were

slightly less active than the parent drug. Sulphoxidation of chlorpromazine, however, produced inactive metabolites. Samuels and Carey (1978) investigated the effects of chlorpromazine hydrochloride and its metabolites on the Mg^{2+}-, and Na^{+}, K^{+}-ATPase activities of canalicular-enriched rat liver plasma membranes. They reported that chlorpromazine inhibits both bile salt-dependent and independent bile flow in primates in a predictable way, which led them to their study in rat liver plasma membranes. They found that chlorpromazine hydrochloride inhibited the activities of both Mg^{2+}-, and Na^{+}, K^{+}-ATPase linearly. Of the metabolites of chlorpromazine, 7-hydroxychlorpromazine was found to be as potent as the parent drug and two sulfoxides of chlorpromazine were found to be the least potent, namely chlorpromazine sulfoxide and 7-hydroxychlorpromazine sulfoxide. They postulated that chlorpromazine-induced cholestasis might be due to a direct effect on the ATPase activities in the canalicular membranes; and that the degree of cholestasis might be influenced by the metabolic conversion of the drug to its more active metabolites i.e. free radicals or the less active metabolites i.e. sulfoxides of chlorpromazine and by the local environment of the canalicular membrane such as the pH and glutathione concentration.

Traficante *et al.* (1979) investigated the *in vitro* sulfoxidation of chlorpromazine by human hepatic and extrahepatic tissues. They reported that chlorpromazine sulfoxide is inactive pharmacologically and a possible end product of the deactivation of chlorpromazine. They found that increase in sulfoxide formation in blood corresponded to a decrease in the parent compound and that the very fast rate is dependent on the volume of whole blood added. Tavaloni and Boyer in 1980, investigated the relationship between hepatic metabolism of chlorpromazine and the cholestatic effect in isolated perfused rat liver. They reported that the sulfoxide of chlorpromazine is much less toxic than the parent compound, which agrees with Traficante *et al.* (1979). They found that chlorpromazine caused a significant decrease in bile flow, hepatic perfusate flow and bile acid excretion. Addition of 7,8-dihydroxy chlorpromazine, caused a significant decrease in bile flow and bile acid excretion. However, addition of chlorpromazine sulfoxide failed to produce any effects. They suggested that the toxicity of chlorpromazine is modulated by its metabolism and the cholestatic effect might be enhanced by slower metabolic transformation of chlorpromazine

to the less toxic chlorpromazine sulfoxide. They also postulate that the toxicity of chlorpromazine might be enhanced if selective formation of multiple ring-hydroxylated metabolites such as 7, 8-dihydroxy chlorpromazine occurred.

4.1.1 Study Details

Study number 98053 carried out at Pfizer, Centre de Recherche, Amboise, France.

Study Number	**Compound**	**Study Group**	**Dose of toxin administered (mg/kg)**	**Animal Number**	**Euthanased**	
					Day 2	**Day 8**
98053	Saline	Control	0	1-10	6-10	1-5
	Chlorpromazine in saline	Low Dose	30	301-310	306-310	301-305
		High Dose	60	401-410	406-410	401-405

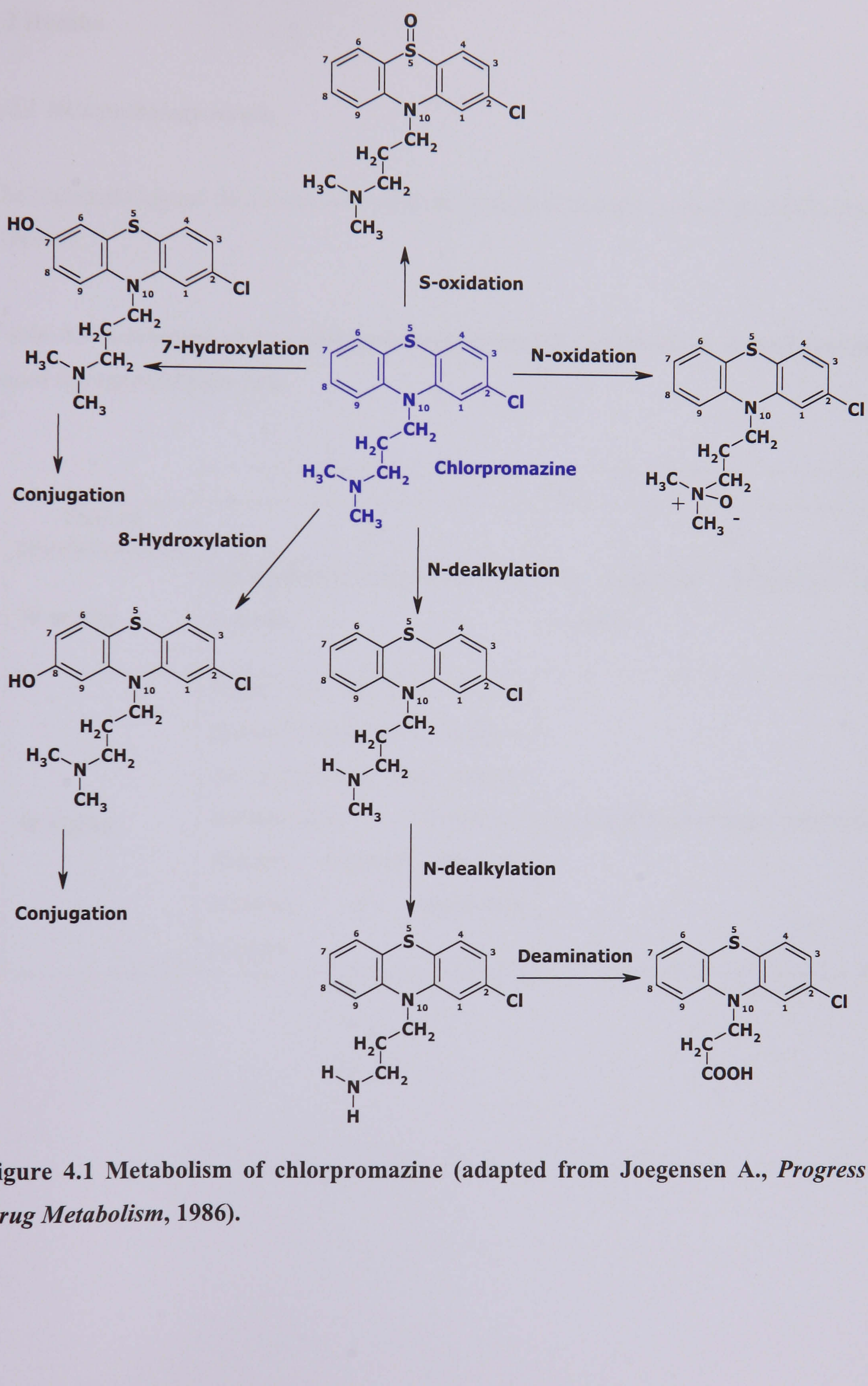

Figure 4.1 Metabolism of chlorpromazine (adapted from Joegensen A., *Progress in Drug Metabolism*, 1986).

4.2 Results

4.2.1 Histopathology results

The histopathological observations for chlorpromazine-dosed rats are summarised below in Table 4.1.

Table 4.1 Summary of the histopathological changes observed in chlorpromazine-dosed Sprague-Dawley rats.

	Day	
Dose of chlorpromazine	**2**	**8**
30 mg/kg	No significant differences from controls.	No significant differences from controls.
60 mg/kg	Three out of five animals showed deposition of lipids in the centrilobular areas. Diffuse hepatocellular cytoplasmic changes observed but no evidence of cholestatic changes.	No significant changes observed.

4.2.2 Clinical chemistry results

The clinical chemistry data indicated minimal changes in both dose groups on Day 2 and Day 8. Details of the clinical chemistry findings are summarised in Table 4.2.

Table 4.2 Summary of the plasma changes observed by clinical chemistry in chlorpromazine-dosed Sprague-Dawley rats.

	Day	
Dose of chlorpromazine	**2**	**8**
30 mg/kg	Triglycerides: ↓ (46% (***) ASAT: ↑ (61% **) ALAT: ↑ (53% **)	No group differences were found although γ-glutamyltransferase (GGT), bilirubin and triglycerides were elevated in animal 101.
60 mg/kg	ASAT: ↑ (64% *) Triglycerides: ↓ (64% ***).	No group differences were found. TBA elevated in animals 201 and 204. Animal 202 showed unusually low creatinine.

4.2.2.1. Principal Component Analysis of Day 2 Plasma Clinical Chemistry Data

PCA scores and loadings plots for the first two components of the control/chlorpromazine Day 2 clinical chemistry data are shown in Figure 4.2. In the scores plot, the data points are colour-coded and labelled so as to identify the treatment (e.g. **black** for control, **bright green** for low dose and for high dose) and animal number.

The scores plot of the low dose chlorpromazine data (Figure 4.2A) indicates separation between the low dose group and controls along the first principal component, and the corresponding loadings plot (Figure 4.2B) showed a decrease in triglycerides and increases in urea, ALAT and ASAT as the major contributors to the separation.

However, PCA scores plot of the high dose chlorpromazine data (Figure 4.2C) indicates partial separation between the dosed group and controls. The separation involves combination of both the first and second principal component with the high dose animals separated from the controls at a diagonal. An important feature observed in the corresponding loadings plot (Figure 4.2D) along the first principal component is the generalised increase in both aminotransferases, ALAT and ASAT, which are indicative of hepatocellular damage. The loadings plot also shows increases in 5' nucleotidase, γ-glutamyl transferase and bile acids, which are specific markers of hepatobiliary function (Handler *et al.* 1994); and decreases in glucose and triglycerides which contributed to the separation along the first principal component. The loadings plot also indicates increases in albumin, albumin/globulin ratio, urea and cholesterol as the contributors to the separation along the second principal component.

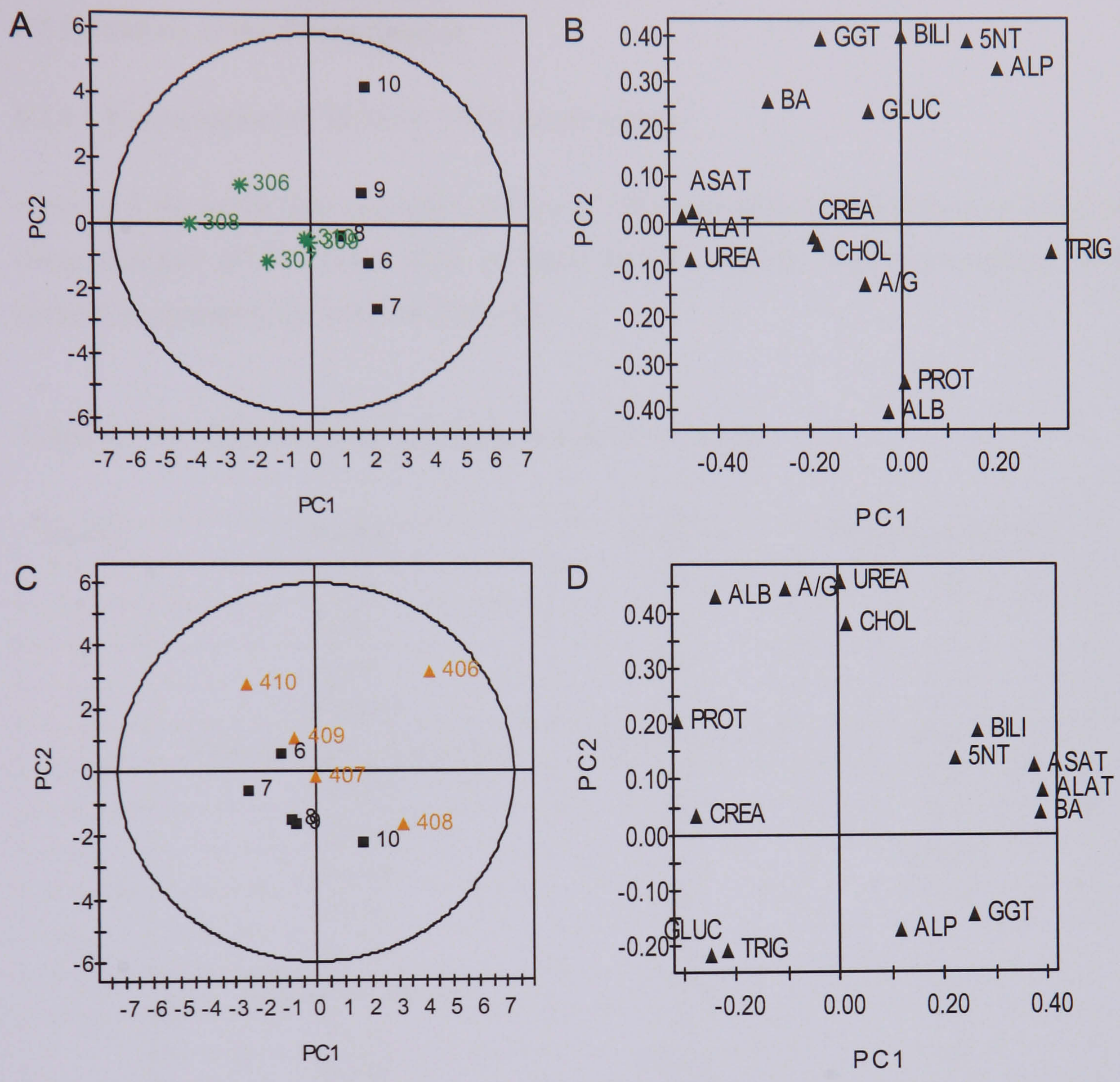

Figure 4.2 (A) Scores plot from PCA of control and low dose chlorpromazine Day 2 clinical chemistry data, and (B) corresponding loadings plot. (C) Scores plot from PCA of control and high dose chlorpromazine Day 2 clinical chemistry data, and (D) corresponding loadings plot.

4.2.3 Analysis of the Tissue Spectra

4.2.3.1 Examination of ^{1}H MAS NMR tissue spectra

Figure 4.3 shows the dose-dependent effects of chlorpromazine hepatotoxicity as visualised using standard 1D ^{1}H MAS NMR of intact Day 2 rat liver. The corresponding NMR spectral assignments are listed in Table 4.3.

Table 4.3 ^{1}H NMR resonance assignments for liver tissue.

Peak No.	Molecule	Assignment	1H chemical shift (ppm)
1	Valine	**CH_3**	1.04
2	Lactate	**CH_3**	1.33
3	Acetate	**CH_3**	1.95
4	Glutamine	**CH_2**	2.39
5	Glucose/glycogen/α-H amino acids	**Ring protons/α-CH**	3.35-4.00
6	β-Glucose	**C_1H**	4.64
7	α-Glucose	**C_1H**	5.23
8	Glycogen	**CH**	5.38-5.45
9	Alanine	**CH_3**	1.48
10	Glutamate	**CH**	2.15
11	Choline/phosphocholine	$N^+(\mathbf{CH_3})_3$	3.22
12	TMAO	**CH_3**	3.27
	Taurine	**$CH_2SO_3^-$**	3.25
13	Lipids	**CH_3**-(CH_2)n	0.90
14	Lipids	CH_3-(**CH_2**)n	1.29
15	Lipids	CO-CH_2-**CH_2**	1.61
16	Lipids	CH=CH-**CH_2**-CH_2	2.07
17	Lipids	CO-**CH_2**-CH_2	2.25
18	Lipids	=CH-**CH_2**-CH=	2.78
19	Lipids	**-CH=CH-**	5.30-5.35

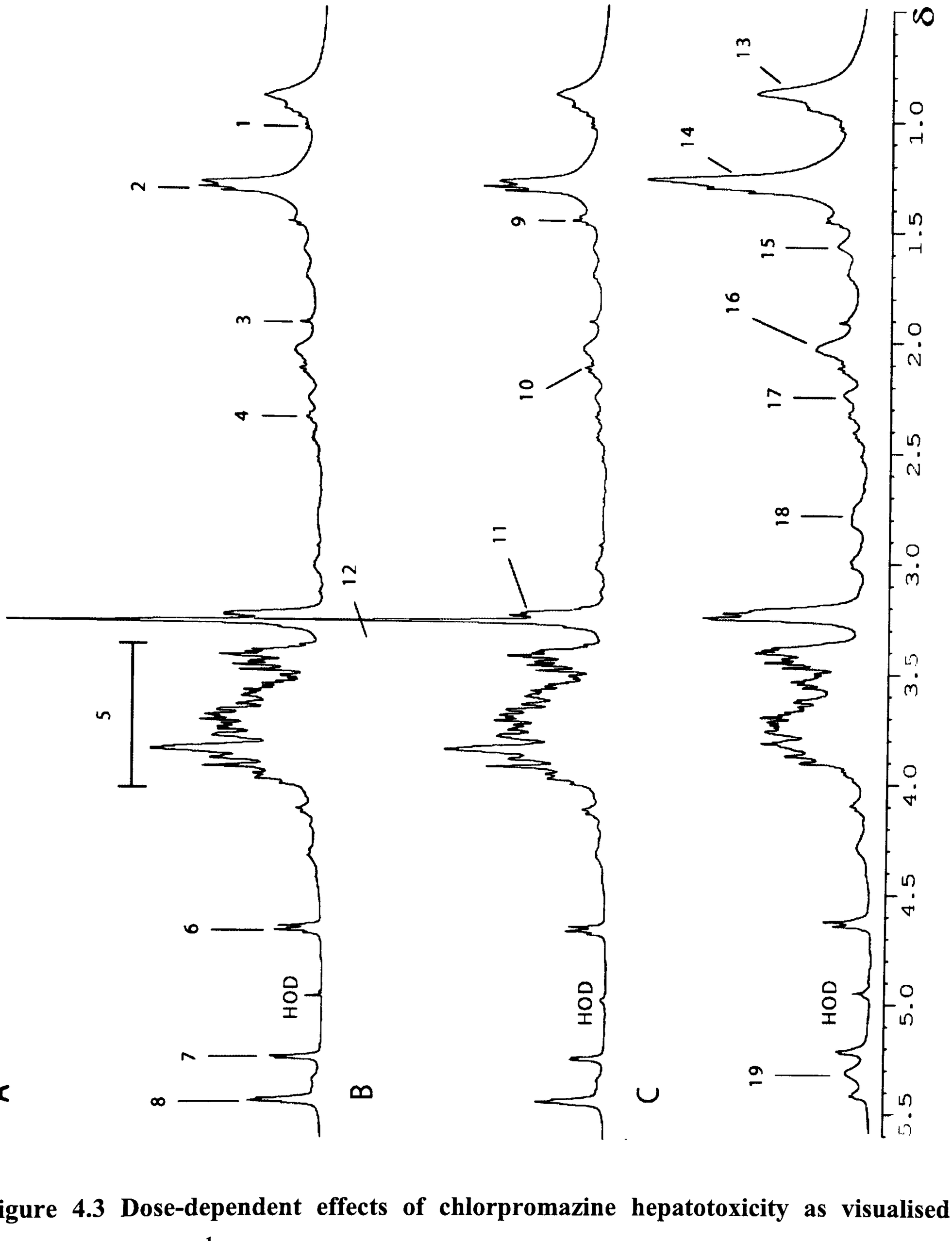

Figure 4.3 Dose-dependent effects of chlorpromazine hepatotoxicity as visualised using standard 1D ^{1}H MAS NMR spectroscopy of intact Day 2 rat liver. A. Control liver. Liver from an animal administered: (B) Low-dose chlorpromazine and (C) High-dose chlorpromazine.

Visual inspection of the Day 2 MAS NMR spectra indicates that administration of low dose chlorpromazine appears to have little effect on the rat liver (Figure 4.3B) with small increases in lipids as well as some decrease in TMAO. However, the administration of high dose chlorpromazine appears to have considerable effect on the rat liver (Figure 4.3C). The liver trimethylamine N-oxide (TMAO) signal at δ3.27 decreases drastically in all high dose animals, with animals 407 & 410 showing the biggest decrease, animals 408 & 409 showing moderate decrease and animal 406 showing the least decrease. In addition, the CH_2 and CH_3 moieties of the liver lipids increase in high dose animals 406, 408 and 409 as compared to that of the controls with animal 408 showing the biggest increase and animal 409 showing the smallest increase. Depletion of liver glucose and glycogen levels are also observed in high dose animals 406, 408 and 409. The changes observed are in contrast with the histopathology observations which revealed minimal changes. The Day 8 MAS NMR spectra indicated minimal effects indicating recovery. Details of the MAS NMR observations for chlorpromazine-dosed rats are summarised below in Table 4.4 and the changes reported were quantified according to the method described in Chapter 2.

Table 4.4 Summary of the liver tissue changes observed by MAS NMR in chlorpromazine-dosed Sprague-Dawley rats.

Dose of chlorpromazine	Day	
	2	8
Low dose (30 mg/kg)	Changes were minimal, but: Lipids: ↑ (*) Glucose region: ↓ (NS); animals 306 & 307 showed relative decrease in the resonance at δ5.233 (glucose). TMAO: ↓ (*); 3/5 animals (306, 308 & 310) showed relative decreases in TMAO at δ3.27. Choline: ↑ (NS)	The spectra indicated minimal changes compared to controls.
High dose (60 mg/kg)	Changes varied within the high dose animals. TMAO: ↓ (*) Lipids: ↑ (NS) Glucose (between δ 3.40 and δ 4.00): ↓ (NS) Glycogen (δ3.80 and δ5.42): ↓ (NS) Choline: ↑ (NS)	The spectra indicated minimal changes compared to controls.

4.2.3.2 Principal Component Analysis of Day 2 Liver NMR Data

Principal component analysis of the control/low dose Day 2 data set reveals some dose related structure to the variation in the data. The scores plot (Figure 4.4A) shows that combination of the first and second principal component separates two low dose animals from the rest of the animals. The first principal component describes the variation between low dose animals and control animals, showing partial separation between the low dose animals and the control animals with low dose animals 306 and 307 separated from the rest of the animals. One control animal, C6, is situated away from the rest of the controls due to lower lipids content. The second principal component described some variation in the data set that was related to the treatment of the animals with chlorpromazine. The corresponding loadings plot (Figure 4.4B) indicates that a decrease in TMAO is the main contributor to the separation along the first principal component. Increases in the regions attributed to lipids, and decrease in the region attributed to glucose and glycogen were also identified as the contributors for the separation between the dosed-animals and control animals along the first and second principal component.

Figure 4.4C shows the scores plot for the first two components of the control/high dose Day 2 tissue NMR data. The scores plot shows clear dose-related structure to the variation in the data with the controls and high dose group separated on a diagonal by a combination of the first and second principal component. The scores plot also reveals that the high dose animals are separated into two clusters. The first cluster which consists of animals 406 and 408, were separated from the controls along the first principal component and the second cluster which consist of animals 407, 409 and 410, were separated from the controls along the second principal component. The corresponding loadings plot (Figure 4.4D) indicates that increases in the regions attributed to lipids and decreases in the region attributed to glucose and glycogen as the major contributors to the separation along the first principal component, whilst a decrease in liver TMAO level is the main contributor to the separation along the second principal component. The changes observed in the principal component plots agree with the changes seen in the MAS NMR spectra of Day 2 high dose animals.

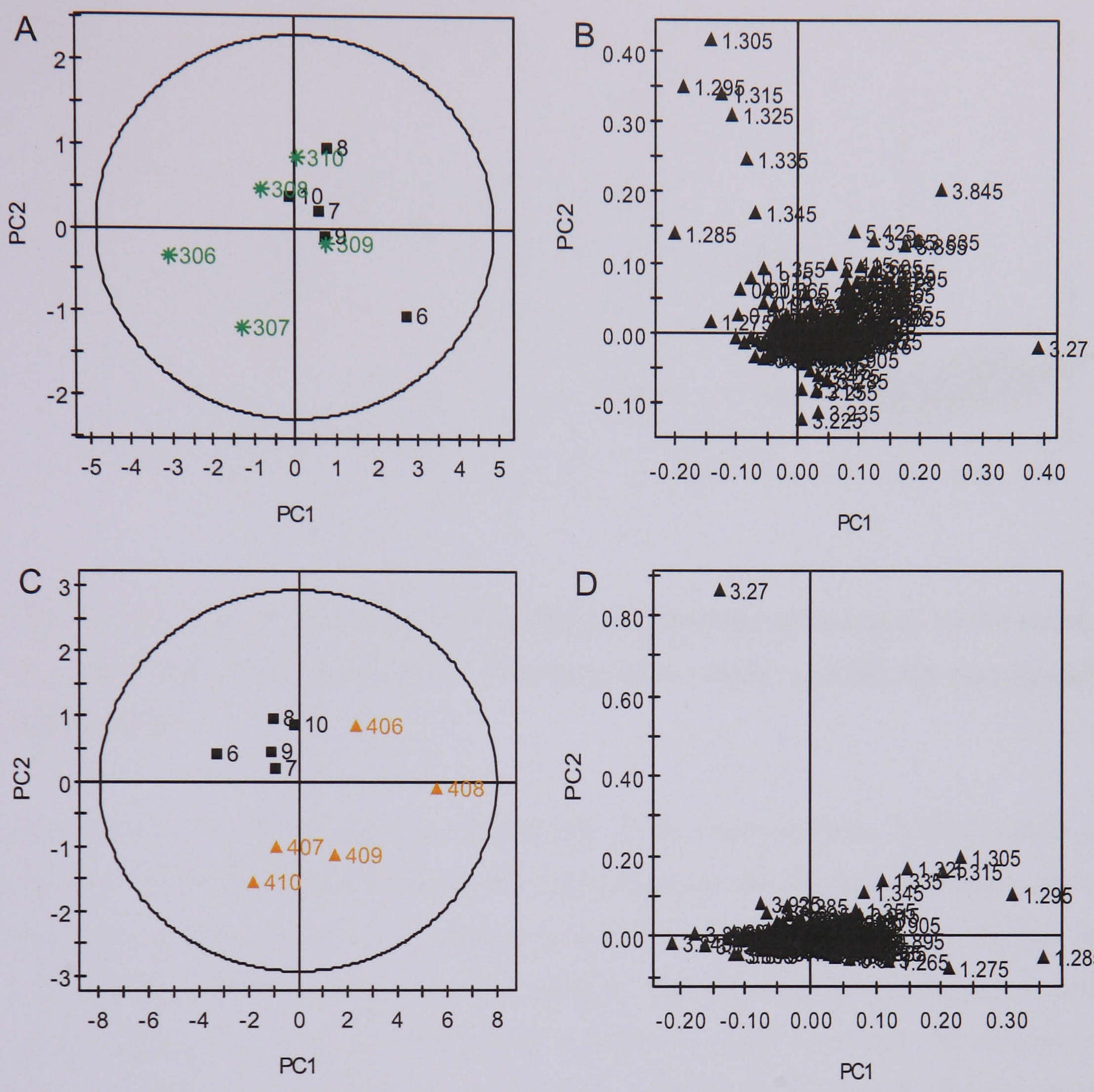

Figure 4.4 (A) PCA scores plot of the ^{1}H MAS NMR spectra of chlorpromazine-dosed liver samples from Day 2 low dose versus control groups, and (B) the corresponding loadings plot. (C) PCA scores plot of the ^{1}H MAS NMR spectra of chlorpromazine-dosed liver samples from Day 2 high dose versus control groups and (D) the corresponding loadings plot.

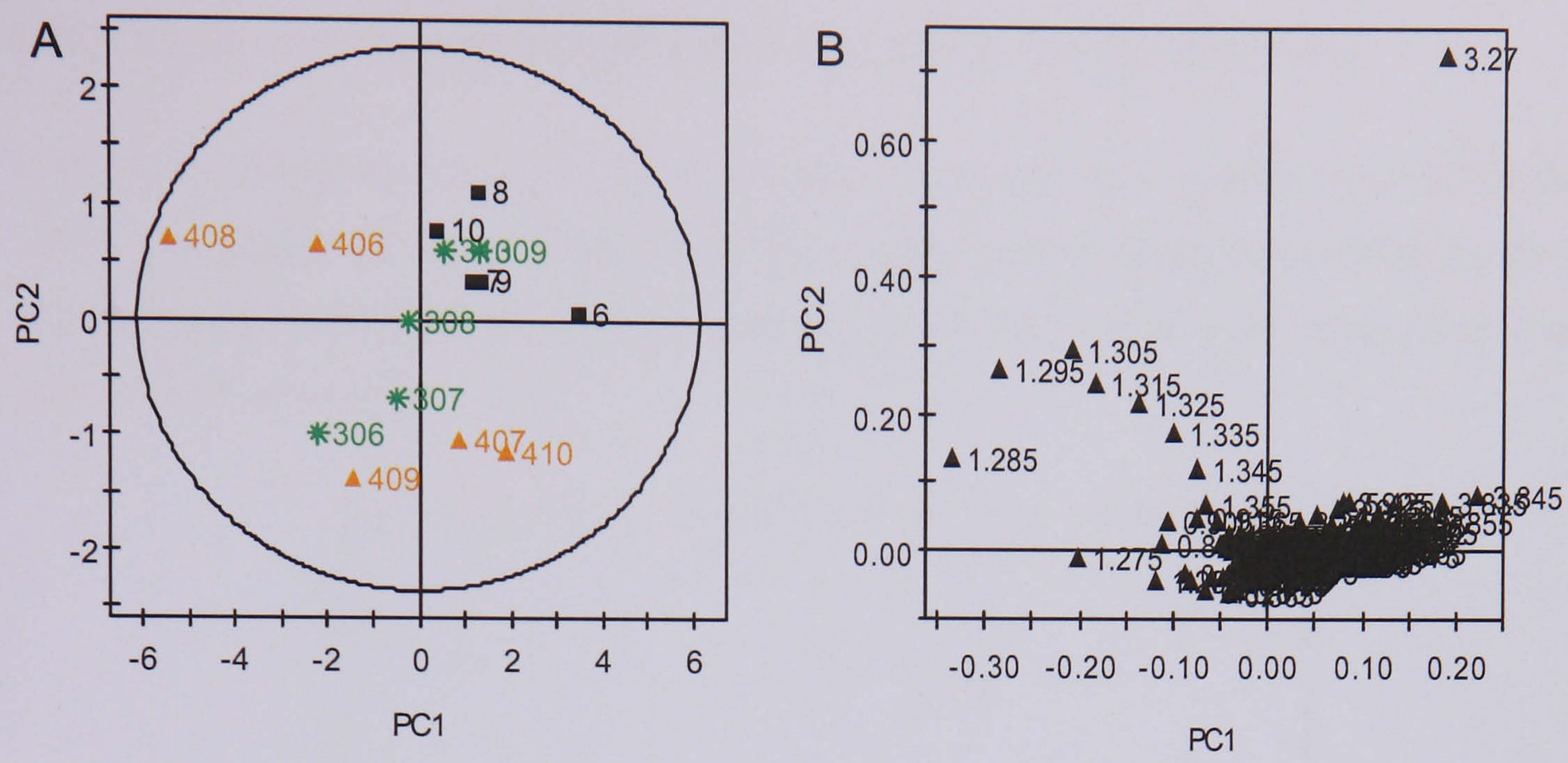

Figure 4.5 (A) PCA scores plot for the first two principal components of the standard ^{1}H MAS NMR spectra of the Day 2 chlorpromazine study, and (B) the corresponding loadings plot.

PCA scores plot of the first two components of the combined Day 2 MAS NMR data (Figure 4.5A) showed some dose-related progression from the low dose animals to the high dose animals. The first principal component describes the variation between the high dose animals 408 and 406 and the rest of the animals. The second principal component shows partial separation between the low dose and control animals as well as the separation of high dose animals 407, 409 and 410 from the control group. The corresponding loadings plot (Figure 4.5B) shows that chlorpromazine-induced increases in lipids, and decreases in glucose and glycogen are the major contributors to the separation along the first principal component, whereas chlorpromazine-induced decrease in TMAO is the major contributor and an important factor to the separation along the second principal component.

4.2.3.3 PLS – Discriminant Analysis (PLS-DA) of Day 2 Liver NMR Data

In an effort to improve class separation and information recovery from the tissue NMR data a PLS-DA model was constructed, where the samples were classified according to one of three mutually orthogonal classes with **control** being class 1, **low dose** being class 2 and **high dose** being class 3.

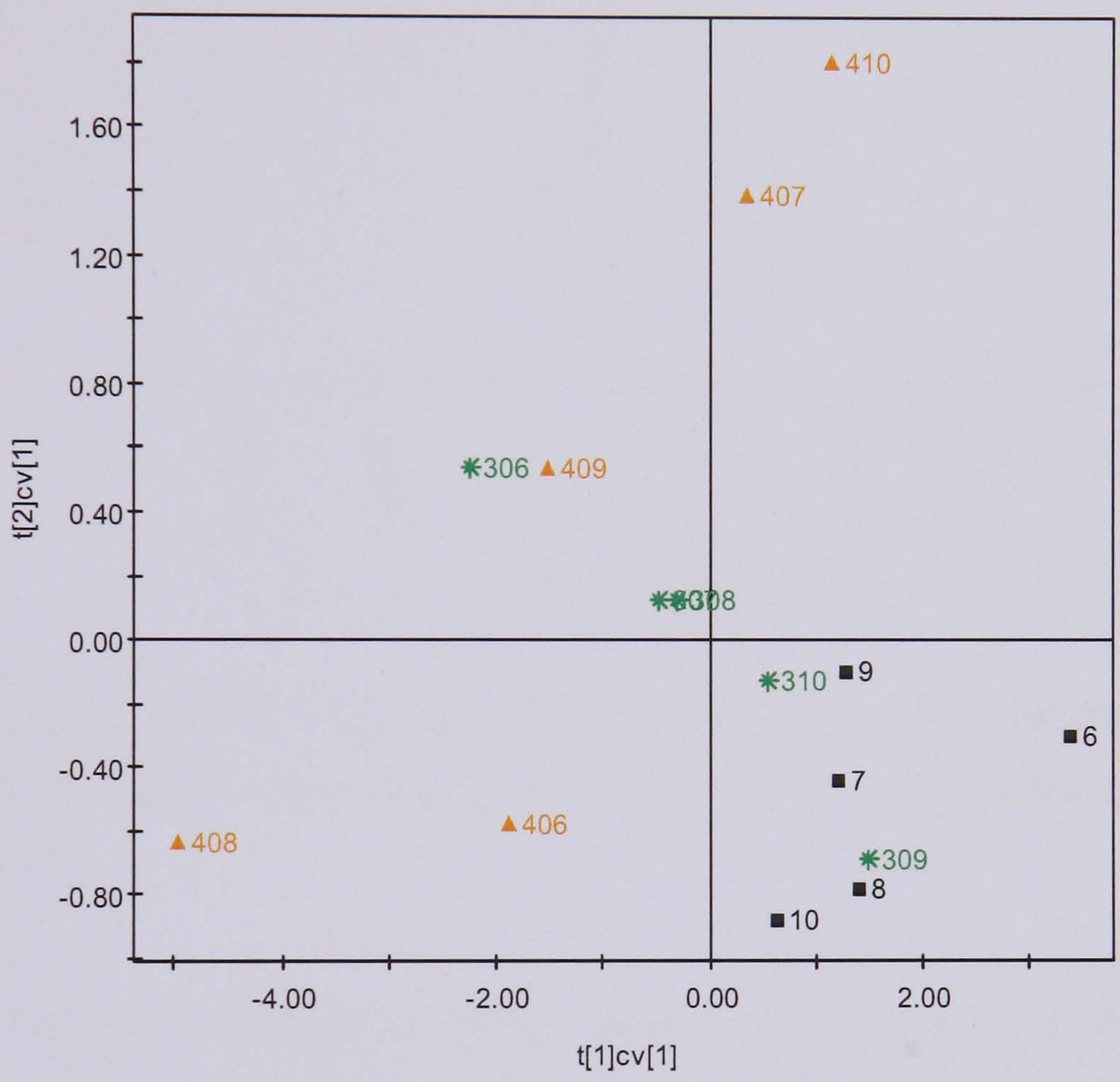

Figure 4.6 PLS-DA cross validated scores plot of the standard ^{1}H MAS NMR spectra of the Day 2 chlorpromazine study.

The X-matrix cross validated scores of the first two components of the model shows some improvement in the separation between the low dose animals and the control animals as can be seen in Figure 4.6. A combination of the first and second PLS component partially separates the low dose animals (animals 306, 307, & 308) from the controls. Again, the high dose animals are separated into two clusters with one cluster (animals 406 & 408) separated along the first PLS component and another cluster (animals 407, 409 and 410) separated along the second PLS component.

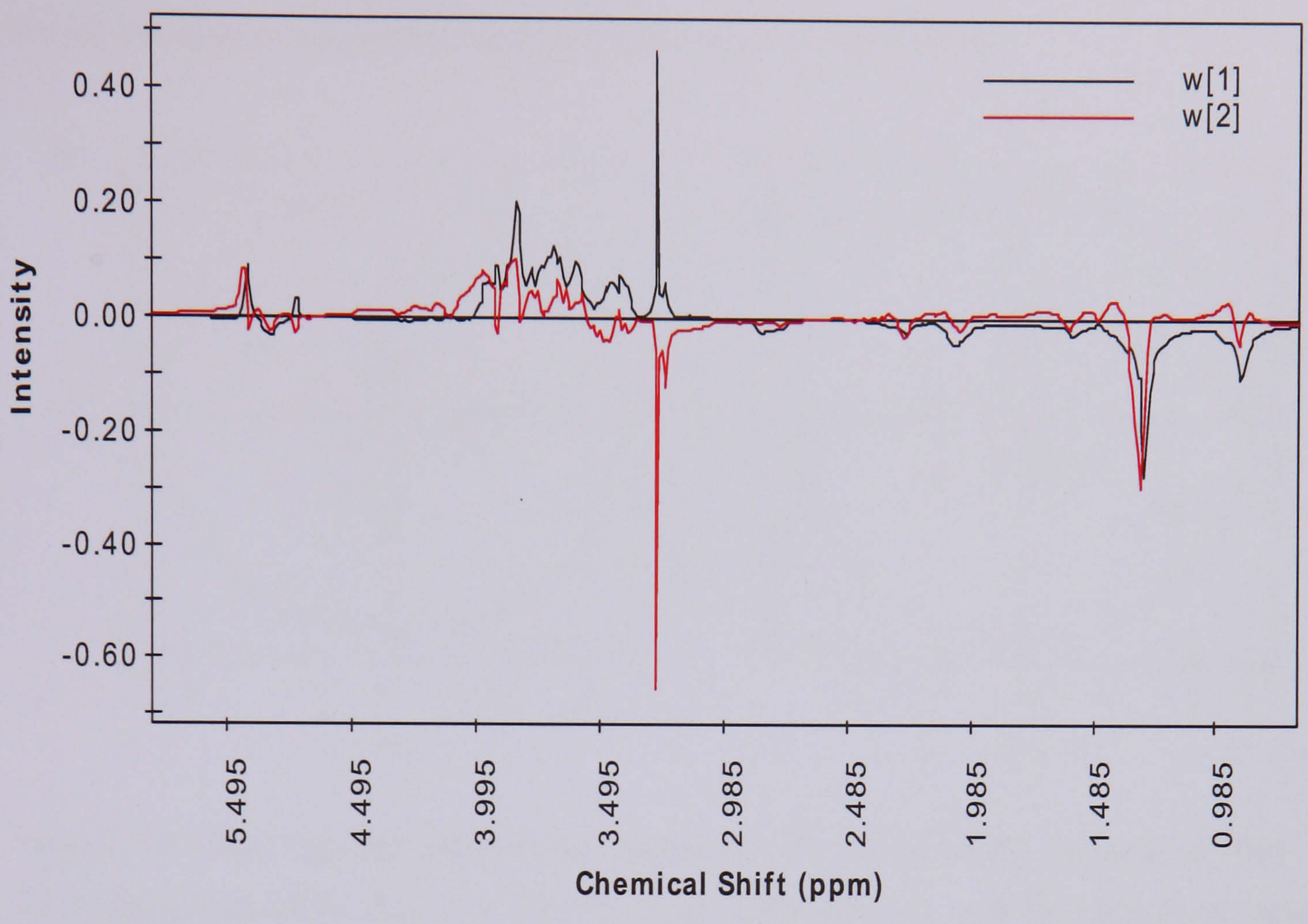

Figure 4.7 PLS weights from the standard ^{1}H MAS NMR spectra of the Day 2 chlorpromazine study tissue samples (W[1] = PLS component 1, W[2] = PLS component 2).

The corresponding X-block PLS loadings plot (Figure 4.7) indicates that the first PLS component, describing the general variation between the high dose animals 406 and 408 and the rest of the animals, is due to increases in liver lipids and decreases in liver glucose and glycogen levels. The second PLS component, describing the variation between the dosed animals and the control animals, is due to the drastic decrease in liver TMAO levels. These observations confirmed the findings made from the ^{1}H MAS NMR spectra (Table 4.4) and PCA analyses of the Day 2 tissue NMR data (Figure 4.4).

4.2.3.4 Principal Component Analysis of Day 8 Liver NMR Data

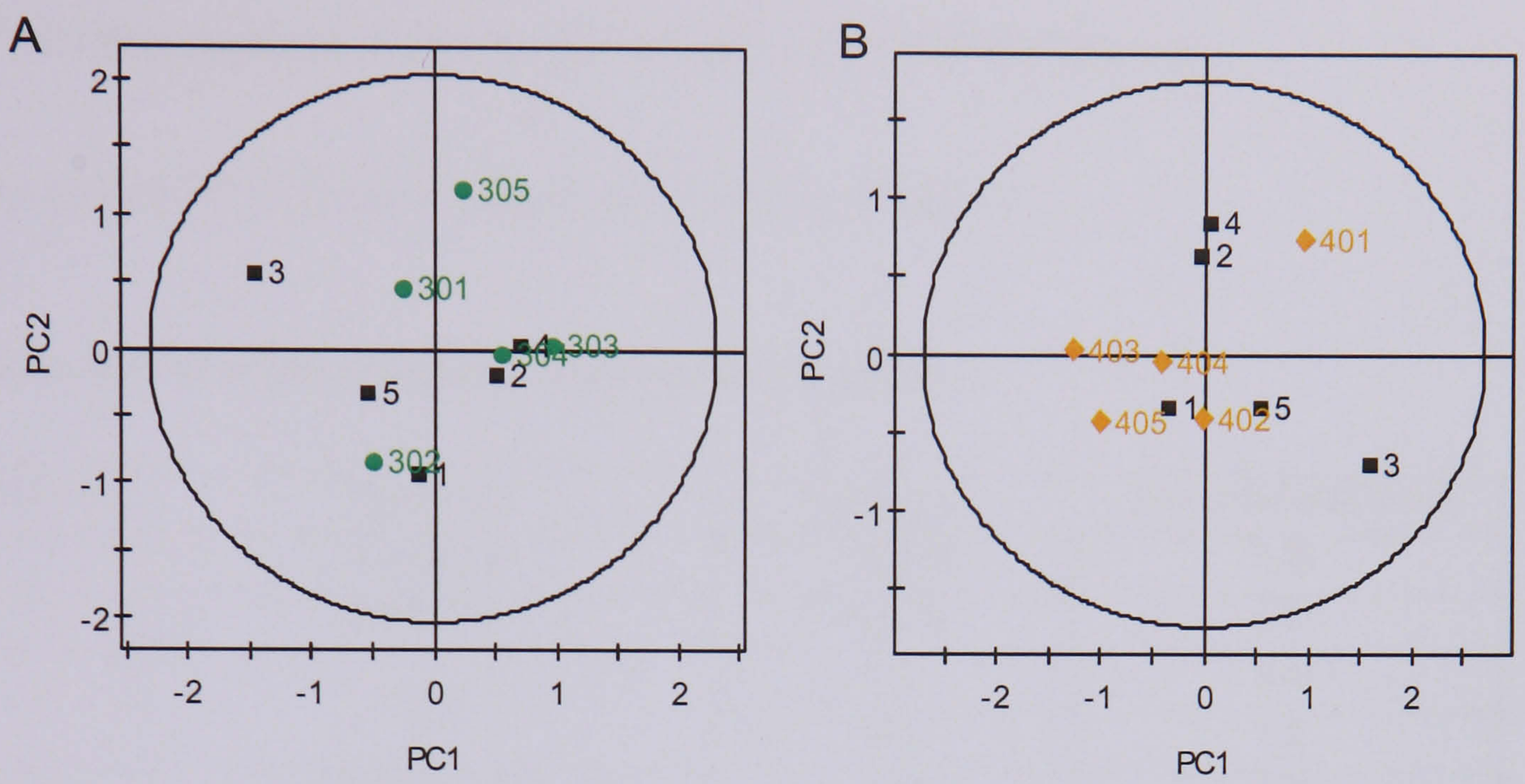

Figure 4.8 PCA scores plot of the standard ^{1}H MAS NMR spectra of Day 8 chlorpromazine study. (A) Low dose versus Control data set, and (B) High dose versus Control data set.

The PCA scores of plot of the chlorpromazine Day 8 tissue samples (Figure 4.8 A and B) indicated no clear separation between the dosed and the control groups. This indicates recovery by Day 8 compared to Day 2.

4.2.4 Analysis of the Plasma Spectra

4.2.4.1 Examination of plasma CPMG spin-echo ^{1}H NMR spectra

The plasma NMR spectral assignments are listed in Table 4.5.

Table 4.5 ^{1}H NMR resonance assignments for plasma.

Peak No.	Molecule	Assignment	^{1}H chemical shift (ppm)
1	Lipids (LDL)	$-CH_2-\mathbf{CH_3}$	0.84
2	Lipids (VLDL)	$CH_2-\mathbf{CH_3}$	0.87
3	Valine	$\mathbf{CH_3}$	0.97
		$\mathbf{CH_3}$	1.02
4	3-D-hydroxybutyrate	$\mathbf{CH_3}$	1.20
		$\mathbf{CH_2}$	2.31, 2.38
5	Lipids (VLDL)	$-(\mathbf{CH_2})n$	1.29
6	Lactate	$\mathbf{CH_3}$	1.33
7	Alanine	$\mathbf{CH_3}$	1.46
8	Acetate	$\mathbf{CH_3}$	1.91
9	Acetoacetate	$\mathbf{CH_3}$	2.22
10	Glutamine	$\mathbf{CH_2}$	2.41
11	Citrate	$\mathbf{CH_2}$	2.52
		$\mathbf{CH_2}$	2.69
12	Choline	$N^+(\mathbf{CH_3})_3$	3.21
13	Glucose/Amino acids resonances	**Ring protons/α-CH**	3.35-4.00
14	Lactate	**CH**	4.10
15	α-Glucose	$\mathbf{C_1H}$	5.23
16	Isoleucine	$\mathbf{CH_3}$	0.93
17	Leucine	$\mathbf{CH_3}$	0.95
18	Isoleucine	$\mathbf{CH_3}$	1.00
19	Threonine	$\mathbf{CH_3}$	1.31
20	N-acetyl glycoproteins	NHCO $\mathbf{CH_3}$	2.04
21	Pyruvate	$\mathbf{CH_2}$	2.36
22	Creatine	$\mathbf{CH_3}$	3.04
23	TMAO	$\mathbf{CH_3}$	3.26
24	Creatine	$\mathbf{CH_3}$	3.93
25	Lipids	**-CH=CH-**	5.30

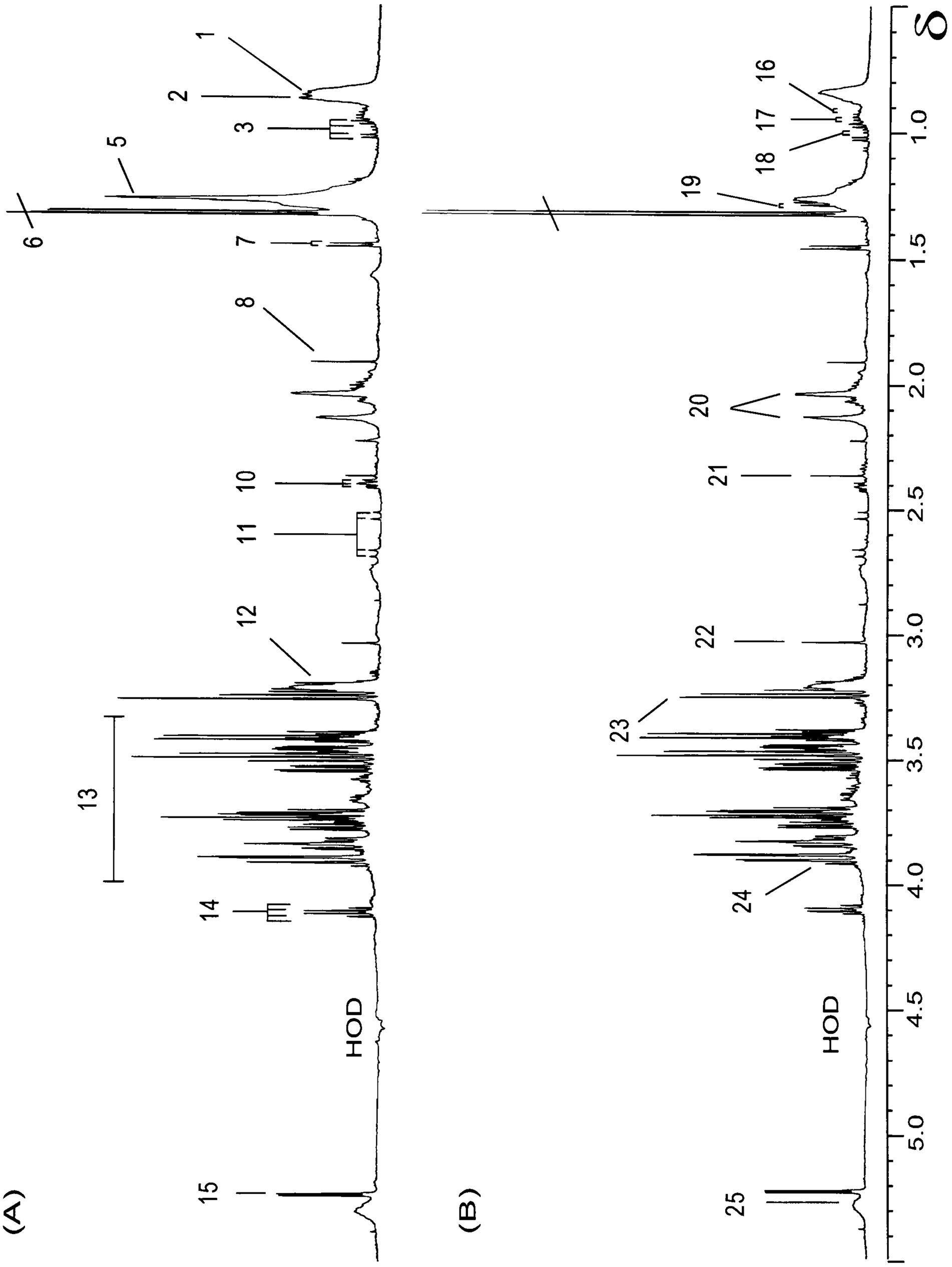

Figure 4.9 Effects of chlorpromazine (60 mg/kg) as visualised using CPMG spin-echo ^{1}H NMR spectra of Day 2 rat plasma. A. Control plasma. B. High-dose chlorpromazine.

Visual inspection of the plasma CPMG spin echo spectra revealed little effects on the low dose animals with an increase in plasma creatine being a common factor (data not shown). Figure 4.9 shows the effects of high dose chlorpromazine as visualised using CPMG spin-echo spectra of Day 2 plasma samples. The corresponding NMR spectral assignments are listed in Table 4.5. It can be seen quite clearly that the signals derived from lipids especially the CH_2 and CH_3 moeties decreased in the high dose animals. Additionally, the majority of the high dose animals show an increase in plasma creatine level. However, within the high dose animals, a sub-group of animals (animals 406, 408, 409) were found to exhibit features of ketosis with increases in the levels of 3-D-hydroxybutyrate and acetoacetate. The presence of these ketone bodies in some of the high dose animals (Figure 4.10) is indicative of reduced food intake possibly induced by the sedative effect of chlorpromazine. The Day 8 CPMG spin echo spectra of the plasma samples indicate minimal effects. Details of the plasma NMR observations for chlorpromazine-dosed rats are summarised below in Table 4.6 and the changes reported being quantified according to the method described in Chapter 2.

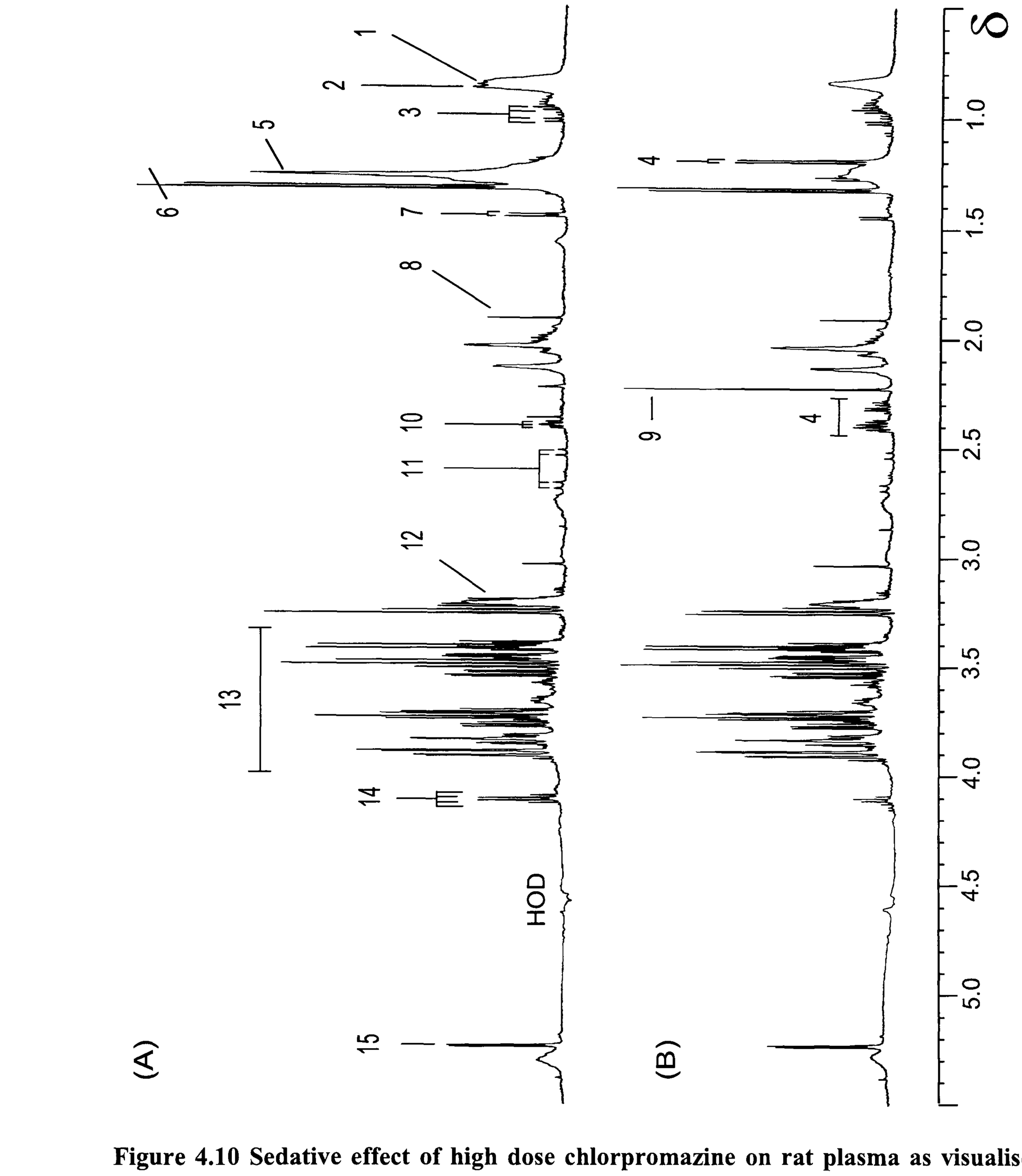

Figure 4.10 Sedative effect of high dose chlorpromazine on rat plasma as visualised using CPMG spin-echo ^{1}H NMR spectra of Day 2 rat plasma. A. Control plasma. B. High-dose chlorpromazine showing presence of 3-D-hydroxybutyrate and acetoacetate.

Table 4.6 Summary of the plasma changes observed by NMR in chlorpromazine-dosed rats.

Dose of chlorpromazine	Day	
	2	8
30mg/kg	Visually, there were some differences from controls. Creatine: ↑ **. Increase in creatine was observed in all animals. Animal 306 showed some signs of ketosis with some increase in 3-D-hydroxybutyrate and acetoacetate. There was some decrease in the VLDL (NS). Total lipids: ↓ (NS).	No differences observed.
60 mg/kg	Clear changes from controls were observed by visual inspection. Creatine: ↑ ** 3-D-hydroxybutyrate and acetoacetate was increased in animals 406, 408 and 409 with the biggest increase in animal 409 and animal 408 showing the smallest increase. No increase was observed in animals 407 and 410. Decrease in plasma VLDL in all animals: ↓*. Total lipids: ↓*	Approximately the same as controls.

4.2.4.2 Principal Component Analysis of Day 2 Plasma NMR Data

An initial principal components analysis of the data set revealed some dose-related structure to the variation in the data. Figure 4.11 shows the scores and loadings plots of the first two principal components of the PCA model between the chlorpromazine-treated animals and the controls.

PCA scores plot of the control/low dose Day 2 data set (Figure 4.11A) indicates differences in the metabolic profiles of the chlorpromazine-treated and control animals. The first principal component describes the variation between the two groups of animals. The scores plot also indicates that the low dose group are separated into two clusters along principal component two. The corresponding loadings plot (Figure 4.11B) reveals that changes in the lipids moeties (VLDL, CH_2 and LDL, CH_3) are the major contributors to the separation between the low dose animals and control animals along the first principal component. The second principal component reveals increases in plasma 3-D-hydroxybutyrate, lactate and choline levels, which contributed to the separation within the high dose animals. Animals 309 and 310 appear to have lower levels of the aforementioned plasma metabolites. The plasma NMR data shows clearer separation as compared to that of the liver NMR data due to the presence of ketone bodies in the blood.

The PCA scores plot of the control/high dose Day 2 plasma data set (Figure 4.11C) indicates clear separation between the high dose animals and the control animals. Again the high dose animals are separated into two clusters with animals 409 and 406 situated on the upper half of the scores plot and animals 408, 407 and 410 situated on the lower half of the scores plot separated along the second principal component, The first principal component, describing the dose-related variation between the two groups, is due to changes in plasma lipid moeties (Figure 4.11D). The loadings plot also reveals that increases in plasma 3-D-hydroxybutyrate and acetoacetate, and decreases in plasma glucose are the major contributors to the separation within the high dose animals. These changes are attributed to the sedative effects of chlorpromazine which caused decreased activity and consequent lack of feeding. Acetoacetate, and 3-D-hydroxybutyrate are ketone bodies which are produced

when excessive amounts of fatty acids are being mobilised and oxidised to produce energy i.e. during starvation.

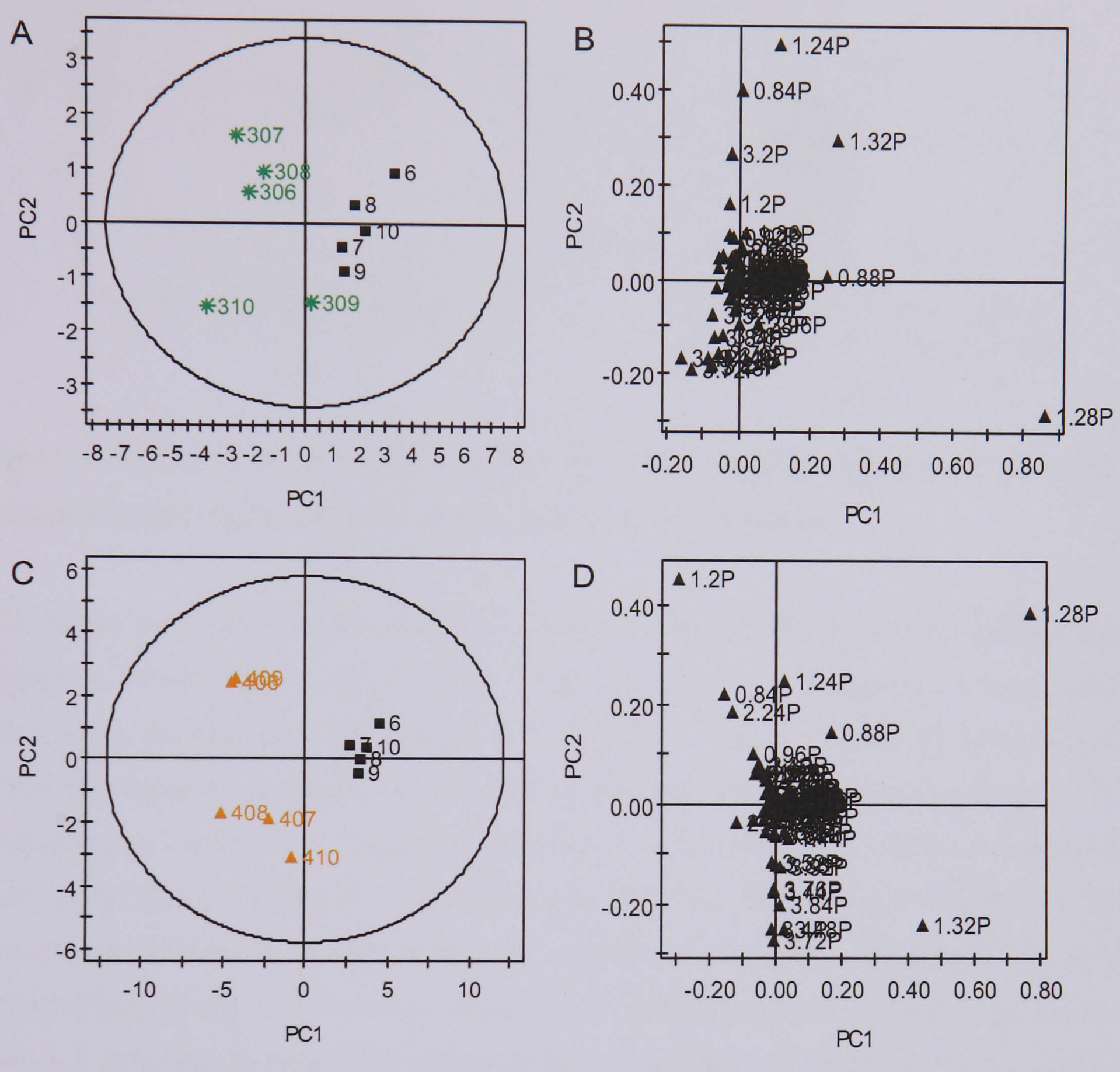

Figure 4.11 (A) PCA scores plot of the ^{1}H CPMG spectra of chlorpromazine-dosed plasma samples from Day 2 low dose versus control groups, and (B) the corresponding loadings plot. (C) PCA scores plot of the ^{1}H CPMG spectra of chlorpromazine-dosed plasma samples from Day 2 high dose versus control groups and (D) the corresponding loadings plot.

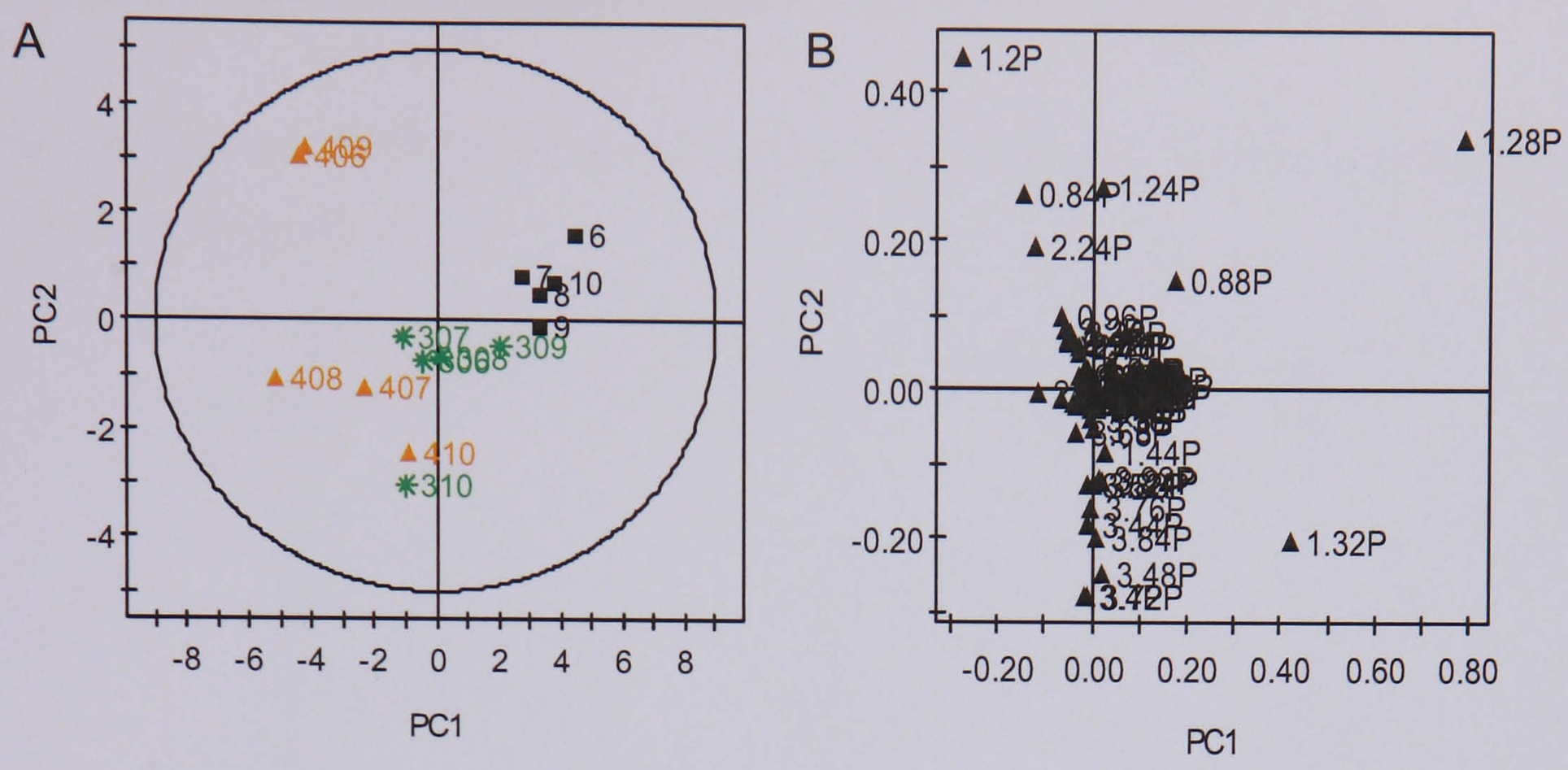

Figure 4.12 (A) PCA scores plot of the ^{1}H CPMG plasma spectra of the Day 2 chlorpromazine study, and (B) the corresponding loadings plot.

PCA scores plot of the combined Day 2 plasma NMR data (Figure 4.12A) showed clear separation between the dosed groups and controls as well as a progressive dose-related effect along the first principal component. Variation within the dosed groups especially within the high dose group can be seen clearly along the second principal component. The corresponding loadings plot (Figure 4.12B) shows that chlorpromazine-induced decrease in lipids is the major contributor to the separation along the first principal component. The dose-related decrease in plasma lipids also contributed to the observed progressive dose-related effects in the scores plot. In addition, the loadings plot also indicates increases in plasma 3-D-hydroxybutyrate and acetoacetate, and decrease in plasma glucose related to the sedative effect of chlorpromazine along the second principal component.

4.2.4.3 PLS – Discriminant Analysis (PLS-DA) of Day 2 Plasma NMR Data

The Day 2 plasma NMR data was analysed using PLS-DA approach to further refine the information recovery.

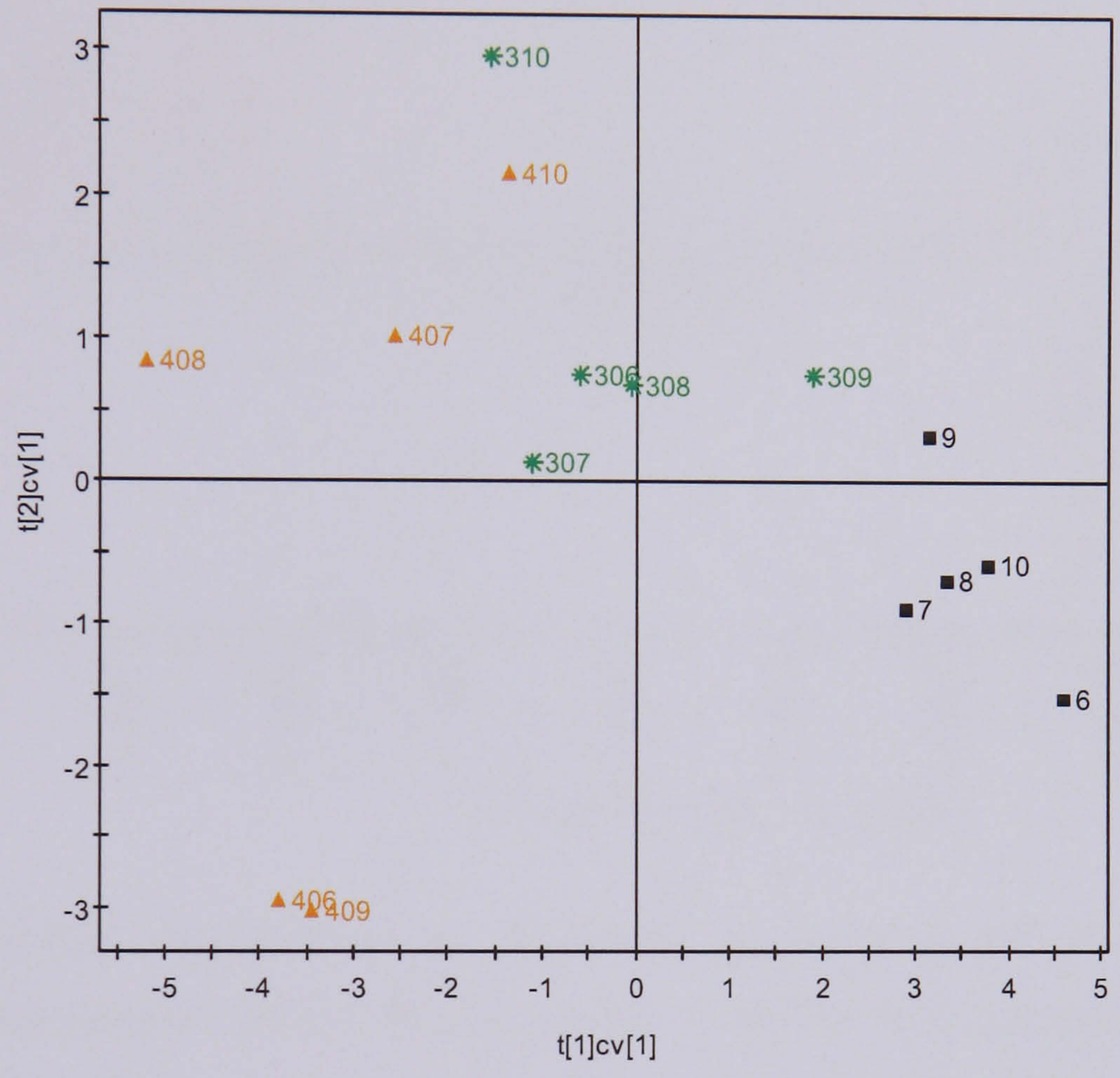

Figure 4.13 PLS-DA cross validated scores plot of the ^{1}H CPMG spectra of the Day 2 chlorpromazine study plasma samples.

The X matrix cross validated scores plot of the first two components (Figure 4.13) shows clear separation between the dosed groups and the control group as well as a clear dose-response effect. The control animals are situated on the lower right quadrant, with the low dose animals are separated between the high dose animals and the control animals. The high dose animals are (to the left of the plot) separated from the control group along the first component. In addition, the high dose animals are separated into two clusters along the second PLS component with animals 407, 408 and 410 on the upper half and animals 406 and 409 on the lower half of the plot.

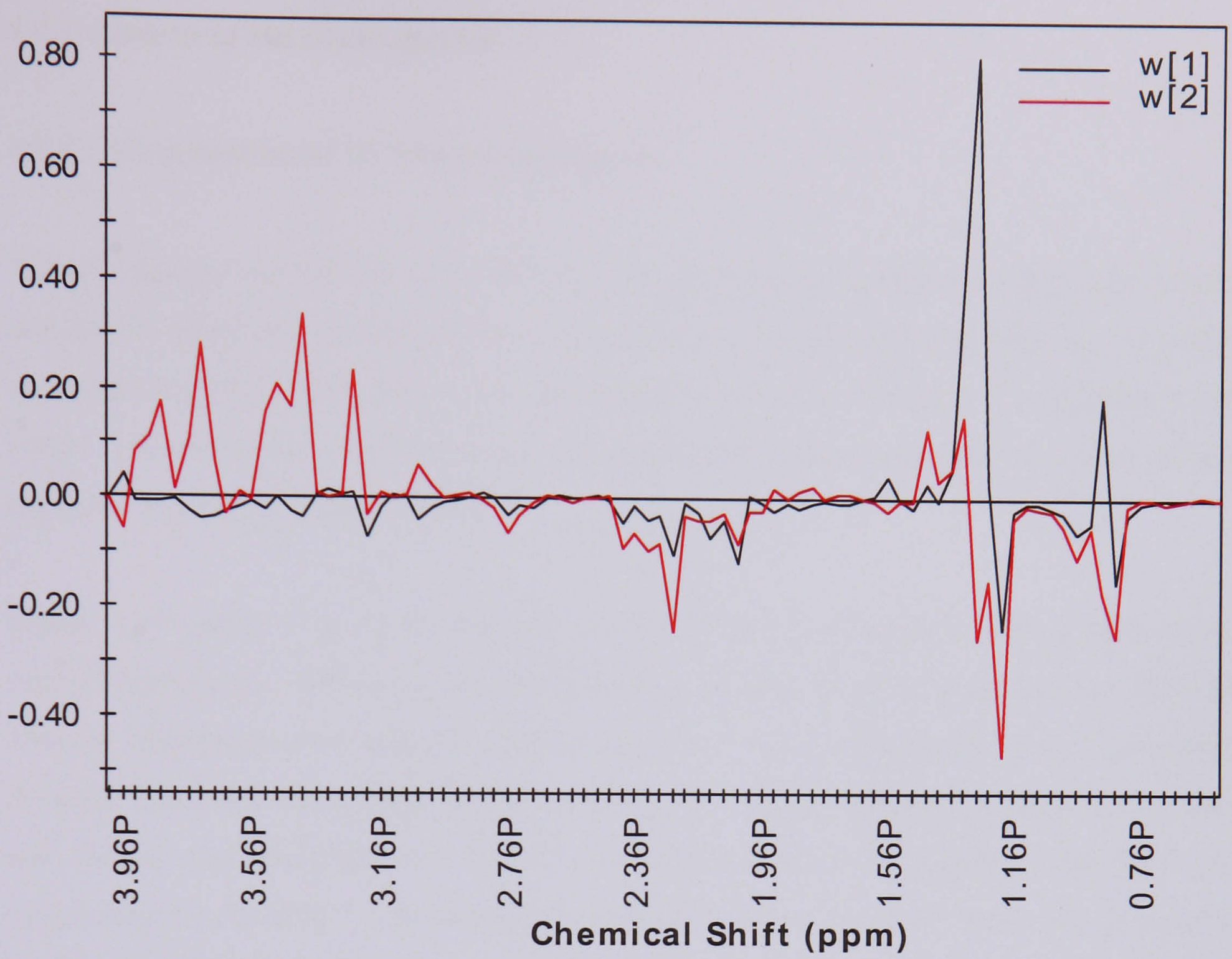

Figure 4.14 PLS weights from the ^{1}H CPMG spectra of the Day 2 chlorpromazine study plasma samples (W[1] = PLS component 1, W[2] = PLS component 2).

The corresponding X block PLS loadings plot (Figure 4.14) indicates that the first component describing the general variation between high dose and control animals is due to decreased plasma lipids. The second component, describing the variation within the high dose animals, is due to decrease in the plasma glucose level as well as increases in the plasma 3-D-hydroxybutyrate and acetoacetate levels which are due to chlorpromazine-induced ketosis. The changes observed in the PLS-DA scores and loadings plots confirmed the findings made from the ^{1}H NMR spectra (Figure 4.10) and PCA analyses of the Day 2 plasma NMR data (Figure 4.11).

4.2.5 Analysis of the Urine Spectra

4.2.5.1 Examination of ^{1}H NMR urine spectra

Visual inspection of the low dose urine spectra show some changes in endogenous urinary metabolites (data not shown). Most of the low dose animals showed increases in taurine and creatine levels. Additionally, the animals also showed decreases in 2-oxoglutarate, and citrate. However, the extent of these changes varied between animals. All five animals appeared to have recovered by Day 7.

Figure 4.15 shows a series of standard ^{1}H NMR spectra of urine covering predose and various time points following the administration of high dose chlorpromazine. The high dose of chlorpromazine induced marked changes in the endogenous urinary metabolite profiles. The dominant changes included increases in urinary phenylacetylglycine, creatine and taurine, and decreases in TMAO, succinate, citrate, 2-oxoglutarate, and hippurate, which lasted up to Day 3 with maximal abnormality being observed in the Day 2 samples. The ^{1}H NMR spectra indicated recovery to normality by Day 7 post-dosing. Details of the urine NMR observations for chlorpromazine-dosed rats are summarised below in Table 4.7, the changes reported being quantified according to the method described in Chapter 2.

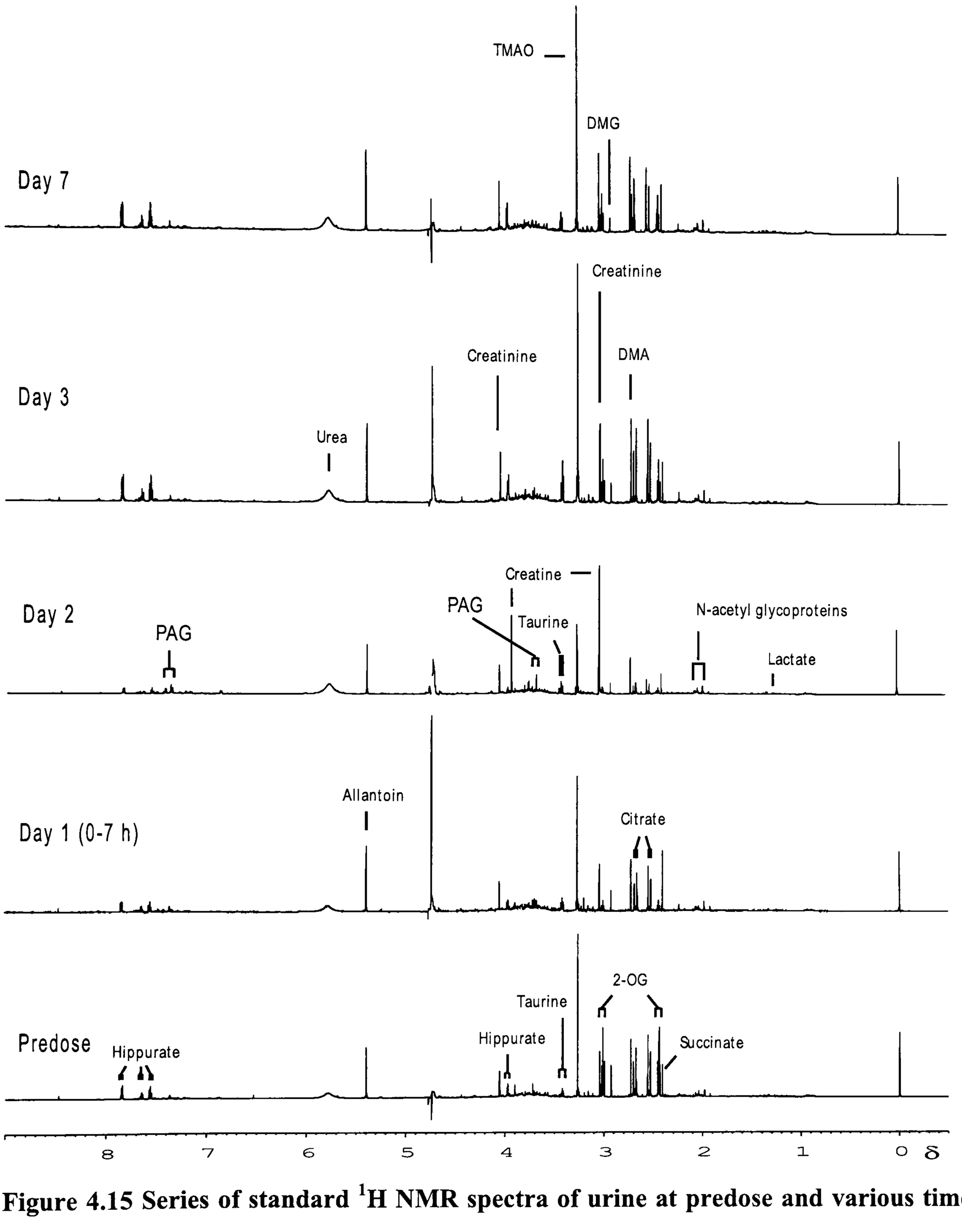

Figure 4.15 Series of standard ^{1}H NMR spectra of urine at predose and various time points following the administration of Chlorpromazine (60 mg/kg). Key: 2-oxoglutarate (2-OG), phenylacetylglycine (PAG), dimethylamine (DMA), dimethylglycine (DMG).

Table 4.7 Summary of the urinary changes observed by NMR in chlorpromazine-dosed rats.

Dose of Chlorpromazine	
30 mg/kg	**60 mg/kg**
Clear changes in the endogenous metabolites were observed: Creatine: ↑ ** Taurine: ↑ * 2-OG: ↓ (NS) Citrate: ↓ (NS)	Marked changes in the endogenous metabolites were detected on various days. On Day 2 the changes were assessed as follows: TMAO: ↓ ** Creatine: ↑ ** Taurine ↑ (NS) 2-OG: ↓ ** Citrate: ↓ ** Succinate: ↓ ** Hippurate: ↓ ** PAG: ↑ **

4.2.5.2 Principal Component Analysis of Urine NMR Data

Figure 4.16 shows a series of PCA scores plots of the first two principal components of the high dose chlorpromazine-treated animals and the controls. The scores plot of the pre-dose urine samples showed partial separation between the two groups. Animals 403 and 405 are separated from the rest of the animals along the second principal component and animals 401 is separated from the rest of the animals along the first principal component. The series of PCA scores plot highlighted that the endogenous biochemical differences between the two groups increased post-dose reaching a maximum at Day 2. Clear separation between the high dose animals and control animals can be observed on Day 1 (0-7h). The Day 2 PCA scores plot shows clear differences between the high dose and control animals. Additionally, the Day 2 scores plot also shows animal 401 separated from the rest of the animals along the second principal component. The PCA scores plot of Day 3 urine samples shows clear separation between the two groups although variation within the high dose animals can be seen clearly. Finally, the scores plot of Day 7 shows some separation indicating partial recovery. These observations confirm that there are biochemical changes between the groups upon administration of high dose chlorpromazine that is becoming more prominent with increasing time until a time maxima of Day 2 before gradual recovery from the toxic insult on Day 3 onwards.

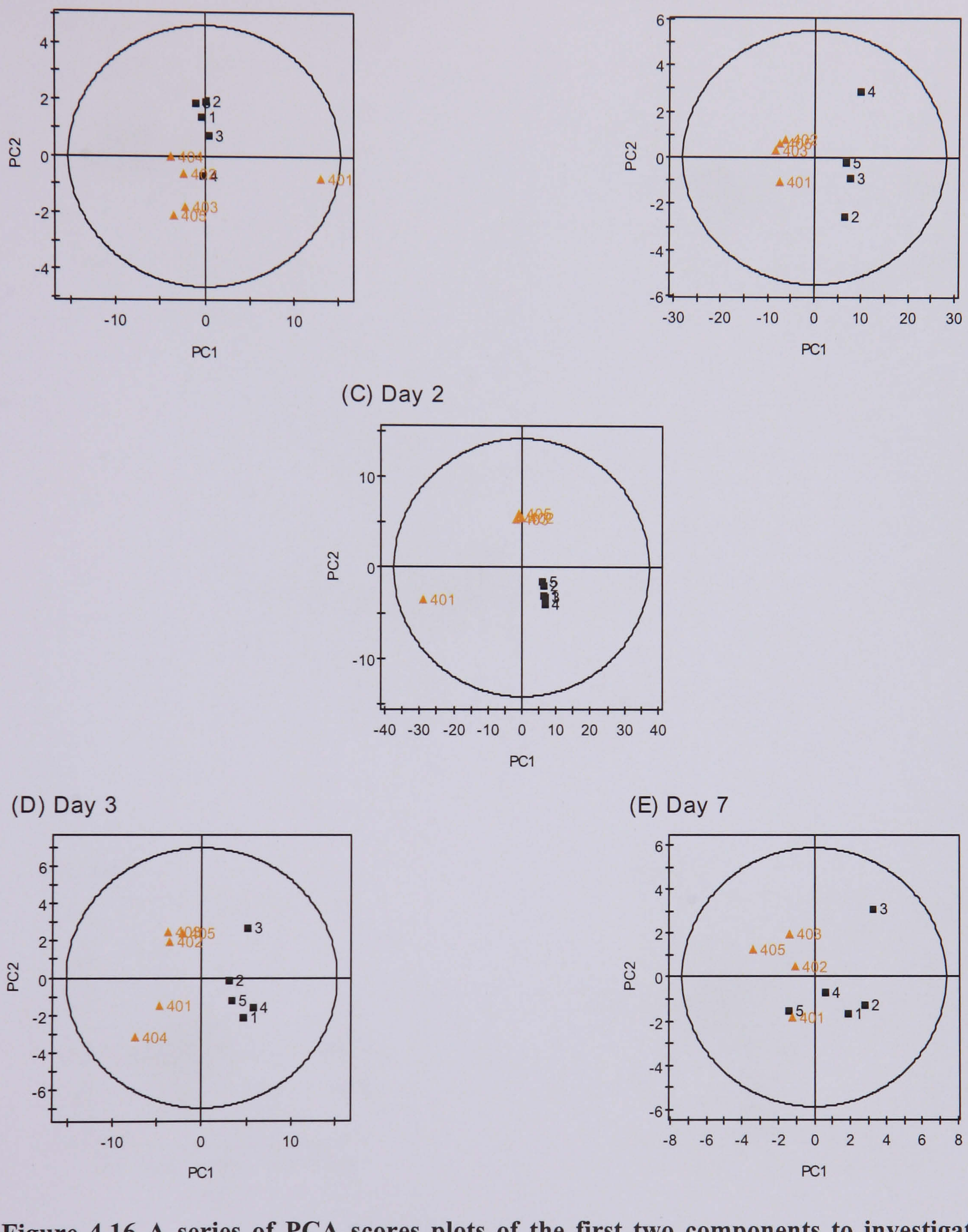

Figure 4.16 A series of PCA scores plots of the first two components to investigate time related metabolic differences associated with the effects of high dose chlorpromazine in the animals.

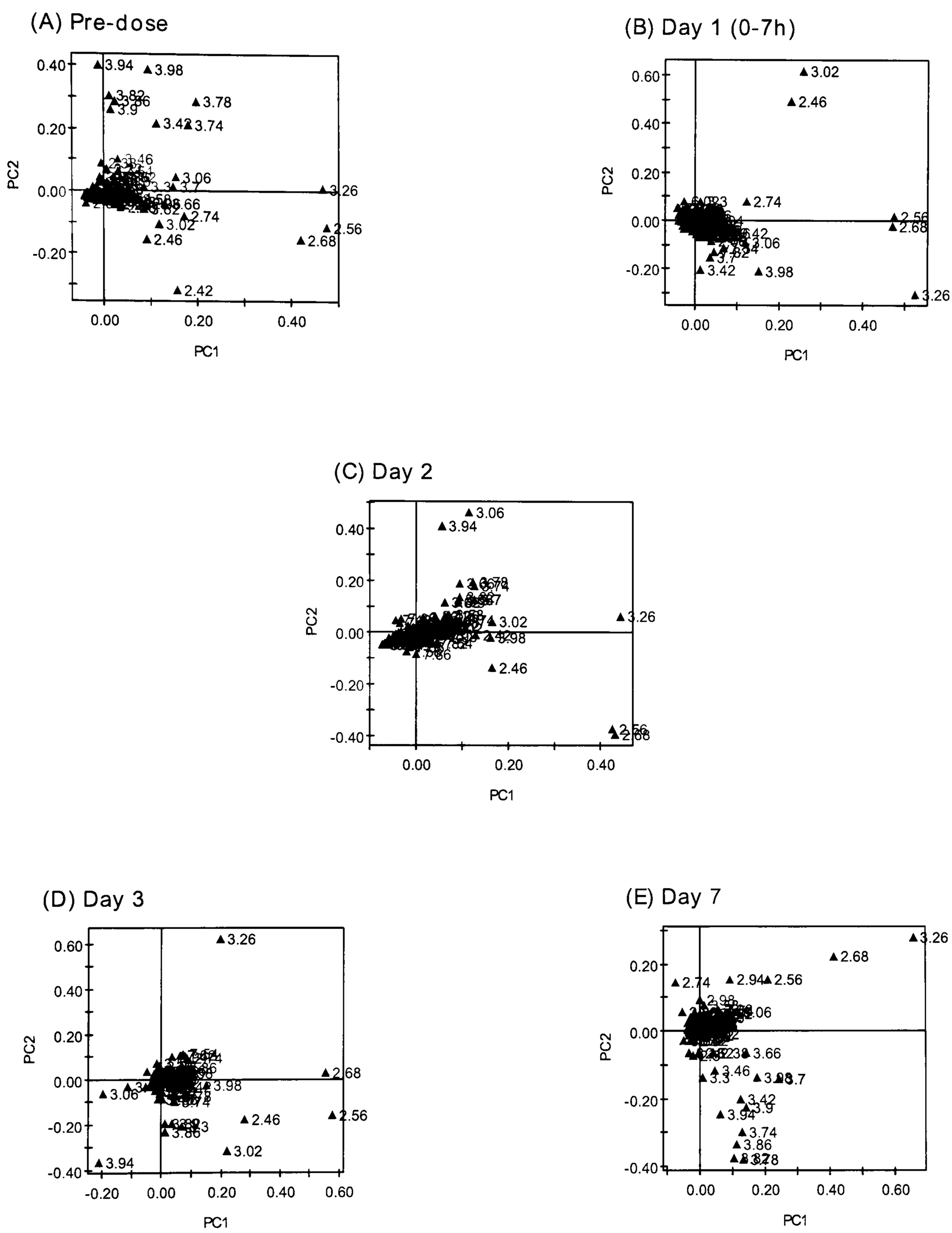

Figure 4.17 A series of corresponding PCA loadings plots of the first two components to investigate time related metabolic differences associated with the effects of high dose chlorpromazine in the animals.

Figure 4.17 shows a series of PCA loadings plots of the first two principal components of the high dose chlorpromazine-treated animals and the controls. The loadings plot for the pre-dose data indicated that high dose animals 403 and 405 have lower urinary glucose and creatine as compared to the rest of the animals. The loadings plot also shows that animal 401 has higher levels of urinary TMAO and citrate. Careful inspection of the urinary NMR data confirmed that high dose animals 403 and 405 have lower levels of urinary glucose and creatine; and that animal 401 has high level of urinary TMAO and citrate. Overall the loadings plots show that the trends seen in the PCA scores plots (Figure 4.16) were attributed to relative changes in the urinary endogenous metabolites. The loadings plot for Day 1(0-7h) indicates that decreases in urinary TMAO, citrate and 2-oxoglutarate are the biggest contributors to the separation along the first principal component. The loadings plot also identifies a decrease in urinary hippurate as the contributor to the separation between the high dose and control animals. However, on Day 2, increase in urinary creatine, and decreases in urinary citrate and 2-oxoglutarate are the biggest contributors to the separation between the two groups. In addition, the loadings plot shows increase in urinary phenyacetylglycine and decrease in urinary hippurate which contributed to the separation along the second principal component. The loadings plot also shows decrease in urinary TMAO level as the sole contributor to the separation between animal 401 and the rest of the animals. These changes can be seen clearly in the series of urinary NMR spectra (Figure 4.15). The loadings plot for Day 3 indicated increases in urinary taurine and creatine as well as decreases in urinary citrate, TMAO, hippurate and 2-oxoglutarate contributed to the separation along the first principal component. The loadings plot also shows that variation in urinary TMAO level contributed to the variation within the high dose animals with animals 402, 403 and 405 showing higher level of TMAO as compared to animals 401 and 404. The loadings plot for Day 7 shows some changes in the levels of endogenous metabolites with changes in urinary glucose and TMAO as the most prominent.

4.2.5.3 PCA Mean Trajectory of Urine NMR Data

A PCA mean trajectory was calculated using the ^{1}H NMR spectra of urine sample for all high dose animals over five time points as above to extract time-related metabolic changes in rat urine samples in response to the xenobiotic insult. The PCA mean trajectory was derived as described in chapter 2.

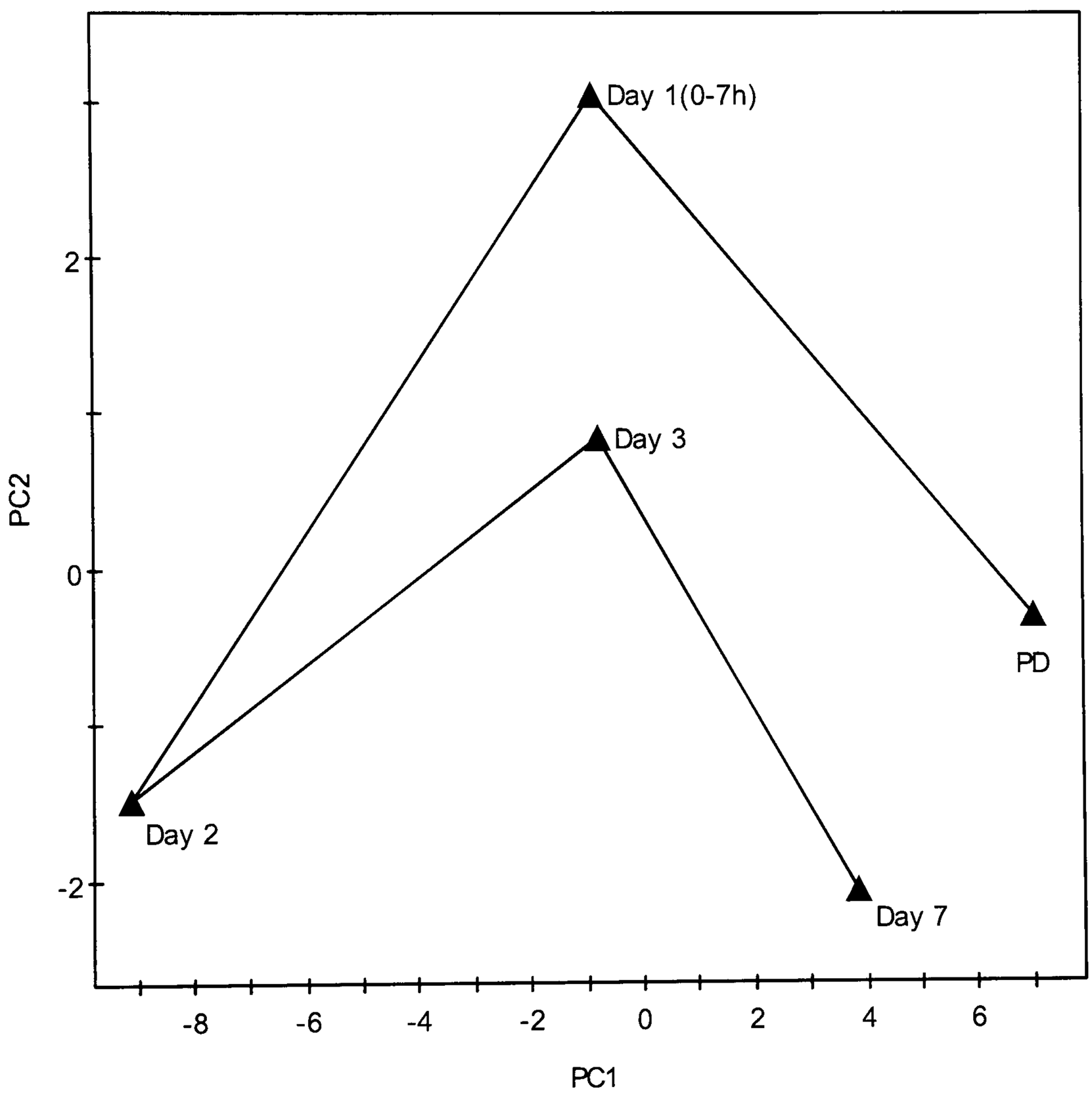

Figure 4.18 PCA mean metabolic trajectory plot mapping the average position of standard ^{1}H NMR high dose chlorpromazine urine spectra over five time points.

A PCA mean trajectory plot (Figure 4.18) was constructed from the complete data-reduced ^{1}H NMR spectra, excluding the region of water and urea (δ 4.0-6.0). The first two PCs described 94.9% of the total variance in X. The modelled metabolic evolution comprised four distinct phases. In phase one, corresponding to movement to the Day 1 (0-7h) time point, the trajectory of the urine sample coordinates moved away from the pre-dose (PD) position along the second principal component, corresponding to decreases in urinary TMAO, 2-oxoglutarate, hippurate and citrate as well as some increase in urinary taurine level, indicating onset of chlorpromazine-induced toxicity. In phase two, corresponding to movement to the Day 2 time point, the trajectory changes direction moving away from the origin along the first principal component corresponding to the concomitant increase in urinary creatine, taurine and phenylacetylglycine, and more severe decrease in urinary TMAO, 2-oxoglutarate, citrate succinate and hippurate with the changes reaching maximal level on Day 2. Thereafter in phase three, corresponding to movement to the Day 3 time point, the trajectory of the urine sample coordinates moved towards the pre-dose position along the second principal component, corresponding to increases in urinary taurine, TMAO and creatine as well as some decreases in urinary 2-oxoglutarate, citrate and hippurate. The changes observed in Day 3 are less severe as compare to the changes in Day 2 indicating the beginning of recovery. In addition, the trajectory between Day 2 and Day 3 time points are almost parallel albeit in opposite direction to the trajectory between Day 1(0-7h) and Day 2 time points indicating a simple recovery response that corresponds with the level of liver toxicity. Finally in phase four, corresponding to movement to the Day 7 time point, the trajectory moved towards the origin along the first principal component corresponding to the levels of urinary metabolites returning to 'normality' with increases in urinary TMAO, citrate, 2-oxoglutarate, hippurate and succinate, and decrease in urinary taurine.

4.2.6 Pattern Recognition Analysis of Concatenated Liver and Plasma NMR Data

4.2.6.1 Concatenated Principal Component Analysis (PCA)

PCA was performed on concatenated liver and plasma NMR data and Figure 4.19 shows the resulting scores and loadings plots. The scores plot for the low dose and control animals (Figure 4.19A) showed separation between the two groups of animals. The first principal component describes the variation between the low dose animals and the control animals, whereas the variation within the dosed group is described by the second principal component with animals 309 and 310 separated from the rest of the low dose animals. The corresponding loadings plot (Figure 4.19B) indicates that decrease in plasma VLDL is the major contributor to the separation between the low dose animals and control animals along the first principal component. The loadings plot also shows that changes in plasma LDL, lactate and choline as well as liver TMAO are the contributors to the separation within the low dose animals along the second principal component.

The PCA scores plot of the high dose liver and plasma data (Figure 4.19C) revealed clear separation between the high dose animals and the control animals. The first principal component describes the variation observed between the high dose animals and the control animals. Additionally, the scores plot also revealed differences within the high dose animals with animals 406 and 409 located on the upper half of the plots and the remaining three animals on the lower half of the scores plot separated along the second principal component. The corresponding loadings plot (Figure 4.19D) indicates that decreases in plasma lipids and lactate as well as decreases in liver TMAO are the contributors to the variation along the first principal component, with the change in the plasma lipids at δ1.28 being the dominant factor. Additionally, the loadings plot also indicates that increases in plasma 3-D-hydroxybutyrate (δ1.20) and acetoacetate (δ2.24), and decreases in plasma glucose as well as changes in liver TMAO level are the major contributors to the separation along the second principal component, with animals 406 and 409 showing signs of ketosis separated from the rest of the high dose animals.

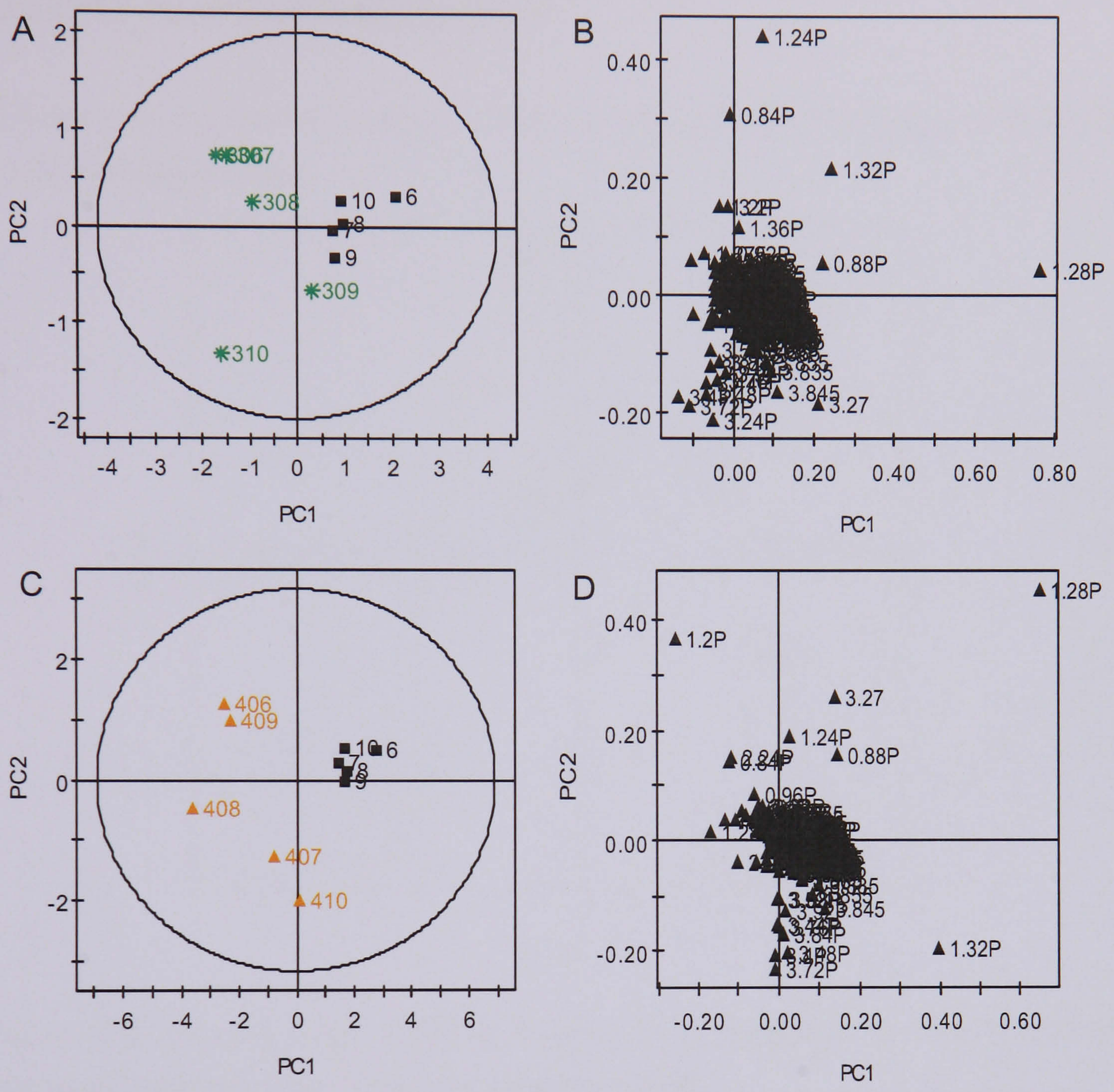

Figure 4.19 Concatenated PCA models for the first two components of the Day 2 standard 1D NMR spectra of chlorpromazine-dosed liver and CPMG spin-echo plasma NMR spectra. (A) Low-dose vs. control data and the corresponding loadings plot (B). (C) High-dose vs. control data and the corresponding loadings plot (D).

4.2.6.2 PLS-Discriminant Analysis (PLS-DA)

PLS-DA was also used to determine which variables in the liver and plasma NMR data predict the sample classes.

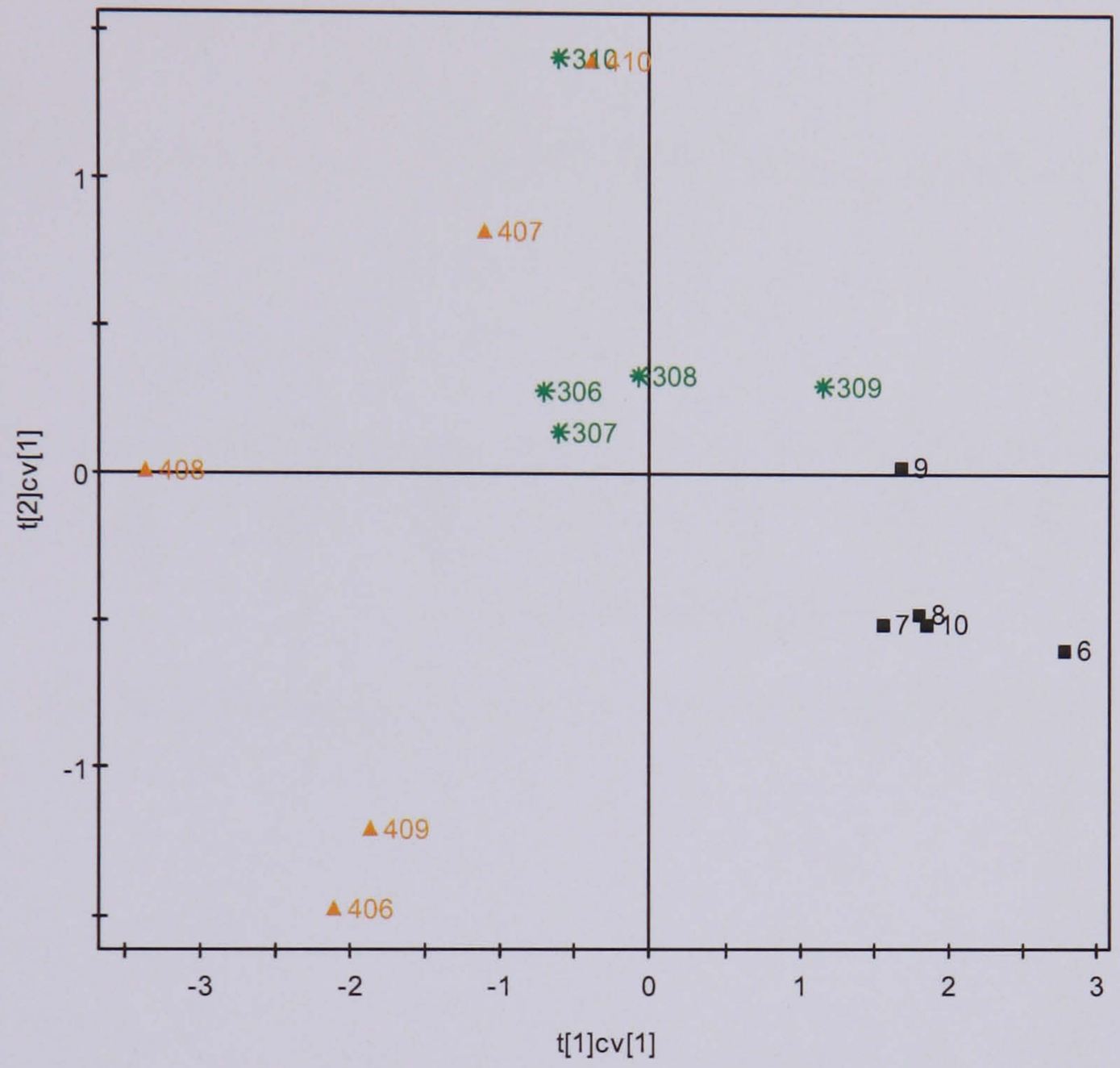

Figure 4.20 PLS-DA cross validated scores plot of standard ^{1}H NMR spectra of chlorpromazine Day 2 liver tissue and plasma samples.

Figure 4.20 shows the PLS-DA cross validated scores plot for the first two components of the chlorpromazine Day 2 liver tissue and plasma NMR data. The scores plot revealed clear separation between the controls and the dosed groups particularly between the low dose and control groups. The high dose animals are separated from the control animals along the first component. Similarly, the low dose animals are distinguished from the control animals along the first component situated between the control animals and high dose animals. Additionally, the scores plot also revealed separation within the high dose animals with animals 406 and 409 separated from the rest of the animals on the lower left quadrant of the scores plot along the second principal component.

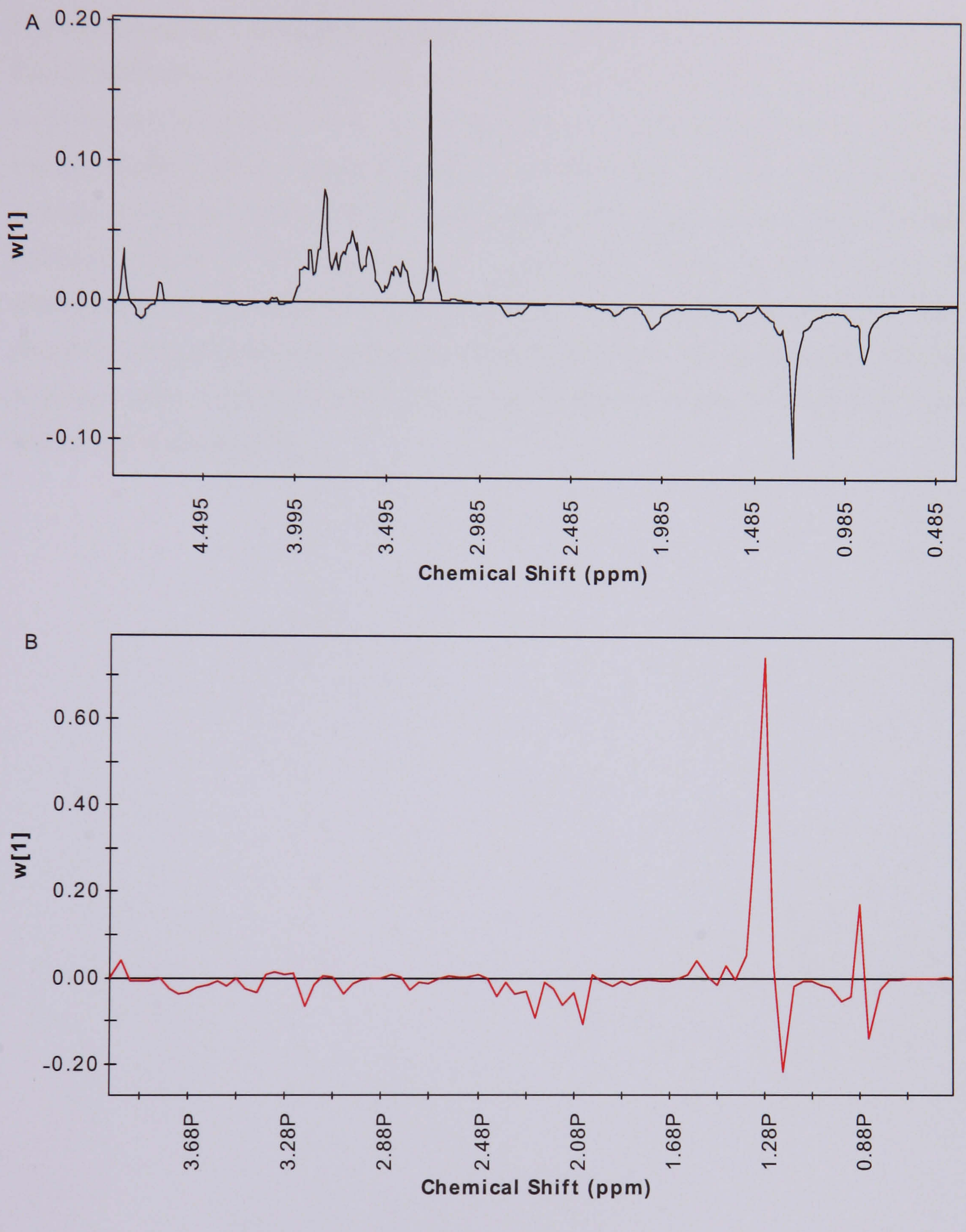

Figure 4.21 Corresponding PLS loadings plot (W[1]) for the first component from the Day 2 (A) liver NMR data (—), and (B) plasma NMR data (—).

The corresponding X block first component PLS loadings attributed to the liver tissue and plasma NMR data are shown in Figure 4.21. The plot shows the general effects of dosing on liver tissue and plasma along the first component. It indicates that animals dosed with chlorpromazine exhibit elevated liver lipids and lower levels of liver carbohydrates and glycogen storage as well as TMAO (Figure 4.21A), with changes in liver TMAO being the dorminant factor in the liver tissue. Additionally, Figure 4.21B indicates that administration of chlorpromazine caused decreases in plasma lipids and some increase in plasma N-acetyl glycoproteins along the first PLS component. The plot indicates a decrease in plasma lipids is the major contributor to the separation between the high dose animals and the rest of the animals.

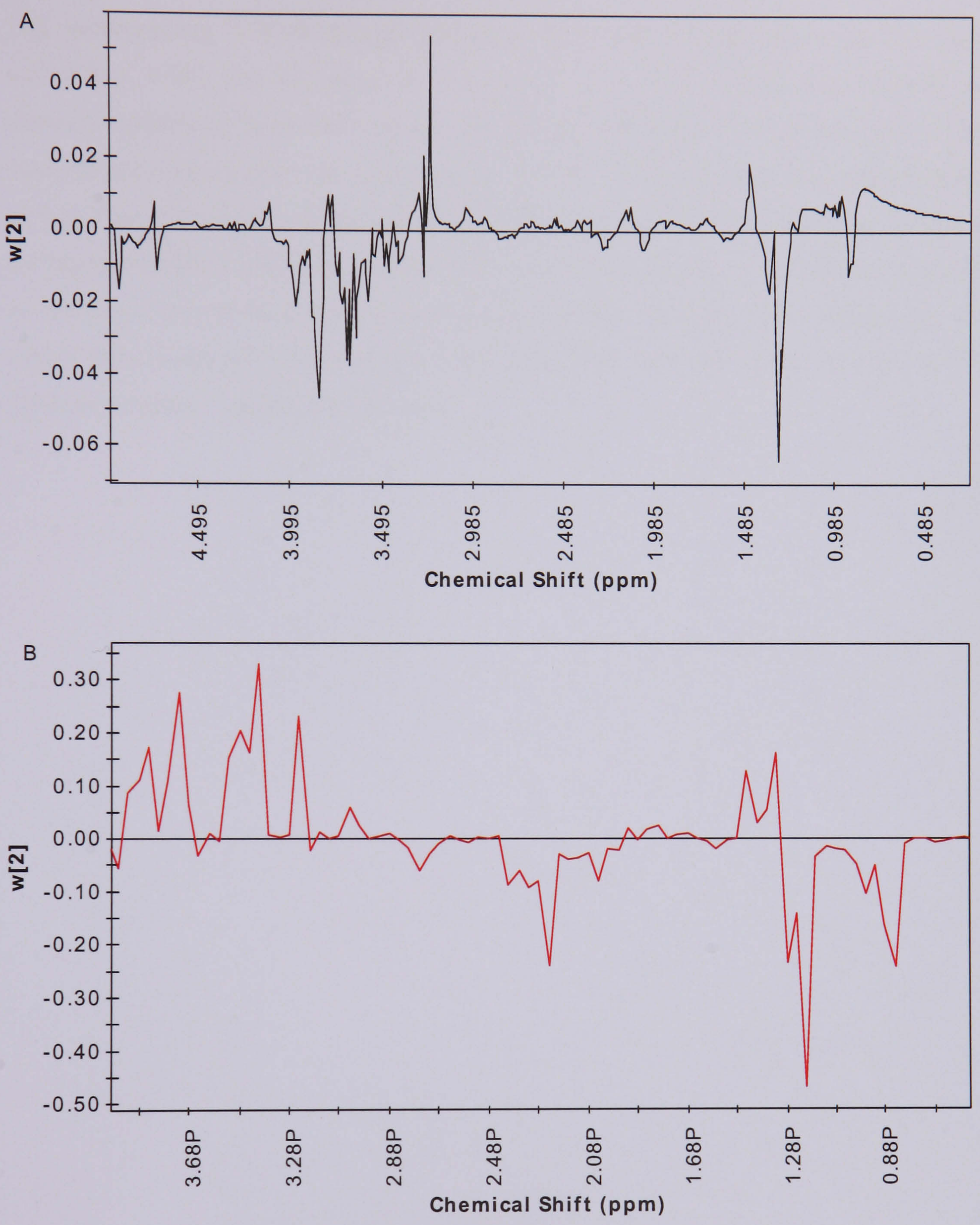

Figure 4.22 Corresponding PLS loadings plot (W[2]) for the second component from the Day 2 (A) liver NMR data (—), and (B) plasma NMR data (—).

The corresponding X block second component PLS loadings attributed to the liver tissue and plasma NMR data are shown in Figure 4.22. The second component loadings plot shows the effects of chlorpromazine on liver tissues and plasma. The administration of low dose chlorpromazine does not induce lack of activity in the rats. However, administration of high dose chlorpromazine induces lack of activity in animals 406 and 409 as reflected in the plasma loadings with increases in plasma 3-D-hydroxybutyrate and acetoacetate as well as decreases in plasma glucose levels indicating reduce feeding. The loadings plot also shows that animals 407 and 410 have higher level of liver choline and lower level of liver lipids as compare to animals 406 and 409.

4.2.6.3 Partial Least Square Projection to Latent Structures Approach (PLS)

Having established that there were intrinsic differences between groups, the data matrices were combined and analyzed using PLS that enabled determination of plasma NMR features that correlated with the liver MAS NMR biomarkers. The NMR data was mean centred prior to modelling.

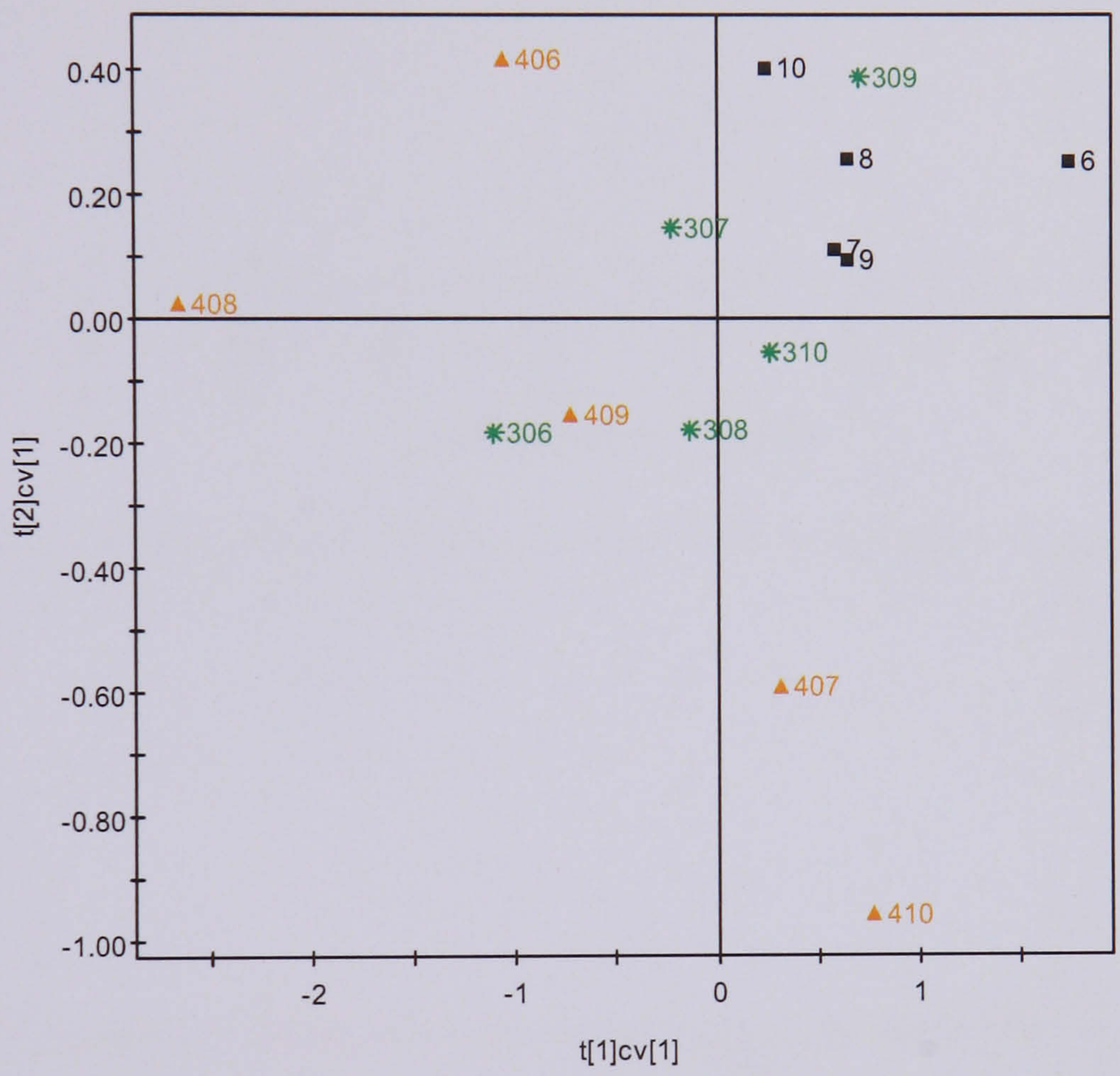

Figure 4.23 PLS cross validated scores plot of Day 2 standard ^{1}H NMR spectra of chlorpromazine liver tissue and CPMG spin-echo NMR data plasma samples.

By treating liver NMR data as X matrix and plasma NMR data as Y matrix, the cross validated scores plot (Figure 4.23) revealed clear separation between the high dose samples and the controls along the second component. However, partial separation occurs between the low dose and control groups. Again, variation within the high dose animals can be seen in the scores plot along the first component. Unlike the PLS-DA scores plot in Figure 4.20, the scores plot here revealed that animals 406, 408 and 409 are separated from animals 407 and 410.

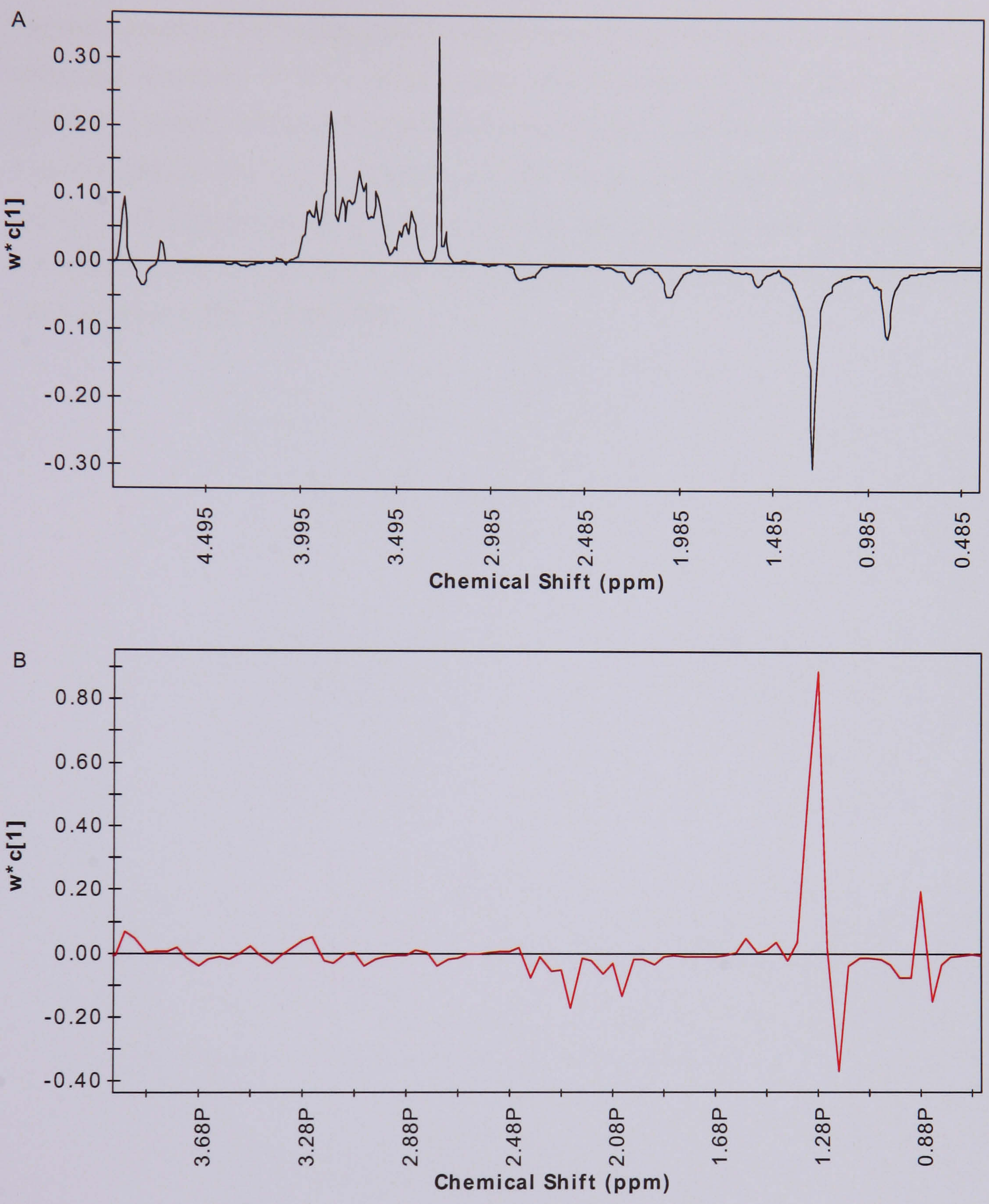

Figure 4.24 First component PLS weight (W*[1]) from the PLS model attributed to (A) ^{1}H MAS NMR data of Day 2 liver tissues (—), and (B) CPMG spin-echo NMR data of Day 2 plasma samples (—).

The corresponding PLS loadings plot for the first component revealed that increases in liver lipids and decreases in liver carbohydrates and glycogen (Figure 4.24A) as well as increases in plasma 3-D-hydroxybutyrate and acetoacetate, and decreases in plasma lipids (Figure 4.24B) are the major contributors to the separation of high dose animals 406, 408 and 409 from high dose animals 407 and 410. The loadings plot reveals the sedative effect of chlorpromazine as indicated by the raised plasma 3-D-hydroxybutyrate and acetoacetate levels in animals 406, 408 and 409.

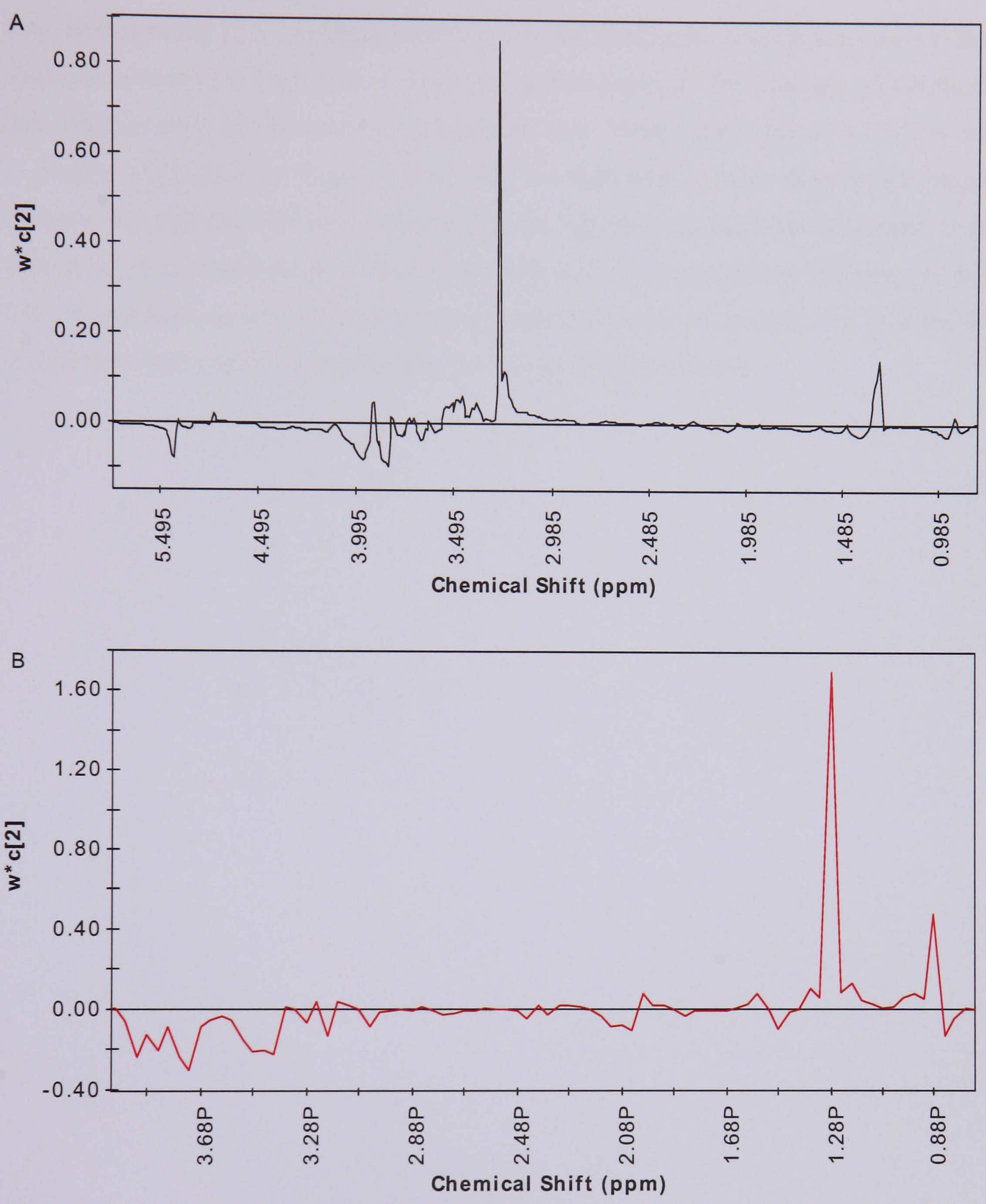

Figure 4.25 Second component PLS weight (W*[1]) from the PLS model attributed to (A) ^{1}H MAS NMR data of Day 2 liver tissues (—), and (B) CPMG spin-echo NMR data of Day 2 plasma samples (—).

The corresponding PLS loadings plot for the second component describes the dose related variation between the high dose animals and control animals. The loadings plot indicates that administration of chlorpromazine decreases liver TMAO level (Figure 4.25A) as well as plasma lipids profiles (Figure 4.25B) with the high dose animals showing the biggest changes. The loadings plot also indicates that the high dose animals react differently to the high dose of chlorpromazine with animals 407 and 410 experiencing decreases in liver TMAO and lipids as well as decreases in plasma lipids whereas animals 406, 408 and 409 suffers from chlorpromazine-induced ketosis as described previously.

4.3 Discussion

4.3.1 Effects of Chlorpromazine on rat liver

At the high dose, chlorpromazine induced mild changes in the liver as revealed by the histopathological data. However, the NMR findings indicate decrease in liver TMAO levels. Trimethylamine (TMA) is converted to its N-oxide derivative, trimethylamine-N-oxide (TMAO), in the liver through the action of flavin monooxygenase (FMO) with flavin adenine dinucleotide (FAD) as its cofactor (Baker and Chaykin, 1962; Ziegler, 1993; Maschke *et al.*, 1997). The decrease in liver TMAO, as seen in the low dose and high dose animals, could indicate that chlorpromazine inhibits FMO activity and chlorpromazine has been shown to inhibit D-amino acid oxidase enzyme activity by competing and/or complexing with FAD (Yagi *et al.*, 1956; Lasslo and Meyer, 1959). The chlorpromazine-FAD complex was also found to be not easily reversible (Lasslo and Meyer, 1959). Further investigation by Yagi *et al.* (1960) demonstrated that chlorpromazine formed complexes with FAD, riboflavin, riboflavin 5-monophosphate and flavin monophosphate. The study also indicated that chlorpromazine binds at the site of the adenosine monophosphate moiety of FAD.

Decrease in liver glucose and glycogen indicated an increase in energy demand and chlorpromazine has been shown to reduce the efficiency of coupled phosphorylation in mitochondria (Dawkins *et al.*, 1959a). Chlorpromazine has also been shown to inhibit electron transport between reduced diphosphopyridine nucleotide and cytochrome *c* reductase involving an intermediate (Dawkins *et al.*, 1959b) and inhibit adenosine triphosphate (ATP)-adenosine diphosphate (ADP) reaction (Dawkins *et al.*, 1960). Löw (1959a) reported that flavin is involved in mitochondrial ATPase reaction. Löw, (1959b) suggested that the phosphorylated intermediate, which reacts with chlorpromazine, was a flavoprotein. Low (1959b) also found that chlorpromazine, inhibits the exchange of organic phosphate (P_i) with the terminal phosphate of ATP during ATP-P_i exchange in both liver and brain mitochondria. In addition, Medina *et al.* (1964) has shown that chlorpromazine inhibited the metabolic activity of mitochondria and the addition of a higher concentration

of chlorpromazine caused shrinking of mitochondria and disruption of its internal fine structure. The inhibition of ATP production in mitochondria by chlorpromazine and disruption of mitochondrial activity as well as mitochondrial structure may lead to decreased ATP production thus increasing energy demand for ATP. This may lead to glycogenolysis and gluconeogenesis, which would enable the production of ATP though less efficiently. The increase in liver lipids could be due to chlorpromazine-induced inhibition of ATP production in liver mitochondria, as well as the disruption of mitochondrial structure. Decreased ATP production could lead to reduced protein synthesis and thus a decrease in lipid transport out of the liver. The decrease in liver glucose could also reflect the effect of chlorpromazine on the activity and feeding of the animals. Chlorpromazine is a sedative and the current results indicated that at least two of the high dose animals showed signs of chlorpromazine-induced ketosis characterised by severe decreases in liver glucose and glycogen.

4.3.2 Effects of Chlorpromazine on blood plasma and urine

The effects of chlorpromazine on blood plasma are characterised by increases in aspartate aminotransferase, which are indicative of hepatocellular damaged and a decrease in plasma triglycerides. Generally the highly variable results in the plasma samples reflects the effect of the chlorpromazine-induced changes in the animals, with some high dose animals (407 and 410) showing some signs of chlorpromazine toxicity characterised by decrease in plasma lipids and an increase in plasma creatine, and some animals (406, 408 and 409) suffering ketosis attributed to the sedative effects of chlorpromazine. Again, the reduction in the plasma VLDL could be due to reduced lipid secretion from liver. The increases in plasma 3-D-hydroxybutyrate and acetoacetate and decrease in plasma glucose as identified by ^{1}H NMR spectroscopy in animals 406, 408 and 409 reflects chlorpromazine-induced ketosis due to lack of activity and feeding. Acetoacetate and 3-D-hydroxybutyrate are ketone bodies, produced when excessive amounts of fatty acids are being mobilised and oxidised to produce energy i.e. during starvation (Figure 4.26). The presence of these ketone bodies are useful markers of reduced food intake although the clinical chemistry data showed that the Day 2 blood glucose levels were not substantially depleted by dosing

with high dose of chlorpromazine. It, therefore, appears that ketosis occurred in animals 406, 408 and 409 whilst animals 407 and 410 showed no signs of ketosis through analysis of the CPMG spin-echo plasma NMR spectra.

In the urine, a clear decrease in urine TMAO was observed. TMAO and related methylamine compounds are involved in methane metabolism. A number of these compounds are dietary derived, synthesised from precursors in the diet by the gut microflora. Trimethylamine is normally oxidised by the activity of the flavin monooxygenase (FMO) system to the odourless, TMAO, in the liver which is excreted in the urine. A decreased TMAO level as observed in urine NMR spectra reflects the inhibitory effects of chlorpromazine towards FMO. This observation further supports the similar observation made in liver tissue NMR spectra. Hippurate, synthesised in the kidney and liver from glycine and benzoic acid, is secreted by the renal tubular cells and continually excreted in the urine. A significant decrease of this metabolite in urine may be indicative of a metabolic alteration or increased phenylacetylglycine (PAG) synthesis.

2-Oxoglutatrate, citrate and succinate are all compounds related to energy metabolism within the organism particularly in the tricarboxylic acid (TCA) cycle. Decreases of these TCA intermediates in urine samples could indicate changes in energy metabolism in response to chlorpromazine. Reduced urinary excretion of TCA cycle intermediates is a common non-specific effect of toxic injury (Waters *et al.* 2005, *Antti et al.* 2002). Additionally, increases in taurine and creatine were also observed in the urine. These are well-known urinary biomarkers of liver injury (Waterfield *et al.* 1993b, Timbrell *et al.* 1995b, Timbrell 1998). The increase in urinary taurine also suggested impaired protein synthesis or a link to increased cysteine synthesis. The chlorpromazine-induced increases in urinary creatine may be related to cysteine biosynthesis from methionine as postulated by Clayton *et al*. (2003a).

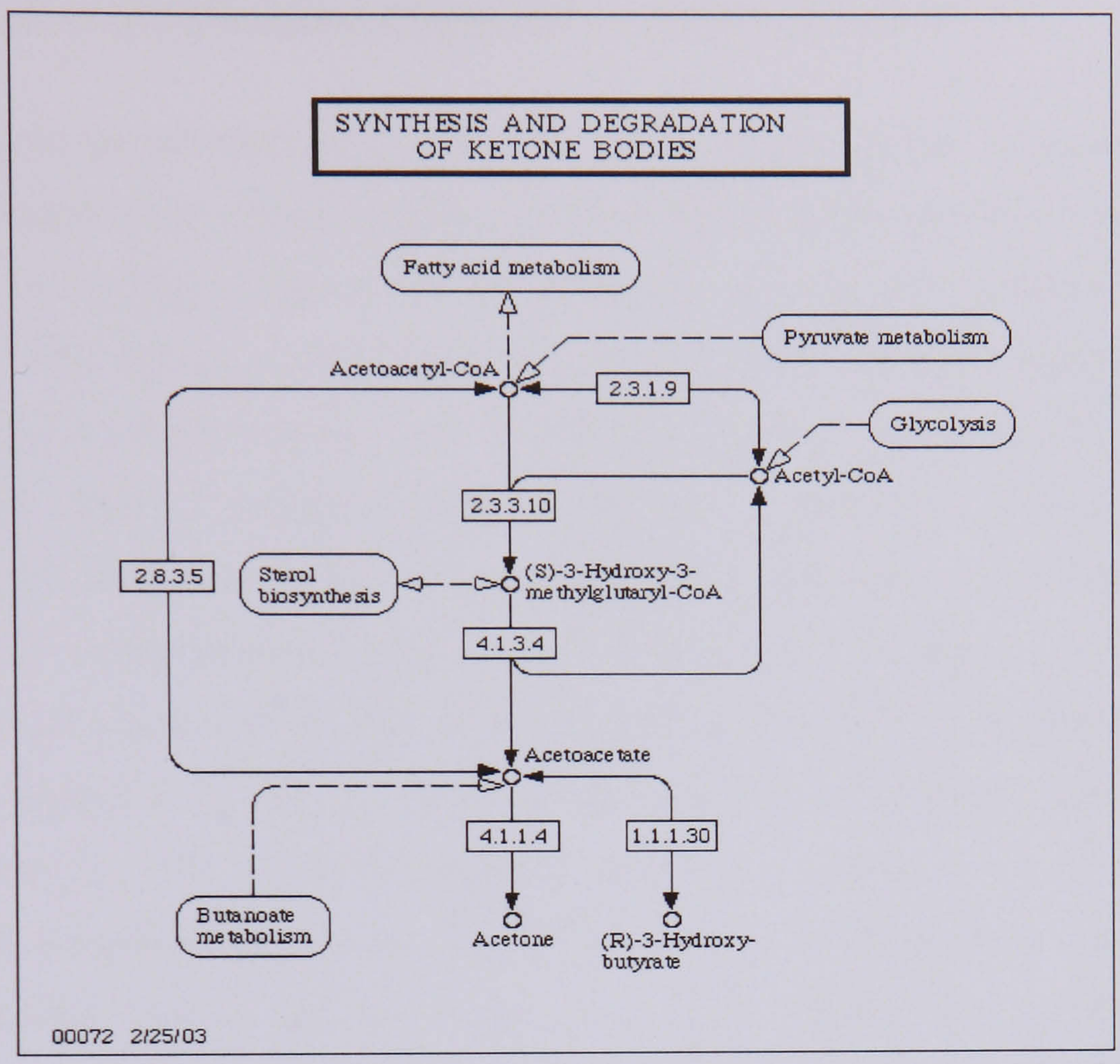

Figure 4.26 Synthesis and degradation of ketone bodies (adapted from http://www.genome.jp/kegg/pathway/map/map00072.html).

4.3.3 Comparison of Information Obtained from Different Sources

Table 4.8 shows the summary of the effects of chlorpromazine in rats. In general, the NMR findings indicated clear chlorpromazine-induced effects in the low dose and high dose animals. These findings disagree with the histopathology and clinical chemistry findings which show little effects in the treated animals. However, the high dose animals were separated into two distinct groups; with one group consisting of animals 406, 408 and 409 showing clear signs of chlorpromazine-induced ketosis indicating reduced activity and feeding brought on by the sedative effect of chlorpromazine, and another group showing clear signs of chlorpromazine-induced toxicity. The Day 8 standard ^{1}H NMR spectra showed minimal effects and this was reflected in the PCA plots. This suggests that recovery was largely complete by Day 8. This is consistent with the histopathology and clinical chemistry findings. The integrated approach proves to be more useful in analysing the conventional toxicological data and NMR data collectively to describe chlorpromazine-induced metabolic flux in the rats. In this case, NMR spectroscopy proved to be more sensitive in identifying chlorpromazine-induced toxicity at the high dose, since histopathology failed to show any clear signs of liver toxicity or cholestasis and clinical chemistry data showed mild changes which include increases in aspartate aminotransferase (ASAT) activity and decrease in triglycerides. Blood glucose is relatively invariant due to tight homeostatic control, and therefore is relatively unhelpful for elucidating nutritional status because one of the functions of liver is to keep constant blood glucose level by glycogenolysis, gluconeogenesis etc. However, ^{1}H NMR spectroscopy of blood plasma clearly provided a much more useful insight into chlorpromazine-induced effects than was available from the clinical chemistry data as it was able to detect ketosis-induced changes in plasma glucose as well as presence of ketone bodies such as 3-D-hydroxybutyrate and acetoacetate.

Table 4.8 Summary of the effects of chlorpromazine.

Dose of Chlorpromazine	Histopathology	Clinical Chemistry	Liver NMR	Plasma NMR	Urine NMR
30 mg/kg	No significant differences from controls.	Triglycerides: ↓ (***) ASAT: ↑ (**) ALAT: ↑ (**)	Minimal change	Minimal change	Creatine: ↑ (**) Taurine: ↑ (*) 2-OG: ↓ (NS) Citrate: ↓ (NS)
60 mg/kg	Mild lipid changes in the centrilobular areas and diffuse hepatocellular cytoplasmic changes. No evidence of cholestasis.	Triglycerides: ↓ (***) ASAT: ↑ (*)	TMAO: ↓ (*) Glucose: ↓ (NS) Glycogen: ↓ (NS) Lipids: ↑ (NS) Choline: ↑ (NS)	Creatine: ↑ (**) VLDL: ↓ (*) Total lipids: ↓ (*) 3-D-hydroxybutyrate and acetoacetate increased in 3/5 animals.	TMAO: ↓ (**) Creatine: ↑ (**) Taurine: ↑ (NS) 2-OG: ↓ (**) Citrate: ↓ (**) Succinate: ↓ (**) Hippurate: ↓ (**) PAG: ↑ (**)

Key: ASAT = aspartate aminotransferase, ALAT = alanine aminotransferase, TMAO = trimethylamine-N-oxide, VLDL = very low density lipoprotein, 2-OG = 2-oxoglutarate, PAG = phenylacetylglycine.

MAS NMR spectroscopy of the liver showed that chlorpromazine (30 & 60 mg/kg) induced a clear decrease in the liver TMAO level. Increased biosynthesis of phospholipids could reduce the formation of TMAO and at the high dose of chlorpromazine, increase in urinary phehylacetylglycine (PAG) was observed, which Nicholls *et al.* (2000) have suggested may be a marker of phospholipidosis. If an increase in urinary PAG is due to increased phospholipids synthesis, it could lead to a decrease in TMAO by diversion of the choline utilisation. However, the Day 2 MAS NMR data showed no increase in liver phospholipids indicating that phospholipidosis did not occur in the liver. Trimethylamine undergoes N-oxidation to trimethylamine N-oxide in the liver through the action of flavin monooxygenase (FMO) enzymes (Ziegler 1990, Ziegler 1993) and excreted in the urine (Smith *et al.* 1994). Like many monooxygenases, FMO requires NADPH and oxygen as co-substrates in the oxidation of trimethylamine to trimethylamine N-oxide. The catalytic cycle of TMA N-oxidation by FMO enzyme is shown in Figure 4.27. Step 1 and 2 involves the reduction and oxidation of FMO to form the highly reactive 4a-hydroperoxyflavin form (Ziegler 1993). Due to the high reactivity of the 4a-hydroperoxyflavin form of FMO, any soft nucleophile including trimethylamine that makes contact with this potent monooxygenating agent will be oxidised as shown in step 3. Step 4, 5, 1 and 2 simply regenerates the enzyme-bound oxygenating agent from NADPH and oxygen. Chlorpromazine is a known inhibitor of FMO (Yagi *et al.* 1956, Lasslo and Meyer 1959, Ayesh and Smith 1990). Therefore, inhibition of FMO by chlorpromazine will lead to a decrease in formation of TMAO in the liver as well as reduce excretion of this metabolite in the urine.

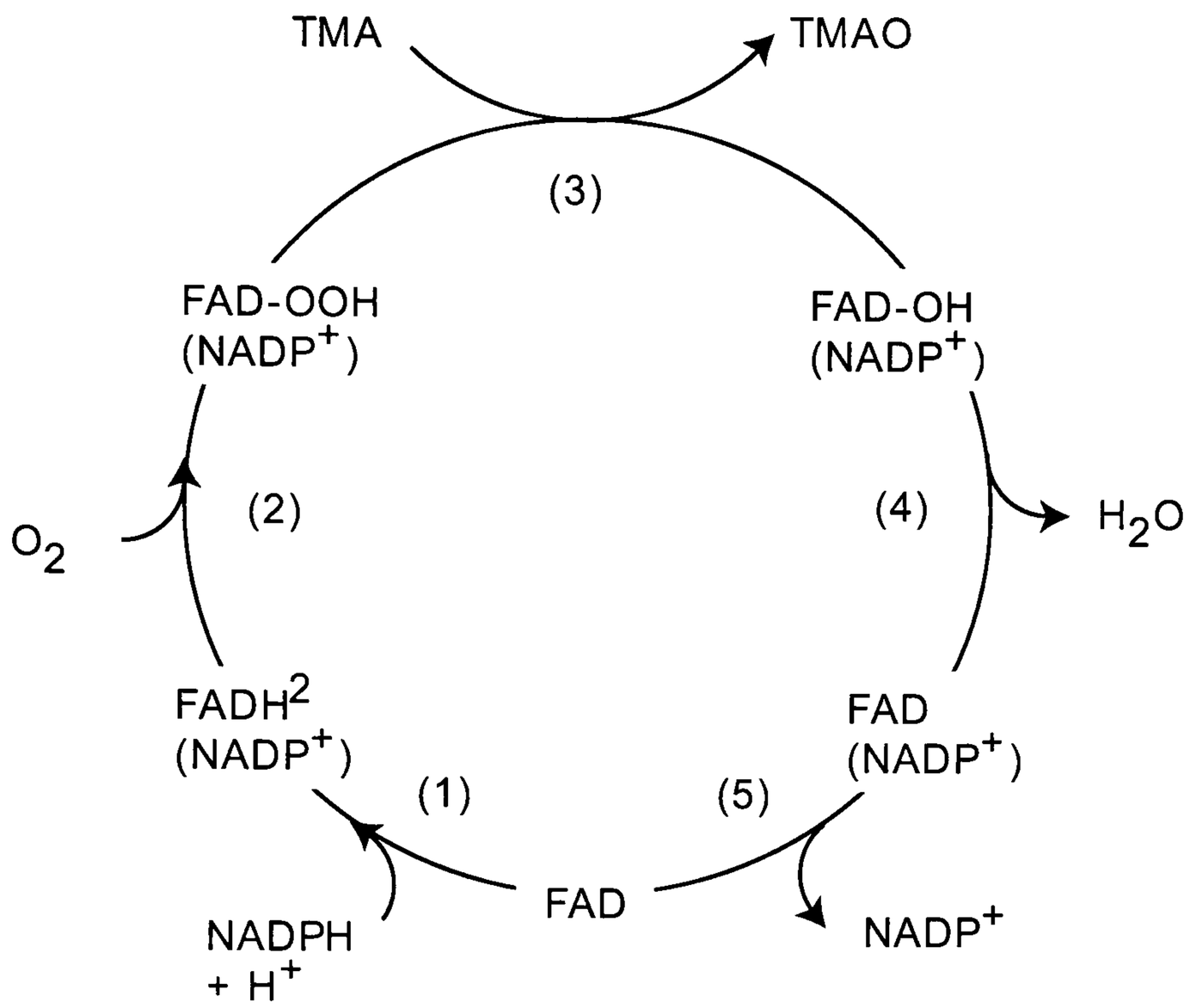

Figure 4.27 Catalytic cycle for N-oxidation of TMA by flavin monooxygenase (FMO) enzymes to TMAO (adapted from Ziegler 1993).

MAS NMR spectroscopy of the liver also showed that chlorpromazine (60 mg/kg) induced hepatic lipidosis and depletion of liver glucose and glycogen in all the animals. However, these changes were much clearer in three of the high dose animals as compared to the remaining two. These changes are indicative of increased energy demand in the liver and possible mitochondrial dysfunction since chlorpromazine has been shown to reduce the efficiency of coupled phosphorylation in mitochondria (Dawkins *et al.*, 1959a) and chlorpromazine inhibits the metabolic activity of mitochondria and caused shrinking of mitochondria and disruption of its internal fine structure (Medina *et al.* 1964). Loss of ATP and mitochondrial disruption will reduce lipid transport out of the liver. This could explain the changes observed in high dose animals 407 and 410 where both suffered decreases in liver glycogen and glucose as well as an increase in liver lipids. However, three of the high dose animals (406, 408 and 409) showed severe decrease in liver glucose and glycogen and the corresponding plasma NMR data indicated increases in ketone bodies 3-D-hydroxybutyrate and acetoacetate. Raised levels of plasma 3-D-hydroxybutyrate and

acetoacetate indicated a shift in energy metabolism toward ketone body formation and utilisation. These changes are indicative of reduced food intake due to chlorpromazine-induced sedation in the animals. The differences in effects of chlorpromazine within the high dose animals could explain the inability for the univariate statistical ANOVA method to produce significant results shown in Table 4.4.

The Day 2 plasma NMR data showed clear increases in the plasma tyrosine level in all high dose animals except animal 406. Animal 410 showed the biggest increase in plasma tyrosine as compared to the rest of the high dose animals as shown in Table 4.9. It is also the animal that showed the biggest change in liver TMAO and plasma lipids. However, since chlorpromazine is not a liver necrotic agent, no correlation in the level of plasma tyrosine with severity of chlorpromazine-induced toxicity is expected.

Table 4.9 Plasma tyrosine changes.

Animal Number	**Concentration of Day 2 plasma Tyrosine (multiple of average control level)**
406	0.9 x control average
408	1.1 x control average
409	1.2 x control average
407	1.3 x control average
410	1.7 x control average

Table 4.10 Changes in Day 2 plasma cholesterol, LDL and VLDL levels.

Chlorpromazine Dose Group	Increase in Day 2 Plasma Cholesterol (clinical chemistry data, %)	Increase in Day 2 Plasma LDL (NMR data, %)	Decrease in Day 2 Plasma VLDL (NMR data, %)
LD	0.3	5.8	32.7
HD	6.9	10.7	55.3

Additionally, the Day 2 plasma NMR data also showed increase in plasma creatine in two of the high dose animals. Increase in plasma creatine level normally leads to increase in urinary creatine level, which is evident in the current study. The Day 2 plasma revealed an increase in plasma LDL and a decrease plasma VLDL in both low dose and high dose animals (Table 4.10). The increase in plasma LDL level measured by NMR correlated with the increase in plasma cholesterol measured by plasma clinical chemistry. This is expected as plasma LDL is cholesterol-rich (Mason 1998). Although chlorpromazine is a cholestatic agent, the result shown indicates that it is not a reliable one. The use of PLS analysis on concatenated liver and plasma data (Figure 4.23 and 4.24) showed an increase in liver triglycerides that correlated to a decrease in plasma VLDL, which could indicate reduced lipid transport from the liver to the plasma. In addition, Figure 4.24 also showed increases in plasma LDL which agree with the plasma clinical chemistry finding.

The urine NMR data showed decreases in citrate, 2-oxoglutarate and hippurate. Reduced urinary excretion of TCA cycle intermediates would suggest mitochondrial dysfunction (Antii *et al.* 2002) and increased energy metabolism (Waters *et al.* 2005). In addition, the urine NMR data also revealed clear decrease in urinary TMAO level. Changes in the level of TMAO can be directly related to the diet. The major route of biosynthesis of TMAO derives from the degradation of dietary choline which is metabolised to trimethylamine by the enzymes of the gut microflora. As discussed earlier, TMA is converted to TMAO in the liver through the action of flavin monooxygenase enzyme (FMO). TMAO is then excreted in the urine. Chlorpromazine is a known FMO inhibitor thus a decrease in TMAO is

expected. Therefore, the severe decrease in liver TMAO, observed in this study, will lead to a decrease in urinary TMAO level. The decrease in urinary hippurate level could be related to increase in urinary phenylacetylyglycine as discussed in chapter 3.

4.3.4 Summary

The use of NMR spectroscopy of liver and biofluids coupled with multivariate analysis and conventional clinical chemistry enabled differentiation of the disparate effects the chlorpromazine had on rats following administration. The treatment with chlorpromazine seems to have two distinct effects in the rat. In the first case, chlorpromazine induced severe decrease in liver TMAO levels. This was followed by concomitant decrease in urinary TMAO levels. The treatment also caused depletion in liver glucose and glycogen followed by reduced urinary excretion of TCA cycle intermediates, citrate and 2-oxoglutarate indicating toxic injury. This in turn caused disruption in lipid metabolism with accumulation of triglycerides in the liver and reduced transport of lipids from the liver to the blood. In the second case, chlorpromazine caused reduced activity and feeding in three out of five rats characterised by the appearance of ketone bodies, 3-D-hydroxybutyrate and acetoacetate in the blood plasma. This is also evident in the corresponding liver NMR spectra with severe decreases in liver glycogen and glucose indicating glycogenolysis. In conclusion, the use of high resolution NMR spectroscopy to study intact liver tissue and biofluids i.e. blood plasma and urine, prove to be more sensitive in detecting chlorpromazine-induced biochemical perturbation in the rats as compared to conventional histopathological and clinical chemistry methods.

Chapter 5: Integrated Thioacetamide Studies

5.1 Background: Metabolism and hepatotoxicity of thioacetamide

According to the US Department of Health and Human Services' National Toxicological Program, Thioacetamide (TAA) is used as a replacement for hydrogen sulfide in qualitative analyses. It has also been used as an organic solvent in the leather, textile, and paper industries, as an accelerator in the vulcanization of buna rubber, and as a stabilizer of motor fuel. Grant and Rees (1958) investigated the correlations of histological and biochemical changes in thioacetamide-treated rats and found that administration of thioacetamide to rats caused changes in the parenchymatous cells of the liver, bile duct proliferation and development of tumours. Their results also showed a progressive decrease in mitochondrial nitrogen content and phospholipid. Additionally, the nuclear fraction of the treated animals had an increase in nitrogen and RNA content. Their results also showed a decrease in mitochondrial content and the phenomenon of 'ageing' mitochondria. RNA synthesis was also reduced but the incorporation of glycine into nuclear protein was increased. These findings led them to conclude that the decrease in mitochondrial respiration is due to the action of an inhibitor.

Thioacetamide is known to cause central lobular necrosis (Klaassen 2001, Haschek *et al.* 2002). This localised effect is believed to be due mainly to the higher concentration of cytochrome P-450 and other enzymes associated with drug metabolism in the central lobular region, which ultimately resulted in higher concentration of toxicant in this region. Rees *et al.* (1966) investigated the metabolism of trititated thioacetamide in the rat. The rats were fed with thioacetamide-^{3}H at a level known to cause liver tumours. They found that less than 1% of the tritiated thioacetamide was excreted unchanged in the urine. Radioactivity was found in all the organs examined as well as in the chemical constituents of all the cell fractions. Over 95% of the thioacetamide was converted to acetate in 24 hours. Incubation of liver slices with thioacetamide indicated that metabolism occurred via acetamide formation. Liver slices were found to be more active than kidney slices in converting thioacetamide to acetamide. They postulated that thioacetamide was first

converted to acetamide and that the acetamide was further hydrolysed to acetate. They also suggested that this metabolic step is a pre-requisite for thioacetamide to exert its toxic and carcinogenic effects.

Porter and Neal (1978) investigated the metabolism of thioacetamide and thioacetamide-S-oxide. They found that thioacetamide is oxidised to thioacetamide-S-oxide by rat liver microsomes and the NADPH-driven mixed-function oxidase system. Thioacetamide-S-oxide is further metabolised to acetamide and unidentified polar products through the action of rat liver microsomes. They also found that the introduction of the mixed-function oxidase inducer, Phenobarbital, increased the metabolism of thioacetamide and thioacetamide-S-oxide. Their data also suggested that thioacetamide-S-oxide is an obligatory intermediate in the conversion of thioacetamide to acetamide, polar products and microsome-bound products. Porter *et al.* (1979) studied the pharmacokinetics of thioacetamide and thioacetamide-S-oxide in the rat. They found that thioacetamide-S-oxide is a more potent hepatotoxin as compared to thioacetamide. They suggested that metabolism of thioacetamide to thioacetamide-S-oxide through the action of mixed-function oxidase and the subsequent conversion of thioacetamide-S-oxide to reactive intermediates is the basis underlying the toxicity of thioacetamide (Figure 5.1). They also postulated that the reactive intermediate can bind to either the liver macromolecules or be further metabolised to acetamide and polar products.

Hunter *et al.* (1977) examined the role of the mixed-function oxidase enzyme system in thioacetamide-induced hepatic necrosis. They found that treatment of liver with an inducer of the mixed-function oxidase enzyme, phenobarbital, potentiated the hepatic necrosis produced by both thioacetamide and thioacetamide-S-oxide. Thioacetamide-S-oxide was found to be a more potent hepatotoxin than thioacetamide. They postulated that hepatotoxicity of thioacetamide is mediated by the metabolism of thioacetamide to thioacetamide-S-oxide, which is then metabolised to an ultimate toxic metabolite. Timbrell (2000) stated that thioacetamide undergoes S-oxidation to yield thioacetamide-S-oxide.

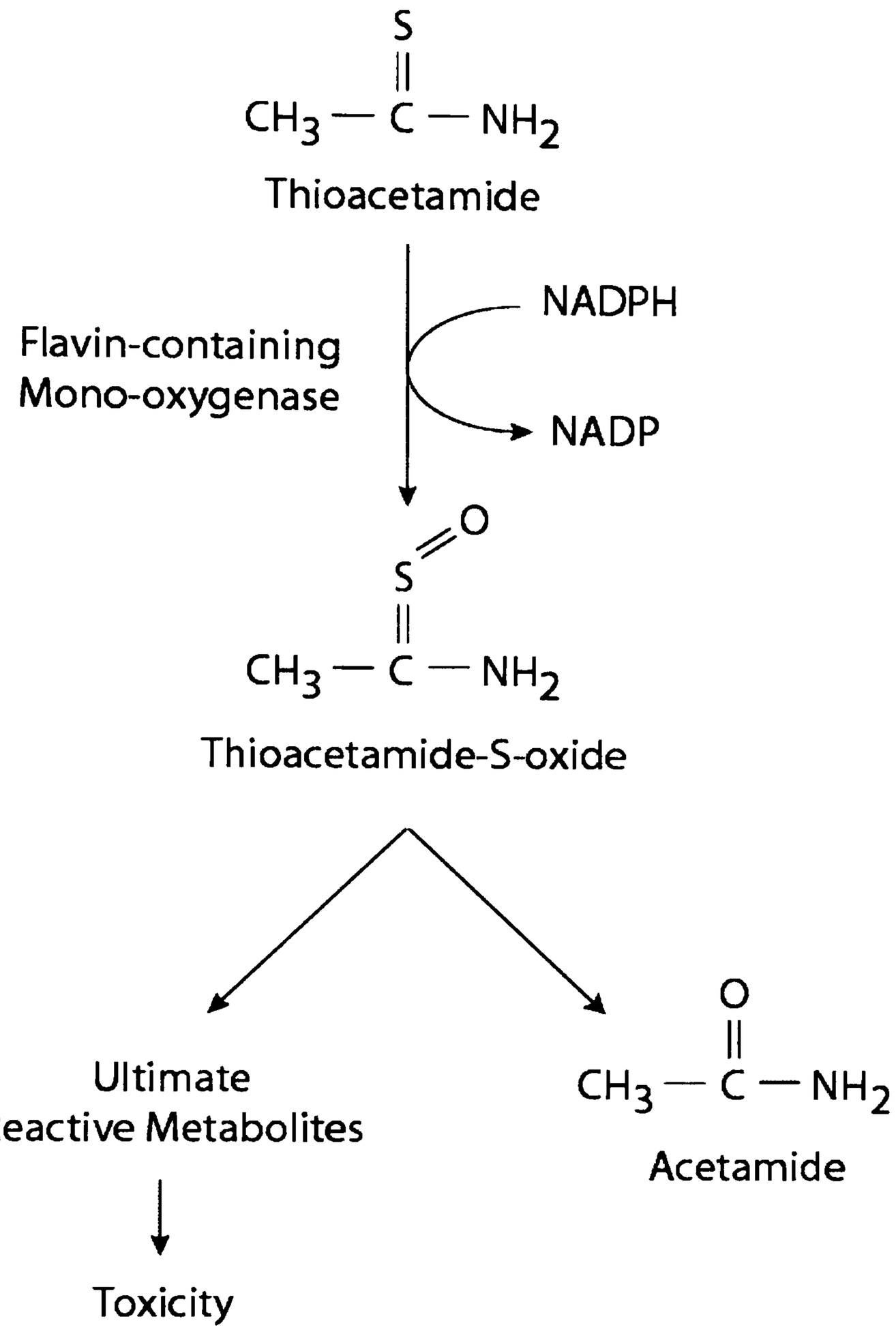

Figure 5.1 Metabolism of thioacetamide.

Dyroff and Neal (1981) examined the *in vivo* covalent binding of thioacetamide to rat liver protein and found that N-ε-acetyllysine, with the acetyl groups derived from thioacetamide, was the major modified amino acid that binds to cytosolic proteins. This led them to investigate the mechanism of thioacetamide-S-oxide metabolism in rat liver microsomes (1982). They found that apart from N-ε-acetyllysine, acetamide was another product of thioacetamide-S-oxide metabolism. They suggested that both acetamide and N-ε-acetyllysine were derived from a common intermediate during thioacetamide-S-oxide

metabolism. The predominant microsomal enzyme involved in the metabolism of thioacetamide-S-oxide is flavin-containing monooxygenase. They also found that N-ε-acetyllysine was the predominant amino acid adduct formed at pH 7.4 during the oxidation of thioacetamide-S-oxide by hydrogen peroxide in the presence of bovine serum albumin. De Ferreyra *et al.* (1980) investigated the effect of different chemicals on thioacetamide-induced liver necrosis. They found evidence suggesting that liver microsomal flavin-containing monooxygenase controls the critical activation of thioacetamide to the ultimate necrogenic agent and that cytochrome P-450 does not play a major role in this bioactivation.

Kleinfield and Haam (1959) studied the effect of thioacetamide on rat liver regeneration and found that thioacetamide induced an increase in nuclear ribonucleoproteins. A study by Steele and Busch (1966) on thioacetamide-treated rats found that thioacetamide is a hepatic carcinogen, which increases nucleolar RNA biosynthesis and blocked the formation of ribosomal RNA. The liver nuclei of the thioacetamide-treated rats were characterised and the result showed that prolonged administration of thioacetamide caused an increase in high molecular weight RNA. It also induced an increase in the biosynthesis and accumulation of guanine/cytosine-rich RNA. The results correlated with the enlargement of nucleoli, increased levels of nuclear RNA and decreased levels of cytoplasmic ribosomal RNA. Kizer *et al.* (1966) investigated the relationship between increased adenylic acid deaminase activity and changes in nuclear RNA metabolism in thioacetamide-treated rat liver. They found that thioacetamide induced an increase in AMP deaminase activity and the reaction was not affected by the simultaneous administration of actinomycin or 5-fluorouracil, both inhibitors of RNA biosynthesis. They also found that rat liver AMP deaminase was activated by ATP. Their study also revealed a thioacetamide-induced increase in both nuclei and nucleoli diameter. Fausto (1970) studied the metabolism of nuclear RNA and amine synthesis in the liver of rats administered with thioacetamide. This study found that thioacetamide induced a sharp increase in ornithine decarboxylase activity. The rise in the activity this enzyme coincides with the labelling of ribosomal RNA and is usually associated with liver regeneration. Additionally, he also found that repeated injections of

thioacetamide caused the accumulation of RNA in the nucleus and increases in spermidine and spermine levels.

Barker and Smuckler (1972) studied the effects of thioacetamide on hepatic mixed-functions oxidases and found that microsomal cytochrome b_5 decreased 16 hours after the administration of thioacetamide. In addition, cytochrome P-450 declined to 32% of control after four days. The functional state of this enzyme after thioacetamide administration was tested and it was found that the enzyme function was depressed. The activities of aryl hydrocarbon hydroxylase, N-demethylase, N-oxidase, lipid peroxidase and NADPH 2-neotetrazolium reductase were also depressed. Chakrabartty and Schneider (1978) found that thioacetamide induced an increase in liver messenger RNA as well as albumin synthesis in thioacetamide-treated rats. This is followed by another investigation by Chakrabartty *et al.* (1982) to study the basis for the increase in albumin synthesis in rat liver following thioacetamide administration. They found that thioacetamide-induced increase in translational activity of messenger RNA was responsible for the increased rate of total protein and albumin synthesis. Clawson *et al.* (1980) investigated the effects of thioacetamide on nuclear envelope nucleoside triphosphatase activity and transport of RNA from rat liver nuclei. They found that thioacetamide enhanced the transport of RNA, which was related to hydrolysis of high-energy nucleoside triphosphate esters. They postulated that an enhanced NTPase activity is an early indication of carcinogen exposure. Clawson *et al.* (1981) studied the nuclear envelope alterations accompanying thioacetamide-induced enlargement of nucleus in thioacetamide-treated rats and found that the increase in nuclear swelling coincides with alterations in sedimentation properties of isolated nuclei.

Franke *et al.* (1985) studied the effects of single dose thioacetamide (100 mg/kg) on intra- and extrahepatic VLDL output. They showed that there were functional differences between hepatocytes of the periportal and centrilobular region of the liver in terms of VLDL accumulation. Their data indicated that thioacetamide lowers the hepatic VLDL-triglycerides output by 50% in comparison to controls. However, the unchanged level of serum triglycerides after dosing with thioacetamide indicated that clearance of triglycerides from serum is diminished to the same extent as the hepatic output. They postulated that

thioacetamide inhibited the intracellular formation of VLDL. Cascales *et al.* (1986) reported that short-term administration of thioacetamide caused an increase in accumulation of triacylglycerols in the rat liver. They postulated that this could be due to a combination of increased synthesis due to fatty acid mobilization and a decrease in the secretion of VLDL. They also found that thioacetamide caused an increase in ornithine decarboxylase activity and a decrease in tyrosine aminotransferase activity. Increased ornithine decarboxylase activity is associated with the stimulation of cell growth and tumour formation. Nozu *et al.* (1992) studied the effects of thioacetamide on hepatic mitochondrial fatty acid metabolism. Their results indicated an increased diversion of cytosolic long chain acyl-coenzyme A into the mitochondria for β-oxidation rather than their esterification and use in lipogenesis. This is a reflection of the whole-body catabolic state in response to toxic insult for maintaining energy homeostasis. Shukla *et al.* (1992) demonstrated that thioacetamide (100 and 200 mg/kg) reduced the volume of bile secreted by rats accompanied by reductions in the secretion of bile acids and bile salts.

Mesa *et al.* (1996) investigated the protective role of S-adenosyl-L-methionine against changes in the rat liver gene expression induced by thioacetamide. Their result indicated that thioacetamide induced changes in the expression of genes related to β-actin and albumin. The introduction of S-adenosyl-L-methionine to the rats prevented the thioacetamide-induced changes. They proposed a glutathione-dependent mechanism for S-adenosyl-L-methionine protection against thioacetamide hepatotoxicity in the rat. The role of glutathione in protecting against thioacetamide appears to be in combating oxidative stress and mechanisms by which it destroys free radicals and peroxides are well known, rather than in conjugation. Bruck *et al.* (1999) reported that hydroxyl radical scavengers i.e. dimethylsulphoxide and dimethyurea protected rats against thioacetamide-induced liver injury. Spira and Raw (2000) investigated the effect of thioacetamide on the expression and activity of glutathione-S-transferase (GST). They proposed that the covalent binding of thioacetamide or its derivatives to the GST subunits does not affect the activity of the enzyme. However, the inhibition of GST activity is due to the deleterious effect of thioacetamide on GST transcription. Sun *et al.* (2000) evaluated the thioacetamide-induced oxidative stress on the levels of antioxidant in the rats. They found that thioacetamide (500

mg/kg) increased the activity of caspase-3-like protease, an enzyme involve in the activation of apoptosis. Their data also showed an increase in the level of liver lipid hydroperoxides and decreases in the levels of vitamin C and vitamin E. They proposed that decrease of antioxidants and formation of lipid hydroperoxides after thioacetamide administration support the view that extensive radical reactions accur in the liver during the necrotic process.

5.1.1 Study Details

Study number 99057 carried out at Pfizer, Centre de Recherche, Amboise, France.

Study Number	Compound	Study Group	Dose of toxin administered (mg/kg)	Animal Number	Euthanased	
					Day 2	Day 8
99057	Saline	Control	0	1-10	6-10	1-5
	Thioacetamide in saline	Low Dose	50	301-310	306-310	301-305
		High Dose	200	401-410	406-410	401-405

5.2 Results

5.2.1 Histopathology Results

The histopathological observations for thioacetamide-dosed rats are summarised below in Table 5.1.

Table 5.1 Summary of the histopathological changes observed in thioacetamide-dosed Sprague-Dawley rats.

	Day	
Dose of thioacetamide	**2**	**8**
50 mg/kg	Mild hepatocellular centrilobular necrosis was observed in all animals.	No significant differences from controls.
200 mg/kg	Moderate hepatocellular centrilobular necrosis was observed in all animals.	No significant differences from controls.

5.2.2 Clinical Chemistry Results

Clear signs of toxicity were observed in both the low dose and high dose Day 2 animals. The clinical chemistry data indicates minimal changes in the Day 8 animals. Details of the clinical chemistry findings are summarised in Table 5.2.

Table 5.2 Summary of the plasma changes observed by clinical chemistry in thioacetamide-dosed Sprague-Dawley rats.

	Day	
Dose of thioacetamide	**2**	**8**
50 mg/kg	Glucose: ↓ (***) Cholesterol: ↓ (*) Bilirubin: ↑ (***) ASAT: ↑ (***) ALAT: ↑ (***) 5NT: ↑ (**) GGT: ↑ (**) Bile Acids: ↑ (***)	No group differences were found.
200 mg/kg	Variable liver necrosis and cholestatic damage: Glucose: ↓ (**) Cholesterol: ↓ (*) Triglycerides: ↓ (**) Albumin/Globulin: ↑ (*) Bilirubin: ↑ (***) ASAT: ↑ (***) ALAT: ↑ (***) 5NT: ↑↑ (***) GGT: ↑ (**) Bile acids: ↑↑ (***)	No group differences were found except for slightly elevated bile acids (2 fold).

5.2.2.1. Principal Component Analysis of Clinical Chemistry Data

PCA scores and loadings plots for the first two components of the control/thioacetamide Day 2 UV-scaled clinical chemistry data are shown in Figure 5.2. In the scores plot, the data points are colour-coded and labelled so as to identify the treatment (e.g. **black** for control, **mauve** for low dose and **green** for high dose) and animal number.

The scores plot of the control/low dose thioacetamide data (Figure 5.2A) indicates clear separation between the dosed and control groups along the first principal component. The corresponding loadings plot (Figure 5.2B) along the first principal component showed decreases in glucose, urea and cholesterol, and increases in bilirubin, bile acids, 5' nucleotidase, γ-glutamyl transferase, ALAT and ASAT as the major contributors to the separation between the low dose animals and the control animals.

Figure 5.2C shows clear separation between the high dose group and controls along the first principal component. The changes observed were almost identical with the changes observed in the low dose animals. One of the main features observed in the corresponding loadings plot (Figure 5.2D) along the first principal component are the generalised increase in both aminotransferases, ALAT and ASAT, which is indicative of hepatocellular damage in the high dose animals. The loadings plot also showed increases in 5' nucleotidase, γ-glutamyl transferase and bile acids, which are markers of hepatobiliary damage (Handler *et al.* 1994). In addition, the loadings plot also indicates decreases in triglycerides, cholesterol and glucose levels as contributors to the separation between the high dose animals and the control animals. The decrease in plasma triglycerides level in the high dose animals is in contrast to the low dose animals which showed no change in plasma triglycerides level.

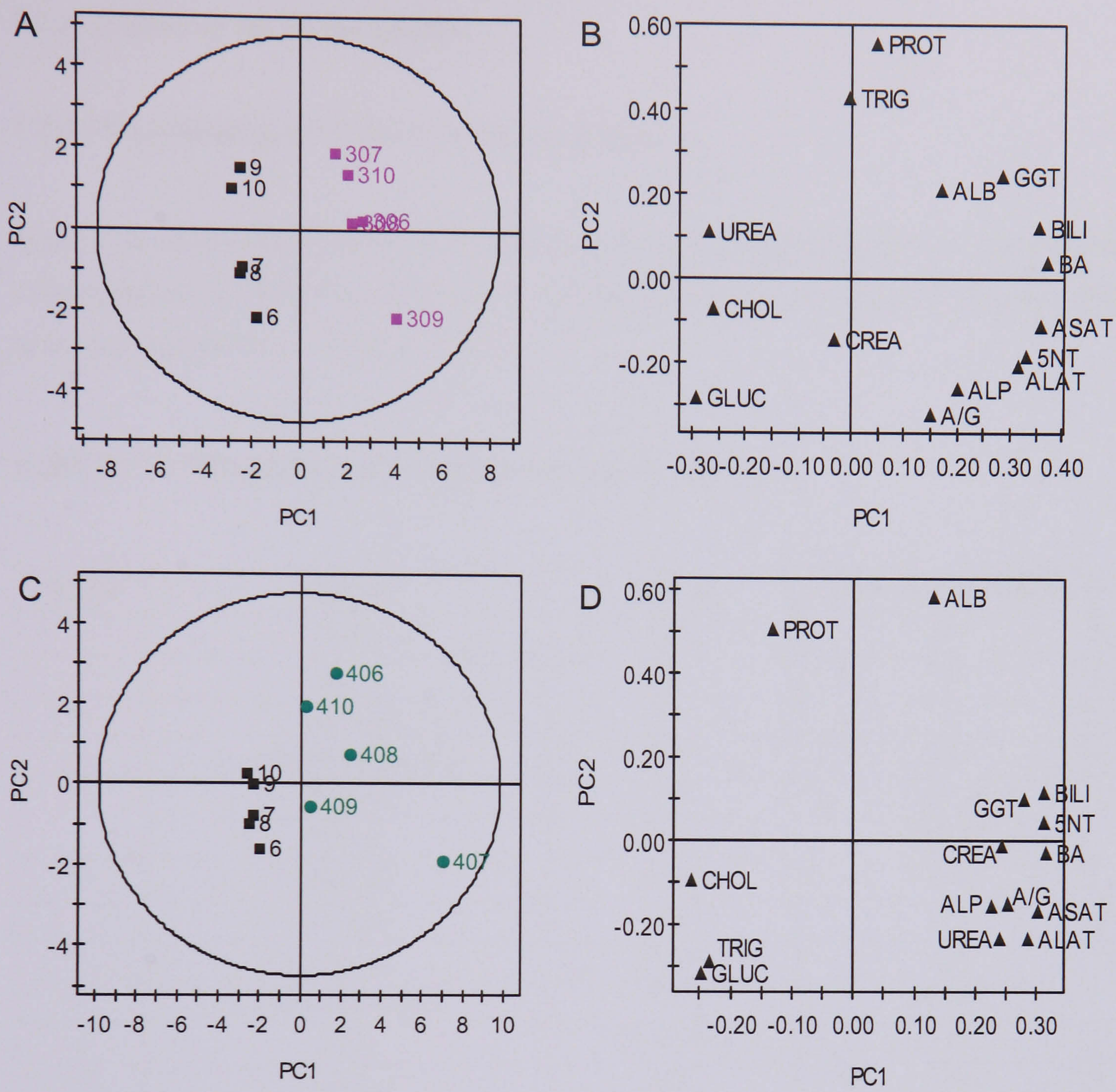

Figure 5.2 (A) PCA scores plot of low dose thioacetamide Day 2 clinical chemistry data, and (B) corresponding loadings plot. (C) PCA scores plot of high dose thioacetamide Day 2 clinical chemistry data, and (D) corresponding loadings plot.

5.2.3 Analysis of the Tissue Spectra

5.2.3.1 Examination of ^{1}H MAS NMR tissue spectra

Figure 5.3 shows the dose-dependent effects of thioacetamide hepatotoxicity as visualised using standard 1D ^{1}H MAS NMR spectra of intact Day 2 rat liver. The corresponding NMR spectral assignments are listed in Table 5.3.

Table 5.3 ^{1}H NMR resonance assignments for liver tissue.

Peak No.	Molecule	Assignment	1H chemical shift (ppm)
1	Valine	**CH_3**	1.04
2	Lactate	**CH_3**	1.33
3	Glutamate	**CH**	2.15
4	Choline/phosphocholine	$N^+(CH_3)_3$	3.22
5	TMAO	**CH_3**	3.24-3.27
	Taurine	**$CH_2SO_3^-$**	3.24-3.27
6	β-Glucose	**C_1H**	4.64
	Glycogen	**CH**	4.65
7	α-Glucose	**C_1H**	5.23
8	Leucine/Isoleucine	**CH_3**	0.93-0.95
9	Lipids	CH_3-(**CH_2**)n	1.29
10	Alanine	**CH_3**	1.48
11	Lipids	CH=CH-**CH_2**-CH_2	2.07
12	Glutamine	**CH_2**	2.39
13	Glucose/glycogen/α-H amino acids	**Ring protons/α-CH**	3.35-4.00
14	Glycogen	**CH**	5.38-5.45
15	Lipids	**CH_3**-(CH_2)n	0.90
16	3-D-hydroxybutyrate	**CH_3**	1.20
17	Lipids	CO-CH_2-**CH_2**	1.61
18	Acetate	**CH_3**	1.95
19	Lipids	CO-**CH_2**-CH_2	2.25
20	Lipids	=CH-**CH_2**-CH=	2.78
21	Lactate	**CH**	4.13
22	Lipids	**-CH=CH-**	5.30-5.35

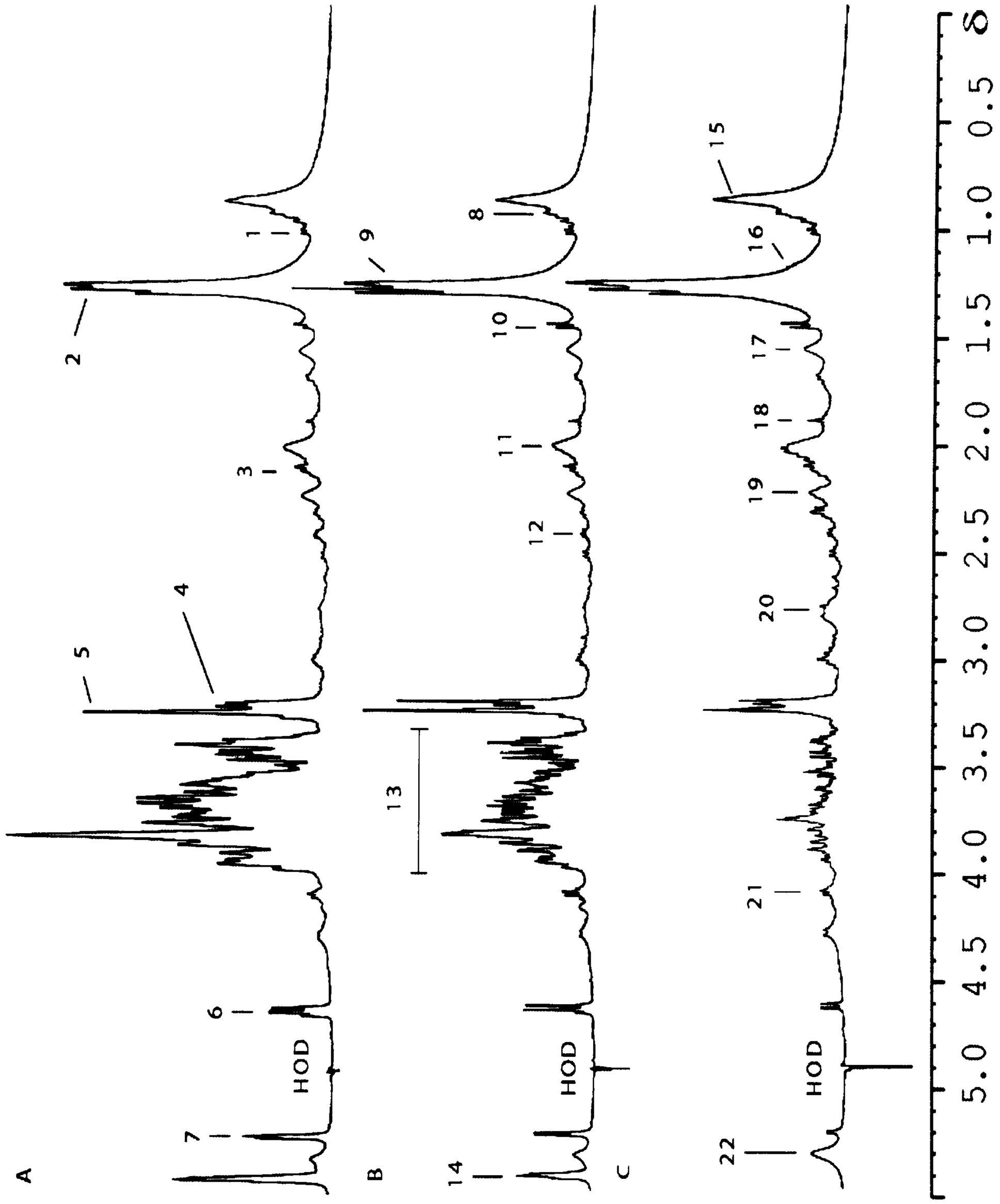

Figure 5.3 Dose-dependent effects of thioacetamide hepatotoxicity as visualised using standard 1D ^{1}H MAS NMR spectroscopy of intact Day 2 rat liver. A. Control liver. Liver from an animal administered: (B) Low-dose thioacetamide and (C) High-dose thioacetamide.

Visual inspection of the standard 1D NMR spectra of the Day 2 tissue samples showed that control animal 9 had a higher lipids content that the others. Administration of the low dose of thioacetamide appears to induce some dose related differences between the low dose animals and the control animals (Figure 5.3B). The changes are generally mild with some increases in lipids and choline, and decreases in glycogen and glucose levels. However, the administration of the high dose of thioacetamide resulted in clear effects on the rat liver (Figure 5.3C). The effects are severe with clear decreases in liver glucose and glycogen levels. Also noticeable is an increase in the levels of liver lipids, particularly at δ 0.90 ($(CH_2)_n$-**CH_3**), δ 1.29 ($(\mathbf{CH_2})_n$), δ 1.61 (**CH_2**-CH_2-CO), δ 2.07 (CH_2-**CH_2**-CH=CH), δ 2.25 (CH2-**CH_2**-CO), δ 2.78 (=CH-**CH_2**-CH=) and δ 5.30 (-**CH=CH**-) moeties as compared to the control animals. Additionally, a clear decrease in the TMAO level is also observed in the high dose animals. Only the Day 2 liver samples were analysed for this study. Details of the MAS NMR observations for thioacetamide-dosed rats are summarised below in Table 5.4 and the changes reported were quantified according to the method described in Chapter 2.

Table 5.4 Summary of the liver tissue changes observed by MAS NMR in thioacetamide-dosed Sprague-Dawley rats.

Dose of thioacetamide	Day
	2
Low dose (50 mg/kg)	Relative to controls, the changes observed in the low dose spectra were generally mild. Lipids: ↑* Choline: ↑* Glucose: ↓ (NS) Glycogen: ↓ (NS)
High dose (200 mg/kg)	Lipids: ↑* Animals 409 & 410 showed the smallest overall changes, animal 406 showed an intermediate change, and animals 407 & 408 showed the biggest change in terms of the lipid changes. Choline: ↑* TMAO: ↓* Glucose: ↓* Glycogen: ↓*

5.2.3.2 Principal Component Analysis of Day 2 Liver NMR Data

Principal component analysis of the control/low dose Day 2 data set revealed some dose-related structure to the variation in the data. Some separation between the low dose animals and control animals can be observed in the scores plot on the first principal component (Figure 5.4A). In addition, control animal 9 shows an aberrant position and is situated away from the rest of the controls along the first principal component. The second principal component, however, described very little variation in the data set that was related to the treatment of the animals with thioacetamide. The corresponding loadings plot (Figure 5.4B) identifies the NMR spectral regions that are responsible for separation seen in the scores plot in Figure 5.4A. Increases in the regions attributed to lipids, and decrease in the region attributed to liver glucose were identified as the major contributors for the separation between the dosed and control animals. Additionally, the loadings plot also revealed higher lipids content in control animal 9, which contributed to its separation from the rest of the controls.

Figure 5.4C is a scores plot for the first two components of the control/high dose Day 2 data set. There is very clear treatment-related variation in the data set, which is described mainly by the first principal component. The separation occurred in opposite direction as compared to the control/low dose scores plot due to scaling effect. The corresponding loadings plot (Figure 3.5D) indicates increases in the regions attributed to lipids and choline, and decreases in the regions attributed to glucose, glycogen and TMAO as the major contributors for the separation between the high dose animals and control animals along the first principal component.

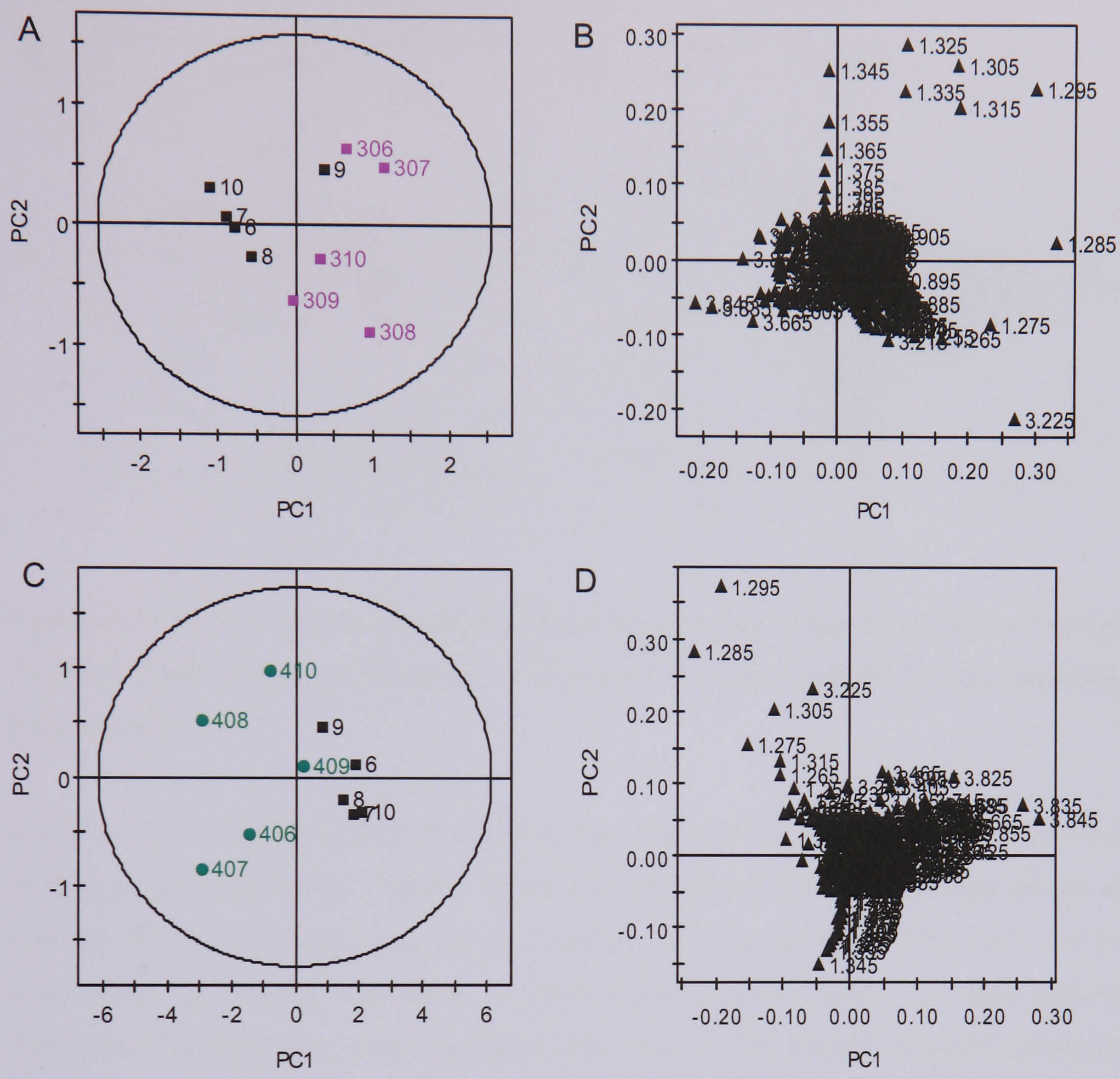

Figure 5.4 (A) PCA scores plot of the ^{1}H MAS NMR spectra of thioacetamide-dosed liver samples from Day 2 low-dose versus control groups, and (B) the corresponding loadings plot. (C) PCA scores plot of the ^{1}H MAS NMR spectra of thioacetamide-dosed liver samples from Day 2 high-dose versus control groups and (D) the corresponding loadings plot.

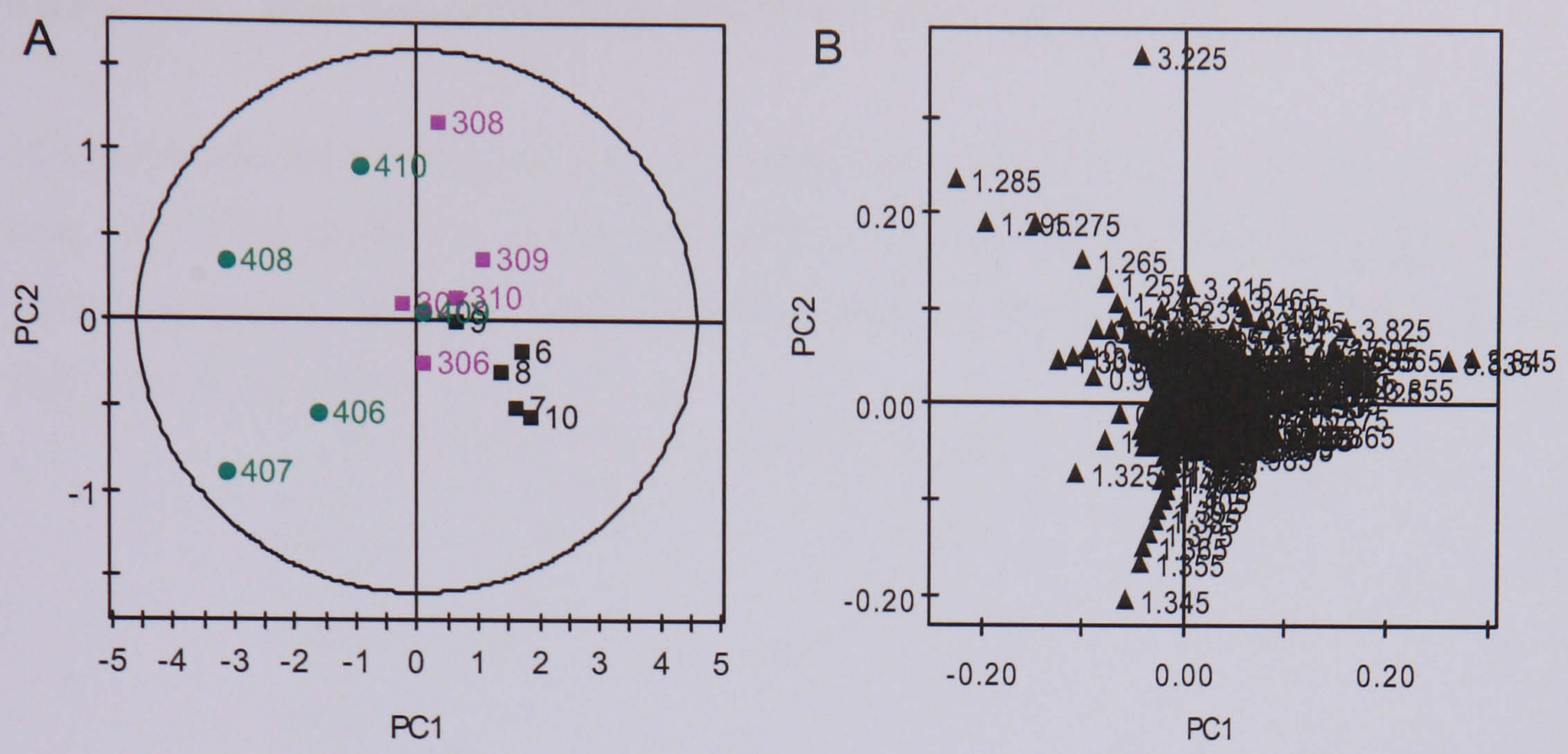

Figure 5.5 (A) PCA scores plot for the first two principal components of the standard ^{1}H MAS NMR spectra of the Day 2 thioacetamide study, and (B) the corresponding loadings plot.

A scores plot of the first and second components from a PCA of all the Day 2 liver MAS NMR spectra for this study (Figure 5.5A) showed separation between the dosed groups and controls. The first principal component describes the dose-dependent effect with the low dose group of animals appearing at intermediate position along the first principal component between the control and high dose groups. The second principal component decribes the variation within the dosed animals. The corresponding loadings plot (Figure 5.5B) shows that thioacetamide-induced increases in lipids and choline and decreases in glucose and glycogen are the major contributors to the separation along the first principal component, whereas thioacetamide-induced increase in choline and some increase in lipids are the major contributors to the variation along the second principal component.

5.2.3.3 PLS – Discriminant Analysis (PLS-DA) of Day 2 Liver NMR Data

In order to maximise the separation between the dose classes based on the liver MAS NMR data, a PLS-DA model was constructed, where the samples were classified assigned to one of three mutually orthogonal classes with **control** being class 1, **low dose** being class 2 and **high dose** being class 3.

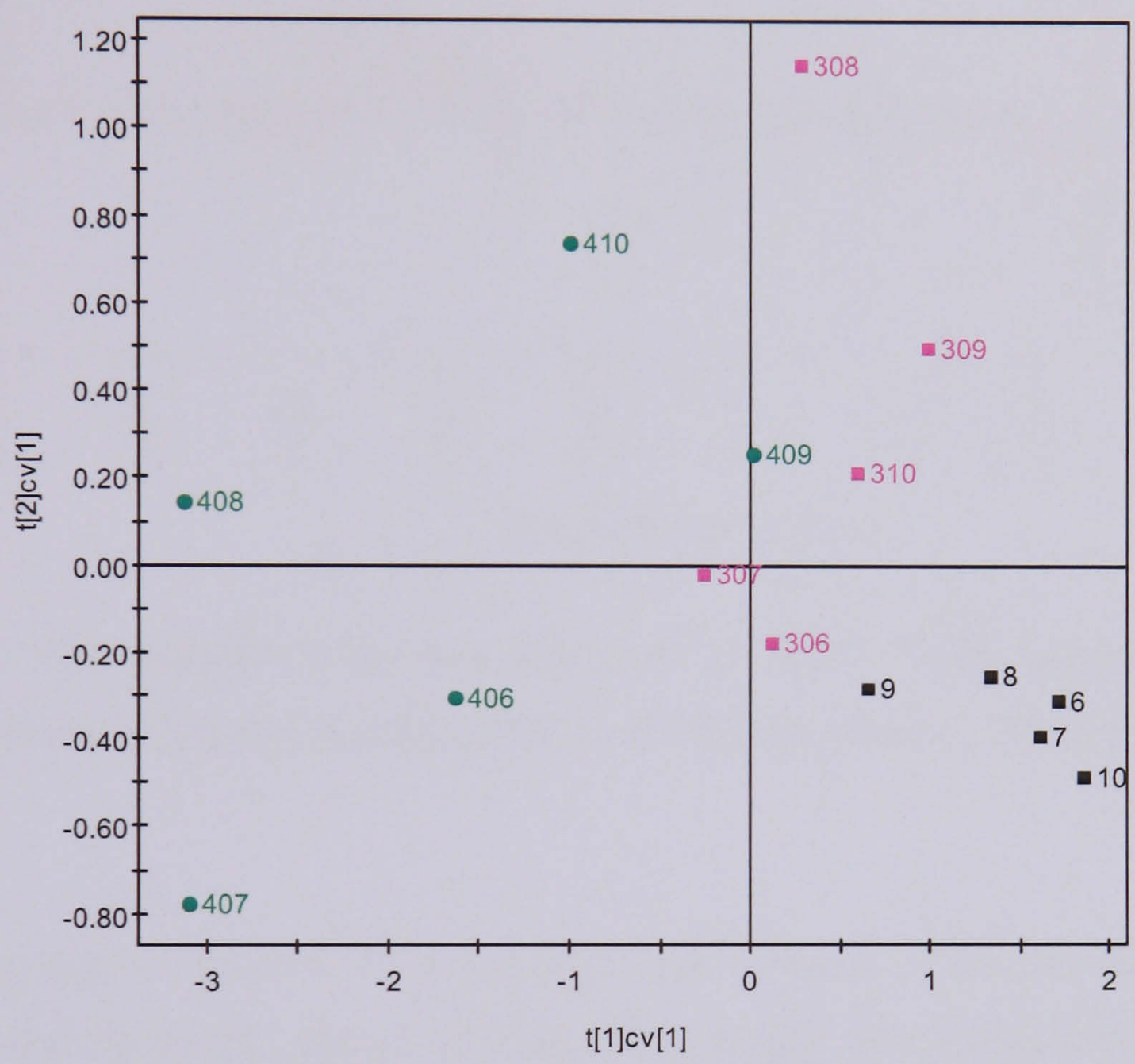

Figure 5.6 PLS-DA cross validated scores plot of the standard ^{1}H MAS NMR spectra of the Day 2 thioacetamide study.

The resultant PLS-DA X-matrix cross validated scores plot of the first two components (Figure 5.6) shows distinct segregation of the three sample classes. The cluster of control is located on the lower right quadrant of the scores plot. In addition, control animal 9 is somewhat separated from the cluster of control animals. The low dose animals are separated from the control animals along the second PLS component, whereas the high dose animals are separated from the control animals along the first PLS component. The plots indicated variable effects in the high dose animals which agrees with visual inspection of the liver NMR spectra.

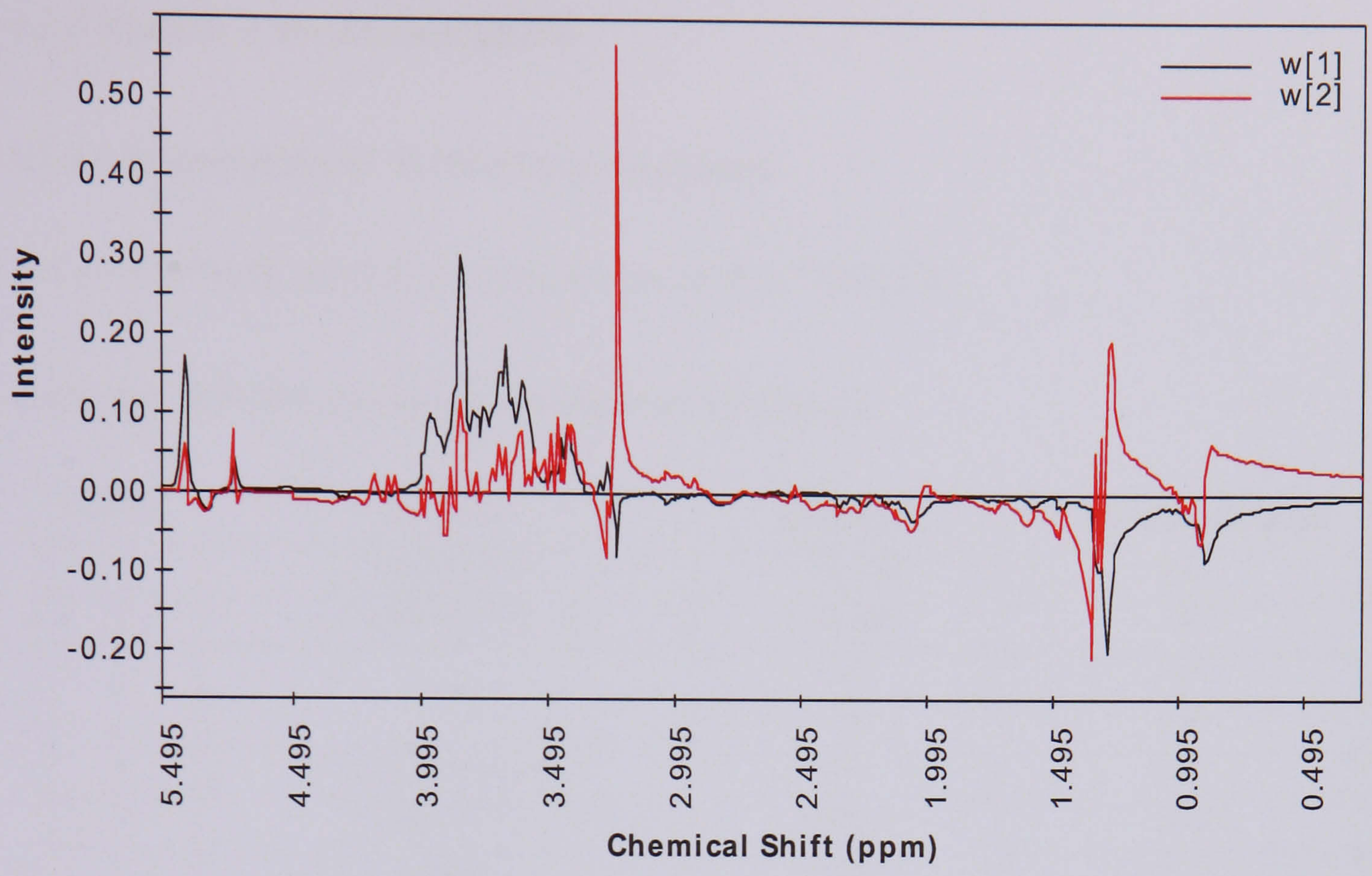

Figure 5.7 PLS weights from the standard ^{1}H MAS NMR spectra of the Day 2 thioacetamide study tissue samples (W[1] = PLS component 1, W[2] = PLS component 2).

The corresponding X-block PLS loadings plot (Figure 5.7) indicates that the first component describing the general variation between high dose and control animals is due to elevated and altered liver lipids profiles, some increase in liver choline and decreases in liver glucose, glycogen and TMAO levels. The second component, describing the variation between low dose and control animals, is due to elevated liver choline level as well as some increase in the liver lipids profiles. The observations made from both PLS-DA scores and loadings plots confirmed the findings made by inspection of the ^{1}H MAS NMR spectra (Table 5.4) and from the PCA analyses of the Day 2 tissue NMR data (Figure 5.4).

5.2.4 Analysis of the Plasma Spectra

5.2.4.1 Examination of ^{1}H NMR plasma spectra

The plasma NMR spectral assignments are listed in Table 5.5.

Table 5.5 ^{1}H NMR resonance assignments for plasma.

Peak No.	Molecule	Assignment	^{1}H chemical shift (ppm)
1	Lipids (LDL)	$-CH_2-\mathbf{CH_3}$	0.84
2	Lipids (VLDL)	$CH_2-\mathbf{CH_3}$	0.87
3	Valine	$\mathbf{CH_3}$	0.97
		$\mathbf{CH_3}$	1.02
4	3-D-hydroxybutyrate	$\mathbf{CH_3}$	1.20
5	Lipids (VLDL)	$-(\mathbf{CH_2})n$	1.29
6	Lactate	$\mathbf{CH_3}$	1.33
7	Alanine	$\mathbf{CH_3}$	1.46
8	Acetate	$\mathbf{CH_3}$	1.91
9	Acetoacetate	$\mathbf{CH_3}$	2.22
10	Glutamine	$\mathbf{CH_2}$	2.41
11	Citrate	$\mathbf{CH_2}$	2.52
		$\mathbf{CH_2}$	2.69
12	Choline	$N^{+}(\mathbf{CH_3})_3$	3.21
13	Glucose/Amino acids resonances	**Ring protons/α-CH**	3.35-4.00
14	Lactate	**CH**	4.10
15	α-Glucose	$\mathbf{C_1H}$	5.23
16	Isoleucine	$\mathbf{CH_3}$	0.93
17	Leucine	$\mathbf{CH_3}$	0.95
18	Isoleucine	$\mathbf{CH_3}$	1.00
19	Threonine	$\mathbf{CH_3}$	1.31
20	N-acetyl glycoproteins	NHCO $\mathbf{CH_3}$	2.04
21	Pyruvate	$\mathbf{CH_2}$	2.36
22	Creatine	$\mathbf{CH_3}$	3.04
23	TMAO	$\mathbf{CH_3}$	3.26
24	Creatine	$\mathbf{CH_3}$	3.93
25	Lipids	**-CH=CH-**	5.30

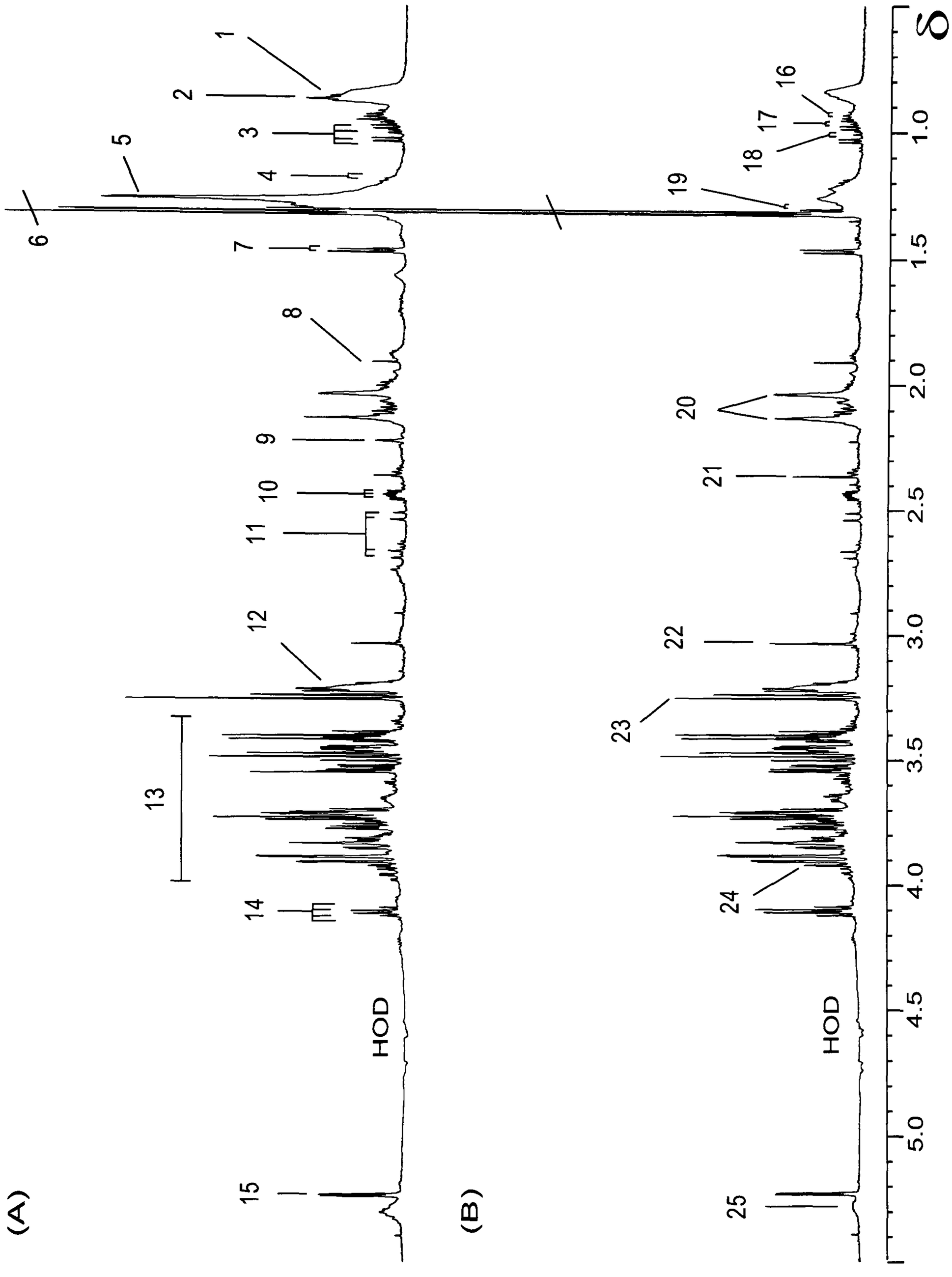

Figure 5.8 Effects of thioacetamide (200 mg/kg) as visualised using CPMG spin-echo ^{1}H NMR spectra of Day 2 rat plasma. A. Control plasma. B. High-dose thioacetamide.

Inspection of the plasma CPMG spin echo spectra of the thioacetamide-dosed Day 2 plasma samples revealed little effects on the low dose animals as compared to the control animals. Figure 5.8 shows the dose-dependent effects of high dose thioacetamide heptatotoxicity as visualized using CPMG spin echo spectra of Day 2 plasma samples and the corresponding NMR spectral assignments are listed in Table 5.5. The main visual changes that can be observed in the high dose animals is a clear decrease in lipids especially the CH_2 (VLDL) and CH_3 (VLDL/LDL) moieties. The changes in the plasma lipids profiles correlated well with the changes observed in the liver lipids profiles (Table 5.4). In addition, detailed spectral inspection reveals more subtle biochemical variation between the spectral profiles of the high dose animals and control animals represented by increases in creatine, pyruvate and acetate. Details of the plasma NMR observations for thioacetamide-dosed rats are summarised below in Table 5.6 and the changes reported being quantified according to the method described in Chapter 2.

Table 5.6 Summary of the plasma changes observed by NMR in thioacetamide-dosed rats.

Dose of thioacetamide	Day
	2
50 mg/kg	The changes observed were generally mild relative to controls: Creatine: ↑ (NS). Lipids: 24.6% ↓ (NS). Acetate: ↑ (NS). Pyruvate: ↑ (NS).
200 mg/kg	Clear changes were observed relative to controls Creatine: ↑ (NS). Lipids: 53.4 % ↓ **. (Animals 407 & 408 marked, animal 406 intermediate, animals 409 & 410 minimal) Clear changes in lipoproteins (NS) (Clearest change: animals 406 & 408, clear change: animals 407 & 409, least clear change: 410) Acetate: ↑ (NS). Pyruvate: ↑ (NS) (Animals 407 & 408 marked, animals 406 & 410 moderate, animal 409 mild).

5.2.4.2 Principal Component Analysis of Day 2 Plasma NMR Data

Figure 5.9 shows the scores and loadings plots of the first two principal components of the PCA model based on the spectral intensities in the CPMG NMR spectra between the drug-treated animals and the controls. The PCA scores plot of the low dose Day 2 plasma data set (Figure 5.9A) revealed no dose related variation between the low dose animals and the control animals.

The PCA scores plot of the control/high dose data set (Figure 5.9C) indicates clear differences in the metabolic profiles of thioacetamide-treated and control animals. The first principal component describes the variation between the two groups of animals. The corresponding loadings plot (Figure 5.9D) reveals that changes in the lipid moieties (VLDL, CH_2 and LDL, CH_3) are the major contributors to the separation between the high dose animals and control animals along the first principal component. In addition, the loadings plot also reveals variation in plasma lactate that leads to the variation within the high dose animals along the second principal component.

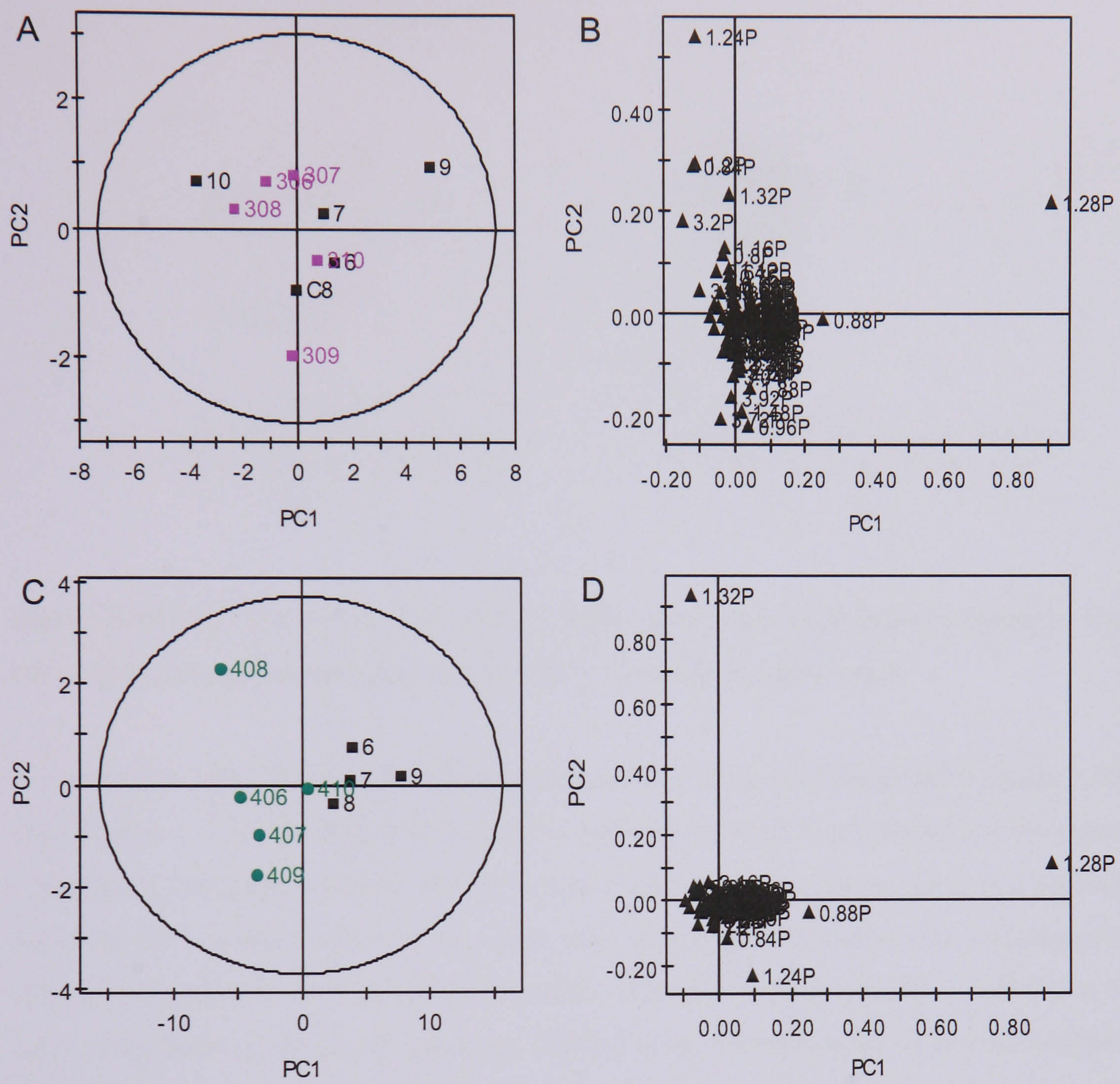

Figure 5.9 (A) PCA scores plot of the CPMG spin-echo NMR plasma spectra of thioacetamide-dosed plasma samples from Day 2 low-dose versus control groups, and (B) the corresponding loadings plot. (C) PCA scores plot of the ^{1}H CPMG spectra of thioacetamide-dosed plasma samples from Day 2 high-dose versus control groups and (D) the corresponding loadings plot.

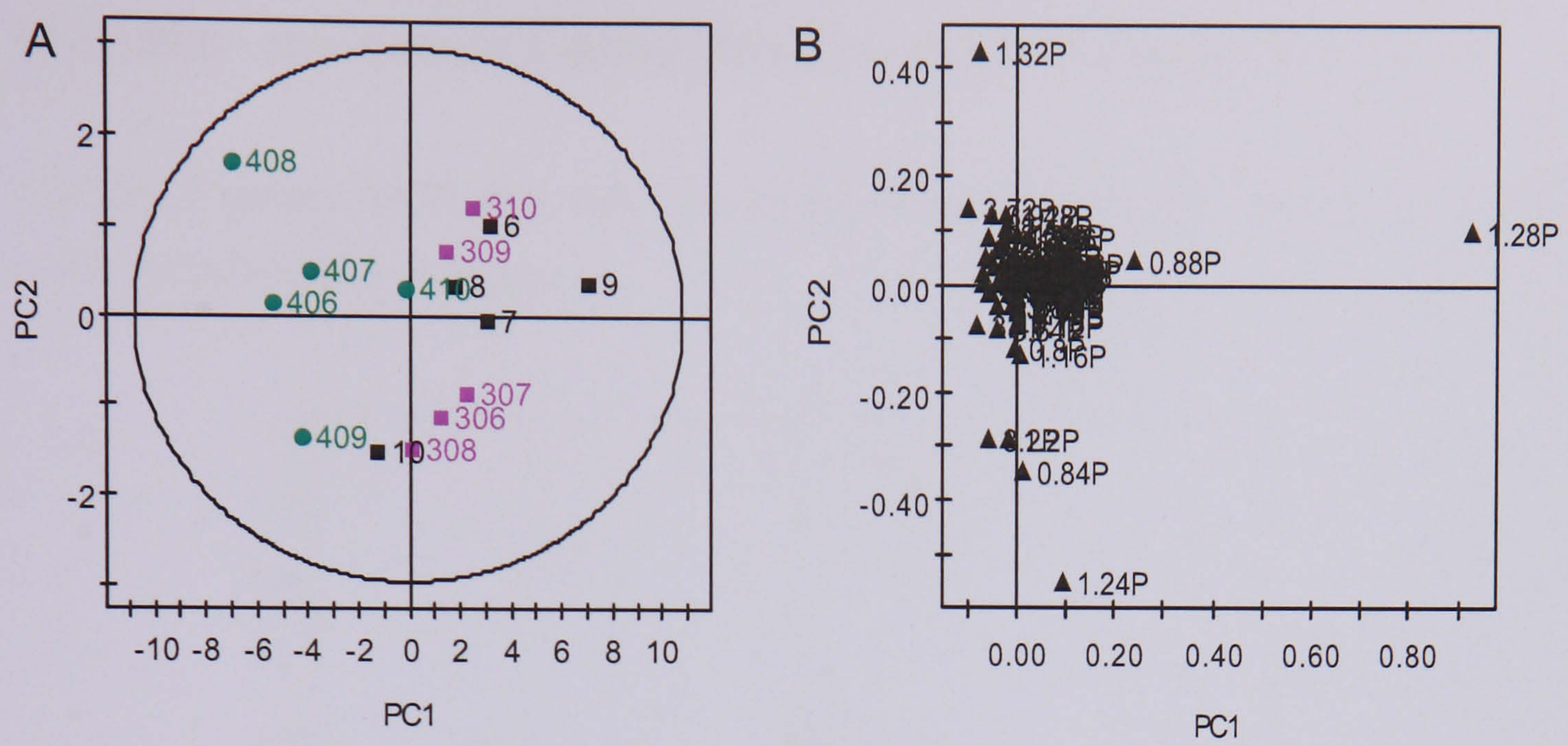

Figure 5.10 (A) PCA scores plot of the CPMG spin-echo NMR plasma spectra of the Day 2 thioacetamide study, and (B) the corresponding loadings plot.

A scores plot of the first two components from a PCA of the combined Day 2 plasma NMR data (Figure 5.10A) showed clear separation between the high dose animals and the control animals but little separation between the control and low dose groups. The first component describes the variation between the high dose and control animals. The corresponding loadings plot (Figure 5.10B) shows that a thioacetamide-induced decrease in lipids is the major contributor to the separation along the first principal component, whereas changes in lactate, choline, 3-D hydroxybutyrate and LDL are contributors to the variation within the dosed groups.

5.2.4.3 PLS – Discriminant Analysis (PLS-DA) of Day 2 Plasma NMR Data

The Day 2 plasma NMR data were also analysed using the PLS-DA approach to further refine the information recovery.

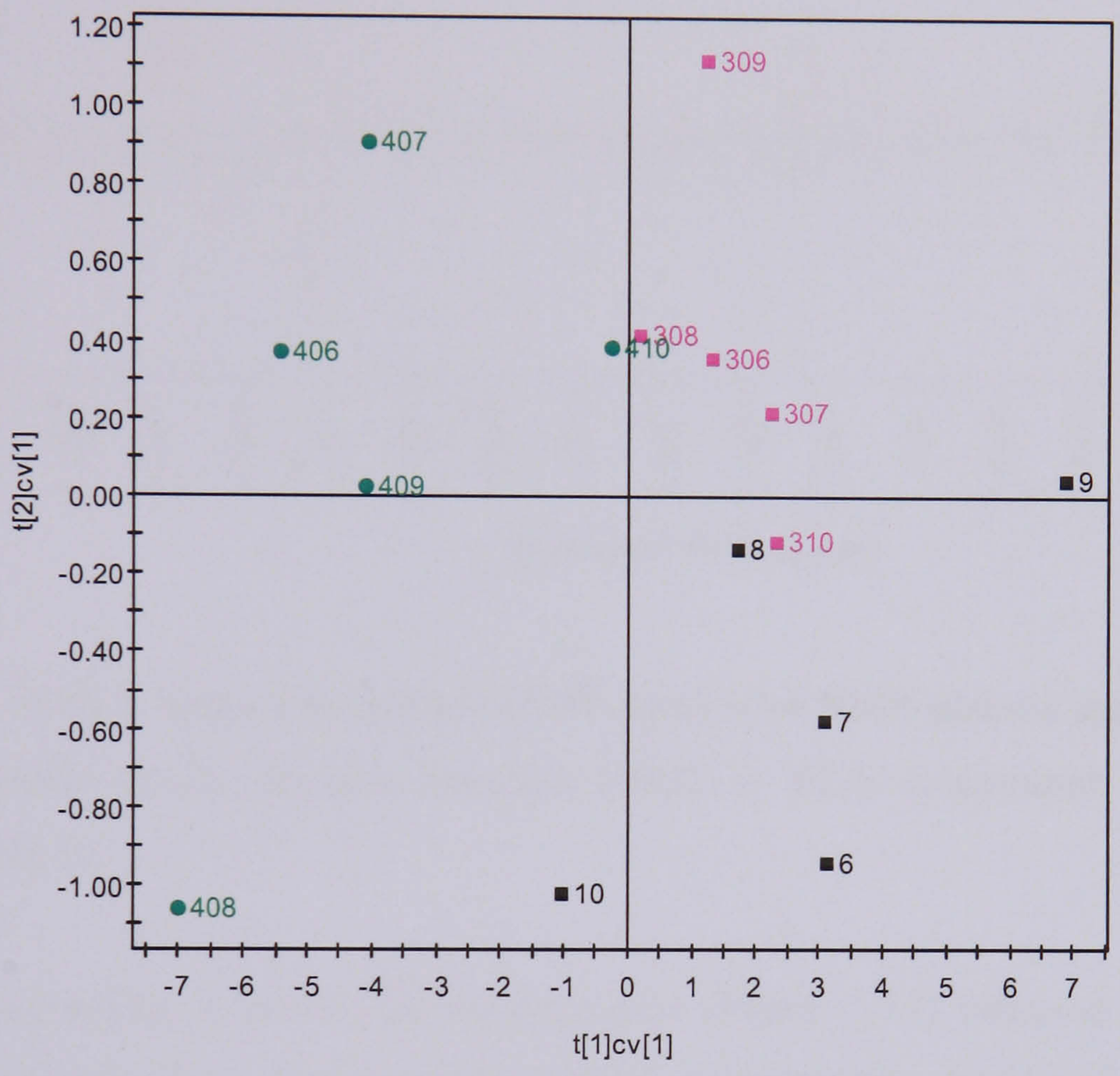

Figure 5.11 PLS-DA cross validated scores plot of the CPMG spin-echo NMR plasma spectra of the Day 2 thioacetamide study plasma samples.

The X matrix PLS-DA cross validated scores plot of the first two components (Figure 5.11) shows separation between the dosed groups and control group. The PLS-DA has now forced some separation between the control and low dose groups. The control group is situated on the lower right quadrant, with the low dose group (upper right quadrant) partially separated from the control group along PLS component two. The high dose group is (to the left of the plot) separated from the control group along PLS component one.

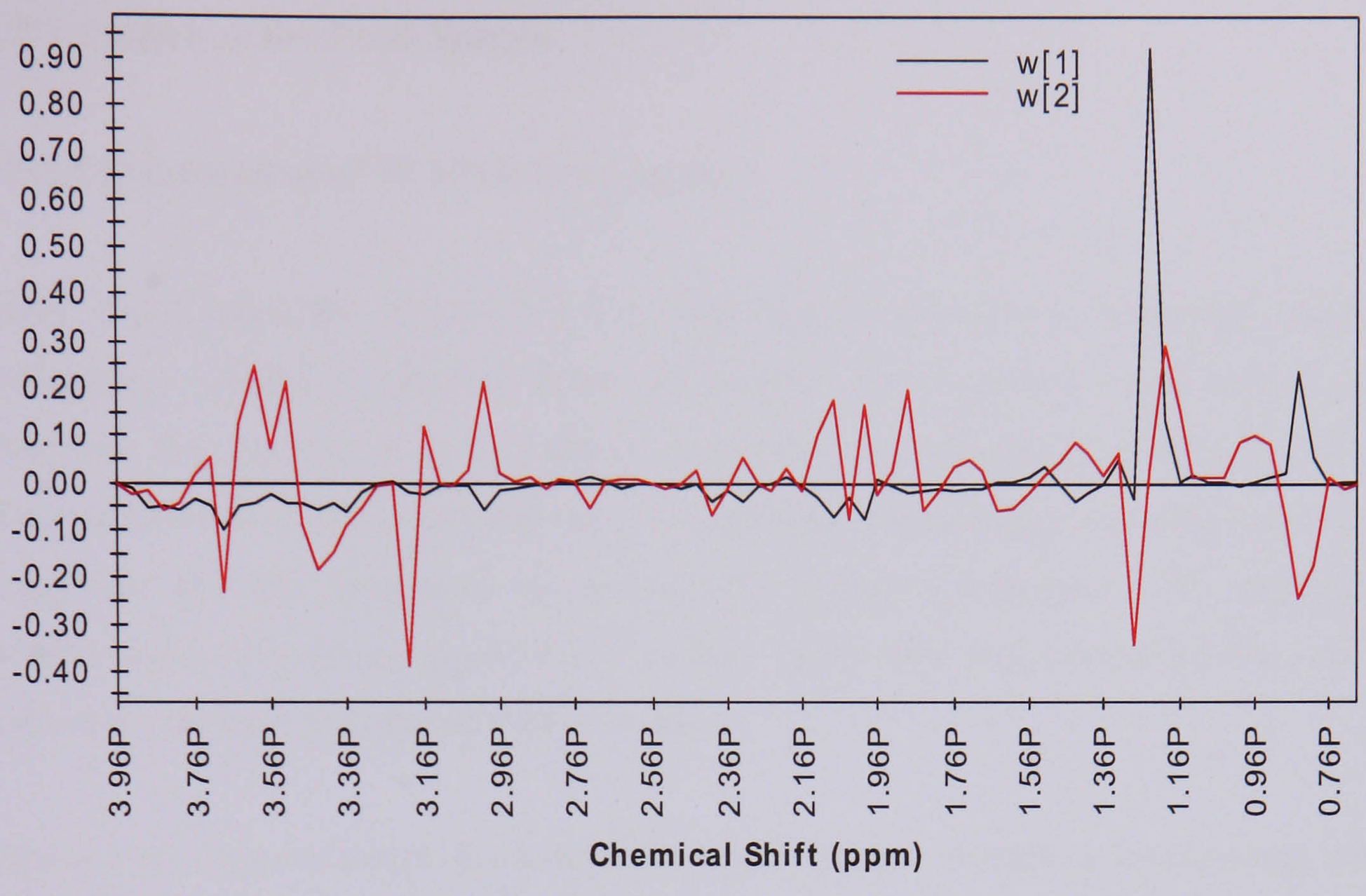

Figure 5.12 PLS weights from the CPMG spin-echo NMR plasma spectra of the Day 2 thioacetamide study plasma samples (W[1] = PLS component 1, W[2] = PLS component 2).

The corresponding X block PLS loadings plot (Figure 5.12) indicates that the first PLS component, describing the general variation between high dose and control/low dose animals, is due to a decrease in plasma lipids. The second PLS component, describing the variation between low dose and control animals, is due to changes in the plasma choline level as well as some decrease in the plasma lipids.

5.2.5 Analysis of the Urine Spectra

5.2.5.1 Examination of ^{1}H NMR urine spectra

Initial visual inspection of the low dose urine spectra showed no substantial changes in endogenous urinary metabolites (data not shown) as compared to the control group. However, the presence of thioacetamide metabolites was detected in Day 1 (0-7 h post-dose) urine samples from both the low dose and high dose animals. The effects of the high dose thioacetamide treatments on endogenous urinary metabolites were assessed, as follows, using only the group euthanased at Day 8 post-dose, which provided a sequence of daily urine samples covering the whole study.

Figure 5.13 shows a series of standard ^{1}H NMR spectra of urine at predose and various time points following the administration of high dose thioacetamide. The high dose of thioacetamide induced marked changes in the endogenous urinary metabolite profiles. The dominant changes included increases in creatine, taurine and guanidinoacetic acid, and decreases in citrate, 2-oxoglutarate, TMAO and hippurate, which lasted up to Day 3 with maximal abnormality being observed in the samples obtained from Day 2 post-dose samples. In addition, the presence of glucose, lactate and alanine in the urine samples of animals 402, 403 and 404 was detected on Day 2 and Day 3, possibly indicating renal dysfunction. The ^{1}H NMR spectra indicated recovery to normality by Day 7 post-dosing. Details of the urine NMR observations for thioacetamide-dosed rats are summarised below in Table 5.7.

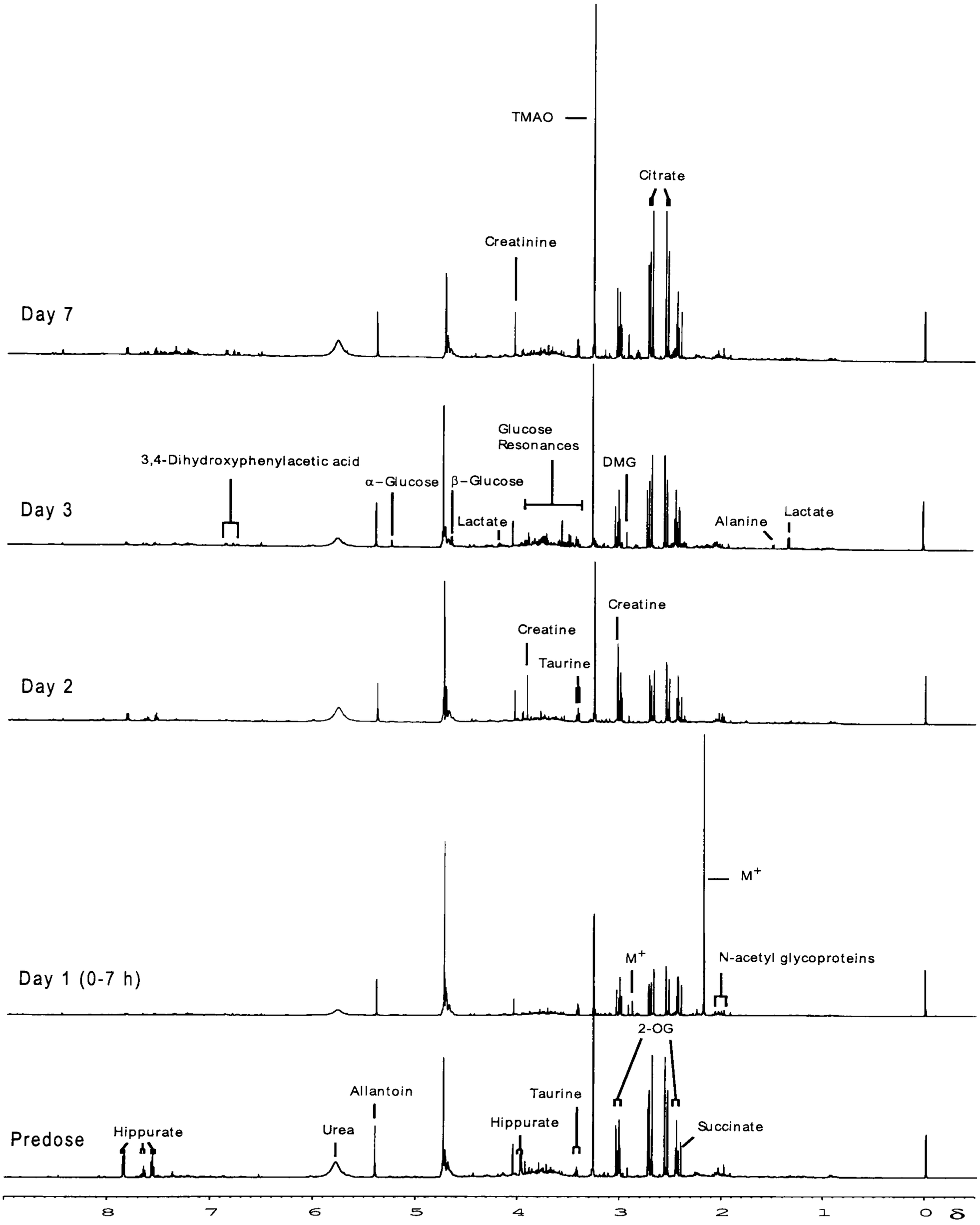

Figure 5.13 Series of standard ^{1}H NMR spectra of urine at predose and various time points following the administration of thioacetamide (200 mg/kg). Key: Metabolite of thioacetamide (M*), 2-oxoglutarate (2-OG), dimethylglycine (DMG).

Table 5.7 Summary of the urinary changes observed by NMR in thioacetamide-dosed rats.

Dose of Thioacetamide	
50 mg/kg	**200 mg/kg**
Thioacetamide metabolites (3 singlet peaks at δ 2.89, δ 2.43 and δ 2.19) were clearly observed in the Day 1 (0-7 hours) urine samples.	Thioacetamide metabolites (δ 2.89, δ 2.43 and δ 2.19) were clearly observed in the Day 1 (0-7 hours) urine samples at a stronger intensity relative to the low dose group. In addition, thioacetamide itself was detected in the Day 1 (0-7 hours) urine samples with animals 401 & 405 showing more thioacetamide than animals 402-404.
Creatine: ↑ **. Taurine: ↑ (NS). Lactate: ↑ (NS).	Marked changes in the endogenous metabolites were detected on various days. On Day 2 the changes were assessed as follows: Hippurate: ↓ in 4/5 animals (NS). 2-Oxoglutarate (2-OG): ↓ (NS). Citrate: ↓ (NS). Creatine: ↑ **. Taurine: ↑ (NS). Guanidinoacetic acid (GAA): ↑ in 3/5 animals (NS). Lactate: ↑ (NS). Glucose: ↑ (NS). Alanine: ↑ (NS). TMAO: ↓ (NS).

5.2.5.2 Principal Component Analysis of Urine NMR Data

Figure 5.14 shows a series of PCA scores plots of the first two principal components of the high dose thioacetamide-treated animals and the controls. Overall the series of PCA scores plot highlighted that the biochemical differences between the two groups increases as the time point at which the sample was taken increases until it reaches a maximum on Day 2, thereafter recovery sets in. The scores plot of the pre-dose urine samples shows some separation between the two groups. Animal 402 is separated from the rest of the animals along the second principal component. Clear separation between the high dose and control animals can be seen on Day 1(0-7h). However, separation between high dose animals and control animals on Day 1(0-7h) was mainly due to the presence of the thioacetamide metabolite, thioacetamide S-oxide (δ 2.19). The Day 2 PCA scores plot shows clear differences between the high dose and control animals. The scores plot indicated that the high dose animals are separated from the control animals along the second principal component with the exception on animal 402 which is separated from the control/high dose animals along the first principal component. The PCA scores plot of Day 3 urine samples shows clear separation between the two groups along the first principal component although it appears that one of the high dose animals (animal 405) had recovered by Day 3. The scores plot also shows that animal 401 is separated from the control/high dose animal along the second principal component. Finally, the scores plot of Day 7 shows some separation indicating partial recovery. These observations confirm that there are biochemical changes between the groups upon administration of high dose thioacetamide that is becoming more prominent with increasing time until a time maxima of Day 2 before gradual recovery from the toxic insult on Day 3 onwards. This graphical approach is a good way to visualise time-dependent biochemical effects and also allows understanding of inter-animal variation.

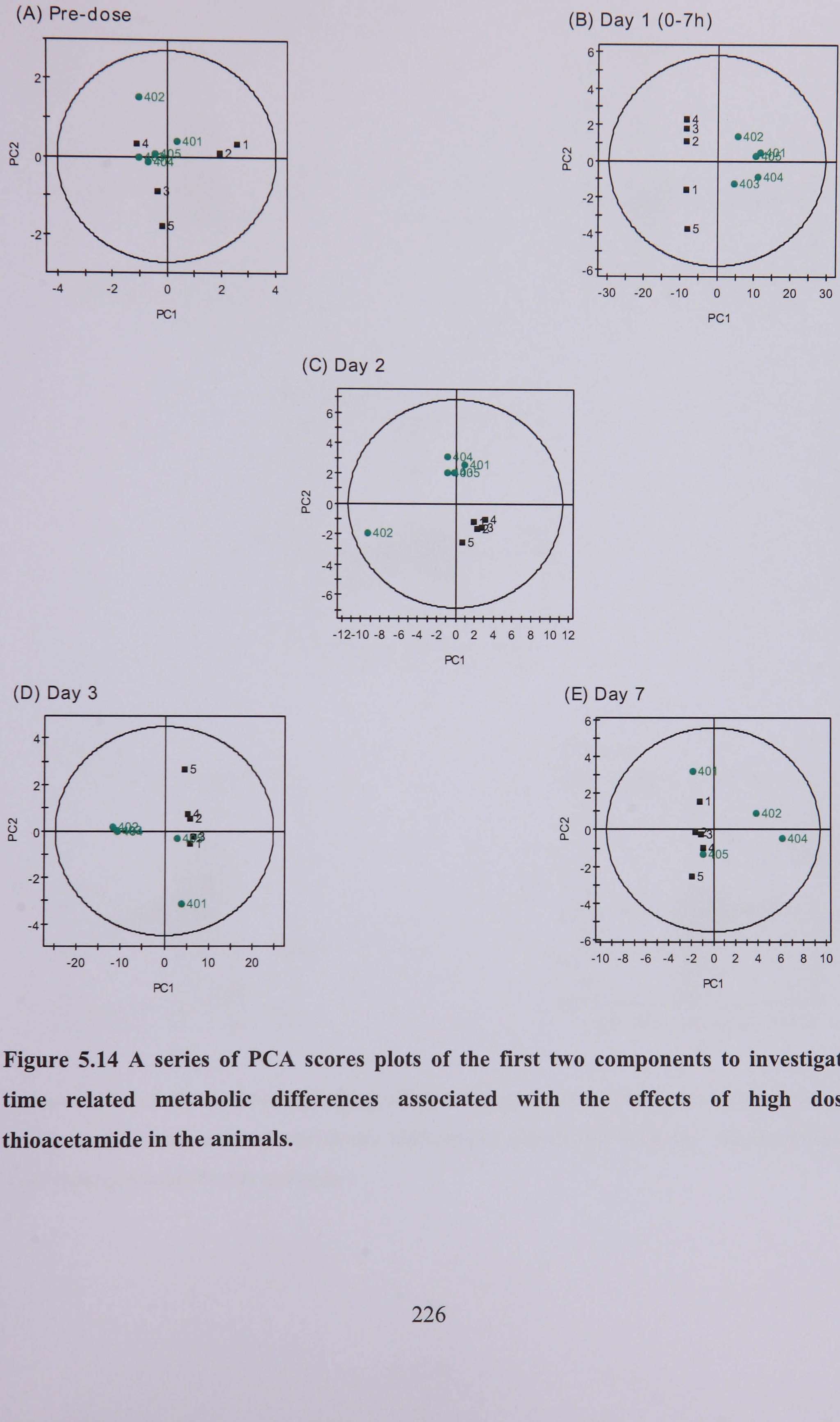

Figure 5.14 A series of PCA scores plots of the first two components to investigate time related metabolic differences associated with the effects of high dose thioacetamide in the animals.

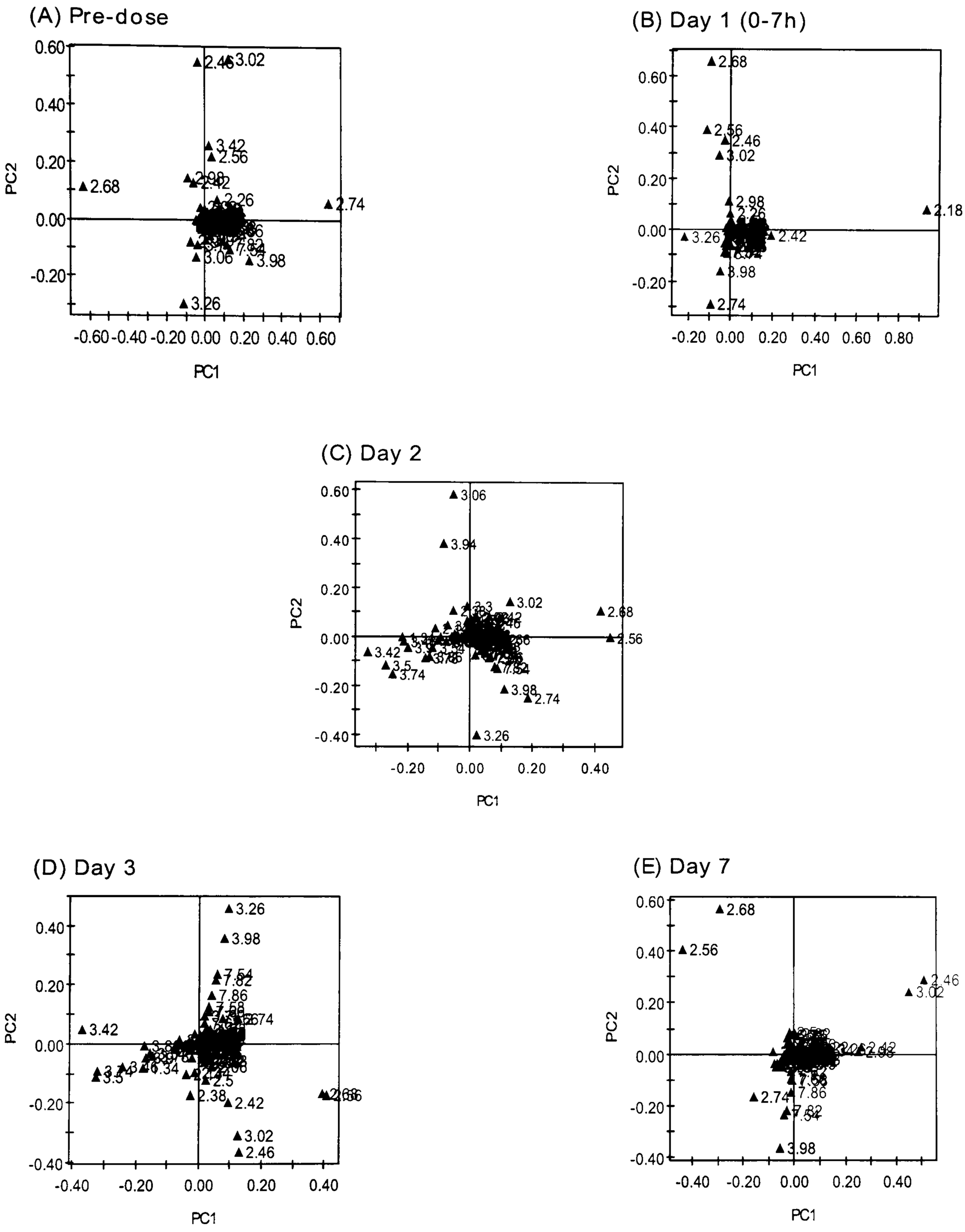

Figure 5.15 A series of corresponding PCA loadings plots of the first two components to investigate time related metabolic differences associated with the effects of high dose thioacetamide in the animals.

Figure 5.15 shows a series of PCA loadings plots of the first two principal components of the high dose thioacetamide-treated animals and the controls. The loadings plot for the pre-dose data indicated that high dose animal 402 has higher urinary 2-oxoglutarate and lower urinary TMAO levels which contributed to the separation from the rest of the animals. Overall the loadings plots show that the trends seen in the PCA scores plots (Figure 5.14) were attributed to relative changes in the urinary endogenous metabolites, with the exception of Day 1 (0-7h). The Day 1 (0-7h) loadings plot indicates mainly the presence of thioacetamide metabolites (δ 2.18 and δ 2.42), which are the major contributors to the separation between the high dose animals and the control animals along the first principal component. Additionally, variation in urinary endogenous metabolites contributed to the variation within the control animals along the second principal component. The loadings plot for Day 2 shows increase in urinary creatine and decreases in urinary TMAO, dimethylamine and hippurate as the major contributor to the separation between the high dose animals and the control animals except high dose animal 402. The loadings plot indicates that increases in urinary taurine, glucose and lactate as well as decreases in urinary hipurate, citrate and 2-oxoglutarate contributed to the separation of high dose animal 402 from the control/high dose animals along the first principal component. These changes can be seen clearly in the series of urinary NMR spectra (Figure 5.13). The loadings plot for the Day 3 shows increases in urinary taurine, glucose, lactate and alanine and a decrease in urinary citrate contributed to the separation between the high dose and control animals along the first principal component. In addition, the loadings plot also shows increase in urinary 2-oxoglutarate and decreases in urinary TMAO and hippurate, which contributed to the separation of animal 401 from the rest of the animals along the second principal component. The presence of urinary glucose could indicate renal dysfunction in the high dose animals. The loadings plot for Day 7 shows some changes in the urinary endogenous metabolites mainly from 2-oxoglutarate, TMAO and succinate indicating partial recovery by Day 7.

5.2.5.3 PCA Mean Trajectory of Urine NMR Data

The mean principal component position was computed for each dose group at each time point and this PCA mean trajectory was performed using the ^{1}H NMR spectra of urine sample for all high dose animals over five time points as above to extract time-related metabolic changes in rat urine samples in response to xenobiotic insult. PCA mean trajectory was carried as described in chapter 2.

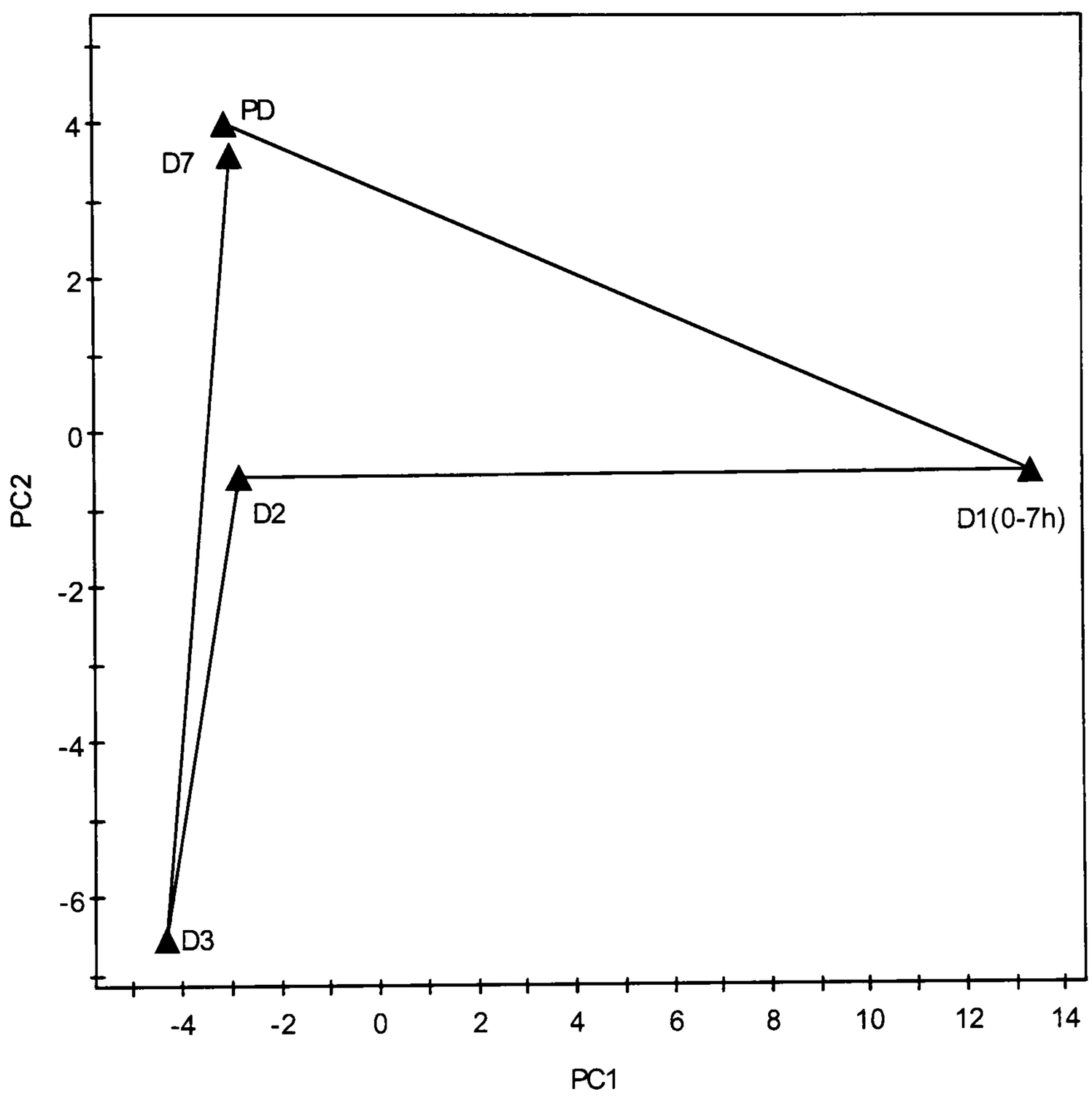

Figure 5.16 PCA mean metabolic trajectory plot mapping the average position of standard ^{1}H NMR high dose thioacetamide urine spectra over five time points.

The PCA mean trajectory plot (Figure 5.16) was constructed from the complete data-reduced ^{1}H NMR spectra, excluding the region of water and urea (δ 4.0-6.0). The first two PCs described 94.3% of the total variance in X. The modelled metabolic evolution comprised four distinct phases. In phase one, corresponding to movement to the Day 1(0-7h) time point, the trajectory of the urine sample coordinates moved away from the pre-dose (PD) position along the first principal component, corresponding to the appearance of the metabolites of thioacetamide (δ 2.18 and δ 2.42) in the urine. In phase two, corresponding to movement to the Day 2 time point, the trajectory changes direction moving away from Day 1(0-7h) time point along the first component corresponding to the disappearance of the metabolites of thioacetamide and the concomitant decreases in urinary endogenous metabolites citrate, succinate, 2-oxoglutarate, TMAO and hippurate as well as increases in taurine and creatine. In phase three, the trajectory changes direction moving away from origin along the second principal component, corresponding to the appearance of urinary glucose, alanine and lactate, indicating a second type of toxicity, namely renal dysfunction on Day 3 as well as decreases in urinary endogenous metabolites citrate, succinate, 2-oxoglutarate, TMAO and hippurate, and increases in taurine, lactate, alanine and creatine. Maximal changes in urinary endogenous metabolites were observed in Day 3 samples which is in contrast with PCA of the urine NMR spectra (Figure 5.14). Finally, in phase four, the trajectory move towards the origin along the second principal component corresponding to the levels of urinary metabolites returning to 'normality' indicating total recovery by Day 7. These changes were in good agreement with the changes observed in the urinary ^{1}H NMR spectra.

5.2.6 Pattern Recognition Analysis of Concatenated Liver and Plasma NMR Data

5.2.6.1 Concatenated Principal Component Analysis (PCA)

The PCA of concatenated liver and plasma NMR data did not improve the separation between the low dose animals and the control animals (Figure 5.17A) as compared to the PCA of tissue samples alone (Figure 5.4A). Only three out of the five low dose animals were separated from the control animals along the second principal component. In addition, control animal 9 was separated from the rest of the control animals along the first principal component. The corresponding loadings plot (Figure 5.17B) indicated that increase in liver lipids as well as changes in plasma lipids are the major contributors to the separation between the two groups. The loadings plot also revealed changes in plasma choline, glucose and amino acids regions that contributed to the separation between the low dose animals and the control animals. Control animal 9, which showed high liver lipids, was separated from the rest of the control animals.

The PCA scores plot of the high dose Day 2 liver and plasma data (Figure 5.17C) revealed separation between the high dose animals and the control animals. The first principal component as well as the second principal component describes the variation observed between the high dose animals and the control animals. Additionally, the scores plot also revealed differences within the high dose animals with animals 406 and 409 located on the lower half of the plots and the remaining three animals on the lower half of the scores plot separated along the second principal component. The corresponding loadings plot (Figure 5.17D) indicates that decrease in plasma lipids is the major contributors to the variation along the first principal component. On the other hand, changes in liver lipids and decreases in liver glucose as well as changes in plasma lipid, choline and glucose regions are the major contributors to the variation within the dosed groups along the second principal component.

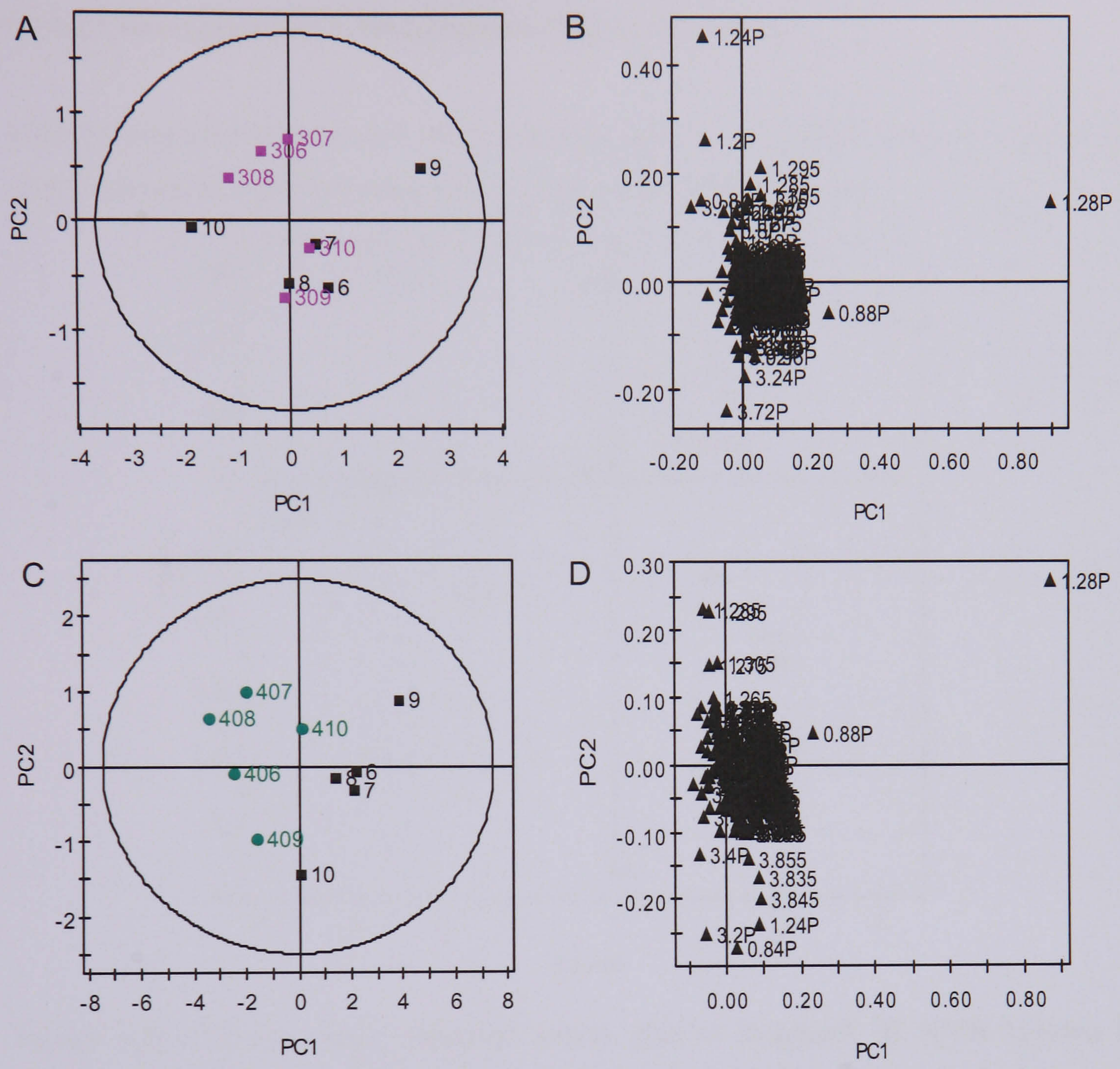

Figure 5.17 Concatenated PCA models for the first two components of the standard 1D NMR spectra of thioacetamide-dosed Day 2 liver and CPMG spin-echo plasma NMR spectra. (A) Low-dose vs. control data set and the corresponding loadings plot (B). (C) High-dose vs. control data set and the corresponding loadings plot (D).

5.2.6.2 Concatenated PLS-Discriminant Analysis (PLS-DA)

PLS-DA was used to determine which variables in the concatenated NMR data predict the sample classes as well as to refine information recovery from the data.

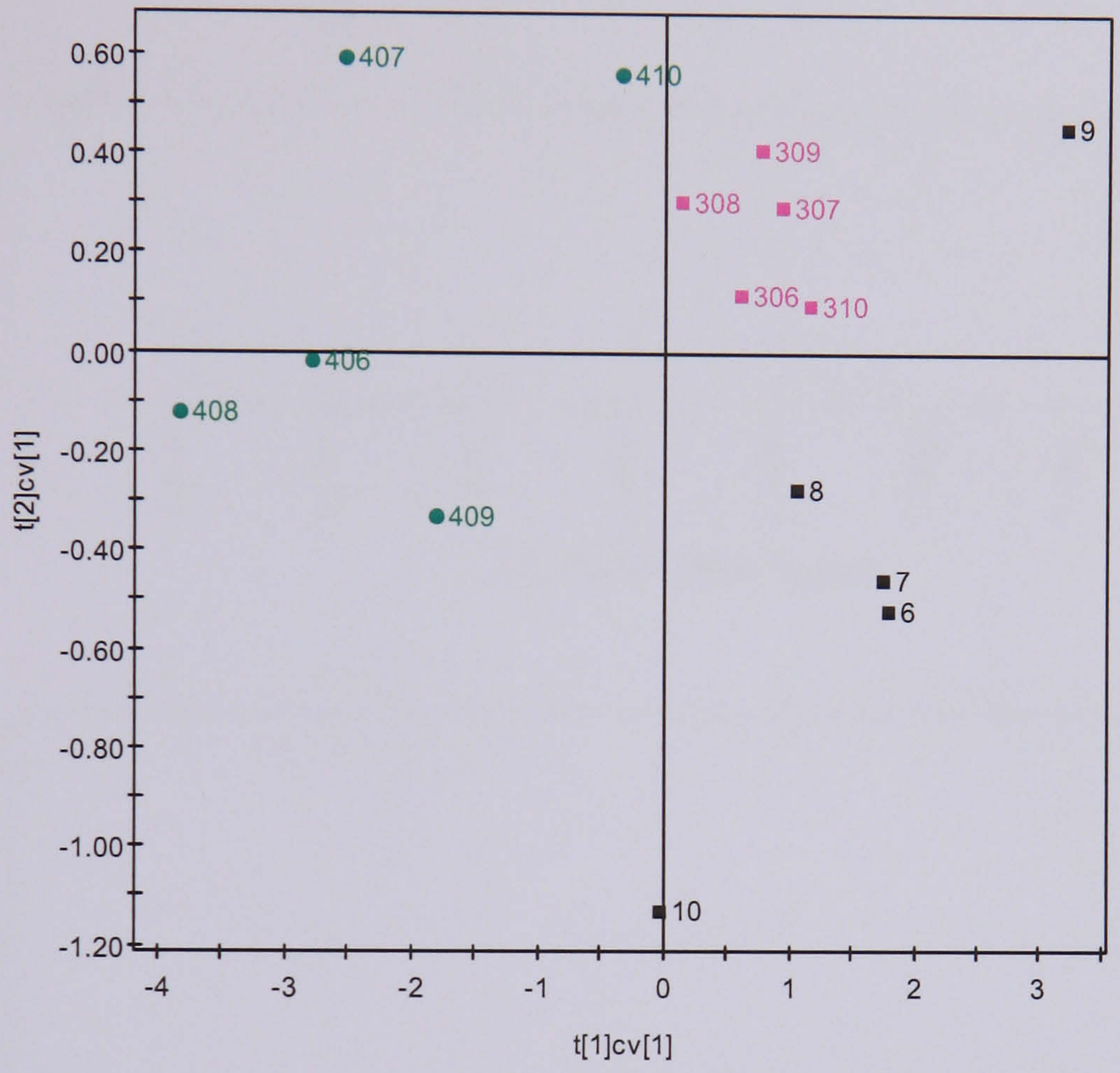

Figure 5.18 PLS-DA cross validated scores plot of standard ^{1}H NMR spectra of thioacetamide Day 2 liver tissue and CPMG spin-echo NMR of Day 2 plasma samples.

Figure 5.18 shows the PLS-DA cross validated scores plot for the first two components of the thioacetamide Day 2 liver tissue and plasma NMR data. The scores plot now revealed clear separation between the control and dosed groups. Animals 9 and 10 are separated by a combination of the first and second PLS component. The first PLS component describes the variation between the high dose animals and the control animals whereas the second PLS component describes the variation between the low dose animals and the control animals.

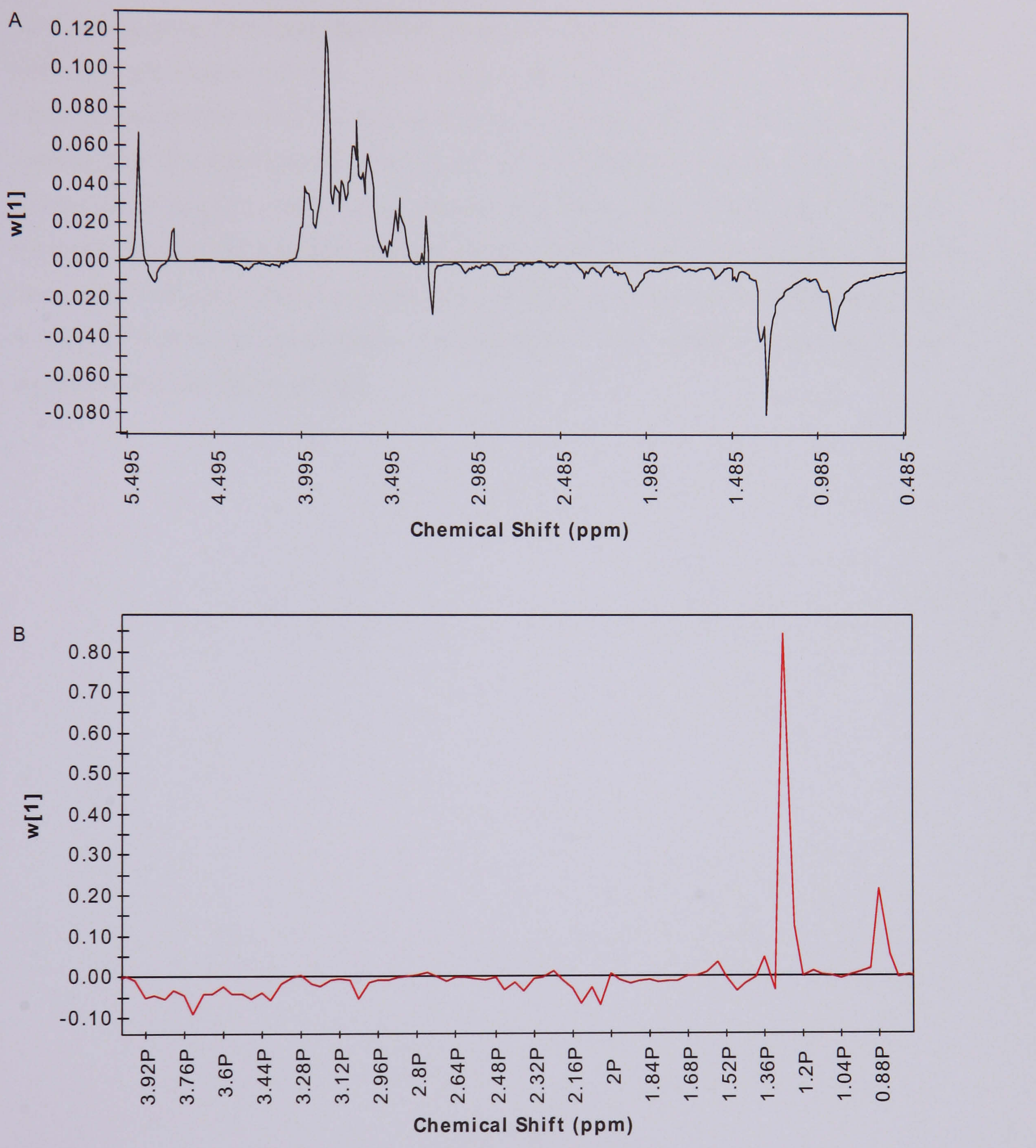

Figure 5.19 First component PLS weight (W[1]) from the PLS-DA model attributed to (A) ^{1}H MAS NMR data of Day 2 liver tissues (—), and (B) CPMG spin-echo NMR data of Day 2 plasma samples (—).

The corresponding first component PLS loadings attributed to the liver tissue and plasma NMR data are shown in Figure 5.19A and B respectively. The plot shows the general effects of dose related variations on liver tissues and plasma along the first component. The loadings plot revealed thioacetamide-induced severe decreases in plasma lipids and liver glucose and glycogen as well as an increase in liver lipids are the major contributor to the separation between the high dose animals and the control animals. In addition, the first PLS component loadings plot also indicates some increase in plasma glycoprotein and glucose as well as increase in liver choline and decrease in liver TMAO contributing to the separation between the two groups.

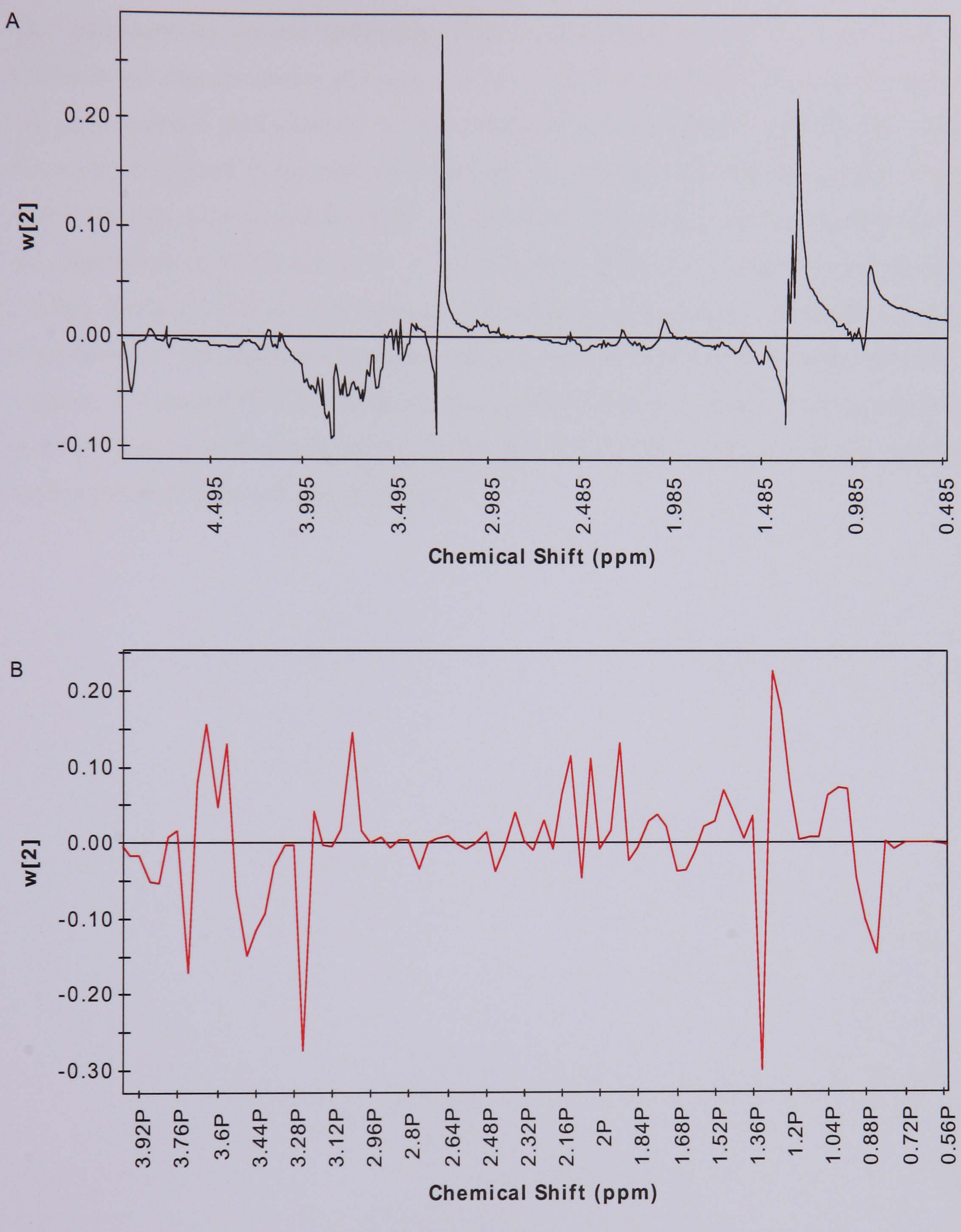

Figure 5.20 Second component PLS weight (W[2]) from the PLS-DA model attributed to (A) ^{1}H MAS NMR data of Day 2 liver tissues (—), and (B) CPMG spin-echo NMR data of Day 2 plasma samples (—).

The corresponding second component PLS loadings attributed to the liver tissue and plasma NMR data are shown in Figure 5.20A and B. Generally, the effects observed in the low dose animals were identical to that observed in the high dose animals only milder. However, in contrast to the high dose animals, the loadings plot indicated greater increase in liver choline in the low dose animals. The second component loadings plot indicated that the administration of the low dose of thioacetamide induced increases in liver lipids and choline levels as well as decreases in liver glucose and glycogen levels as the major contributors to the separation between the low dose animals and the control animals. In addition, the second PLS component also revealed decreases in plasma lipids and choline levels as well as increases in plasma lactate and TMAO that contributed to the separation between the low dose and control groups.

5.2.6.3 Partial Least Square Projection to Latent Structures Approach (PLS)

Having established that there were intrinsic differences between groups, the data matrices were combined and analyzed using PLS to further improve classification between groups.

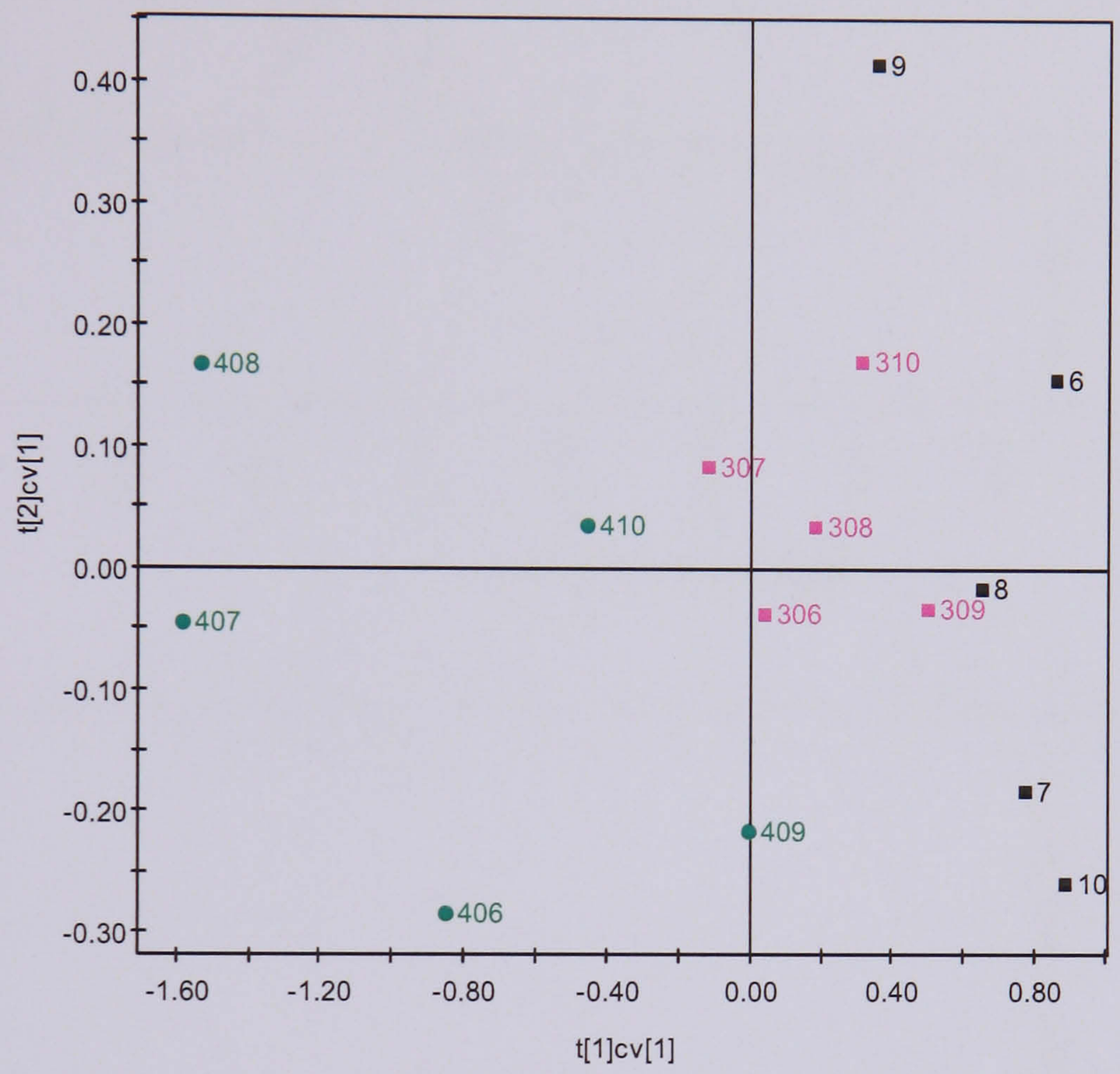

Figure 5.21 PLS cross validated scores plot of standard ^{1}H NMR spectra of thioacetamide Day 2 liver tissue and CPMG spin-echo NMR data of Day 2 plasma samples.

By treating liver NMR data as the X matrix and plasma NMR data as the Y matrix, the cross validated scores plot (Figure 5.21) revealed clear separation between the dosed animals and the control animals along the first component. The scores plot also revealed the progression from low dose to high dose which is related to the severity of thioacetamide-induced metabolic changes in both the liver and the plasma. In addition, variation within the high dose animals, which correlated to the varying degree of severity in the changes of both liver and plasma lipids profiles, can be seen in the scores plot along the first component.

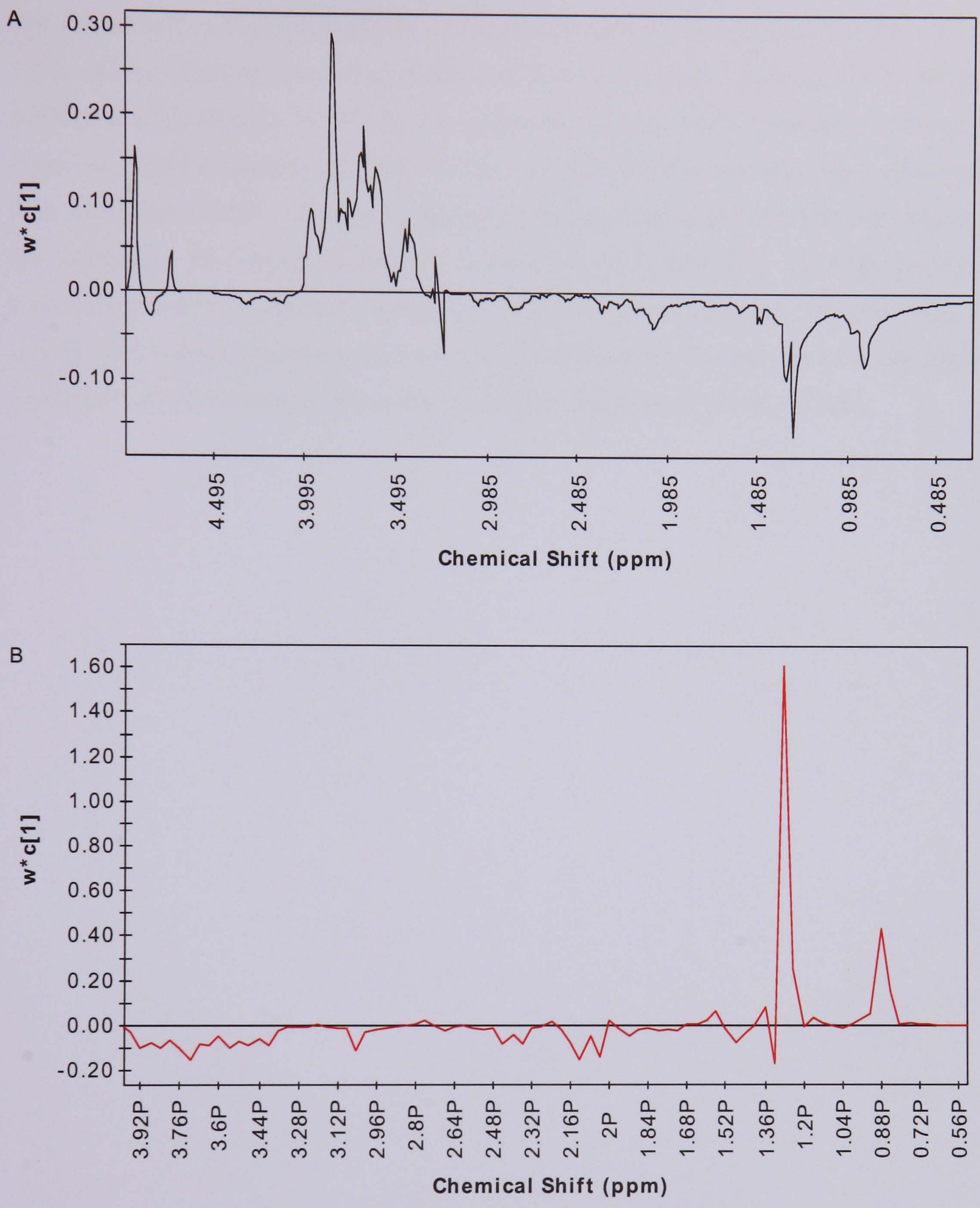

Figure 5.22 First component PLS weight (W*[1]) from the PLS model attributed to (A) ^{1}H MAS NMR data of Day 2 liver tissues (—), and (B) CPMG spin-echo NMR data of Day 2 plasma samples (—).

The corresponding PLS loadings plot for the first component revealed that increases in liver lipids and decreases in liver carbohydrates and glycogen (Figure 5.22A) as well as decrease in plasma lipids (Figure 5.22B) are the major contributors to the separation between the dosed and control animals. In addition, the loadings plot also revealed some increase in liver and plasma choline as well as changes in plasma glucose levels which contributed to the separation. The degree of severity induced by thioacetamide is the only factor that contributed to the separation between the high dose animals and the low dose animals. Again, the loadings plot revealed a correlation between the changes in liver and plasma lipids profiles which contributed to the separation within the high dose animals.

5.3 Discussion

5.3.1 Effects of Thioacetamide on rat liver

At the high dose, thioacetamide induced moderate hepatic centrilobular necrosis as revealed by the histopathological data. Severe depletion of liver glucose and glycogen, as detected by the MAS NMR of liver tissues, suggests increased energy demands within the liver. The latter finding suggests increased rate of hepatic glycogenolysis, which is consistent with the depletion of hepatic ATP following mitochondrial impairment (Trennery and Waring 1983). Since structure and function of mitochondria are closely linked, changes in the structure of mitochondria will affect the overall mitochondrial functions and therefore ATP production. Thioacetamide has been shown to change the permeability of cell membrane (Anghileri *et al.* 1977), induce loss of respiratory control in the mitochondria and reduced mitochondria cytochrome levels (Moller and Dargel, 1984), and induce functional disturbances in the mitochondria as well as structural alterations of the inner mitochondrial membrane (Moller and Dargel, 1985). With impairment of mitochondrial ATP-production, glycolysis would enable some ATP production as glucose is converted to lactate in the cytosol and glycogenolysis would increase the supply of glucose for this process.

As discussed previously, the observed increase in liver lipid could arise either through impaired transport from the liver or through impaired protein synthesis within the liver. Teck *et al.* (2004) found that administration of thioacetamide down-regulates the enzymes involved in hepatic fatty acid β-oxidation thus leading to impaired ATP production and fatty acid accumulation. Moller and Dargel (1984) also found evidence of decreased fatty acid oxidation in thioacetamide-treated rat liver. Severe and prolonged impairment of β-oxidation in the mitochondria is known to cause steatosis and, in some severe cases, liver failure and death (Fromenty and Pessayre 1995). In addition, the transport of triglycerides out of the liver is likely to be decreased if protein synthesis is impaired. Impaired protein synthesis could arise simply through thioacetamide-induced ATP-depletion, and study has shown that thioacetamide stops glycine incorporation into liver protein (Reynolds 1972). This result also showed that thioacetamide-induced structural changes to the endoplasmic

reticulum and such damage would be expected to lead to the disruption of protein synthesis of the whole organelle. The endoplasmic reticulum is also involved in the homeostatic control of cellular calcium sequestration. Therefore, damage to the endoplasmic reticulum will lead to the disruption of calcium ion homeostasis and hence to apoptosis.

Additionally, Lin *et al.* (1996) demonstrated that an increase in the intracellular bile acids concentration inhibits the secretion of VLDL-associated triglycerides from hepatocytes as well as the secretion of apolipoprotein associated with transport of VLDL namely apoB-100. Thioacetamide causes some biliary damage and the plasma clinical chemistry results in the current study indicated an increase in total bile acids (TBA). This could have an inhibitory effect on triglyceride secretion leading to accumulation of triglycerides in the liver.

5.3.2 Effects of Thioacetamide on blood plasma and urine

The effects of thioacetamide on blood plasma are characterised by increases in creatine, lactate, acetate and pyruvate, and by a reduction in lipids and in the VLDL/LDL ratio. The reduction in the ratio of VLDL/LDL could be because of reduced lipid secretion from the liver. In the urine, increases in taurine and creatine were observed together with the presence of thioacetamide metabolites. Decreases in urinary citrate, 2-oxoglutarate and succinate are indicative of disruption in the tricarboxylic acid (TCA) cycle.

The urinary taurine increase would be consistent with impaired protein synthesis. but could also be the result of increased cysteine synthesis. The thioacetamide-induced increases in urinary creatine may be related to cysteine biosynthesis from methionine as postulated by Clayton *et al.* (2003a). Cysteine is used to synthesise GSH, taurine and proteins. During this biosynthesis, S-adenosylmethionine donates a methyl group to the methyl acceptor, guanidinoacetic acid (GAA). The methylated-GAA is then converted to creatine. Combining the findings in this study with the literature findings on thioacetamide metabolism and toxicity suggests that thioacetamide may stimulate glutathione synthesis in response to thioacetamide-induced oxidative stress. Sun *et al.* (2000) have shown that

thioacetamide reduces vitamin C and vitamin E levels in treated rat livers. Bruck *et al.* (2001) found that free radical scavengers prevented the development of thioacetamide-induced liver cirrhosis supporting the concept of oxidative stress involvement in thioacetamide toxicity. In addition, Avni *et al.* (2004) found increased level of malondialdehyde, an end product of lipid peroxidation, in thioacetamide-treated rat liver, suggesting oxidative stress. However, in this study, malondialdehyde was not detected by NMR. The presence of thioacetamide-derived reactive polar compounds or free radicals that might react directly with glutathione could lead to glutathione depletion and hence to glutathione synthesis and increased oxidative stress and lipid peroxidation can also stimulate glutathione synthesis This could explain the increased synthesis of cysteine as evident by increased urinary creatine as both glutathione and taurine play an important role in cellular protection against free radicals and oxidative stress.

The presence of glucose, acetate and lactate in the urine are indicative of renal dysfunction. Thioacetamide is known to cause glomerular atrophy in the cortical tubules (Virtanen and Lassila 1986) and treatment of a monkey kidney cell line with thioacetamide was shown to cause nucleolar and mitotic alterations (Mironescu *et al.* 1969).

Table 5.8 Summary of the effects of thioacetamide.

Dose of Thioacetamide	Histopathology	Clinical Chemistry	Liver NMR	Plasma NMR	Urine NMR
50 mg/kg	Mild hepatocellular centrilobular necrosis.	ASAT: ↑ (***) ALAT: ↑ (***) TBA: ↑ (***) GGT: ↑ (**) Bilirubin: ↑ (***) 5NT: ↑ (**)	Lipids: ↑ (*) Choline: ↑ (*)	Creatine: ↑ (NS) Total lipids: ↓ (NS) Acetate: ↑ (NS) Pyruvate: ↑ (NS)	Appearance of thioacetamide metabolites.
200 mg/kg	Moderate hepatocellular centrilobular necrosis.	Triglycerides: ↓ (**) ASAT: ↑ (***) ALAT: ↑ (***) TBA: ↑↑ (***) GGT: ↑ (**) Bilirubin: ↑ (***) 5NT: ↑↑ (***)	TMAO: ↓ (*) Glucose: ↓ (*) Glycogen: ↓ (*) Lipids: ↑ (*) Choline: ↑ (*)	Creatine: ↑ (NS) Total lipids: ↓ (**) Acetate: ↑ (NS) Pyruvate: ↑ (NS)	TMAO: ↓ (NS) Creatine: ↑ (**) Taurine: ↑ (NS) 2-OG: ↓ (NS) Citrate: ↓ (NS) Hippurate: ↓ (NS) Lactate: ↑ (NS)

Key: ASAT = aspartate aminotransferase, ALAT = alanine aminotransferase, TBA = total bile acids, GGT = γ-glutamyltransferase, TP = total plasma protein, 5NT = 5'-nucleotidase, TMAO = trimethylamine-N-oxide, 2-OG = 2-oxoglutarate.

5.3.3 Comparison of Information Obtained from Different Sources

The integrated approach proves to be useful in analysing the conventional toxicological data and NMR data of different sample types collectively to describe thioacetamide-induced toxicity in the rats. Table 5.8 shows the summary of the effects of thiuoacetamdie in rats. Overall, the NMR findings are consistent with the clinical chemistry findings as well as the histopathology, which showed clear thioacetamide-induced effects in high dose animals. However, histopathology findings indicated no dose related effects in the Day 2 low dose animals which are in contrast to the clinical chemistry and NMR spectral data observations.

The MAS NMR showed a decrease in the liver TMAO level in the high dose thioacetamide animals. Increased phospholipids could lead to a decrease in TMAO levels, however, the MAS NMR data did not show any increase in liver phospholipids that would have suggested phospholipidosis although liver choline level had increased. In liver, the drop in liver TMAO levels suggests a thioacetamide-induced block in this N-oxidation pathway or a reduction in the supply of trimethylamine (TMA) reacting in the liver. The lipid intermediary metabolites, choline and TMAO, were present in the blood plasma before excretion into the urine. The decrease in TMAO could then be related to decrease NADPH-dependent flavin monooxygenase enzyme, which catalyses the oxidation of TMA to TMAO since thioacetamide has been shown to inhibit protein synthesis (Reynolds 1972, Platt and Cockrill 1967). The decrease in liver TMAO could also explain the increase in liver and plasma choline since choline is the precursor of TMAO. Schriewer and Lohmann (1976) found that thioacetamide impaired phospholipid metabolism in both the liver and mitochondria, thus the elevated liver choline could also indicate disruption in phospholipid metabolism (Figure 5.23).

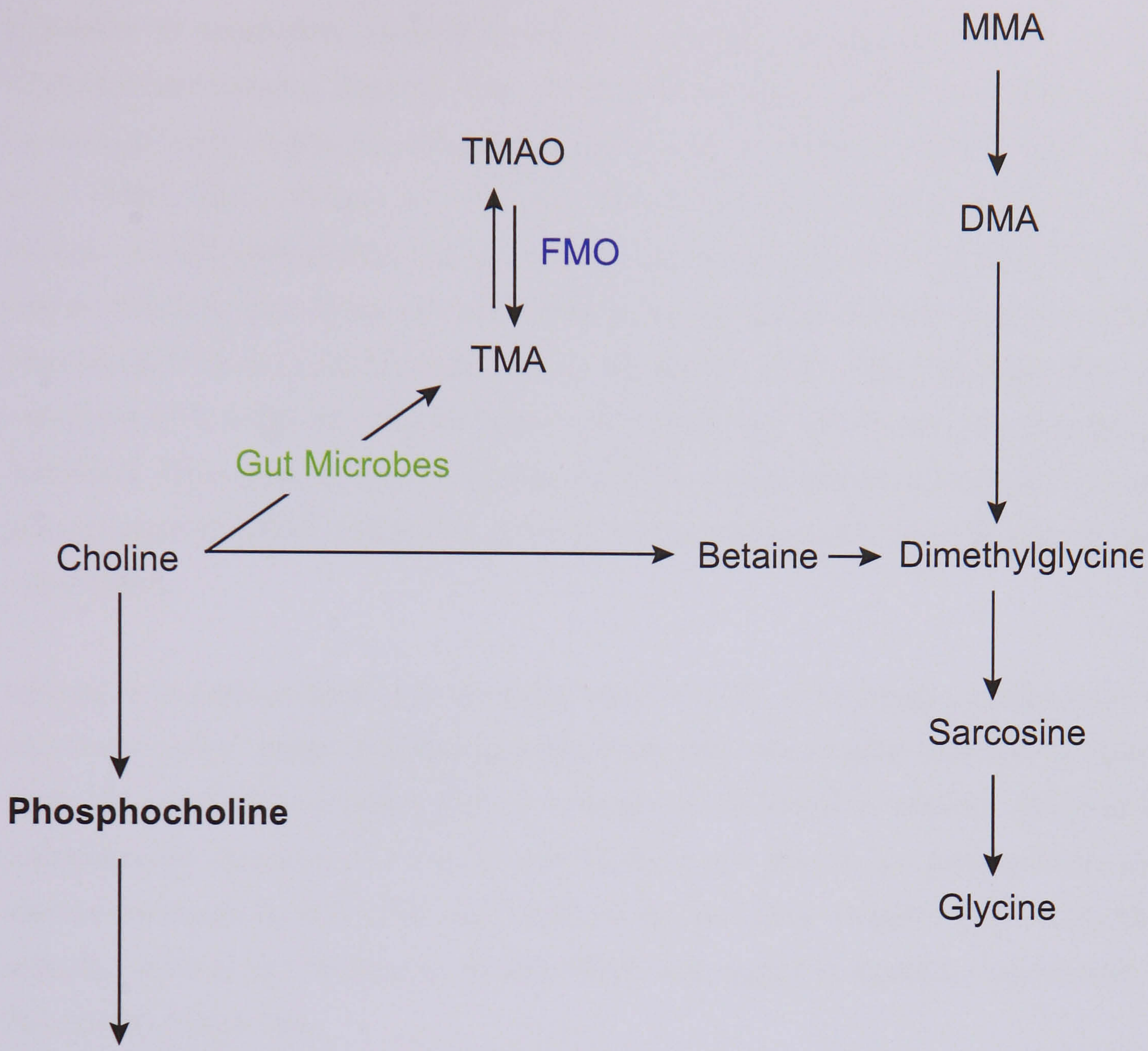

Figure 5.23 Choline and its involvement in the metabolism of methylamines and phospholipids (adapted from Smith *et al.* 1994, Podo 1999). Key: MMA = monomethylamine, DMA = dimethylamine, TMA = trimethylamine, TMAO = trimethylamine N-oxide, FMO = flavin monooxygenase system.

A number of metabolites involved in energy generation were perturbed as a result of thioacetamide treatment. Depleted liver glucose and glycogen on Day 2 was accompanied by elevated lactate in plasma suggesting extensive glycogenolysis and glycolysis (Cascales *et al.* 1992). These changes are indicative of increase energy demand in the liver and possible mitochondria dysfunction. In addition, the increase levels of plasma lactate and alanine indicates gluconeogenesis suggesting increased energy demand. Reduced urinary excretion of TCA cycle intermediates, citrate, succinate, and 2-oxoglutarate might also be a consequence of energy metabolism disruption but might also result from changes in the gut microflora. Glycosuria on Day 2 and Day 3 without any detected perturbation of plasma glucose suggests kidney damage as opposed to saturation or inhibition of kidney glucose reabsorption.

Increase in plasma creatine level normally leads to increase in urinary creatine level, as seen in the current study. The Day 2 plasma NMR data also revealed decreases in plasma lipids. However, these changes did not correlate to the extent of necrosis observed by histopathology. Analysis of the LDL and VLDL peaks seen in the plasma NMR data showed decreases in both LDL and VLDL in the low dose animals. In the high dose animals, however, the decrease in plasma VLDL was bigger in magnitude as compare to that of LDL (Table 5.9).

Table 5.9 Changes in Day 2 plasma LDL and VLDL levels

Thioacetamide Dose Group	Percentage Decrease in Day 2 Plasma LDL (NMR data, %)	Percentage Decrease in Day 2 Plasma VLDL (NMR data, %)
LD	14.3	21.7
HD	26.6	60.6

^{1}H NMR spectroscopic analysis of Day 1(0-7h) urine samples detected the primary metabolite of thioacetamide, thioacetamide-S-oxide. The available evidence suggests that the development of hepatic necrosis after the administration of thioacetamide occurs following metabolism of thioacetamide through the action of flavin-containing

monooxygenase (FMO) in the liver to thioacetamide-S-oxide. Since both thioacetamide and TMA require FMO in their oxidation reaction, the conversion of thioacetamide to its S-oxide would be expected to compete with the conversion of TMA to TMAO for FMO as evident by the reduced level of liver TMAO.

Thioacetamide-S-oxide is then converted to an intermediate capable of reacting with tissue macromolecules in a cytochrome P450 monooxygenase-catalysed reaction. Finally, the formation of irreversibly bound products of thioacetamide-S-oxide metabolism may initiate changes in hepatic cellular function resulting in cell death (Rees *et al.* 1966, Hunter *et al.* 1977, Porter and Neal 1978, Porter *et al.* 1979, Dyroff and Neal 1982).

5.3.4 Summary

^{1}H MAS NMR spectroscopy coupled with ^{1}H NMR spectroscopy of biofluids and multivariate data analysis as well as conventional histopathological and clinical chemistry data has enabled the detailed study of biochemical perturbations in liver tissue, blood plasma and urine following treatment with thioacetamide. NMR-based metabonomic approach appears to be more sensitive in picking up subtle thioacetamide-induced changes particularly in the low dose as compare to conventional histopathological method. The treatment with thioacetamide had several effects in the rats in that it disrupted energy metabolism characterised by depletion in liver glycogen and glucose followed by reduced urinary TCA cycle intermediates, citrate and 2-oxoglutarate. The treatment also caused disruption in lipid metabolism. The accumulation of triglycerides is a common cellular response to toxic compounds, which is normally reversible. This can occur by increased synthesis or uptake of lipid, decreased lipid metabolism, or inhibition of lipid transport from the cell. In the case of thioacetamide, the latter of these is the most likely case as the observed hepatic lipidosis was concomitant with hypolipidaemia as in the case of allyl formate toxicity. The urinary excretion of thioacetamide-S-oxide indicated the likely involvement of flavin-containing monooxygenase system as a route for the elimination and inadvertently, the hepatotoxicity of thioacetamide through the formation of reactive intermediates. In conclusion, this study has utilised high resolution ^{1}H MAS NMR

spectroscopy to study intact liver tissues, which provides the essential link between the metabolite profiles obtained from biofluid NMR and the structural progression of the lesion observed by histopathological technique.

Chapter 6: Global Pattern Recognition Analysis

6.1 Introduction

The differing effects of allyl formate, chlorpromazine and thioacetamide were compared by pattern recognition analysis of combined data. The clinical chemistry data and ^{1}H NMR spectra were analysed separately and in certain combinations using principal component analysis (PCA) and partial least square (PLS) analysis. Possible correlation between liver and plasma NMR data was examined. It should be noted again that the Day 2 tissue and plasma samples and the Day 2 urine samples were provided by different sets of animals and were therefore not directly comparable. The data sets analysed as well as the sample labelling and codes are summarised in Table 6.1. Prior to concatenating the plasma and liver NMR data, each segmented spectral region of the reduced and normalised plasma data was labelled with its segment number and ending with the letter P (designating plasma). All data were mean centered, unless stated otherwise, prior to pattern recognition analysis. All subsequent data analysis was performed using SIMCA-P (version 10.5, Umetrics AB, Umea, Sweden) software.

Table 6.1 NMR data Analysed and Sample Labelling and Code.

Compound	Day 2 NMR Spectral Type	Study Group	Sample Label
Allyl Formate	Liver – Standard 1D Plasma – CPMG	Control	C6-C10
		Low Dose (25 mg/kg)	ALD106-ALD110
		High Dose (75 mg/kg)	AHD206-AHD210
	Urine – Standard 1D	Control	C1-C5
		Low Dose (25 mg/kg)	ALD101-ALD105
		High Dose (75 mg/kg)	AHD201-AHD205
Chlorpromazine	Liver – Standard 1D Plasma – CPMG	Control	C6-C10
		Low Dose (30 mg/kg)	CPLD306-CPLD310
		Highdose (60 mg/kg)	CPHD406-CPHD410
	Urine – Standard 1D	Control	C1-C5
		Low Dose (30 mg/kg)	CPLD301-CPLD305
		High Dose (60 mg/kg)	CPHD401-CPHD405
Thioacetamide	Liver – Standard 1D Plasma – CPMG	Control	TC6-TC10
		Low Dose (50 mg/kg)	TLD306-TLD310
		High Dose (200 mg/kg)	THD406-THD410
	Urine – Standard 1D	Control	TC1-TC5
		Low Dose (50 mg/kg)	TLD301-TLD305
		High Dose (200 mg/kg)	THD401-THD405

6.2 Global Pattern Recognition of Day 2 Plasma Clinical Chemistry Data

PCA analysis was performed on the Day 2 plasma clinical chemistry data with individual variables being unit variance-scaled prior to modelling. In the scores plot, the data points are labelled so as to identify the treatment (e.g. C for control, LD for low dose and HD for high dose) and animal number. The data points and labels are colour-coded by treatment. For the loadings plot, the data points are labelled according to the clinical chemistry parameters that they represent.

6.2.1 PCA of Clinical Chemistry Data

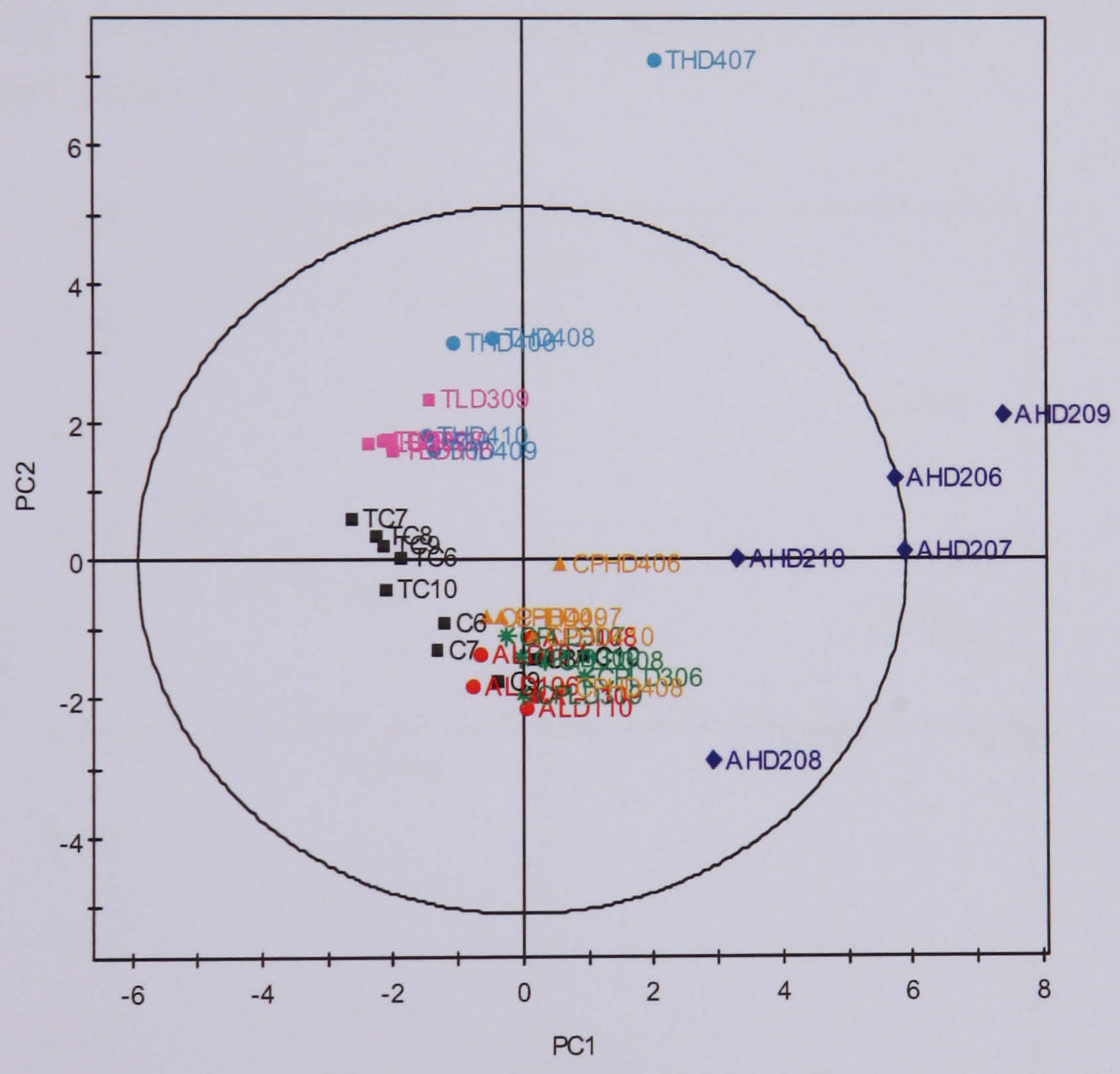

Figure 6.1 PCA scores plot for the first two components of the Day 2 plasma clinical chemistry of the three hepatotoxin-dosed samples.

Principal component analysis of the Day 2 data set revealed some dose-related structure to the variation in the data with the thioacetamide-treated animals being separated from the control animals along the second principal component and the high dose allyl formate animals separated from the controls along the first principal component (Figure 6.1). The first principal component describes the variation between the high dose allyl formate and chlorpromazine-treated animals and the controls animals. The high dose animals are well separated from the controls except for chlorpromazine dosed animals which are partially separated from the controls along the first principal component. The second principal component describes the variation between the high dose thioacetamide-treated animals from the controls. In addition the control animals for the two studies are separated along the second principal component indicating some biochemical variations between the two groups of control animals.

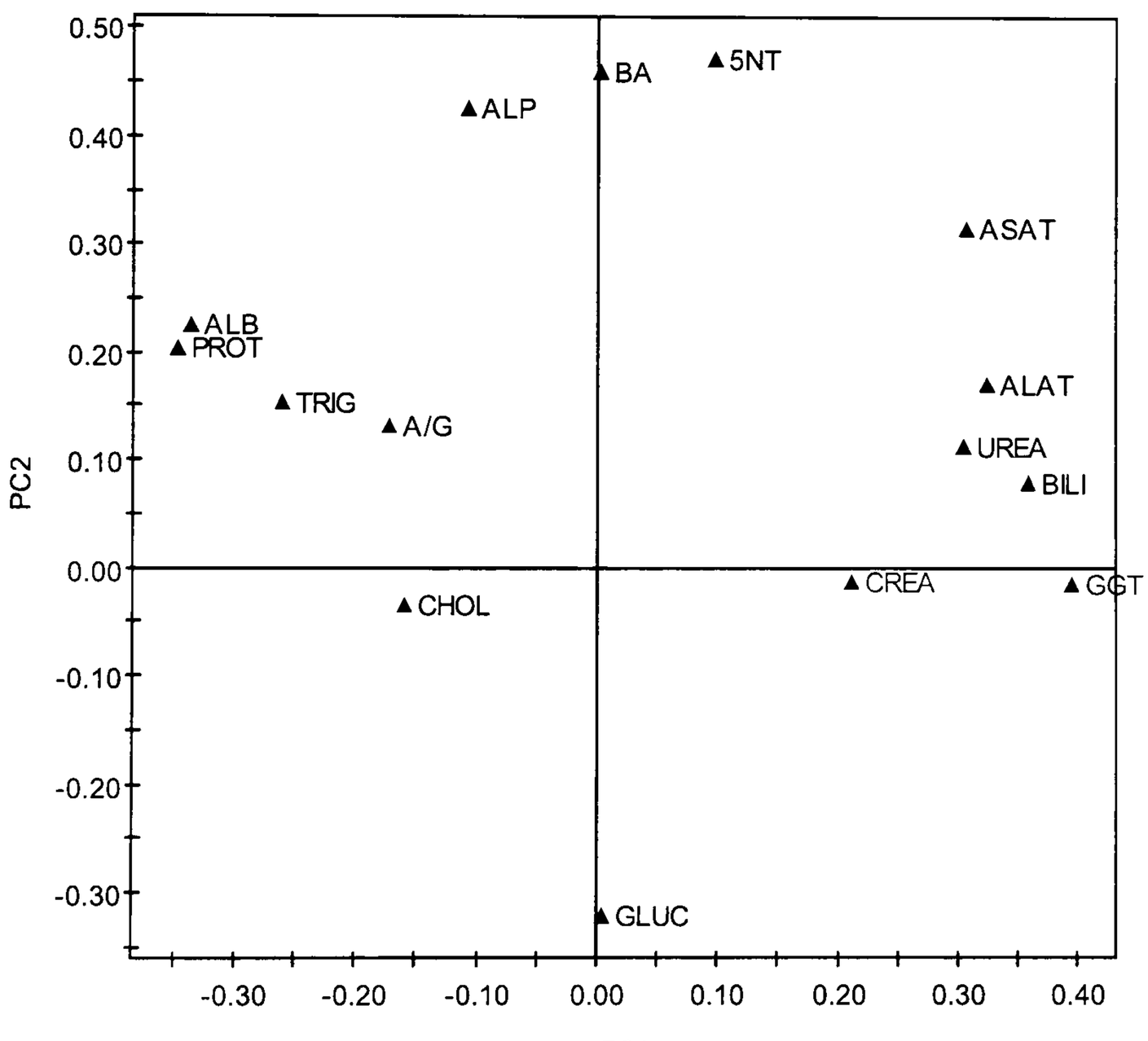

Figure 6.2 PCA loadings plot for the first two components of the Day 2 plasma clinical chemistry of the three hepatotoxin-dosed samples.

The corresponding loadings plot of the PCA model (Figure 6.2) indicated that the high dose of allyl formate caused increases in γ-glutamyl transferase and bilirubin, which are markers of hepatobiliary damage. Another important feature observed in the loadings plot along the first principal component is the generalised increase in both aminotransferases, ALAT and ASAT, which are indicative of hepatocellular damage in the high dose allyl formate-dosed animals. Animals treated with high dose of allyl formate also showed decreases in plasma albumin, protein and triglycerides as compared to the control animals.

However, animals treated with high dose of thioacetamide showed increases in plasma bile acids, 5NT, ALP and ASAT, which contributed to the separation along the second principal component. These changes are orthogonal to that observed in the allyl formate-treated animals. In addition, animals treated with high dose of thioacetamide also showed decrease in plasma glucose, which contributed to the separation along the second principal component.

6.3 Global Pattern Recognition of Day 2 Standard 1D MAS NMR Spectra of Liver

PCA and PLS-DA analysis were performed on all standard 1D NMR spectra of Day 2 liver samples for all three hepatotoxins. The data were combined, normalised and mean-centered prior to modelling. In the scores plots, the data points are labelled so as to identify the treatment (C for control, LD for low dose and HD for high dose) and animal number. These data points and labels are also colour-coded by treatment. For the loadings plot, the data points are labelled according to the bucket or spectral segment that they represent.

6.3.1 PCA of Liver NMR Data

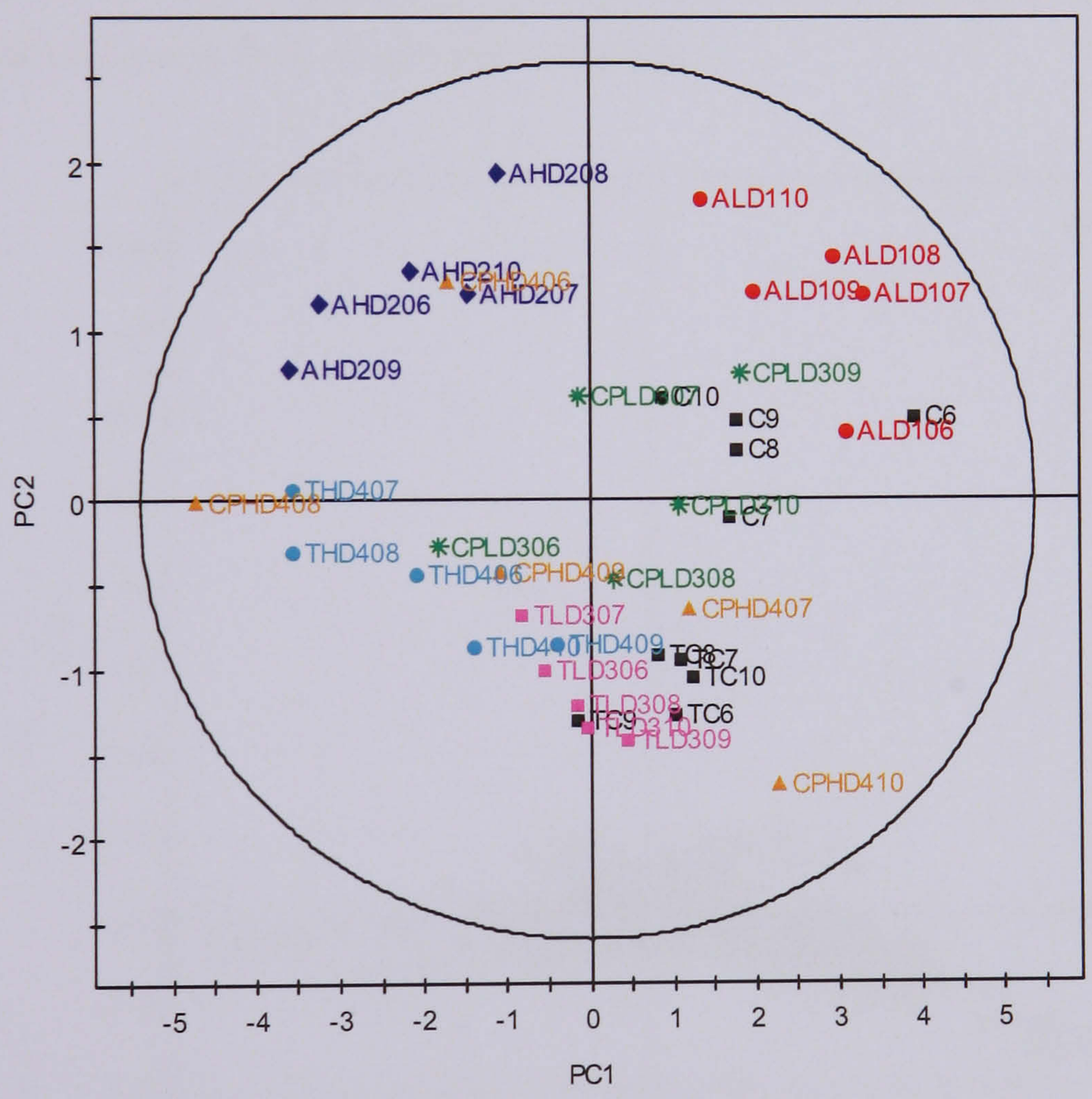

Figure 6.3 PCA scores plot for the first two components of the Day 2 standard 1D ^{1}H MAS NMR spectra of the three hepatotoxin-dosed liver samples.

Principal component analysis of the Day 2 data revealed some treatment-related structure to the variation in the data. The first principal component describes most of the treatment-related variation (Figure 6.3). However, most of the animals treated with the low dose of allyl formate are separated from their controls along the second principal component. The high dose animals are well separated from the controls along the first principal component except for the chlorpromazine-dosed animals where three out of five animals are well separated along the first principal component. Some separation in animals treated with the three different compounds can be observed along the second component but this is partly explained by inter-study differences, as revealed by the controls. Thus, the high dose allyl formate animals are clearly separated from the high dose thioacetamide animals. However, the positions of the high dose chlorpromazine animals on the second principal component are not explainable simply by inter-study variation.

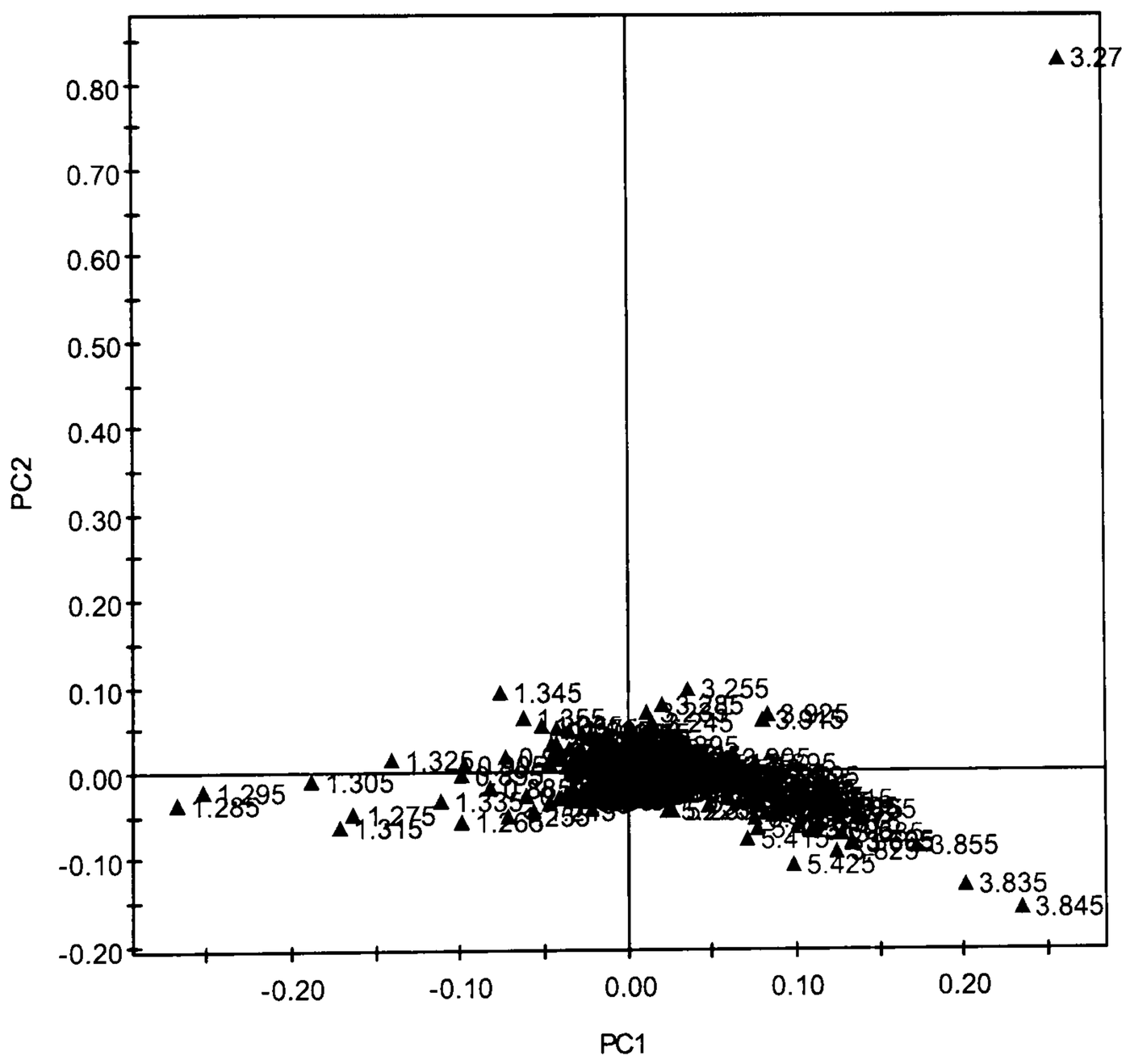

Figure 6.4 Corresponding PCA loadings plot for the first two components of the Day 2 standard 1D ^{1}H MAS NMR spectra of the three hepatotoxin-dosed liver samples.

The corresponding PCA loadings plot (Figure 6.4) indicated that increases in liver lipids and decreases in liver glucose are the main contributors to the separation between the control animals and the dosed-animals along the first principal component. In addition, some increase in the level of liver lactate can also be observed along the first principal component, which contributed to the separation between the dosed and control groups. Variation in the level of liver TMAO is the major contributor to the separation among the three hepatotoxin-groups on the second principal component, with the allyl formate group showing the highest TMAO level situated on the upper half of the scores plot, and the thioacetamide-dosed animals situated on the lower half of the scores plot showing lower liver TMAO level. However, there is also a clear difference in liver TMAO between the two control groups and so the TMAO difference between the high dose allyl formate and thioacetamide groups may not be especially significant. On the other hand, the lower level of TMAO in the high dose chlorpromazine group compared to the high dose allyl formate group is more likely to be significant as these data came from the same study.

6.3.2 PLS-DA of Liver NMR Data

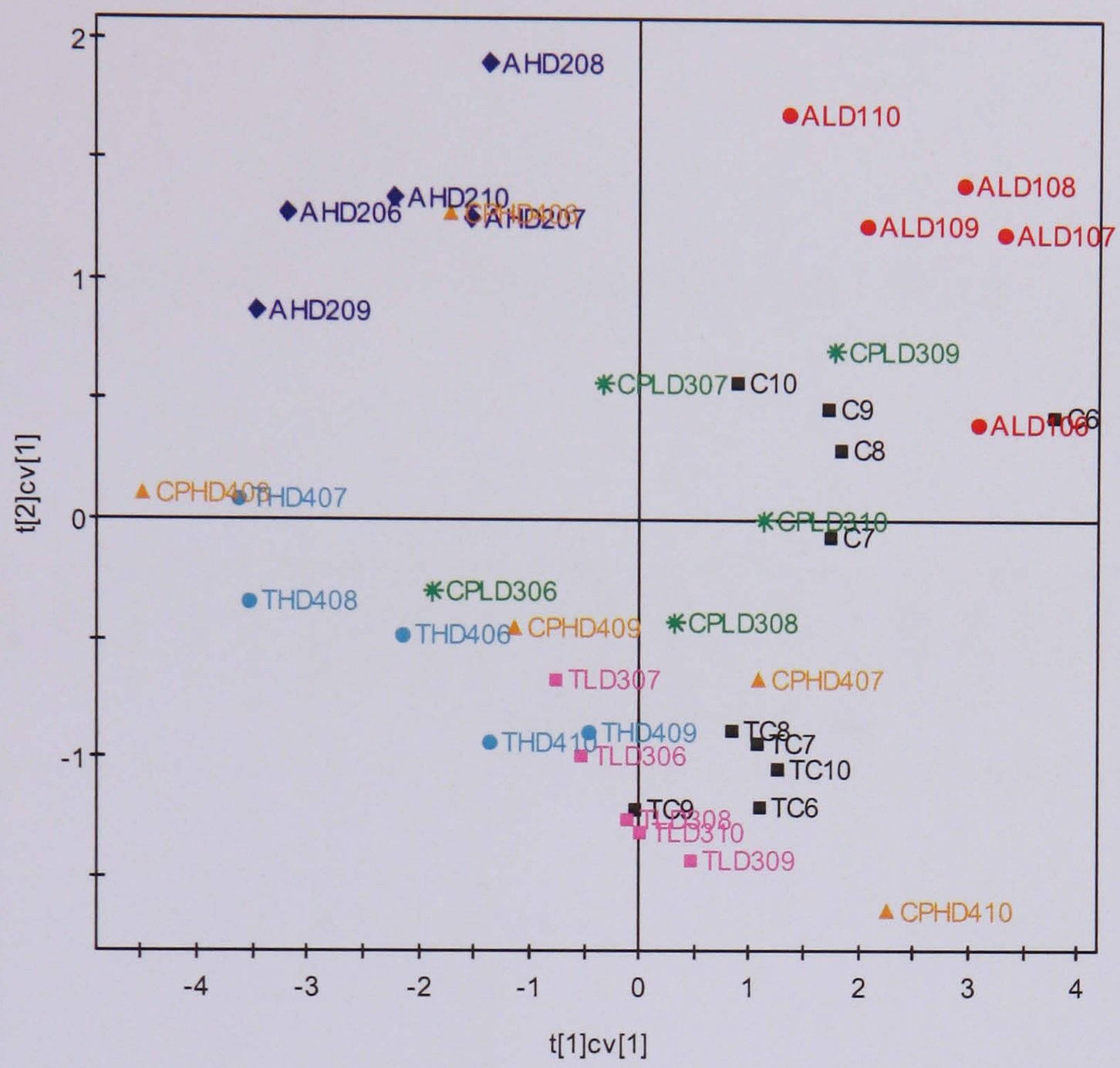

Figure 6.5 PLS-DA cross validated scores plot of the Day 2 standard 1D ^{1}H MAS NMR spectra of the three hepatotoxin-dosed liver samples.

To further refine the information recovery, a PLS-DA model was constructed on the standard 1D MAS NMR data of liver tissues. Figure 6.5 shows the X matrix cross validated scores of the first two components of the Day 2 tissue MAS NMR data. Overall the pattern observed is almost identical to that observed in the PCA scores plot (Figure 6.3). The scores plot shows some treatment-related separation along the first component. Compound-related structure can be observed along the second component with allyl formate-dosed animals situated in the upper half of the scores plot, thioacetamide-dosed animals situated in the lower half of the scores plot and chlorpromazine-dosed animals situated in both halves of the plot. However, the control groups of the two studies remain separated along the second PLS component and this separation parallels that of the allyl formate and thioacetamide dosed animals.

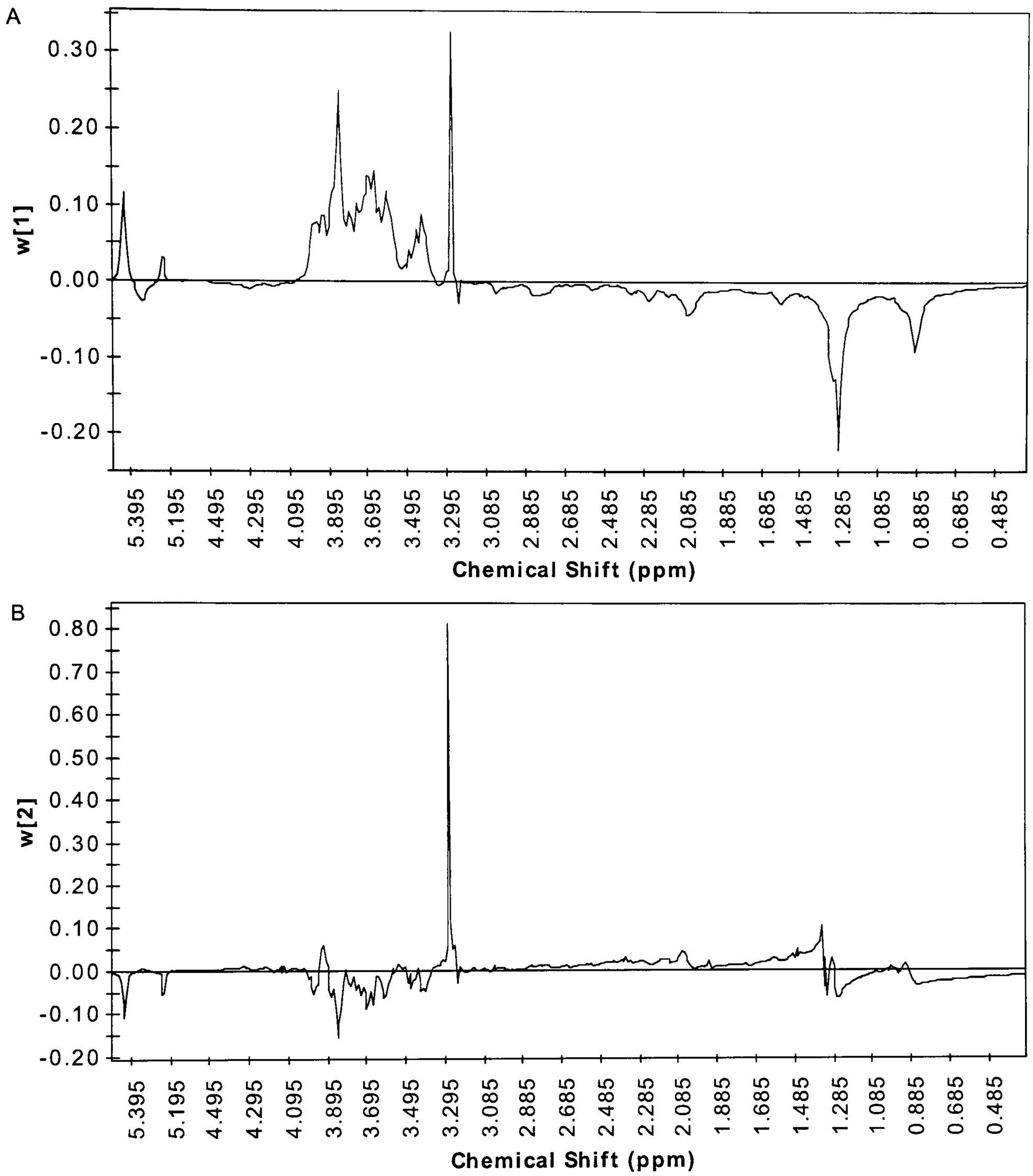

Figure 6.6 Corresponding PLS-DA loadings plot for the first two components (A and B) of the Day 2 standard 1D ^{1}H MAS NMR spectra of the three hepatotoxin-dosed liver samples.

The corresponding X block PLS loadings shown in Figure 6.6 indicates that the first component, describing the general effects of dosing on the animals, is due to increases in liver lipid profiles and decreases in liver TMAO, glucose and glycogen levels. However, the second component mainly describes variation in the liver TMAO level, which is partly study-related as evidenced by the separation of the two sets of controls. Animals treated with high dose of chlorpromazine are separated into two sub-groups with animals 407 and 410 being more like the controls for the two studies and animals 406, 408 and 409 showing changes typical of the high doses of allyl formate and thioacetamide. The latter are the ones that showed chlorpromazine-induced ketosis.

6.4 Global Pattern Recognition of Day 2 CPMG NMR Spectra of Plasma

PCA and PLS-DA analysis were performed on all CPMG 1D NMR spectra of Day 2 plasma samples for all three hepatotoxins. The CPMG NMR spectra were used in preference to the standard 1D NMR spectra because experience indicated that better discrimination is provided by the former in pattern recognition analysis. The data were combined, normalised and mean-centred prior to modelling. In the scores plot, the data points are labelled and colour-coded so as to identify the treatment and animal number. For the loadings plot, the data points are labelled according to the plasma spectral segment that they represent.

6.4.1 PCA of Plasma NMR Data

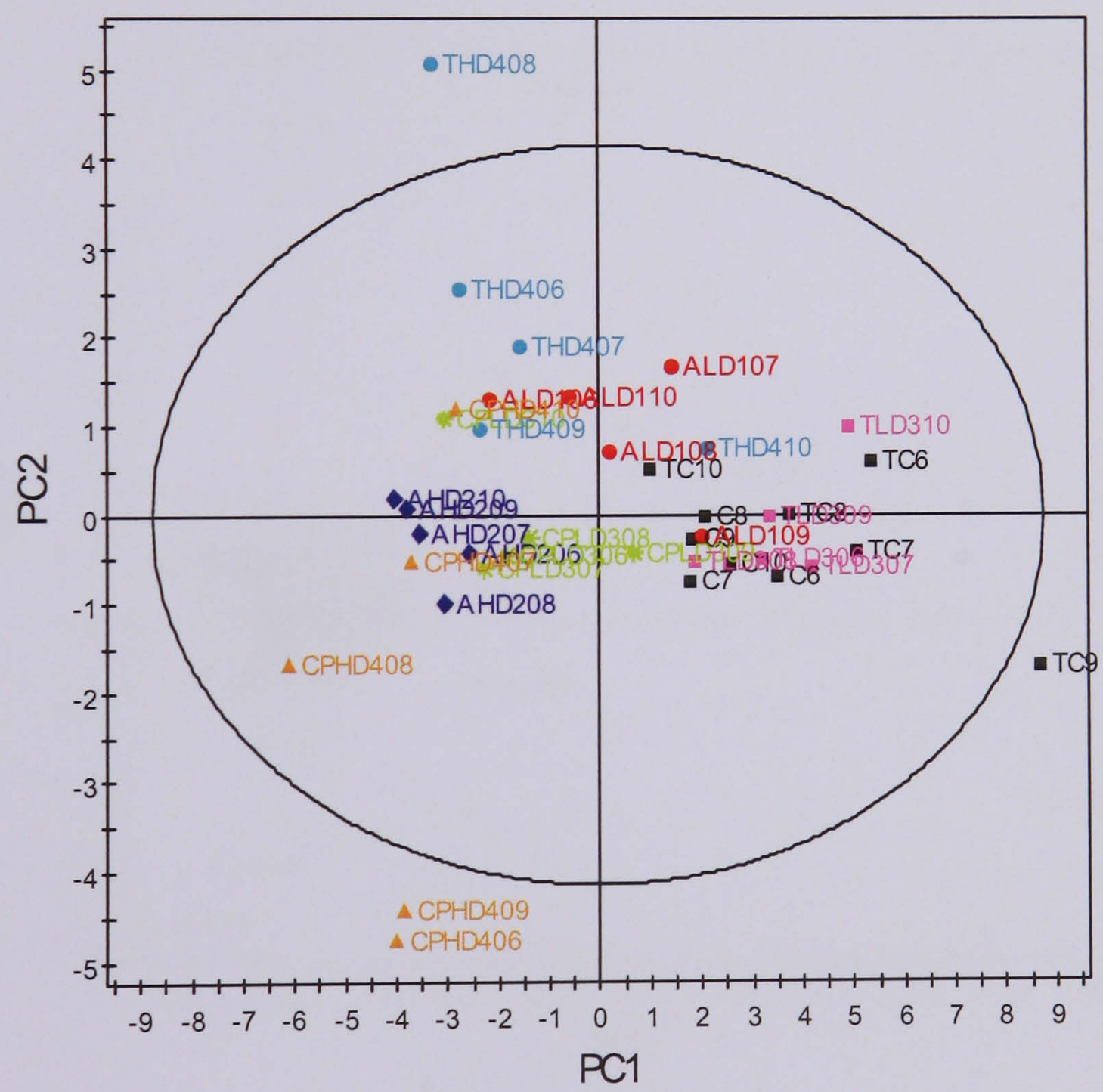

Figure 6.7 PCA scores plot for the first two components of the Day 2 plasma CPMG ^{1}H NMR spectra of the three hepatotoxin-dosed liver samples.

Figure 6.7 shows the scores plot for the first two components of the control/dose Day 2 plasma CPMG NMR data. Little separation between the two control groups can be seen in the scores plot as compare to the scores plot of the tissue MAS NMR data (Figure 6.3). The scores plot shows clear treatment-related separation along the first principal component especially between the high dose and control animals. Some compound-related variation can also be observed along the second principal component. In addition, the scores plot also revealed four outliers, animals CPHD 406 and 409, animal THD408 and control animals TC9. Spectral inspection revealed that both animals CPHD 406 and 409 have higher plasma 3-D-hydroxybutyrate and lower plasma lactate content. Animal THD408 showed higher lactate content as compared to the rest of the high dose thioacetamide-treated animals. Control animal TC9, on the other hand, showed higher plasma VLDL content as compare to the rest of the control animals.

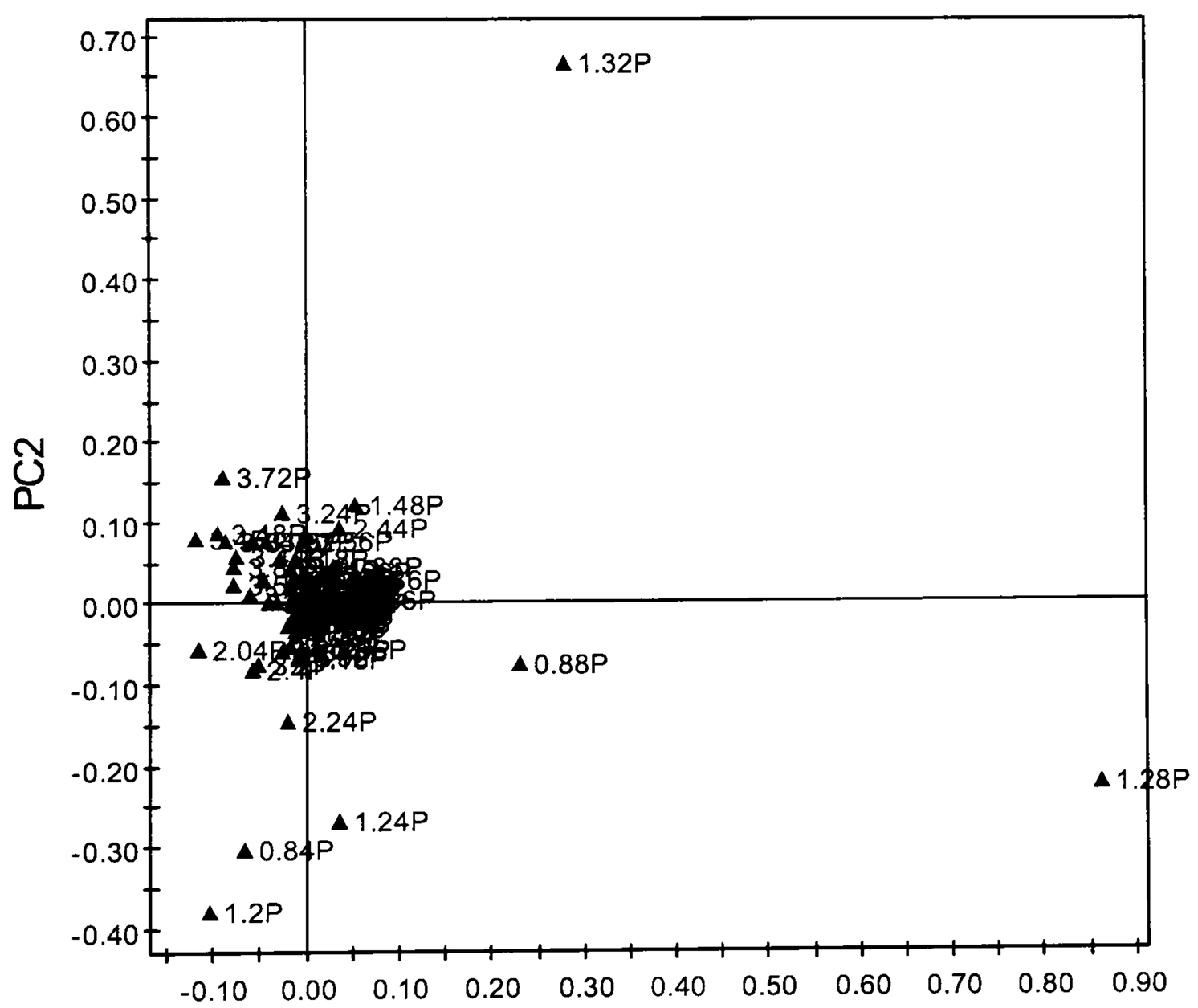

Figure 6.8 Corresponding PCA loadings plot for the first two components of the Day 2 plasma CPMG ^{1}H NMR spectra of the three hepatotoxin-dosed liver samples.

The corresponding loadings plot of the PCA model (Figure 6.8) indicates that decreases in plasma lipid profiles are the major contributor to the separation between the dosed and control animals along the first principal component. The loadings plot also shows changes in plasma lactate, acetoacetate and 3-D-hydroxybutyrate levels as the contributors to compound-related variations along the second principal component. The changes observed in the loadings plot agrees with the changes observe in the plasma NMR spectra whereby visual inspection of the corresponding NMR spectra reveals that both animals CPHD 406 and 409 showed signs of ketosis represented by elevated 3-D-hydroxybutyrate and acetoacetate. Visual inspection of the NMR spectra of animal TH408 shows clear increase in plasma lactate and control animal TC9 showed higher plasma lipids content as compare to the rest of the control animals.

6.4.2 PLS-DA of Plasma NMR Data

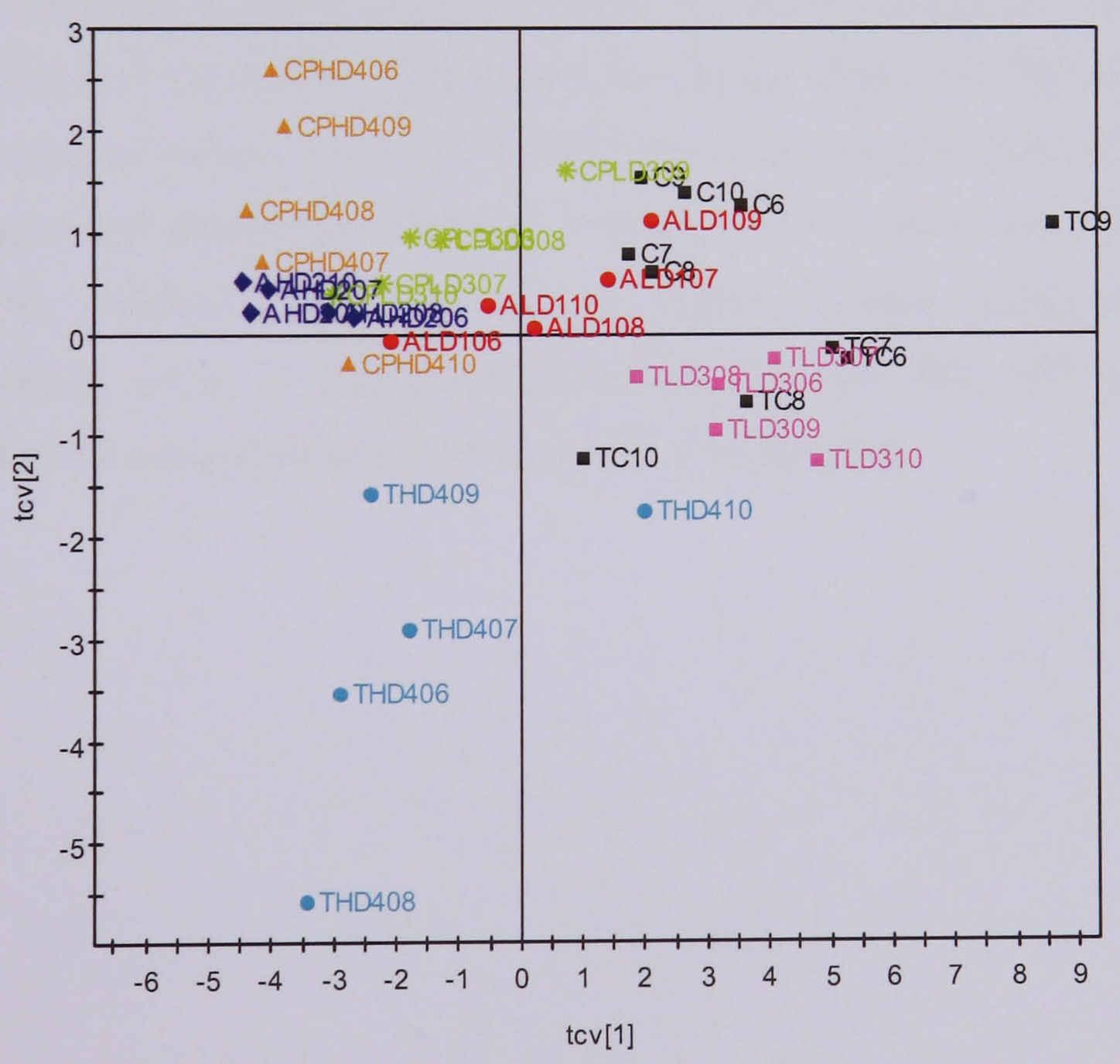

Figure 6.9 PLS-DA cross validate scores plot of the Day 2 plasma CPMG ^{1}H NMR spectra of the three hepatotoxin-dosed liver samples.

Figure 6.9 shows the X matrix cross validated scores plot for the first two components of the Day 2 plasma NMR data. Animals treated with high dose of all three hepatotoxins were clearly separated from the control animals along the first component. The second component describes the variation between the different compounds with animals dosed with high dose thioacetamide situated on the lower left quadrant of the scores plot. Animals treated with high dose allyl formate are located between the thioacetamide and chlorpromazine high dose animals along the second component. The scores plot also showed some degree of overlap between the high dose chlorpromazine animals and the high dose allyl formate animals. However, in the high dose of chlorpromazine, animals showing ketosis (animals 406, 408 and 409) are clearly separated from the remaining two animals along the second PLS component.

The corresponding loadings plot (Figure 6.10A) indicated that a decrease in plasma lipids is the major contributor to the separation between the dosed animals and the control animals along the first PLS component. The second component (Figure 6.10B) is partly related to changes in plasma lactate. Animals treated with thioacetamide showed higher levels of plasma lactate and alanine as compared to that of allyl formate and chlorpromazine. In addition, the loadings plot also reveals higher plasma acetoacetate and 3-D-hydroxybutyrate levels in chlorpromazine-dosed animals 406, 408 and 409, which contributed to the separation along the second PLS component.

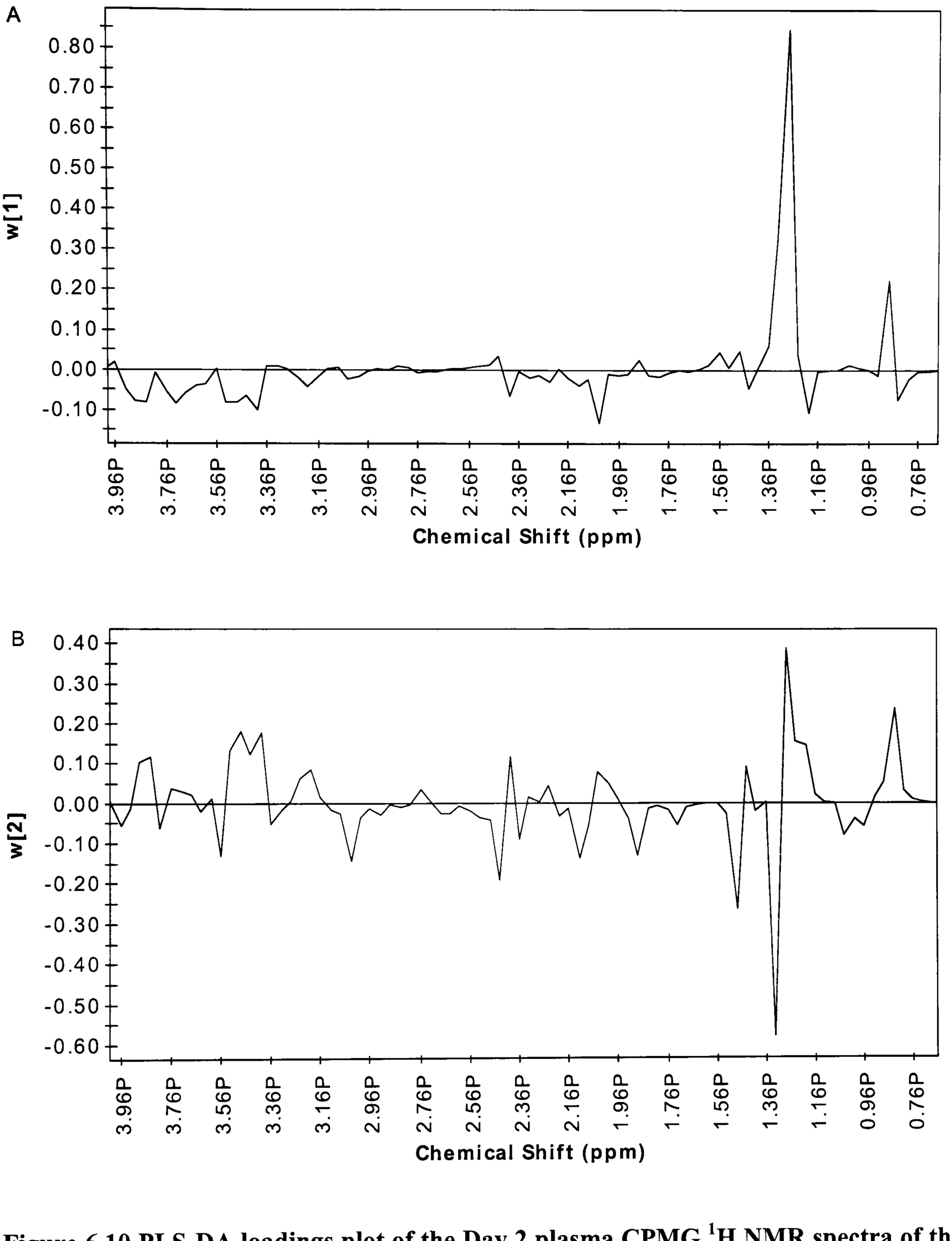

Figure 6.10 PLS-DA loadings plot of the Day 2 plasma CPMG ^{1}H NMR spectra of the three hepatotoxin-dosed liver samples.

6.5 Global Pattern Recognition of Combined Day 2 Liver and Plasma NMR Data

6.5.1 PCA of Liver and Plasma NMR Data

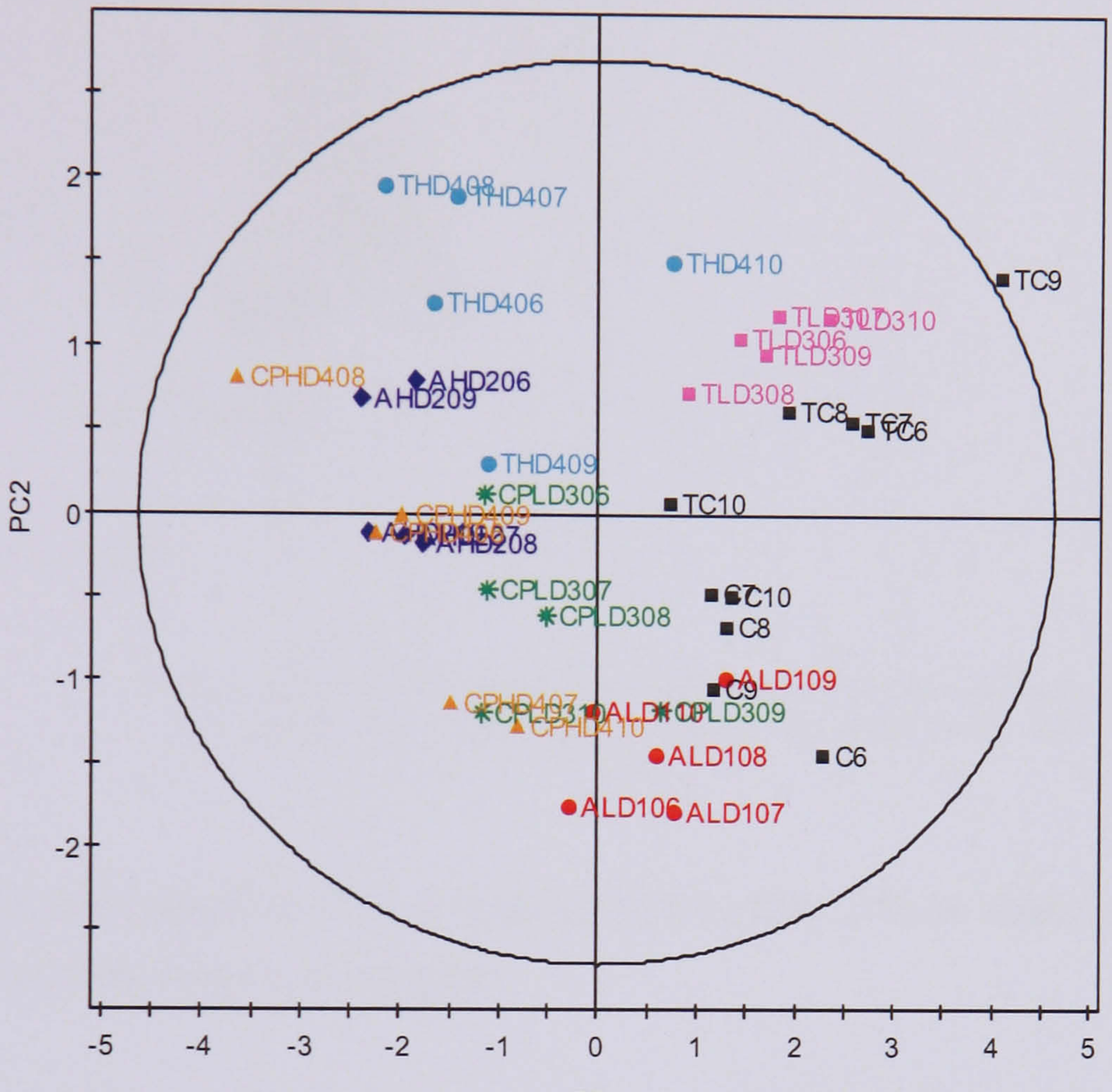

Figure 6.11 PCA scores plot of Day 2 liver tissue and plasma ^{1}H NMR spectra of the three hepatotoxins.

PCA was performed on concatenated liver and plasma NMR data and Figure 6.11 shows the resulting scores and loadings plots. The high dose animals are largely separated from the controls along the first principal component. In addition, the high dose thioacetamide animals are separated from the high dose allyl formate animals along the second principal component, which corresponds to the separation between their control groups. The high dose chlorpromazine animals are separated into two sub-groups with the three ketotic animals (animals 406, 408 and 409) separated from the two non-ketotic animals. The non-ketotic high dose chlorpromazine animals were clearly separated from the rest of the high dose animals along the second principal component.

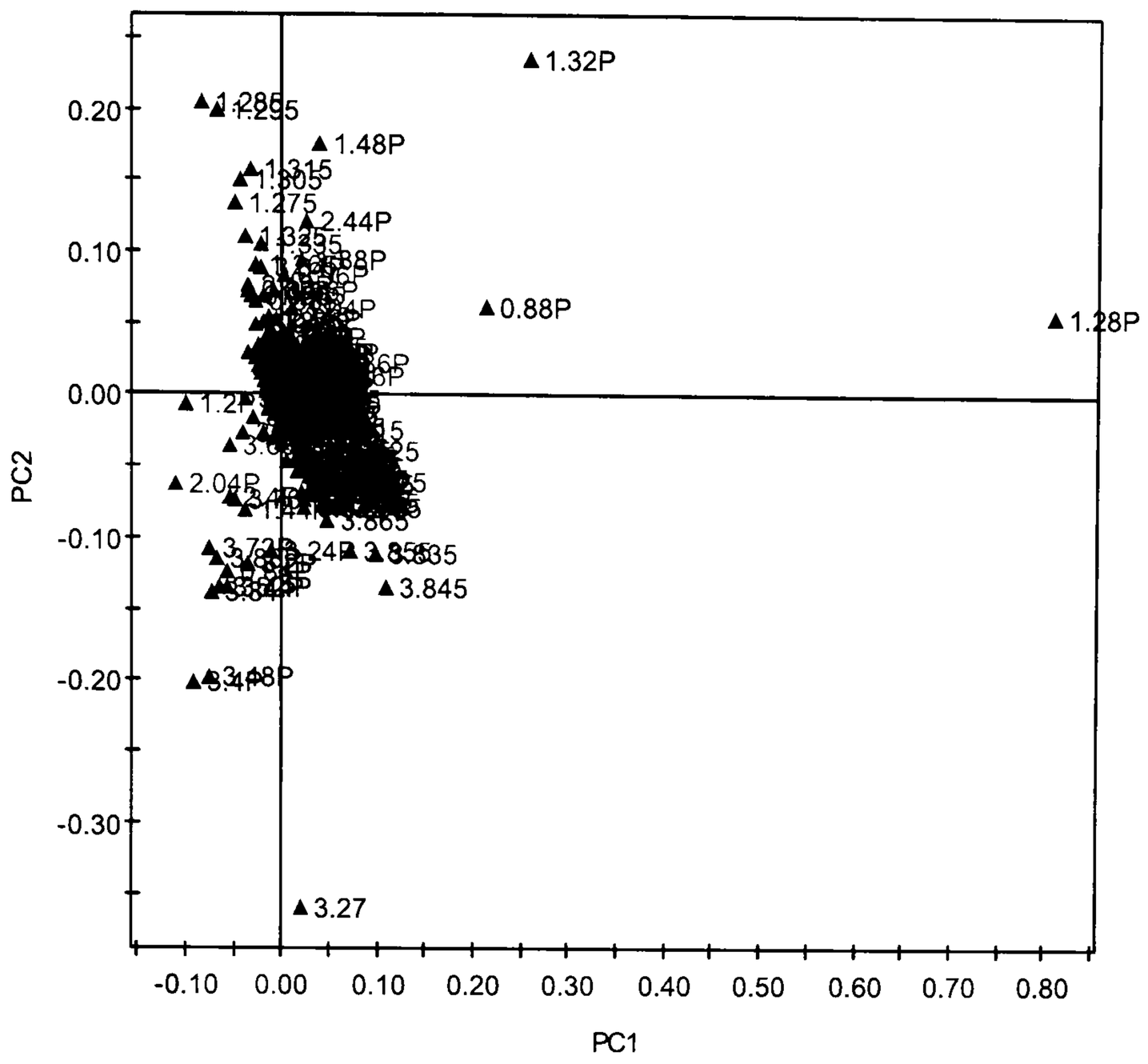

Figure 6.12 Corresponding PCA Loadings plot of Day 2 liver tissue and plasma ^{1}H NMR spectra of the three hepatotoxins.

The corresponding PCA loadings plot (Figure 6.12) revealed that a decrease in plasma lipids in toxin-related animals is the major contributor to the separation along the first principal component whereas increases in liver lipids and decreases in liver TMAO, glucose and glycogen as well as increase in plasma lactate are the major contributors to the separation along the second principal component. The loadings plot also indicates that the high dose thioacetamide-treated animals have higher liver lipids and plasma alanine and lactate content as compared to that of the allyl formate and chlorpromazine treated animals. The general effects of high dose allyl formate seems to be increases in liver lipids and decreases in glucose and glycogen content as well as decrease in plasma lipids. The loadings plot also showed that increases in plasma 3-D-hydroxybutyrate and acetoacetate (ketone bodies) are the major contributor to the separation within the high dose chlorpromazine animals. Although chlorpromazine inhibits the formation of TMAO in the rats, the loadings plot does not reflect its effect. However, looking at the separation

between the two control groups in the PCA scores plot (Figure 6.11), the loadings plot indicated that variation in the liver TMAO level is the major contributor to the separation of the two control groups and visual inspection of the corresponding liver NMR spectra showed that all thioacetamide control animals have lower TMAO levels as compare to the other control animals. The results indicated that both groups of control animals are biochemically non-identical and that they have different biological starting point prior to the commencement of the study.

6.5.2 PLS-DA of Liver and Plasma NMR Data

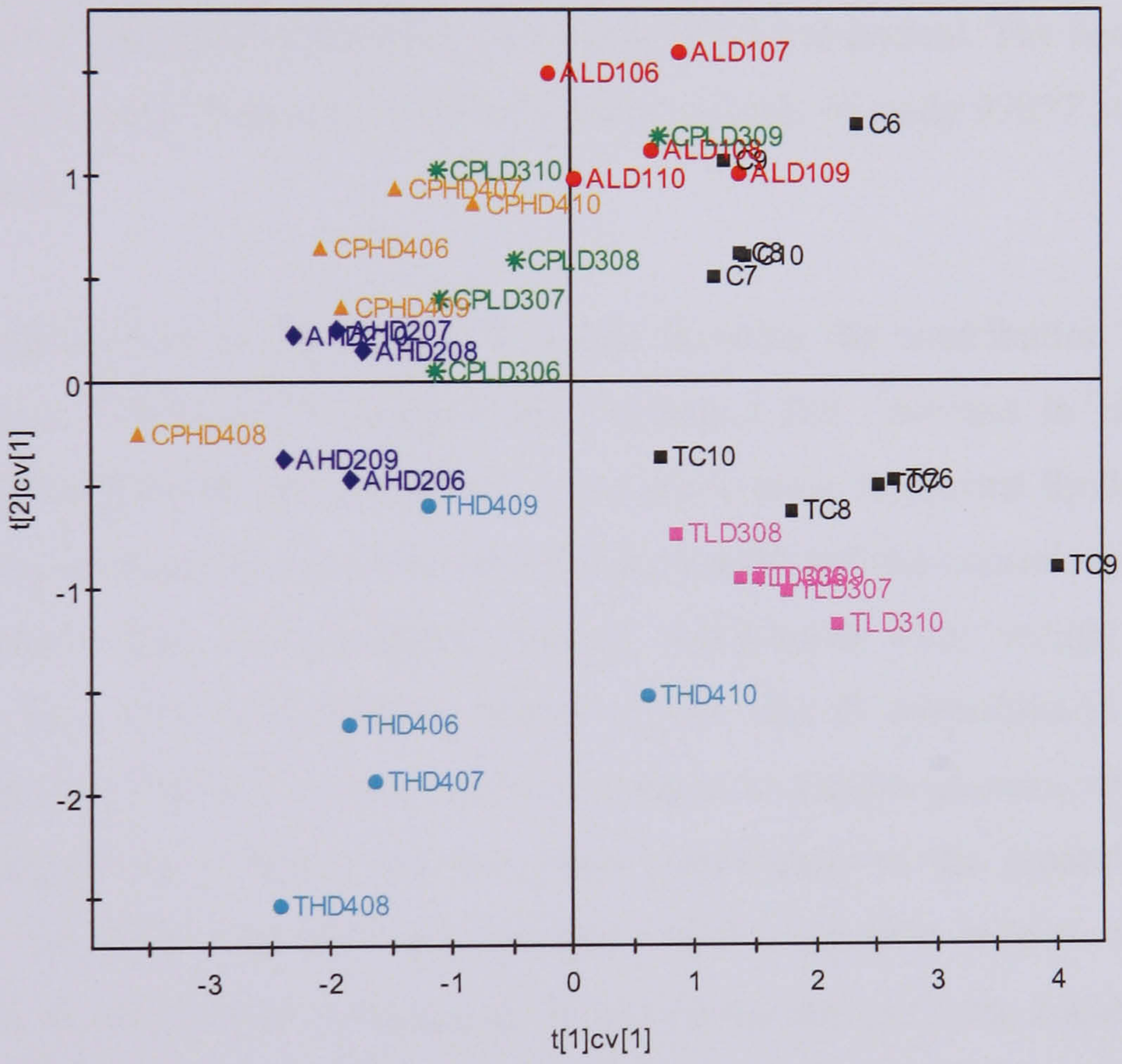

Figure 6.13 PLS-DA cross validated scores plot of Day 2 liver tissue and plasma ^{1}H NMR spectra of the three hepatotoxins.

The Day 2 liver and plasma NMR data was analysed using PLS-DA approach to further refine the information recovery. The data was mean centered prior to modelling. Figure 6.13 shows the cross validated scores plot for the first two components of the data set. The scores plot shows an improvement in the separation between the dosed animals and the control animals as well as the separation in animals treated with the three different hepatotoxins as compare to the PCA scores plot in Figure 6.11. Clear separation can be seen among animals treated with the different hepatotoxins along the second component although some overlap can still be seen. Animals treated with high dose of thioacetamide are separated from the rest of the high dose animals along the second PLS component. Animals treated with high dose of allyl formate are partially separated from animals treated with high dose of chlorpromazine along the second PLS component. The control animals of study 98053 are clearly separated from the control animals of study 99057 along the second PLS component.

The corresponding first component PLS weight showing the contribution from liver and plasma (Figure 6.14A and B respectively) indicated that increase in liver lipids and decreases in liver glucose and glycogen as well as decrease in plasma lipids are the major contributors to the separation between the dosed animals and the control animals along the first component. The corresponding second component PLS weight showing the contribution from liver and plasma (Figure 6.15A and B respectively) indicated that differences in liver TMAO level as well as changes in plasma glucose, creatine, alanine, lactate, glutamine and pyruvate are the major contributors to the separation in animals treated with the three different hepatotoxins. Again, animals treated with high dose thioacetamide showed higher lactate, alanine, glutamine and pyruvate content as compared to animals treated with allyl formate and chlorpromazine respectively. The difference in liver TMAO content in the control animals dominates the second component loadings plot thus shadowing the effects of chlorpromazine on the biological samples.

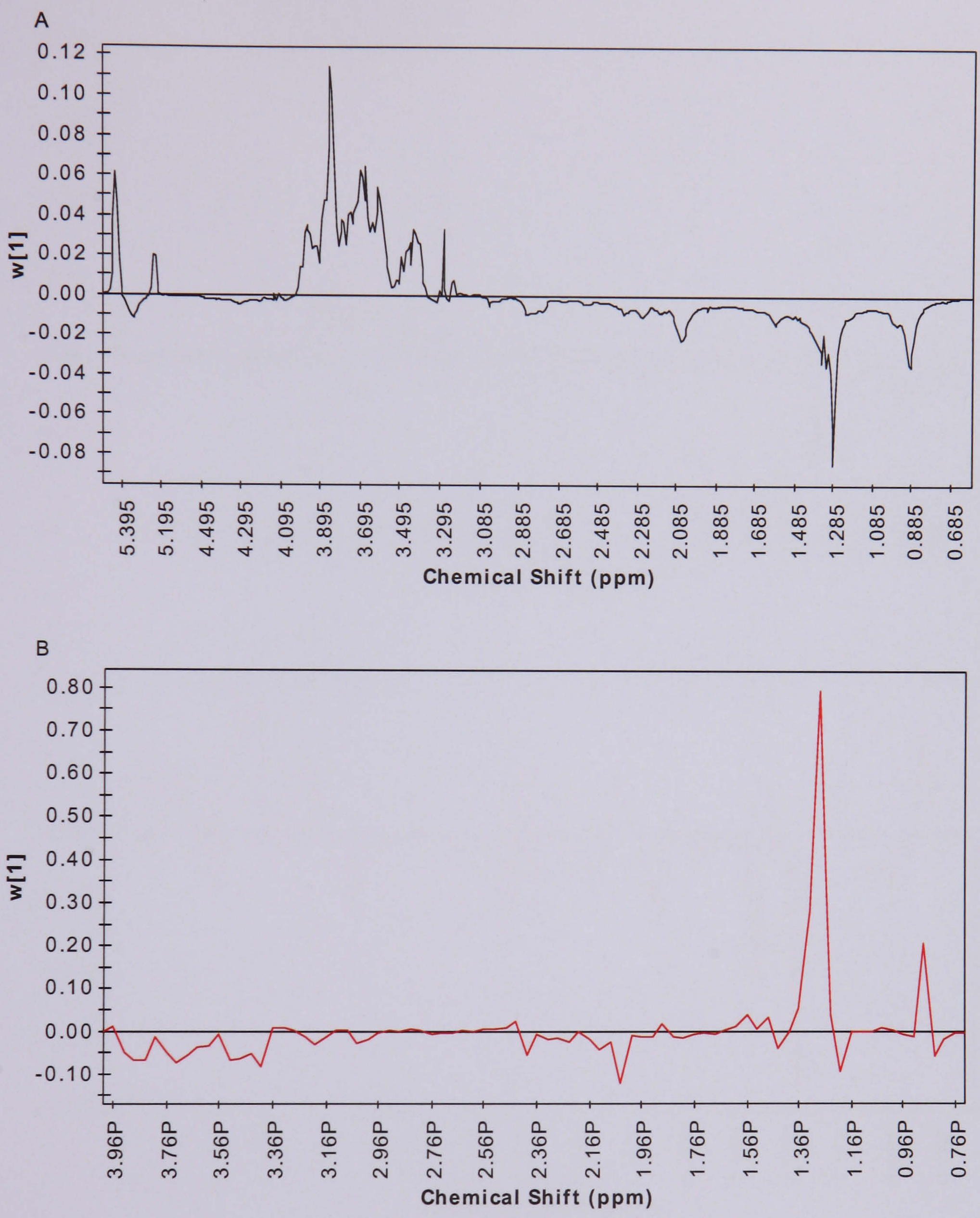

Figure 6.14 First component PLS weight (W[1]) from the PLS-DA model attributed to (A) standard 1D ^{1}H MAS NMR data of Day 2 liver tissues (—), and (B) CPMG ^{1}H NMR data of Day 2 plasma samples (—).

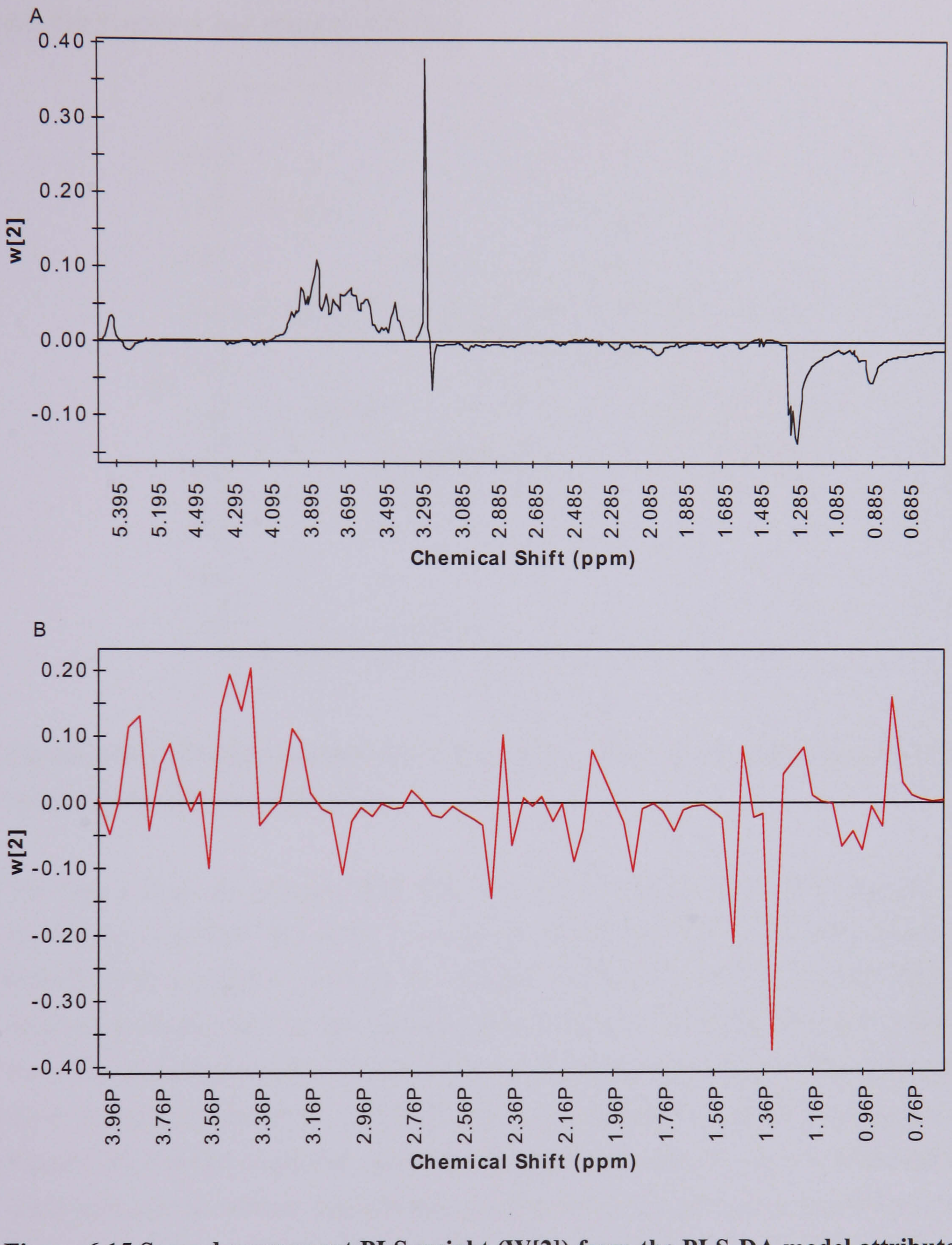

Figure 6.15 Second component PLS weight (W[2]) from the PLS-DA model attributed to (A) standard 1D ^{1}H MAS NMR data of Day 2 liver tissues (—), and (B) CPMG ^{1}H NMR data of Day 2 plasma samples (—).

6.5.3 PLS of Liver and Plasma NMR Data

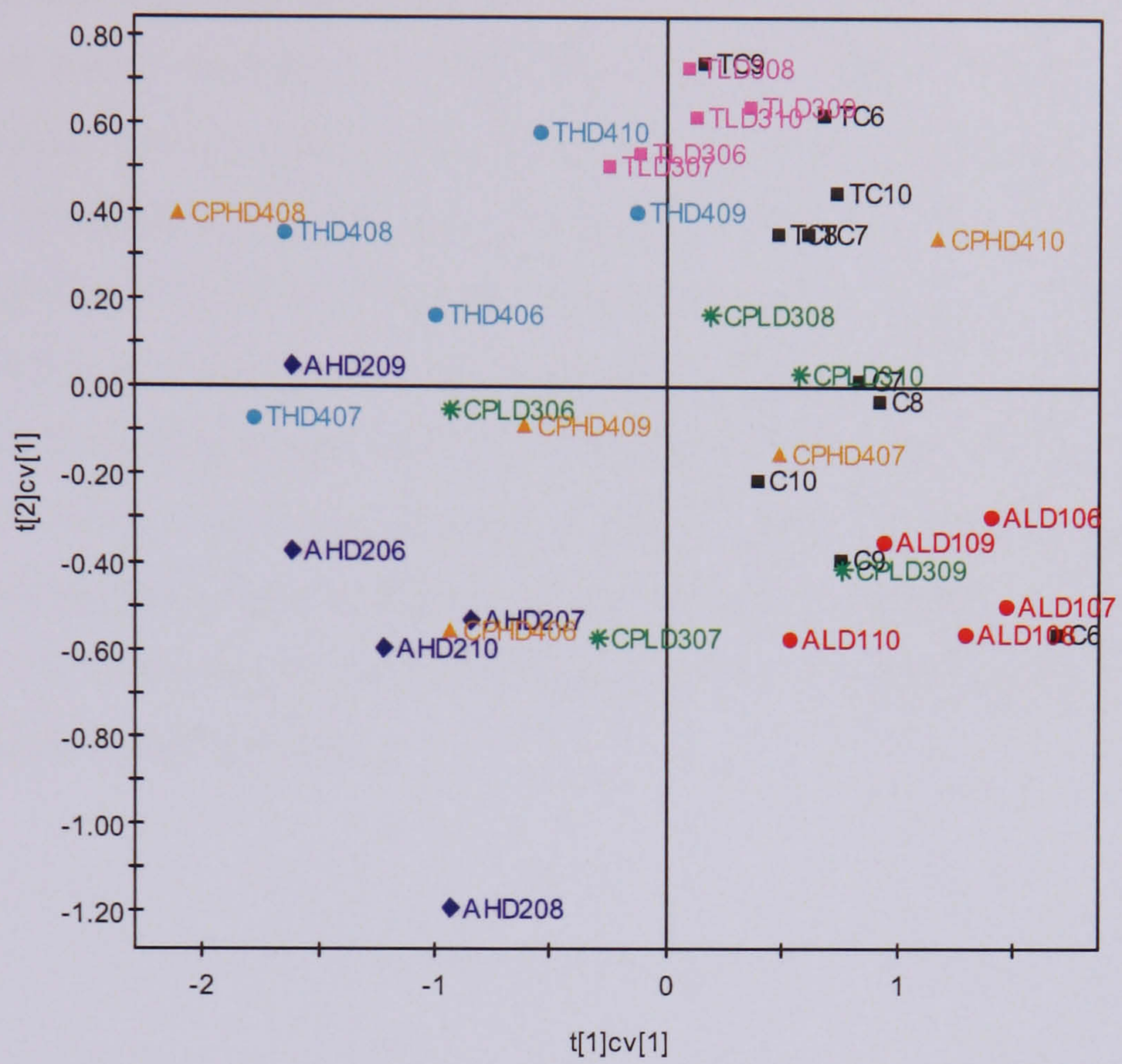

Figure 6.16 PLS cross validated scores plot of Day 2 liver tissue and plasma ^{1}H NMR spectra of the three hepatotoxins.

The Day 2 liver and plasma NMR data was further analysed using PLS approach by treating the liver NMR data as the X matrix and the plasma NMR data as the Y matrix in order to find correlations between the changes observed in the liver and the changes observed in the plasma. The data was mean centered prior to modelling. Figure 6.16 shows the cross validated scores plot for the first two components of the data set. The scores plot shows no improvement in the separation achieved as compared to the PCA scores plot in Figure 6.13. The first component describes the variation between the dosed animals and the control animals. In addition, the high dose chlorpromazine animals were separated into two sub-groups, with animals 406, 408 and 409 separated from animals 407 and 410 along the first PLS component. The second PLS component is dominated by the inter-study variations.

The first component PLS weights (Figure 6.17A and B respectively) indicated that increase in liver lipids and decreases in liver glucose and glycogen as well as decreases in plasma lipids are the major contributors to the separation between the dosed and the control animals along the first component. The loadings also showed a correlation in lipid changes between the liver samples and the plasma samples. In addition, the loadings indicated that increases in plasma 3-D-hydroxybutyrate and acetoacetate are the major contributors to the separation within the high dose chlorpromazine-treated rats. The corresponding second component PLS weights (Figure 6.18A and B respectively) indicated that differences in liver TMAO level as well as changes in plasma glucose, creatine, alanine, lactate, glutamine and pyruvate are the major contributors to the separation in the second PLS component. The difference in liver TMAO content of the control animals dominates the second component loadings plot.

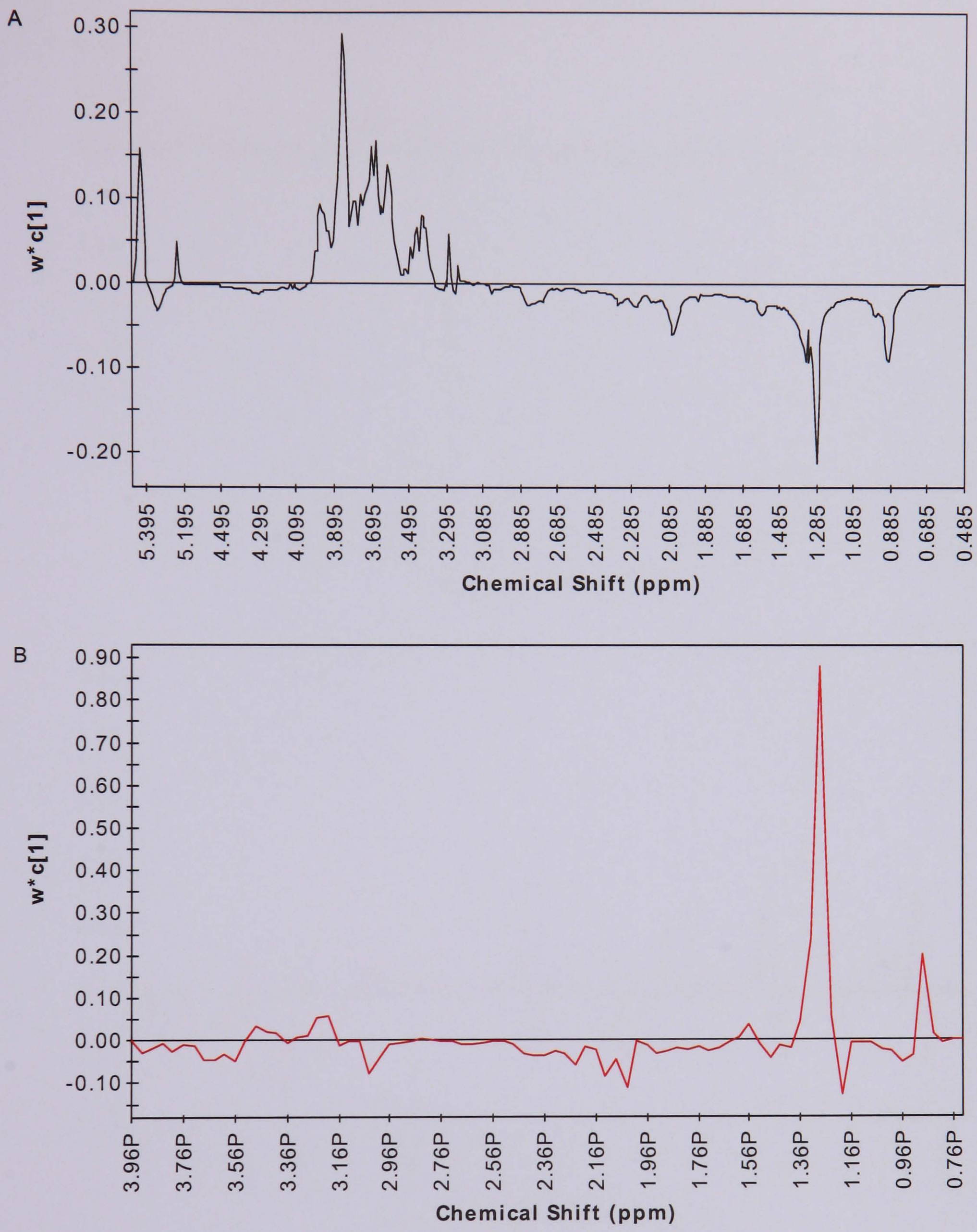

Figure 6.17 First component PLS weight (W*c[1]) from the PLS model attributed to (A) standard 1D ^{1}H MAS NMR data of Day 2 liver tissues (—), and (B) CPMG ^{1}H NMR data of Day 2 plasma samples (—).

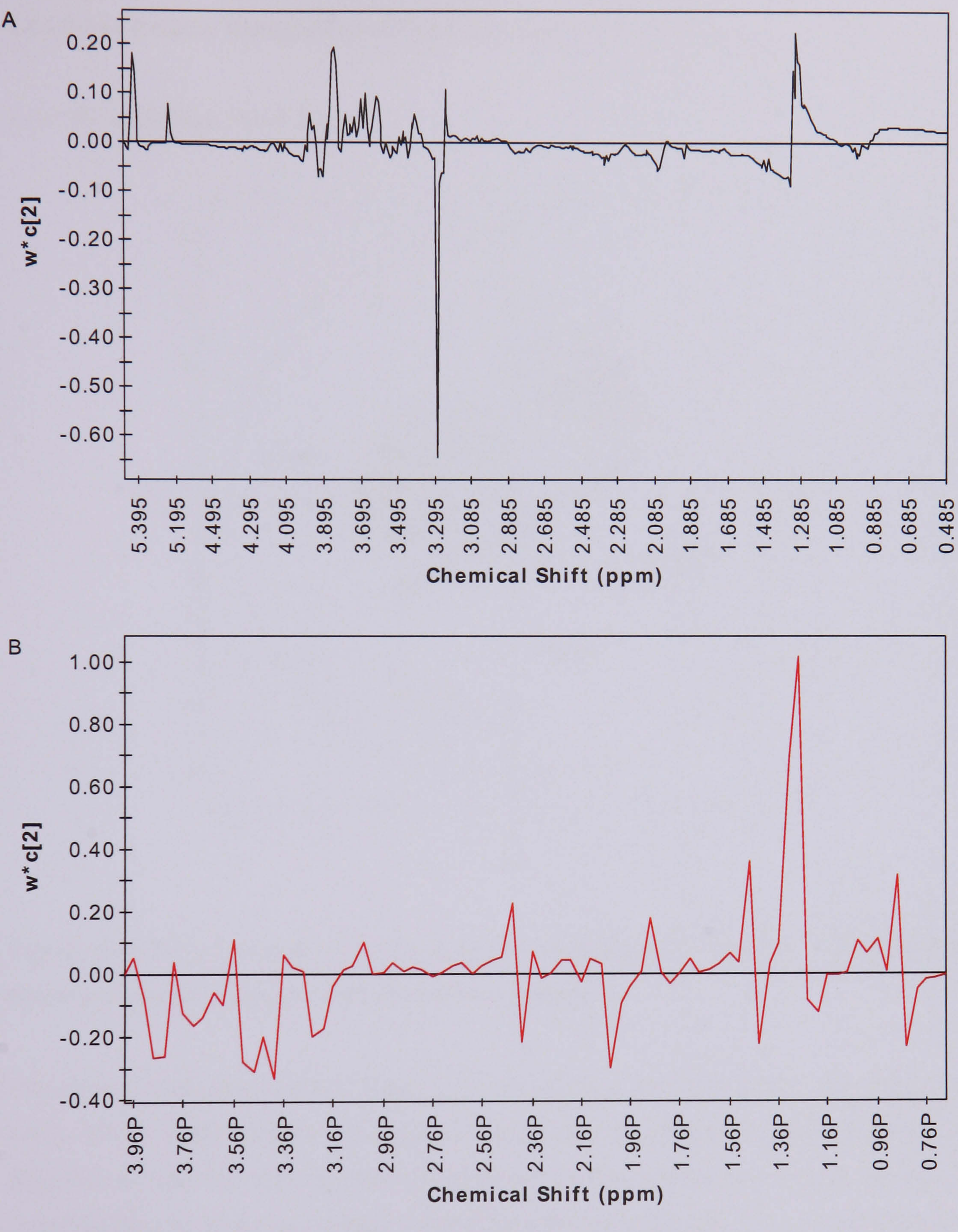

Figure 6.18 Second component PLS weight (W*c[2]) from the PLS model attributed to (A) standard 1D ^{1}H MAS NMR data of Day 2 liver tissues (—), and (B) CPMG ^{1}H NMR data of Day 2 plasma samples (—).

6.6 Global Pattern Recognition of Day 2 Standard 1D NMR Spectra of Urine

6.6.1 PCA of Urine NMR Data

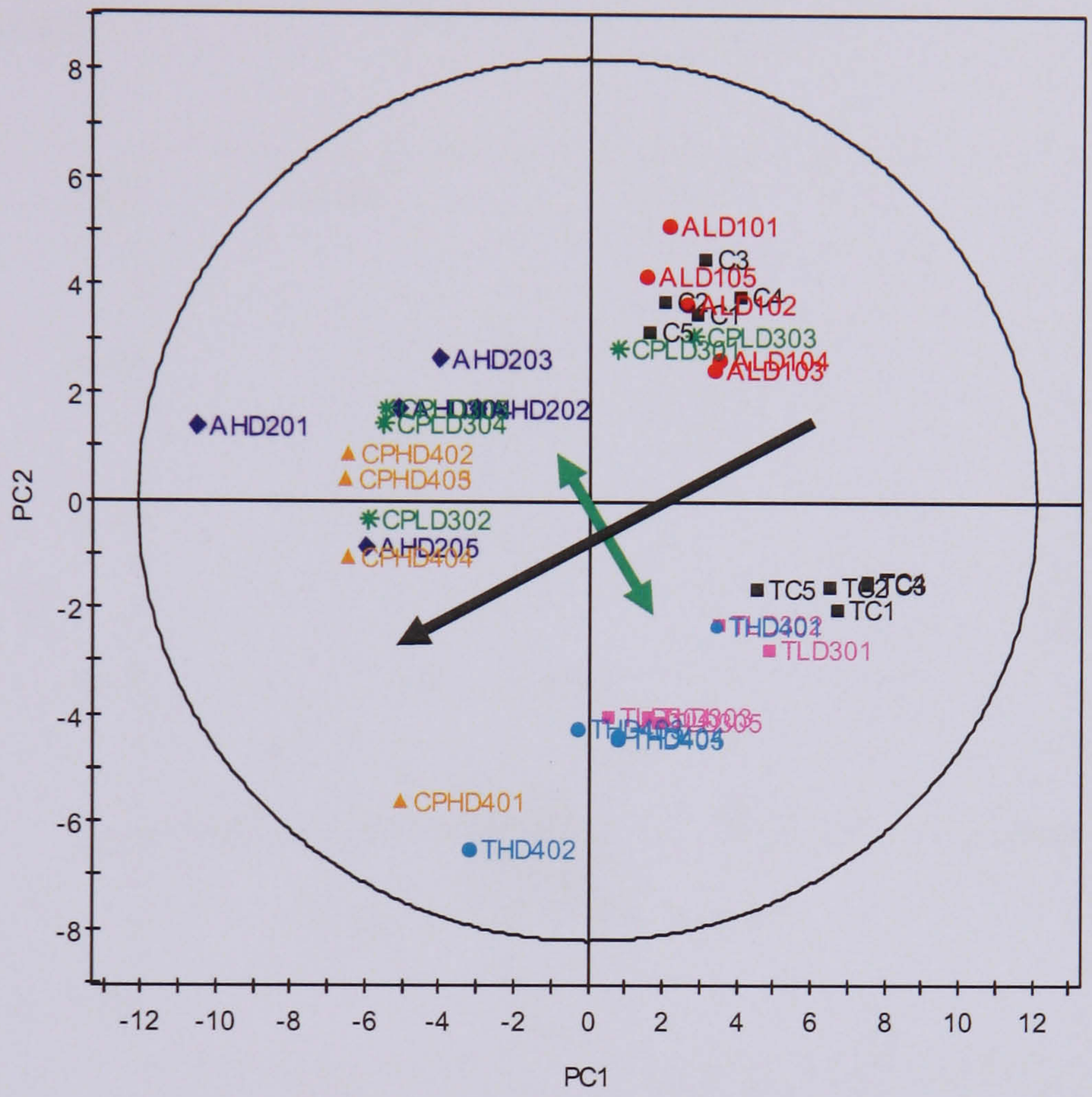

Figure 6.19 PCA scores plot for the first two components of the Day 2 urine ^{1}H NMR spectra of the three hepatotoxin-dosed liver samples.

Principal components analysis shows that the animals were separated into two groups, Study 98053 (allyl formate and chlorpromazine) and Study 99057 (thioacetamide) on a diagonal as can be seen by the green arrow in the scores plot (Figure 6.19). The corresponding loadings plot (Figure 6.20) indicated that difference in urinary TMAO is the major contributor to the separation between the two clusters of animals. Animals in Study 98053 have higher urinary TMAO level as compare to that of Study 99057. The differences in urinary TMAO level dominated the PCA model therefore rendering the model less interpretable although some dose related variation can still be observed along the second

principal component. The loadings plot indicated that changes in urinary endogenous metabolites are the major contributors to the separation along a diagonal from high PC1/PC2 to low PC1/PC2, as indicated by the black arrow in the scores plot, with increases in taurine and creatine, and decreases in urinary citrate, hippurate and 2-oxoglutarate featuring strongly.

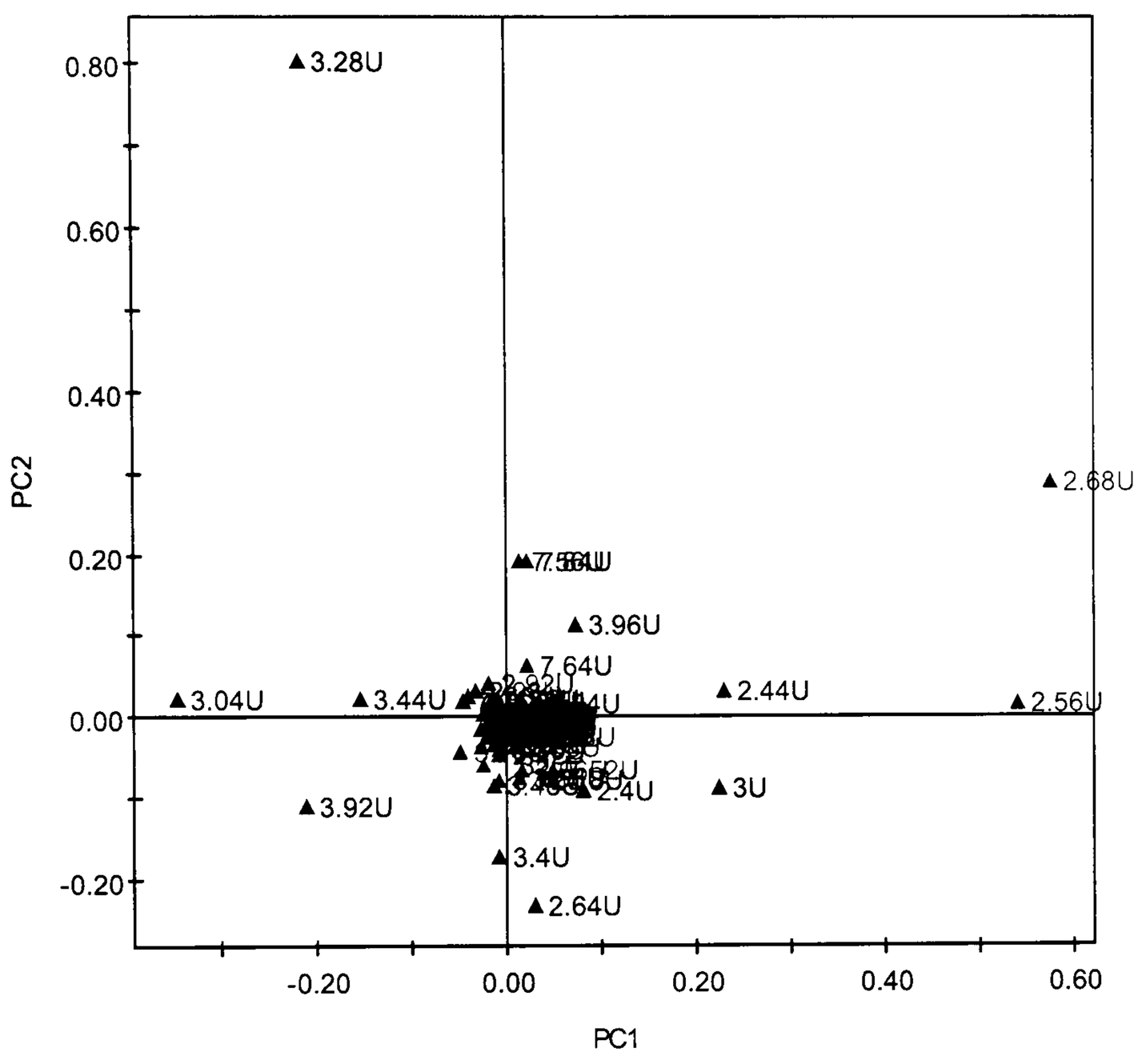

Figure 6.20 Corresponding PCA loadings plot for the first two components of the Day 2 urine ^{1}H NMR spectra of the three hepatotoxin-dosed liver samples.

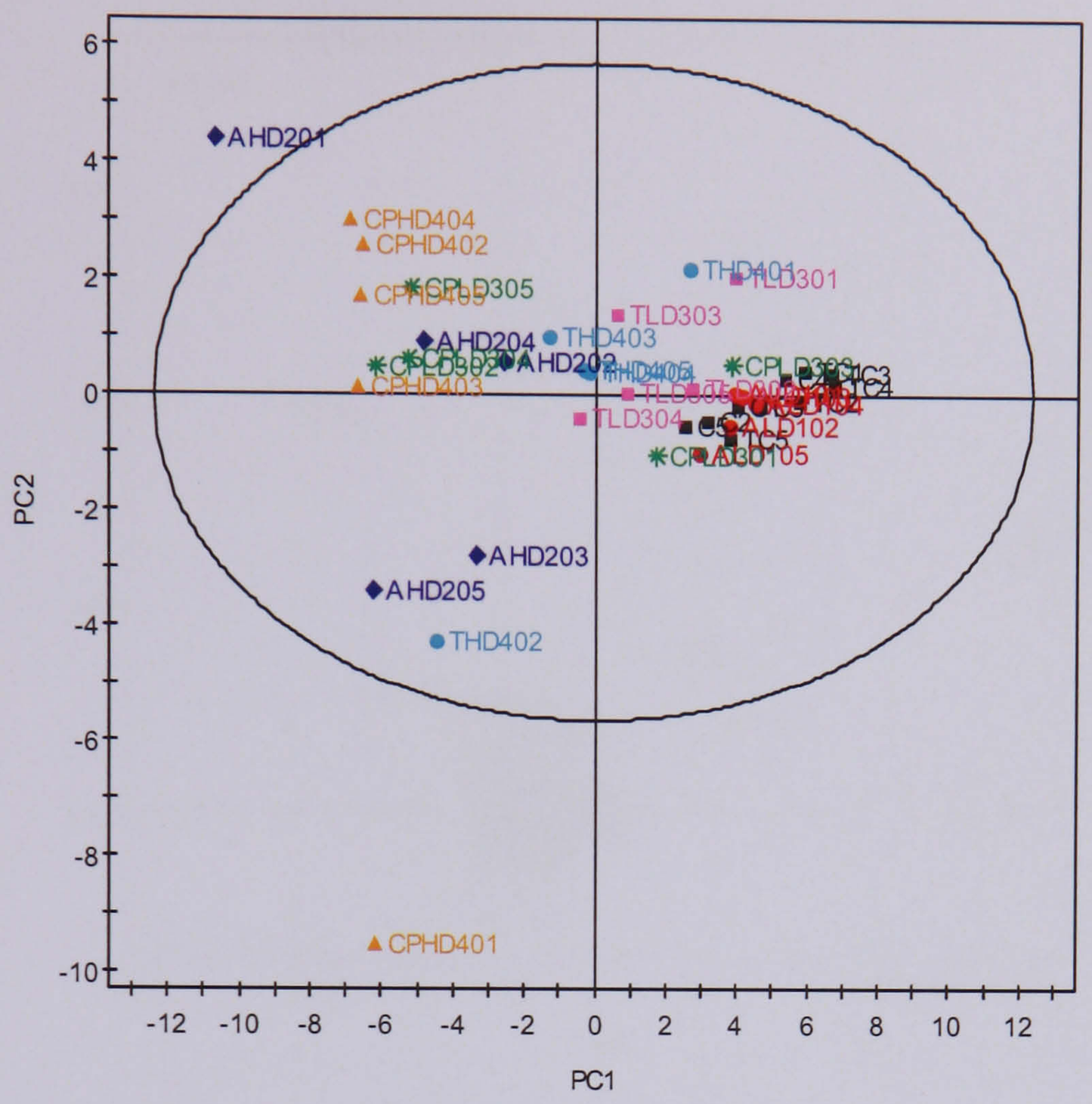

Figure 6.21 Resultant PCA scores plot for the first two components of the Day 2 urine ^{1}H NMR spectra of the three hepatotoxin-dosed liver samples with bucket 3.28 removed.

Due to the dominating effect of TMAO on the interpretability of the PCA model, the buckets representing TMAO was removed and the data were renormalised and mean centre-scaled prior to PCA analysis. Figure 6.21 shows the resultant PCA scores plot for the first two components after the removal of TMAO bucket. The scores plot shows improved interpretability of the PCA model with the two sets of controls overlapping and dose-variation seen in the first principal component. Clear separation between the dosed and control animals can be observed mainly along the first principal component. In addition, variation in the high dose animals can be observed on the second principal component.

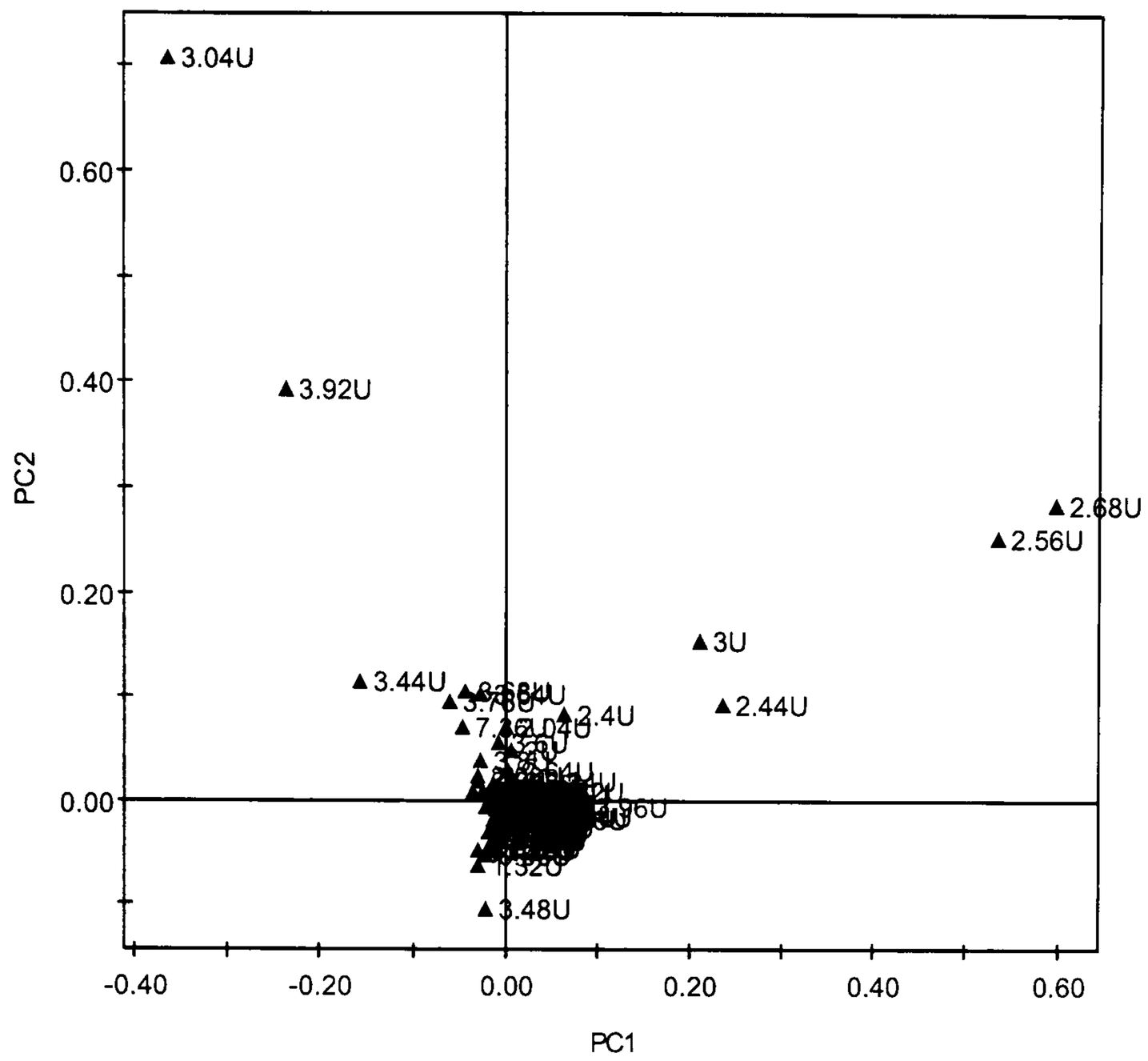

Figure 6.22 Resultant PCA loadings plot for the first two components of the Day 2 urine ^{1}H NMR spectra of the three hepatotoxin-dosed liver samples with bucket 3.28 removed.

The corresponding loadings plot (Figure 6.22) indicated that changes in urinary endogenous metabolites are the major contributors to the separation along the first principal component with increases in taurine and creatine, and decreases in citrate, hippurate and 2-oxoglutarate as major factors. Additionally, a change in urinary PAG was also detected but was not as clear as the other changes. Variation in the urinary creatine level also contributed to the separation along the second principal component with animals AHD 203, AHD 205, THD 402 and CPHD 401 showing lower levels of this metabolite than the rest of the high dose animals.

6.6.2 PLS-DA of Urine NMR Data

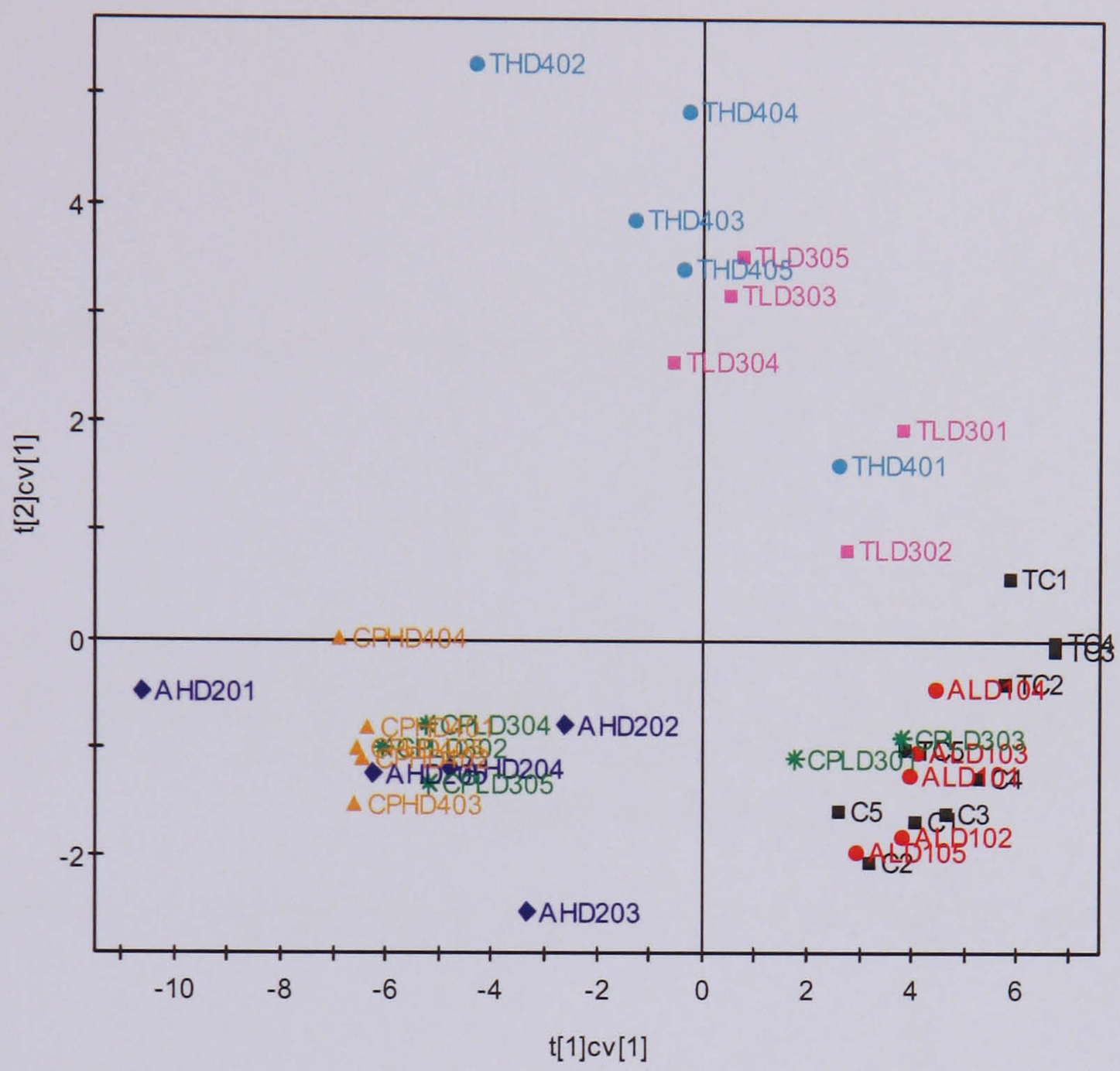

Figure 6.23 PLS-DA cross validated scores plot of the Day 2 ^{1}H NMR spectra of the three hepatotoxin-dosed urine samples with bucket 3.28 removed.

In order to improve interpretability and information recovery from the urine NMR data a PLS-DA model was constructed using the normalised mean centre-scaled data set with the TMAO bucket removed. Figure 6.23 shows the PLS-DA cross validated scores plot for the first two components of the Day 2 urine NMR data. The first X matrix PLS component describes the dose related variation between the dosed animals and the control animals of study 98053 whereas the second X matrix PLS component describes the dose related variation between the dosed animals and the control animals of study 99057. In addition, some separation between the two studies can still be seen along the second component.

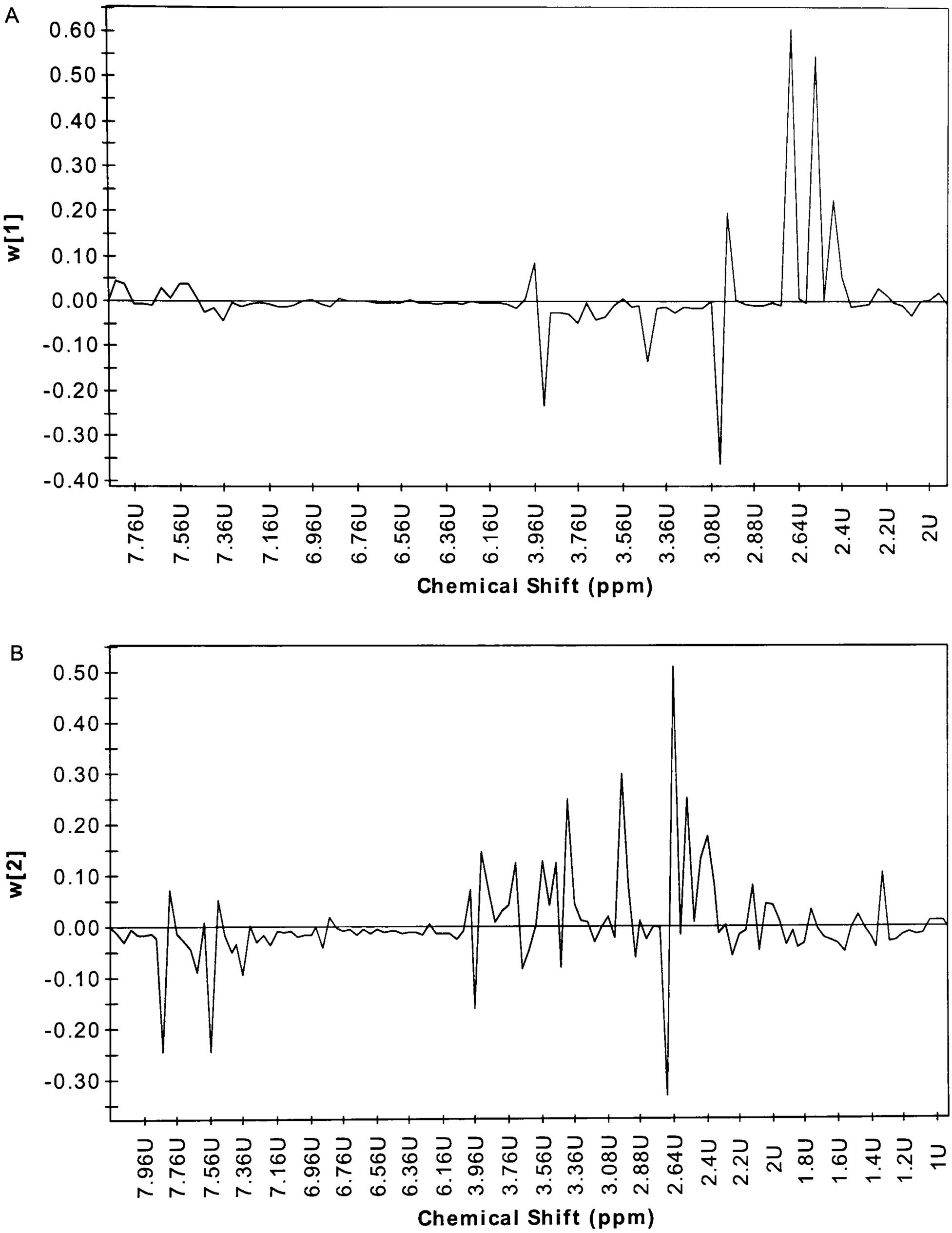

Figure 6.24 Corresponding PLS-DA loadings plot of the Day 2 ^{1}H NMR spectra of the three hepatotoxin-dosed urine samples with bucket 3.28 removed.

The corresponding loadings plot (Figure 6.24) indicated that changes in urinary endogenous metabolites are the major contributors to the separation along the first PLS component with increases in taurine, creatine and PAG, and decreases in urinary citrate, hippurate and 2-oxoglutarate. The change in urinary PAG was not as clear as the rest of the endogenous metabolites. In addition, the corresponding loadings plot of the second PLS component indicated that differences in urinary hippurate, lactate and glucose levels contributed to the separation between the thioacetamide-treated and the allyl formate- and chlorpromazine-treated animals along the second PLS component. Thioacetamide-treated animals showed higher urinary lactate and glucose levels and lower urinary hippurate level as compare to the rest of the high dose animals. The appearance of urinary glucose in thioacetamide-treated animals indicates impaired kidney function in these animals.

6.7 Discussion

The application of pattern recognition methods has enabled the visualisation and comparison of the effects of the three hepatotoxins i.e. allyl formate, chlorpromazine and thioacetamide on the rats. The integrated approach to analysing biological samples renders it possible for pattern recognition techniques to highlight important dose- and compound-related differences in the animals. The use of unsupervised method such as PCA allows visualisation of intrinsic clustering behaviour that is unique to each of the hepatotoxins i.e. chlorpromazine, an FAD inhibitor, reduces TMAO level in biological samples. This approach has revealed changes that are common to all the hepatotoxins administered such as their effects on liver and plasma lipids and has enabled cross-correlation of changes occurring in different biological matrices.

The difference in TMAO level in the control animals appears to dominate majority of the models. Changes in the levels of methylamine intermediates can be directly related to the diet since TMAO is mostly dietary derived, synthesised from its precursor, choline, in the diet by the gut microflora. TMAO is involved in methane metabolism. The differences in TMAO could reflect the biochemical status of the control animals during the course of the study. TMAO has an osmoregulatory role in animals, and may be involved (in a redox fashion) within disulphide/thiol linkage formation/equilibrium. Zethof *et al.* (1994) showed that animal handling can affect the colonic temperature, a condition termed stress-induced hypothermia, which may affect the metabolism in particular the metabolism of methylamines in the gut microflora. The difference in TMAO level in the control rats also highlights the problem of using genetically identical animals which exhibit dissimilar biochemical starting point in toxicological studies.

In pattern recognition analysis of drug-induced toxicity, it is mainly perturbations of the endogenous metabolites that are of interest. Therefore, it is imperative that the NMR spectral data used does not contain any xenobiotic metabolites which will interfere in analysis. Fortunately, all the Day 2 NMR data of allyl formate, chlorpromazine and thioacetamide were free from these interfering peaks. However, it is still possible albeit

time consuming to analyse the data even if the metabolites were present by removing the metabolite peaks and renormalizing the data set. The use of statistical total correlation spectroscopy (STOCSY) could also help in identifying such peaks (Cloarec *et al.* 2005)

Another potential problem with pattern recognition analyses is the segmentation or bucketing of the original spectra into 'buckets'. In biofluid, the bucket size used was 0.04 ppm, therefore, for samples analysed using a 600 MHz spectrometer, the bucket size of 0.04 ppm corresponds to 24 Hz. It is clear that each bucket will include contributions from several NMR peaks instead of just one specific NMR peak. It is vital that the bucket identified by pattern recognition methods be compared with visual inspection of the actual NMR spectra to ensure the results obtained are true representative of the actual effects of the drugs being tested. The use of smaller bucket size i.e. in liver tissue NMR spectra minimises this problem. However, the use of smaller bucket size in biofluids such as plasma and urine NMR spectra is impractical as the later suffers from pH-induced peak shifts. In addition, global pattern recognition tends to involve data acquired over a long period of time and possibly from different laboratories. Therefore, it is of utmost importance to ensure that a set of standard operating procedures including sample preparations, NMR acquisition parameters and pattern recognition steps were practiced to ensure minimal systematic error, which will contribute to the variation in the results obtained.

The application of supervised pattern recognition techniques such as PLS-DA enhanced the separation between the dosed animals and the controls. It also enables construction of mathematical models that can predict the class of each sample. One important feature of PLS-DA is the validity of the models created using this technique can be determined by cross validation. This allows statistical evaluation as to whether the distinction between the classes is significant or not. Cross-validation uses an internal test set of observations to test for the models forecasting veracity. The idea of cross-validation is to remove a portion of the data set, usually one third, out of the model development and then developing a number of parallel models from the remaining data. The removed data is then used to predict the classification of each observation in the test set. The predicted values can then be compared

to the actual values to validate the predictive ability, accuracy and significance of the PLS-DA model. However, due to the small sample size cross validations were not carried out for each model hepatotoxin. The use of PLS analysis by treating the liver NMR data as the X variable and the plasma NMR data as the Y variable has enabled the identification of changes in the liver, which correlates with the changes in the blood plasma. In this case, the increase in liver lipids correlates to a decrease in plasma lipids in all the high dose treated animals. This indicates that all three compounds used in this project caused a decrease in lipid transport from the liver to the blood.

Despite all the potential problems, the application of pattern recognition techniques to NMR data had helped enormously in simplifying the analysis and visualisation of changes in complex biological data especially in identifying small changes that are not easily distinguished by eye. The use of standard operating protocols, good laboratory practice (GLP) and good design of experiment as well as having a consistent set of NMR parameters are paramount in ensuring good quality NMR spectroscopic data are obtained for analysis.

Chapter 7: Summary and Conclusions

7.1 Summary

In this project, the integrated metabonomic approach has been applied in conjunction with conventional toxicological techniques to examine the effects of three model hepatotoxins in rats. This comprehensive analysis provided a complex data set but the use of pattern recognition techniques such as principal components analysis and partial least squares analysis has simplified the analysis and enabled a better understanding of the effects produced. An interesting and novel aspect of this work is that the diverse biochemical profiles generated from the different matrices (liver, plasma and urine) were compared to find interrelationships between the matrices and to gain insights into the toxicological processes.

Table 7.1 Summary of the average levels of certain clinical chemistry parameters in plasma (24 hours post-dose).

Hepatotoxin	Level relative to controls in plasma 24 hours after dosing					
	ASAT	ALAT	Bilirubin	5NU	TBA	GGT
Allyl Formate (75 mg/kg)	45.3X	43.2X	2.2X	1.9X	4.3X	6.2X
Chlorpromazine (60 mg/kg)	1.9X	1.0X	1.3X	0.6X	0.5X	2.0X
Thioacetamide (200 mg/kg)	30.4X	9.3X	1.2X	2.8X	26.1X	1.3X

Key: The levels are expressed as a multiple of the average control level at the same time point. ASAT = aspartate aminotransferase, ALAT = alanine aminotransferase, 5NU = 5' nucleotidase, TBA = total bile acids, GGT = γ-glutamyltransferase.

All three toxins were found to produce some hepatic damages by the conventional methodologies but there was substantial variation in the nature and extent of this damage with allyl formate and thioacetamide producing major effects and chlorpromazine producing minor effects. Table 7.1 summarises some relevant plasma chemistry changes at 24 hours after dosing. Despite substantial variation in the extent of the damage caused by the different toxins, each toxin produced some common biochemical effects (Table 7.2).

Table 7.2 Distinguishing and common toxicological factors induced by the three hepatotoxins.

Hepatotoxins	Distinguishing Factors	Common Factors
Allyl Formate (75 mg/kg)	-	- Changes in TMAO levels. - Disruption in energy and lipid metabolism. - Perturbations in TCA cycle intermediates.
Chlorpromazine (60 mg/kg)	- Presence of ketone bodies in the blood plasma indicating ketosis.	
Thioacetamide (200 mg/kg)	- Presence of lactate and alanine in the blood plasma indicating gluconeogenesis.	

The fundamental mechanism that connects all three hepatotoxins together in biochemical terms, through the analysis of the NMR-generated metabolic data sets, appears to be disruption of energy supply. Tissue MAS NMR data analysis revealed decreases in liver glucose and glycogen and biofluids NMR data analysis revealed decreases in urinary TCA cycle intermediates namely, citrate, succinate and 2-oxoglutarate, which all indicate disruption in energy metabolism. Supporting this, all three compounds administered (allyl formate, chlorpromazine and thioacetamide) are known to cause mitochondrial dysfunction (Rees and Tarlow 1967, Pang *et al*. 1997, Medina *et al*. 1964, Dawkins *et al*., 1960, Moller and Dargel, 1985, Cascales *et al.* 1982). The increases in liver lipids and the decreases in plasma lipids are also consistent with disrupted energy supply. Under conditions of low cellular ATP concentrations, glycogenolysis and glycolysis would be expected to be up-

regulated in order to provide ATP which would account for the decreases in liver glucose and glycogen storage. Disruption in mitochondrial functions often leads to disruption in fatty acids metabolism due to impaired fatty acid oxidation and electron transport chain processes, both highly dependent on mitochondria structural integrity and therefore mitochondrial compartmentalisation. Thus, the increases in liver lipid moeties might arise simply through an inability to metabolise it in the mitochondria but ATP depletion will also inhibit protein synthesis and will, thereby, reduce the secretion of lipoproteins from the liver to the blood. This latter explanation for the increases in liver lipids is more convincing because of the concomitant decreases in plasma lipids.

Impaired protein synthesis through ATP-depletion and/or inhibition of protein synthesis by the compounds administered would also impair apolipoprotein synthesis. Impaired apolipoprotein synthesis would lead to reduced transport of triglycerides out of the liver thus leading to increase triglycerides in the liver and decreases in plasma lipid concentration as observed by NMR spectroscopy of both liver tissues and plasma. In addition, increase in intracellular bile acids concentrations was known to inhibit the secretion of VLDL-associated triglycerides from hepatocytes as well as the secretion of apolipoprotein associated with transport of VLDL namely apoB-100 as demonstrated by Lin *et al.* (1996). Of the three compounds administered, allyl formate and thioacetamide are known to cause biliary damage and the plasma clinical chemistry results in the current study indicated an increase in total bile acids (TBA). Mitochondria dysfunction will incapacitate ATP synthesis. Moreover, it will also waste the remaining sources of ATP because depolarisation of the inner membrane of mitochondria, which forces the ATP synthase to function in the reverse mode, as an ATPase, will hydrolyse ATP. Glycolysis can even be compromised by the insufficient ATP supply to the ATP-driven glycolytic enzymes.

If the metabolic disorders evoked by the toxic agent is so extensive that most or all of the mitochondria were disrupted, a complete bioenergetic catastrophe ensues with severe depletion of ATP, degradative processes such as oxidative and hydrolytic degradation, and intracellular disintegration will go to completion thus causing complete failure in cellular

structure and functions leading to cell lysis or necrosis. ATP availability also determines the form of cell death. Apoptosis is regarded as tissue repair because it intercepted the process leading to necrosis, which is a more harmful sequala than apoptosis and it intercept the process leading to neoplasia by eliminating the cells with potentially mutagenic DNA damage. In apoptosis, the cell shrinks and the nuclear and cytoplasmic materials condense and break into membrane bound fragments, which can then be phagocytosed. In comparison to necrosis, this process is considered to be more orderly as necrosis normally results in the cells and intercellular organelles swelling and disintegrating with membrane lysis, which ends with cellular debris in the extracellular environment. The constituents of necrotic cells attract aggressive inflammatory cells, and the ensuing inflammation amplifies cell injury. However, apoptosis requires ATP. Depletion of ATP by hepatotoxins would deny urgently needed energy to execute apoptotic program, which involves ATP-driven steps to form complexes required for apoptosis. Thiaocetamide is known to induce apoptosis in the low dose thus facilitating tissue repair (Klaassen, 2001). However, at a high dose, thioacetamide induced necrosis. This suggests that necrosis occurs because the injury overwhelms and disables the repair mechanisms including repair of damaged molecules, elimination of damaged cells by apoptosis and replacement of lost cells by cell division.

Elevated and altered triglycerides level in the liver could also be influenced by the toxicological end point of hepatotoxicity. Cells which experienced widespread damage are usually removed through the ATP-dependent process of apoptosis or programmed cell death. During apoptosis, the contents of the damaged dell are digested and packed into vesicles for re-absorption. Necrosis is thought to occur in the same pattern except with the absence of ATP as energy source. Increase in triglycerides could be attributed to accumulation of cytoplasmic lipid bodies in cells undergoing cell death (Iorio *et al.* 2003).

Inter-group differences in liver and urinary TMAO levels were an important and common observation in these studies. As well as seeing toxin-induced changes in liver/urinary TMAO there were also differences in liver/urinary TMAO between the control groups from the two studies. As explained in Chapter 6, TMA is synthesised from dietary choline by the

gut microflora. This trimethylamine is then normally oxidised in the liver by the flavin monooxygenase system (FMO) to TMAO and the TMAO excreted in the urine. TMAO and DMA may play an osmotic role in renal medulla, where they counteract the gap, due to the high urea concentrations, between intracellular and extracellular fluids. Table 7.3 summarises the observed changes in liver and urine TMAO levels on Day 2 after dosing.

Table 7.3 Summary of the observed hepatotoxin-induced change in liver and urinary TMAO levels on Day 2.

Hepatotoxin	Liver TMAO Level	Urinary TMAO Excretion
Allyl Formate (75 mg/kg)	0.64X	0.59X
Chlorpromazine (60 mg/kg)	0.55X	0.39X
Thioacetamide (200 mg/kg)	0.54X	0.77X

Key: The quoted TMAO values are the group averages expressed relative to the appropriate control groups at the same time point.

As discussed earlier, urinary TMAO can either come from the oxidation of TMA, which is derived from dietary choline, or directly from intestinal bacteria (Nicholls *et al.* 2003). In the current work, the diet was kept the same for both studies; therefore it is unlikely that the source of TMAO variation was due to diet. In the case of chlorpromazine, a known inhibitor of FMO (Yagi *et al.* 1956, Lasslo and Meyer 1959, Ayesh and Smith 1990), an inhibition of FMO by chlorpromazine will lead to decreased formation of TMAO in the liver as well as reduced excretion of this metabolite in the urine. The metabolism of thioacetamide to thioacetamide-S-oxide requires FMO, thus, competition for FMO could account for the decrease TMAO levels observed in the liver and urine of animals treated with thioacetamide. However, decreased formation of TMAO would lead to increased

urinary TMA, which was not detected in the current work. The mammalian gut microflora have been shown to exerts significant effects on tissue and biofluid metabolic profiles and thus the control of host mammalian system (Nicholson and Wilson, 2003, Xu *et al.* 2003, Beale. 2002). It is possible that the source of TMAO variation could be due to colonisation and subsequent redistribution of gut microflora, and/or a change in gut microflora excretion (Nicholls *et al.* 2003). Inter-group differences in liver and urinary TMAO levels as well as urinary hippurate level observed in the present studies could be the result of different gut microflora populations as suggested by Nicholls *et al.* (2003).

Hippurate is normally synthesised in the liver and kidney from glycine and benzoic acid. This is then excreted by the renal tubular cells in the urine. Decrease in the level of hippurate in the urine may be indicative of reduced tubular excretion efficiency or metabolic alteration. The hippurate level in the urine is highly dependent on gut microflora (Nicholls *et al.* 2003), and hormonal and environmental influences, the later being diet- and stress-related. Therefore, hippurate presents substantial inter-animal and inter-day variability. Hippurate is also the product of shikimic acid (quinic acid) degradation through the action of intestinal gut microflora. Thus, it is not possible to exclude the influence of food intake and different gut microflora populations in the gastrointestinal track on changes in urine hippurate concentrations.

In the current studies, increased urinary PAG and plasma tyrosine level were observed in allyl formate and chlorpromazine-dosed animals whereas a decrease in urinary PAG and plasma tyrosine level were observed in the thioacetamide-dosed animals as shown in Table 7.4. Under normal conditions, phenylalanine is metabolised to tyrosine by hydroxylation. Phenylalanine is also a well-known source of phenylacetic acid. As discussed previously in Chapter 3, phenylacetic acid and benzoic acid are metabolic precursors of PAG (phenylacetylglycine) and hippurate (benzoylglycine) respectively and both these aromatic acids are normally detoxified via such conjugation with glycine. If glycine was channelled into glutathione and/or PAG production as a defence mechanism, the reduction in urinary hippurate might be explained by insufficient glycine for the conjugation of benzoic acid. In addition, changes in urinary PAG level could be attributed to variability in the gut

microflora (Nicholls *et al.* 2003). β-Oxidation of free phenyl-substituted fatty acids derived from excess lipids may also be one possible source of phenylacetic acid or it might be derived from metabolism of phenylalanine as proposed by Nicholls *et al.* (2000).

Table 7.4 Summary of the observed changes in urinary PAG and plasma tyrosine levels on Day 2.

Hepatotoxin	Urinary PAG Excretion	Plasma Tyrosine Level
Allyl Formate (75 mg/kg)	1.31X	1.97X
Chlorpromazine (60 mg/kg)	1.63X	1.25X
Thioacetamide (200 mg/kg)	0.85X	0.78X

Key: The quoted PAG and tyrosine values are the group averages expressed relative to the appropriate control groups at the same time point.

7.2 Conclusions

Disruption of hepatic energy metabolism appears to be a common effect of the hepatotxins studied. Coen *et al.* (2003) observed similar metabolic effects in studies of acute paracetamol toxicity in mice. Paracetamol induces centrilobular necrosis. Similarly, Craig (2004) showed that administration of methapyrilene, a periportal necrotic agent, in the rats caused disruption in energy metabolism. Although the end point of all the toxins are not entirely equivalent, these common responses seems to suggest that the metabolic changes evidenced here and elsewhere may represent a bigger more common disruption to energy metabolism induced by hepatotoxins. Allyl formate, chlorpromazine, thioacetamide, paracetamol and methapyrilene are compounds which induce mitochondrial dysfunction. The glycogen, glucose and lipid changes appear to be related to mitochondrial disruption which reduces the availability of ATP. This disruption will trigger a switch into carbohydrate catabolism thus resulting in the decreased/disabled utilisation of fatty acids.

It is noteworthy that inter-animal variations were observed in the metabolic profiles of animals from the same dosing groups although these animals are subjected to tight regulation of environmental conditions. These effects were evident in the scores plots of all the treated animals. Historically, these effects have always been observed in studies making single measurements. The concentration of a single compound may be altered in response to more than one disease whereas a combination of metabolic perturbations is more likely to be specifically diagnostic for any particular condition. These inter-animal variations again highlighted the danger of relying on single compound biomarkers, as is the case with other biochemical screening techniques, in that one cannot say for certain, that the single compound change is a marker for the disease or organ dysfunction, or individual susceptibility to disease or toxic insult, which in turn could be related to the gut microbiota.

In conclusion, the work presented in this thesis has demonstrated the applications of NMR-based metabonomic techniques in toxicological studies and the advantage of integrated metabonomic approach to the study and understanding of drug-induced liver toxicity. The integrated metabonomic approach enabled a thorough and enhanced characterisation of an

array of biological samples. The integration of 'omics' technologies could also be adapted to investigate model pharmaceutical toxins or diseases within whole mammalian biosystems as well as the gut microbiota in order to obtain a global view into the biochemical and molecular interactions of the host and its commensal in response to toxicological insult or disease processes.

7.3 Future work

In order to ascertain the exact mechanism that is at work here, a more focused study using ^{13}C labelled metabolites would be required. This will enable more accurate assessment of changes in metabolic fluxes by identifying candidate pathways such as gluconeogenesis, glycolysis, fatty acid degradation and fatty acid synthesis in response to toxic insult. Such studies complemented with measurements of up or down regulation of mRNA and key proteins levels within each pathway would allow the determination of the hepatotoxin-induced metabolic changes and its relation to the concerted changes in the expression pathway components and/or its relation to flux changes in the pathway at the metabolic level. Additionally, it is crucial to understand the dynamics and influences of the gut microbial composition on mammalian metabolism and its relation to the development and expression of disease processes as well as toxic insult (Nicholson and Wilson 2003).

References

1. Abernathy C. O., Lukacs L. and Zimmerman H. J. (1977), Adverse effects of chlorpromazine metabolites on isolated hepatocytes, *Proceeding of the Society for Experimental Biology and Medicine*, 155, 474-478.
2. Adams J. D. and Klaidman L. K. (1993), Acrolein-induced oxygen radical formation, *Free Radical Biology & Medicine*, 15, 187-193.
3. Alarcon R. A. (1976), Formation of acrolein from various amino acids and polyamines under degradation at 100°C, *Environmental Research*, 12: 317-326.
4. Al-Bader A. A., Mathew T. C., Abul H., Al-Mosawi M., Dashti H. M., Kumar D. and Singal P. K. (1999), Thioacetamide induced changes in trace elements and kidney damage, *Journal of Trace Elements in Experimental Medicine*, 12, 1-14.
5. Anand S. S. and Mehendale H. M. (2004), Liver regeneration: a critical toxicodynamic response in predictive toxicology, *Environmental Toxicology and Pharmacology*, 18, 149-160.
6. Andrew E. R. and Szczesniak E. (1995), A historical account of NMR in the solid state, *Progress in Nuclear Magnetic Resonance*, 28, 11-36.
7. Andrew E. R., and Eades R. G. (1959), Removal of dipolar broadening of NMR spectra of solids by specimen rotation, *Nature*, 183, 1802.
8. Anghileri L. J., Heidbreder M., Weiler G. and Dermietzel R. (1977), Hepatocarcinogenesis by thioacetamide: correlations of histological and biochemical changes and possible role of cell injury, *Experimental Cell Biology*, 45, 34-47.
9. Anthony M. L., Beddell C. R., Lindon J. C. and Nicholson J. K. (1993), Raised transaminase activity of blood plasma from rats with experimentally-induced kidney damage detected by spin-echo ^{1}H-NMR spectroscopy. *Journal of Pharmaceutical and Biomedical Analysis*, 11, 897-902.
10. Antti H., Bollard M. E., Ebbels T. M. D., Keun H. C., Lindon J. C., Nicholson J. K. and Holmes E. (2002), Batch statistical processing of ^{1}H NMR-derived urinary spectral data. *Journal of Chemometrics*. 16, 461-468.
11. Arni P. (1989), Review on the genotoxic activity of thioacetamide, *Mutation Research*, 221, 153-162.
12. Avni Y., Shirin H., Aeed H., Shahmurov M., Birkenfeld S. and Bruck R. (2004), Thioacetamide-induced hepatic damage in a rat nutritional model of steatohepatitis, *Hepatology Research*, 30, 141-147.

13. Ayesh R. and Smith R. L. (1990), Genetic polymorphism of trimethylamine N-oxidation, *Pharmacology and Therapeutics*, 45, 387-401.

14. Baker J. R. and Chaykin S. (1962), The biosynthesis of Trimethylamine-N-oxide, *Journal of Biological Chemistry*, 237, 1309-1313.

15. Baker J. R., Struempler A. and Chaykin S. (1963), A comparative study of trimethylamine-N-oxide biosynthesis, *Biochimica Et Biophysica Acta*, 71, 58-64.

16. Bales J. R., Bell J. D., Nicholson J. K., Sadler P. J., Timbrell J. A., Hughes R. D., Bennett P. N. and Williams R. (1988), Metabolic profiling of body fluids by proton NMR: Self poisoning episodes with Paracetamol (acetaminophen), *Magnetic Resonance in Medicine,* 6, 300-306.

17. Ball S. and Borman N. (1998), Pharmacogenetics and drug metabolism, *Nature Biotechnology*, 16, Supplement, 4-5.

18. Barker E. A. and Smuckler E. A. (1972), Altered microsome function during acute thioacetamide poisoning, *Molecular Pharmacology*, 8, 318-326.

19. Barker M. and Rayens W. (2003), Partial least squares for discrimination, *Journal of Chemometrics*, 17, 166-173.

20. Beale B. (2002), Probiotics: Their tiny worlds are under scrutiny, *The Scientist*, 16, 20-22.

21. Beckonert O., Bollard M. E., Ebbels T. M. D., Keun H. C., Antti H., Holmes E., Lindon J. C. and Nicholson J. K. (2003), NMR-based metabonomic toxicity classification: hierarchical cluster analysis and k-nearest-neighbour approaches, *Analytica Chimica Acta*, 490, 3-15.

22. Beckwith-Hall B. M., Holmes E., Lindon J. C., Gounarides J., Vickers A., Shapiro M. and Nicholson J. K. (2002), NMR-based metabonomic studies on the biochemical effects of commonly used drug carrier vehicles in the rat, *Chemical Research Toxicology*, 15, 1136-1141.

23. Beckwith-Hall B. M., Nicholson J. K., Nicholls A. W., Foxall P. J. D., Lindon J. C., Connor S. C., Abdi M., Connelly J. and Holmes E. (1998), Nuclear magnetic resonance spectroscopic and principal components analysis investigations into biochemical effects of three model hepatotoxins, *Chemical Research Toxicology*, 11, 260-272.

24. Beckwith-Hall B. M., Thompson N. A., Nicholson J. K., Lindon J. C. and Holmes E. (2003), A metabonomic investigation of hepatotoxicity using diffusion-edited ^{1}H NMR spectroscopy of blood serum, *Analyst*, 128, 814-818.

25. Belinsky S. A., Badr M. Z., Kauffman F. C. and Thurman R. G. (1986), Mechanism of hepatotoxicity in periportal regions of the liver to allyl alcohol: studies on thiols and energy status, *Journal of Pharmacology & Experimental Therapeutics*, 238, 1132-1137.

26. Berg R. G. (1995), Bacterial translocation from the gastrointestinal tract, *Trends in Microbiology*, 3, 149-154.

27. Bisani M. L., Faraone D., Clementi S., Esbensen K. H. and Wold S. (1983), Principal components and partial least-squares analysis of the geochemistry of volcanic rocks from the Aeolian archipelago, *Analytica Chimica Acta*, 150, 129-143.

28. Blackledge C. A., Nicholson J. K., Evans J. A., Rodgers C. and Wilson I. D. (2002), Application of ^{1}H- and ^{19}F-NMR spectroscopy in the investigation of the urinary and biliary excretion of 3,5-, 2,4-ditrifluoromethylbenzoic and pentafluorobenzoic acids in rat, *Xenobiotica*, 32, 605-613.

29. Blomquist G., Johansson E., Sodersrom B. and Wold S. (1979), Classification of fungi by means of pyrolysis-gas chromatography-pattern recognition, *Journal of Chromatography*, 173, 19-32.

30. Boehme C. L. and Strobel H. W. (1998), High-performance liquid chromatography methods for the analysis of haloperidol and chlorpromazine metabolism in vitro by purified cytochrome P450 isoforms, *Journal of Chromatography B*, 718, 259-266.

31. Bollard M. E., Garrod S., Holmes E., Lindon J. C., Humpfer E., Spraul M. and Nicholson J. K. (2000), High-resolution ^{1}H and ^{1}H-^{13}C magic angle spinning NMR spectroscopy of rat liver, *Magnetic Resonance in Medicine*, 44, 201-207.

32. Bollard M. E., Holmes E., Lindon J. C., Mitchell S. C., Brandstetter D., Zhang W. and Nicholson J. K. (2001), Investigations into the biochemical changes due to diurnal variation and estrus cycle in female rats using high resolution ^{1}H NMR spectroscopy of urine and pattern recognition, *Analytical Biochemistry*, 295, 194-202.

33. Bollard M. E., Murray A. J., Clarke K., Nicholson J. K. and Griffin J. L. (2003), A study of metabolic compartmentation in the rat heart and cardiac mitochondria using high-resolution magic angle spinning ^{1}H NMR spectroscopy, *FEBS Letter*, 553, 73-78.

34. Bollard M. E., Stanley E. G., Lindon J. C., Nicholson J. K. and Holmes E. (2005 – article in press), NMR-based metabonomic approaches for evaluating physiological influences on biofluid composition, *NMR in Biomedicine*.

35. Bollard M. E., Xu J., Purcell W., Griffin J. L., Quirk C., Holmes E. and Nicholson J. K. (2002), Metabolic profiling of the effects of D-galactosamine in liver spheroids using ^{1}H NMR and MAS-NMR spectroscopy, *Chemical Research Toxicology*, 15, 1351-1359.

36. Boor P. J., Sanduja R., Nelson T. J. and Ansari G. A. S. (1987), In-vivo metabolism of the cardiovascular toxin, allylamine, *Biochemical Pharmacology*, 36, 4347-4353.

37. Bruck R., Aeed H., Shitin H., Matas Z., Zaidel L., Avni Y. and Halpern Z. (1999), The hydroxyl radical scavengers dimethylsulfoxide and dimethylthiourea protect rats against thioacetamide-induced fulminant hepatic failure, *Journal of Hepatology*, 31, 27-38.

38. Bruck R., Shirin H., Aeed H., Matas Z., Hochman A., Pines M. and Avni Y. (2001), Prevention of hepatic cirrhosis in rats by hydroxyl radical scavengers, *Journal of Hepatology*, 35, 457–464.

39. Buko V., Egorov A., Karput S.and Prokopchik N. (1998), Correlations between liver hystological structure and mitochondrial respiration in thioacetamide (TAA)-induced liver necroses, *Journal of Hepatology*, 28, Supplement 1, 220.

40. Burcham P. C. and Fontaine F. (2001), Extensive protein carbonylation precedes acrolein-mediated cell death in mouse hepatocytes, *Journal of Biochemistry and Molecular Toxicology*, 15, 309-316.

41. Butcher E. C., Berg E. L. and Kunkel E. J. (2004), Systems biology in drug discovery, *Nature Biotechnology*, 22, 1253-1259.

42. Carey M. C., Hirom P. C., and Small D. M. (1976), A study of the physicochemical interactions between biliary lipids and chlorpromazine hydrochloride: Bile-salt precipitation as a mechanism of phenothiazine-induced bile secretory failure, *Journal of Biochemistry*, 153, 519-531.

43. Cascales M., Martin-Sanz P., Alvarez A., Sanchez-Perez M., Diez-Fernandez C. and Bosca L. (1992), Isoenzymes of carbohydrate metabolism in primary cultures of hepatocytes from thioacetamide-induced rat liver necrosis: Responses to growth factors. *Hepatology*, 16, 232-240.

44. Cascales C., Martin-Sanz P., Pittner R. A., Hopewell R., Brindley D. N. and Cascales M. (1986), Effects of an anti-tumoural rhodium complex on thioacetamide-induced liver tumour in rats: Changes in the activities of ornithine decarboxylase, tyrosine aminotransferase and of enzymes involved in fatty acid and glycerolipid synthesis, *Biochemical Pharmacology*, 35, 2655-2661.

45. Cascales M., Robles-Chillida E. M., Feijoo B., Cerdan S., Martin-Sanz P. And Santos-Ruiz A. (1982), Changes caused by thioacetamide in GOT and GPT aminotransferases and glutamate dehydrogenase in rat liver. Ultrastructural Study, *Revista Espanola de Fisiologia*, 38, 105-112.

46. Cerdan S., Cascales M., and Santos-Ruiz A. (1981), Effect of thioacetamide on the pentose phosphate pathway and other NADP-linked enzymes of rat liver cytosol: Chronology of the perturbations and metabolic significance, *Molecular Pharmacology*, 19, 451-455.

47. Chakrabartty P. K. and Schneider W. C. (1978), Increased activity of the rat liver messenger RNA and of albumin messenger RNA modulated by thioacetamide, *Cancer Research*, 38, 2043-2047.

48. Chakrabartty P. K., Chattopadhyay S. K. and Schneider W. C. (1982), Molecular basis for increased synthesis of albumin in rat liver after thioacetamide administration, *Cancer Research*, 42, 421-428.

49. Chan L. M. S., Lowes S. and Hirst B. H. (2004), The ABCs of drug transport in intestine and liver: efflux proteins limiting drug absorption and bioavailability, *European Journal of Pharmaceutical Sciences*, 21, 25-51.

50. Chasseaud L. F. (1979), The role of glutathione and GST in the metabolism of chemical carcinogens and other agents, *Advances in Cancer Research,* 29, 175-274.

51. Cheng L. L., Chang I., Smith B. L. and Gonzalez R. G. (1998), Evaluating human breast ductal carcinomas with high resolution magic-angle spinning proton magnetic resonance spectroscopy, *Journal of Magnetic Resonance*, 135, 194-202.

52. Cheng L. L., Newell K., Mallory A. E., Hyman B. T. and Gonzalez R. G. (2002), Quantitation of neurons in Alzheimer and control brains with ex vivo high resolution magic angle spinning proton magnetic resonance spectroscopy and stereology, *Magnetic Resonance Imaging*, 20, 527-533.

53. Cheng L. L., Wu C., Smith M. R. and Gonzalez R. G. (2001), Non-destructive quantitation of spermine in human prostate tissue samples using HRMAS ^{1}H NMR spectroscopy at 9.4T, *Federation of European Biochemical Societies Letters*, 494, 112-116.

54. Chtioui Y., Bertrand D. and Barba D. (1996), Reduction of the size of the learning data in a probabilistic neural network by hierarchical clustering. Application to the discrimination of seed by artificial vision, *Chemometrics and Intelligent Laboratory Systems*, 35, 175-186.

55. Clawson G. A., Koplitz M., Moody D. E. and Smuckler E. A. (1980), Effects of thioacetamide treatment on nuclear envelope nucleoside triphosphatase activity and transport of RNA from rat liver nuclei, *Cancer Research*, 40, 75-79.

56. Clawson G. A., Moody D. E., James J. and Smuckler E. A. (1981), Nuclear envelope alterations accompanying thioacetamide-related enlargement of the nucleus, *Cancer Research*, 41, 519-526.

57. Clayton T. A. (2001), PhD Thesis, *^{1}H NMR Spectroscopy investigations on hepatotoxic process*, University of London.

58. Clayton T. A., Lindon J. C., Everett J. R., Charuel C., Hanton G., Le Net J., Provost J. and Nicholson J. K. (2003a), An hypothesis for a mechanism underlying hepatotoxin-induced hypercreatinuria, *Archives of Toxicology*, 77, 208-217.

59. Clayton T. A., Lindon J. C., Everett J. R., Charuel C., Hanton G., Le Net J., Provost J. and Nicholson J. K. (2003b), Hepatotoxin-induced hypercreatinaemia and hypercreatinuria: their relationship to one another, to liver damage and to weakened nutritional status, *Archives of Toxicology*, 78, 86-96.

60. Cloarec O., Dumas M-E., Craig A., Barton R. C., Trygg J., Hudson J., Blancher C., Gauguier D., Lindon J. C., Holmes E. and Nicholson J. (2005), Statistical total correlation spectroscopy: An exploratory approach for latent biomarker identification from metabolic ^{1}H NMR data sets, *Analytical Chemistry*, 77, 1282 -1289.

61. Coen M., Lenz E. M., Nicholson J. K., Wilson I. D., Pognan F. and Lindon J. C. (2003), An integrated metabonomic investigation of acetaminophen toxicity in the mouse using NMR spectroscopy, *Chemical Research Toxicology*, 16, 295-303.

62. Constantinou M. A., Papakonstantinou E., Benaki D., Spraul M., Shulpis K., Koupparis M. A. and Mikros E. (2004), Application of nuclear magnetic resonance spectroscopy combined with principal component analysis in detecting inborn errors of metabolism using blood spots: a metabonomic approach, *Analytica Chimica Acta*, 511, 303-312.

63. Craig A. (2004), PhD Thesis, *Parallel metabonomic and genomic characterisation of experimental hepatotoxicity in the rat*, University of London.

64. Dawkins M. J. R., Judah J. D., and Rees K. R. (1959a), The effect of chlorpromazine on the respiratory chain: Cytochrome Oxidase, *Journal of Biochemistry*, 72, 204-209.

65. Dawkins M. J. R., Judah J. D., and Rees K. R. (1959b), The mechanism of action of chlorpromazine: 2. Reduced diphosphopyridine nucleotide-cytochrome c reductase and coupled phosphorylation, *Journal of Biochemistry*, 73, 16-23.

66. Dawkins M. J. R., Judah J. D., and Rees K. R. (1960), Action of chlorpromazine: 3. Mitochondrial adenosine triphosphatase and the adenosine triphosphate-adenosine diphosphate exchange, *Journal of Biochemistry*, 76, 200-205.

67. De Ferreyra E. C., De Fenos O. M. and Castro J. A. (1980), Effect of different chemicals on thioacetamine-induced liver necrosis, *Toxicology*, 16, 205-214.

68. De Rooij B. M., Boogaard P. J., Commandeur J. N. M., Van Sittert N. J. and Vermeulen N. P. E. (1997), Allylmercapturic acid as urinary biomarker of human exposure to allyl chloride, *Occupational and Environmental Medicine*, 54, 653-661.

69. Di Masi J. A. (2001), New drug development in the United States from 1963-1999, *Clinical Pharmacology & Therapeutics*, 69, 286-296.

70. Draper H. H., Csallany A. S. and Hadley M. (2000), Urinary aldehydes as indicators of lipid peroxidation in vivo, *Free Radical Biology & Medicine*, 29, 11, 1071-1077.

71. Droy B. F., Davis M. E. and Hinton D. E. (1989), Mechanism of allyl formate-induced hepatotoxicity in rainbow trout; *Toxicology and Applied Pharmacology*, 98, 313-324.

72. Dube D. K., Dutta H. N., Pal B., and Ghosh J. J. (1972), Effect of chlorpromazine on induction of different hepatic enzymes, *Biochemical Pharmacology*, 21, 2249-2251.

73. Dyroff M. C. and Neal R. A. (1981), Identification of the major protein adduct formed in rat liver after thioacetamide administration, *Cancer Research*, 41, 3430-3435.

74. Dyroff M. C. and Neal R. A. (1982), Studies of the mechanism of metabolism of thioacetamide S-oxide by rat liver microsomes, *Molecular Pharmacology*, 23, 219-227.

75. Elliot M. A., Walter G. A., Swift A., Vandenborne K., Schotland J. C. and Leigh J. S. (1999), Spectral quantitation by principal component analysis using complex singular value decomposition, *Magnetic Resonance in Medicine*, 41, 450-455.

76. Eriksson L., Johansson E., Kettaneh-Wold N. and Wold S. (2001), *Multi- and megavariate data analysis: Principles and applications*, Umetrics AB, Umea, Sweden.

77. Espina J. R., Shockcor J. P., Herron W. J., Car B. D., Contel N. R., Ciaccio P. J., Lindon J. C., Holmes E. and Nicholson J. K. (2001), Detection of in vivo biomarkers of phospholipidosis using NMR-based metabonomics approaches, *Magnetic Resonance in Chemistry*, 39, 559-65.

78. Esterbauer H., Ertl A. and Scholz N. (1975), The reaction of cysteine with α, β-unsaturated aldehydes, *Tetrahedron*, 32, 285-289.

79. Fan T. W. M. (1996), Metabolite profiling by one- and two-dimensional NMR analysis of complex mixtures, *Progress in Nuclear magnetic Resonance Spectroscopy*, 28, 161-219.

80. Farghali H., Rossaro L., Gavaler J. S. Van Thiel D. H., Dowd S. R., Williams D. S. and Ho C. (1992), ^{31}P-NMR spectroscopy of perfused rat hepatocytes immobilized in agarose threads: application to chemical-induced hepatotoxicity, *Biochimica et Biophysica Acta*, 1139, 105-114.

81. Fausto N. (1970), RNA and amine synthesis in the liver of rats given injections of thioacetamide, *Cancer Research*, 30, 1947-1952.

82. Fernandez M. I., Torres M. I., Gill A. And Rios A. (1997), Steatosis and collagen content in experimental liver cirrhosis are affected by dietary monounsaturated and polyunsaturated fatty acids, *Scandinavian Journal of Gastroenterology*, 32, 350-356.

83. Ferrali M., Ciccoli L. and Comporti M. (1989), Allyl alcohol-induced haemolysis and its relation to iron release and lipid peroxidation, *Biochemical Pharmacology*, 38, 11, 1819-1825.

84. Foxall P. J. D., Bewley S., Neild G. H., Rodeck C. H. and Nicholson J. K. (1995), Analysis of foetal and neonatal urine using proton nuclear magnetic resonance spectroscopy, *Archives of Disease in Childhood*; 46, 199-211.

85. Foxall P. J. D., Spraul M., Farrant R. D., Lindon J. C., Neild G. H. and Nicholson J. K. (1993), 750 MHz ^{1}H-NMR spectroscopy of human blood plasma, *Journal of Pharmaceutical & Biomedical Analysis*, 11, 267-276.

86. Franke H., Zimmerman T. and Dargel R. (1985), Changes in intra- and extrahepatic VLDL in the rat following acute injury by thioacetamide, *Virchows Archive*, 48, 277-288.

87. Fromenty B. and Pessayre D. (1995), Inhibition of mitochondrial beta-oxidation as a mechanism of hepatotoxicity, *Pharmaceutical Therapeutics*, 67, 101-154.

88. Garrod S., Humpher E., Connor S. C., Connelly J. C., Spraul M., Nicholson J. K. and Holmes E. (2001), High-resolution ^{1}H NMR and magic angle spinning NMR spectroscopic investigation of the biochemical effects of 2-bromoethanamine in intact renal and hepatic tissue, *Magnetic Resonance in Medicine*, 45, 781-790.

89. Garrod S., Humpfer E., Spraul M., Connor S. C., Polley S., Connelly J., Lindon J. C., Nicholson J. K. and Holmes E. (1999), High-resolution magic angle spinning ^{1}H NMR spectroscopic studies on intact rat renal cortex and medulla, *Magnetic Resonance in Medicine*, 41, 1108-1118.

90. Gawrisch K., Eldho N. V. and Polozov I. V. (2002), Novel NMR tools to study structure and dynamics of biomembranes, *Chemistry and Physics of Lipids*, 116, 135-151.

91. Gerlach R. W., Kowalski B. R. and Wold H. O. A. (1979), Partial least-squares path modelling with latent variables, *Analytica Chimica Acta*, 112, 417-421.

92. Ghauri F. Y. K., Nicholson J. K., Sweatman B. C., Wood J., Beddell C. R., Lindon J. C. and Cairns N. J. (1993), NMR Spectroscopy of Human Post Mortem Cerebrospinal Fluid: Distinction of Alzheimers Disease from Control using Pattern Recognition and Statistics, *NMR in Biomedicine*, 6, 163-7.

93. Glascort Jr. P. A., Gilfor E., Serroni A. and Farber J. L. (1996), Independent antioxidant action of vitamin E and C in cultured rat hepatocytes intoxicated with allyl alcohol, *Biochemical Pharmacology*, 52, 1245-1252.

94. Goldberg and Frazier (1989), Alternatives to animals in toxicity testing, *Scientific American*, 261, 2, 16-22.

95. Goodwin B. L., Ruthven C. R. and Sandler M. (1994), Gut flora and the origin of some urinary aromatic phenolic compounds, *Biochemical Pharmacology*, 47, 2294-7.

96. Gordon Gibson G. and Skett P. (1994), *Introduction to drug metabolism*, 2nd Edition, Blackie Academic and Professional.

97. Grant H. C. and Rees K. R. (1958), The pre-cancerous liver; correlations of histological and biochemical changes in rats during prolonged administration of thioacetamide and 'butter yellow', *Proceedings of the Royal Society of London, Series B, Biological Sciences*, 148, 117-136.

98. Griffin J. L., Bollard M. E., Nicholson J. K. and Bhakoo K. (2002), Spectral profiles of cultured neuronal and glial cells derived from HRMAS ^{1}H NMR spectroscopy, *NMR in Biomedicine*, 15, 375-84.

99. Griffin J. L., Lehtimaki K. K., Valonen O. K., Grohn O. H. J., Kettunen M. I., Yla-Herttuala S., Pitkanen A., Nicholson J. K. and Kauppinen R. A. (2003a), Assignment of ^{1}H nuclear magnetic resonance visible polyunsaturated fatty acids in BT4C gliomas undergoing ganciclovir-thymidine kinase gene therapy-induced programmed cell death, *Cancer Research*, 63, 3195-3201.

100. Griffin J. L., Pole J. C. M., Nicholson J. K. and Carmichael P. L. (2003b), Cellular environment of metabolites and a metabonomic study of tamoxifen in endometrial cells using gradient high resolution magic angle spinning ^{1}H NMR spectroscopy, *Biochimica et Biophysica Acta*, 1619, 151-158.

101. Griffin J. L., Troke J., Walker L. A., Shore R. F., Lindon J. C. and Nicholson J. K. (2000a), The biochemical profile of rat testicular tissue as measured by magic angle spinning ^{1}H NMR spectroscopy, *FEBS Letters*, 486, 225-229.

102. Griffin J. L., Walker L. A., Garrod S., Holmes E., Shore R. F. and Nicholson J. K. (2000b), NMR spectroscopy based metabonomic studies on the comparative biochemistry of the kidney and urine of the bank vole (Clethrionomys glareolus), wood mouse (Apodemus sylvaticus), white-toothed shrew (Crocidura suaveolens) and the laboratory rat, *Comparative Biochemistry and Physiology*, Part B, 127, 357-367.

103. Griffin J. L., Williams H. J., Sang E., and Nicholson J. K. (2001), Abnormal lipid profile of Dystrophic cardiac tissue as demonstrated by one- and two-dimensional magic-angle spinning ^{1}H NMR spectroscopy, *Magnetic Resonance in Medicine*, 46, 249-255.

104. Gut I. and Conney A. H. (1993), Trimethylamine N-oxygenation and N-demethylation in rat liver microsomes, *Biochemical Pharmacology*, 46, 239-244.

105. Haschek W. M., Rousseaux C. G. and Wallig M. A. (2002), *Handbook of Toxicologic Pathology*, Volume 2, 2nd Edition, Academic Press.

106. Handler J. A., Kossor D. C. and Goldstein R. S. (1994), Assessment of hepatobiliary function in vivo and ex vivo in the rat, *Journal of Pharmacological and Toxicological Methods*, 31, 11-19.

107. Holmes E., Foxall P. J. D., Nicholson J. K., Neild G. H., Brown S. M., Beddell C. R., Sweatman B. C., Rahr E., Lindon J. C., Spraul M. and Neidig P. (1994), Automatic data reduction and pattern recognition methods for analysis of ^{1}H nuclear magnetic resonance spectra of human urine from normal and pathological states. *Analytical Biochemistry*, 220, 284-296.

108. Holmes E., Foxall P. J. D., Spraul M., Nicholson J. K. and Lindon J. C. (1997), 750 MHz ^{1}H NMR spectroscopy characterisation of the complex metabolic pattern of urine from patients with inborn errors of metabolism: 2-hydroxyglutaric aciduria and maple syrup urine disease. *Journal of Pharmaceutical and Biomedical Analysis*, 15, 1647-1659.

109. Holmes E., Nicholls A. W., Lindon J. C., Connor S. C., Connelly J. C., Haselden J. N., Damment S. J. P., Spraul M., Neidig P. and Nicholson J. K. (2000), Chemometric models for toxicity classification based on NMR spectra of biofluids, *Chemical Research Toxicology*, 13, 471-478.

110. Holmes E., Nicholls A. W., Lindon J. C., Ramos S., Spraul M., Neidig P., Connor S. C., Connelly J., Damment S. J., Haselden J. and Nicholson J. K. (1998), Development of a model for classification of toxin-induced lesions using ^{1}H NMR spectroscopy of urine combined with pattern recognition, *NMR in Biomedicine*, 11, 235-244.

111. Horvath J. J., Witmer C. M. and Witz G. (1992), Nephrotoxicity of the 1:1 acrolein-glutathione adduct in the rat, *Toxicology and Applied Pharmacology*, 117, 200-207.

112. Hunter A. L., Holscher M. A. and Neal R. A. (1977), Thioacetamide-induced hepatic necrosis: I. Involvement of the mixed-function oxidase enzyme system, *J. Pharmacology and Experimental Therapeutics*, 200, 439-448.

113. Iorio E., Di Vito M., Spadaro F., Ramoni C., Lococo E., Carnevale R., Lenti L., Strom R., Podo F. (2003), Triacsin C inhibits the formation of ^{1}H NMR-visible mobile lipids and lipid bodies in HuT 78 apoptotic cells, *Biochimica et Biophysica Acta*, 1634, 1 – 14.

114. Jaeschke H., Kleinwaechter C. and Wendel A. (1987), The role of acrolein in allyl alcohol-induced lipid peroxidation and liver cell damage in mice, *Biochemical Pharmacology*, 36, 51-57.

115. Javitt N. B. (1994), Bile acid synthesis from cholesterol: regulatory and auxiliary pathways, *The FASEB Journal*, 8, 1308-1311.

116. Joegensen A. (1986), Metabolism and pharmacokinetics of anti-psychotic drugs, *Progress in Drug Metabolism*, 9, 111-174.

117. Johnson Jr. C. S. (1999), Diffusion ordered nuclear magnetic resonance spectroscopy: principles and applications, *Progress in Nuclear Magnetic Resonance Spectroscopy*, 34, 203-256.

118. Joliffe I. T. (1986), *Principal Component Analysis*, Springer-Verlag.

119. Kakusho O. and Mizoguchi R. (1983), A new algorithm for non-linear mapping with applications to dimension and cluster analyses, *Pattern Recognition*, 16, 109-117.

120. Kaplan L. A. and Pesce A. J. (1989), *Clinical Chemistry: Theory, analysis and correlation*, 2nd Edition, Mosby Company.

121. Kawamura-Yasui N., Kaito M., Nakagawa N., Fujita N., Ikoma J., Gabazza E. C., Watanabe S., Adachi Y. (1999), Evaluating response to nutritional therapy using the branched-chain amino acid/tyrosine ratio in patients with chronic liver disease, *Journal of Clinical Laboratory Analysis*, 13, 31-34.

122. Kaye C. M. (1973), Biosynthesis of mercapturic acids from allyl alcohol, allyl esters and acrolein, *Journal of Biochemistry*, 134, 1093-1101.

123. Kaye C. M., Clapp J. J. and Young L. (1972), The metabolic formation of mercapturic acids in allyl halides, *Xenobiotica*, 2, 129-139.

124. Kershaw W. C., Barsotti D. A., Leonard T. B., Dent J. G. and Lage G. L. (1989), Methoxyfurane enhances allyl alcohol heptatoxicity in rats: Possible involvement of increased acrolein formation, *Drug Metabolism and Disposition*, 17, 117-122.

125. Kizer D. E., Howell B. A., Clouse J. A. and Shirley B. C. (1966), Studies on the relationship between increased adenylic acid deaminase activity and changes in nuclear RNA metabolism in rat liver caused by thioacetamide, *Cancer Research*, 26, 1376-1382.

126. Klaassen C. D. (2001), *Casarett and Doull's Toxicology: The Basic Science of Poisons*, 6th Edition, McGraw Hill.

127. Kleinfield R. G. and Von Haam E. (1959), Effect of thioacetamide on rat liver regeneration. II. Nuclear RNA in mitosis, *Journal of Biophysical and Biochemical Cytology*, 6, 393-396.

128. Knodell R.G. (1975), Effects of chlorpromazine on bilirubin metabolism and biliary secretion in the rat, *Gastroenterology*, 69, 965-972.

129. Lambert J. B. and Mazzola E. P. (2004), *Nuclear Magnetic Resonance Spectroscopy: An introduction to principles, applications, and experimental methods*, Pearson Prentice Hall.

130. Lasslo A., and Meyer A. (1959), Effect of chlorpromazine upon isolated D-Amino-Acid Oxidase systems, *Nature*, 184, 1922-1925.

131. Lee K. R., Lin X., Park D. C. and Eslava S. (2003), Megavariate data analysis of mass spectrometric proteomics data using latent variable projection method, *Proteomics*, 3, 1680-1686.

132. Lin Y., Havinga R., Schippers I. J., Verkade H. J., Vonk R. J. and Kuipers F. (1996), Characterisation of the inhibitory effects of bile acids on very-low-density-lipoprotein secretion by rat hepatocytes in primary culture, *Journal of Biochemistry*, 316, 531-538.

133. Lindon J. C., Holmes E. and Nicholson J. K. (2003), So what's the deal with metabonomics?, *Analytical Chemistry*, 385A-391A.

134. Lindon J. C., Holmes E. and Nicholson J. K. (2004), Toxicological applications of magnetic resonance, *Progress in Nuclear Magnetic Resonance Spectroscopy*, 45, 109-143.

135. Lindon J. C., Holmes E. and Nicholson J.K. (2001), Pattern recognition methods and applications in biomedical magnetic resonance, *Progress in Nuclear Magnetic Resonance Spectroscopy,* 39, 1-40.

136. Lindon J. C., Nicholson J. K. and Everett J. R. (1999), NMR spectroscopy of biofluids, *Annual Reports on NMR Spectroscopy*, 38, 1-88.

137. Lindon J. C., Nicholson J. K., Holmes E. and Everett J. R. (2000), Metabonomics: metabolic processes studied by NMR spectroscopy of biofluids, *Concepts in Magnetic Resonance*, 12, 289-320.

138. Liu M., Nicholson J. K. and Lindon J. C. (1996), High-resolution diffusion and relaxation edited one- and two-dimensional ^{1}H NMR spectroscopy of biological fluids, *Analytical Chemistry*, 68, 3370-3376.

139. Liu M., Nicholson J. K., Parkinson J. A., and Lindon J. C. (1997), Measurement of biomolecular diffusion coefficients in blood plasma using two-dimensional ^{1}H - ^{1}H diffusion edited total-correlation NMR spectroscopy, *Analytical Chemistry*, 69, 1504-1509.

140. Löw H. (1959a), On the participation of flavin in mitochondrial adenosine triphosphatase reactions, *Biochimica Et Biphysica Acta*, 32, 1-10.

141. Löw H. (1959b), The effect of promazines on mitochondrial adenosine triphosphatase reactions, *Biochimica Et Biophysica Acta*, 32, 11-18.

142. Martens H. and Martens M. (2001), *Multivariate Analysis of Quality: An Introduction*, John Wiley & Sons Limited.

143. Maschke S., Wahl A., Azaroual N., Boulet O., Crunelle V., Imbenotte M., Foulard M., Vermeersch G., and Lhermitte M. (1997), 1H-NMR analysis of trimethylamine in urine for the diagnosis of fish-odour syndrome, *Clinica Chimica Acta*, 263, 139-146.

144. Mason T. M. (1998), The role of factors that regulate the synthesis and secretion of very-low-density lipoprotein by hepatocytes, *Critical Reviews in Clinical Laboratory Sciences*, 35, 461-487.

145. Mathews E. J., Benz R. D. and Contrera J. F. (2000), Use of toxicological information in drug design, *Journals of Molecular Graphics & Modelling*, 18, 605-615.

146. Medina H., Dmytraczenko A. and Bacila M. (1964), The effect of certain phenothiazines on the structure and metabolic activity of sarcosomes of Guinea Pig heart, *Biochemical Pharmacology*, 13, 461-467.

147. Mehta M. (2004), *Spectroscopic imaging and molecular profiling of atherosclerosis: an insight into the aortic condition*, PhD Thesis, University of London.

148. Meriles C. A., Sakellariou A. and Pines A. (2002), Resolved magic-angle spinning of anisotropic samples in inhomogeneous fields, *Chemical Physics Letter*, 358, 391-395.

149. Mesa M. L., Carrizosa R., Martinez-Honduvilla C., Benito M. and Fabregat I. (1996), Changes in the rat liver gene expression induced by thioacetamide: Protective role of S-adenosyl-L-methionine by a glutathione-dependent mechanism, *Hepatology*, 23, 600-606.

150. Metz G., Ziliox M. and Smith S. O. (1996), Towards quantitative CP-MAS NMR, *Solid State Nuclear Magnetic Resonance*, 7, 155-160.

151. Miccadei S., Hyle M. E., Gilfor D. and Farber A. L. (1988b), Toxic consequence of the abrupt depletion of glutathione in cultured rat hepatocytes, *Archives of Biochemistry and Biophysics*, 265, 311-320.

152. Miccadei S., Nakae D., Kyle M. E., Gilfor D. and Farber J. L. (1988a), Oxidative cell injury in the killing of cultural hepatocytes by allyl alcohol, *Archives of Biochemistry and Biophysics*, 265, 302-310.

153. Miller J. N. and Miller J. C. (2000), *Statistical and chemometrics for analytical chemistry*, Prentice Hall, UK

154. Millis K. K., Werner E. M., Cory D. G. and Singer S. (1997), Gradient high-resolution, magic angle spinning nuclear magnetic resonance spectroscopy of human adipocyte tissue, *Magnetic Resonance in Medicine*, 39, 399-403.

155. Millis K., Weybright P., Campbell N., Fletcher J. A., Cory D. G. and Singer S. (1999), Classification of human liposarcoma and lipoma using ex vivo proton NMR spectroscopy, *Magnetic Resonance in Medicine*, 41, 257-267.

156. Mironescu St., Burducea O. and Sahnazarov N. (1969), Nucleolar and mitotic abnormalities produced by thioacetamide and hydroxylamine in monkey kidney cells cultivated in vitro, *Experimental Cell Research*, 57, 193-204.

157. Mitchell D. Y. and Petersen D. R. (1989), Metabolism of the glutathione-acrolein adduct, S-(2-aldehydo-ethyl) glutathione, by rat liver alcohol and aldehyde dehydrogenase, *Journal of Pharmacology & Experimental Therapeutics*, 251, 193-198.

158. Moka D., Vorreuther R., Schicha H., Spraul M., Humpfer E., Lipinski M., Foxall P. J. D., Nicholson J. K. and Lindon J. C. (1998), Biochemical classification of kidney carcinoma biopsy samples using magic-angle-spinning ^{1}H nuclear magnetic resonance spectroscopy, *Journal of Pharmaceutical and Biomedical Analysis*, 17, 125-132.

159. Moller B. and Dargel R. (1984), Structural and functional impairment of mitochondria from rat liver chronically injured by thioacetamide, *Acta Pharmacologica et Toxicologica*, 55, 126-132.

160. Moller B. and Dargel R. (1985), Functional impairment of mitochondria from rat livers acutely injured by thioacetamide, *Experimental Pathology*, 28, 55-57.

161. Montgomery R., Conway T. W., Spector A. A. and Chappell D. (1996), *Biochemistry: A case-oriented approach*, 6th Ed., Mosby Inc.

162. Morrison R. T. and Boyd R. N (1992), *Organic Chemistry*, 6th Edition, Prentice Hall.

163. Murphy S. D. (1965), Mechanism of the effect of acrolein on rat liver enzymes, *Toxicology and Applied Pharmacology*, 7, 833-843.

164. Mytilineou C., Kramer B. C. and Yabut J. A. (2002), Review: Glutathione depletion and oxidative stress, *Parkinsonism and Related Disorders*, 8, 385-387.

165. Nicholls A. W., Haselden J. N., Nicholson J. K. and Waterfield C. J. (2000), A metabonomic approach to the investigation of drug-induced phospholipidosis: An NMR spectroscopy and pattern recognition study, *Biomarkers*, 5, 410-423.

166. Nicholls A. W., Mortishire-Smith R. J. and Nicholson J. K. (2003), NMR spectroscopic-based metabonomic studies of urinary metabolite variation in acclimatizing germ-free rats, *Chemical Research in Toxicology*, 16, 1395-1404.

167. Nicholson J. K. and Wilson I. D. (1989), High resolution nuclear magnetic resonance spectroscopy of biological fluids, *Progress in NMR Spectroscopy*, 21, 449-501.
168. Nicholson J. K. and Wilson I. D. (2003), Understanding 'global' systems biology: metabonomics and the continuum of metabolism, *Nature Reviews Drug Discovery*, 2, 668-676.
169. Nicholson J. K., Connelly J., Lindon J. C. and Holmes E. (2002), Metabonomics: a platform for studying drug toxicity and gene function, *Nature Reviews Drug Discovery*, 1, 153-161.
170. Nicholson J. K., Foxall P. J. D., Spraul M., Farrant R. D. and Lindon J. C. (1995), 750 MHz ^{1}H and ^{1}H-^{13}C NMR spectroscopy of human blood plasma, *Analytical Chemistry*, 67, 793-811.
171. Nicholson J. K., Holmes E., Lindon J. C. and Wilson I. D. (2004), The challenges of modelling mammalian biocomplexity, *Nature Biotechnology*, 22, 1268-1274.
172. Nicholson J. K., Lindon J. C. and Holmes E. (1999), 'Metabonomics': understanding the metabolic responses of living systems to pathophysiological stimuli via multivariate statistical analysis of biological NMR spectroscopic data; *Xenobiotica*, 11, 1181-1189.
173. Nozu F., Takeyama N. and Tanaka T. (1992), Changes of hepatic fatty acid metabolism produced by chronic thioacetamide administration in rats, *Hepatology*, 15, 1099-1106.
174. Ohno Y. and Ormstad K. (1985), Formation, toxicity and inactivation of acrolein during biotransformation of cyclophosphamide as studied in freshly isolated cells from rat liver and kidney, *Archives of Toxicology*, 57, 99-103.
175. Ohno Y., Ormstad K., Ross D. and Orrenius S. (1985), Mechanism of allyl alcohol toxicity and protective effects of low-molecular-weight thiols studied with isolated rat hepatocytes, *Toxicology & Applied Pharmacology*, 78, 169-179.
176. Otton S.V., Inaba T., and Kalow W. (1982), Inhibition of sparteine oxidation in human liver by tricyclic antidepressants and other drugs, *Life Sciences*, 32, 795-800.
177. Palmeira C. M. and Rolo A. P. (2004), Mitochondrially-mediated toxicity of bile acids, *Toxicology*, 203, 1-15.
178. Pang J. M., Zaleski J. and Kauffman F. C. (1996), Actions of selected hepatotoxicants on freshly isolated and cryopreserved rat hepatocytes, *Cryobiology*, 33, 226-235.
179. Pang J. M., Zaleski J. and Kauffman F. C. (1997), Toxicity of allyl alcohol in primary cultures of freshly isolated and cryopreserved hepatocytes maintained on hydrated collagen gels, *Toxicology & Applied Pharmacology*, 142, 87-94.

180. Parent R. A., Paust D. E., Schrimpf M. K., Talaat R. E., Doane R. A., Caravello H. E., Lee S. J and Sharp D. E. (1998), Metabolism and distribution of [2, 3-^{14}C]acrolein in Sprague-Dawley rats: Identification of urinary and fecal metabolites, *Toxicological Sciences*, 43, 110-120.

181. Pentilla K. E. (1988), Allyl alcohol cytotoxicity and glutathione depletion in isolated periportal and perivenous rat hepatocytes, *Chemico-Biological Interactions*, 65, 107-121.

182. Platt D. S. and Cockrill B. L. (1967), Liver enlargement and hepatotoxicity: An investigation into the effects of several agents on rat liver enzyme activities, *Biochemical Pharmacology*, 16, 2257-2270.

183. Platt D. S. and Cockrill B. L. (1969), Biochemical changes in rat liver in response to treatment with drugs and other agents – II: Effects of halothane, DDT, and other chlorinated hydrocarbons, thioacetamide, demethylnitrosamine and ethionine, *Biochemical Pharmacology*, 18, 445-457.

184. Podo F. (1999), Tumour phospholipid metabolism, *NMR in Biomedicine*, 12, 413-439.

185. Porter W. R. and Neal R. A. (1978), Metabolism of thioacetamide and thioacetamide S-oxide by rat liver microsomes, *Drug Metabolism and Disposition*, 6, 379-388.

186. Porter W. R., Gudzinowicz M. J. and Neal R. A. (1979), Thioacetamide-induced hepatic necrosis: II. Pharmacokinetics of thioacetamide and thioacetamide-S-oxide in the rat, *J. Pharmacology and Experimental Therapeutics*, 208, 386-391.

187. Provost J. P., Hanton G., and Le Net J. L. (2003), Plasma triglycerides: an overlooked biomarker of hepatotoxicity in the rat, *Comparative Clinical Pathology*, 12, 95-101.

188. Raffelt K., Moka D., Sullentrop F., Dietlein M. S, Hahn J. and Schicha H. (2000), Systemic alterations in phospholipid concentrations of blood plasma in patients with thyroid carcinoma: an in-vitro ^{31}P high-resolution NMR study, *NMR in Biomedicine*, 13, 8-13.

189. Ramu K., Fraiser L. H., Mamiya B., Ahmed T. and Kehrer J. P. (1995), Acrolein Mercapturates: Synthesis, characterisation, and assessment of their role in the bladder toxicity of cyclophosphamide, *Chemical Research Toxicology*, 8, 515-524.

190. Rees K. R. and Tarlow M. J. (1967), Hepatotoxic action of allyl formate, *Journal of Biochemistry*, 104, 757-761.

191. Rees K. R., Rowland G. F. and Varcoe J. S. (1966), The metabolism of tritiated thioacetamide in the rat, *International Journal of Cancer*, 1, 197-206.

192. Reynolds E. S. (1972), Comparison of early injury to liver endoplasmic reticulum by halomethanes, hexachloroethane, benzene, toluene, bromobenzene, ethionine, thioacetamide and dimethylnitrosamine, *Biochemical Pharmacology*, 21, 2555-2561.

193. Rikans L. E., Cai Y. and Hornbrook K. R. (1995), Allyl alcohol cytotoxicity in isolated rat hepatocytes: effects of azide, fasting, and fructose, *Journal of Toxicology and Environmental Health*, 44, 1-11.

194. Robertson D. G., Reily M. D., Sigler R. E., Wells D. F., Paterson D. A. and Braden T. K. (2000), Metabonomics: Evaluation of nuclear magnetic resonance (NMR) and pattern recognition technology for rapid in vivo screening of liver and kidney toxicants, *Toxicological Sciences*, 57, 326-337.

195. Samuels A. M., and Carey M. C. (1978), Effects of chlorpromazine hydrochloride and its metabolites on the Mg2+-, and Na+, K+-ATPase activities of canalicular-enriched rat liver plasma membranes, *Gastroenterology*, 74, 1183-1190.

196. Sanduja R., Ansari G. A. S. and Boor P. J. (1989), 3-Hydroxypropylmercapturic acid: a biologic marker of exposure to allylic and related compounds, *Journal of Applied Toxicology*, 9, 235-238.

197. Schriewer H. and Lohmann J. (1976), Disturbances in the regulation of phospholipids metabolism in the whole liver, mitochondria and microsomes in acute thioacetamide poisoning and the influence of silymarin, *Arzneimittelforschung*, 26, 65-69.

198. Serafini-Cessi F. (1972), Conversion of allyl alcohol into acrolein by rat liver, *Journal of Biochemistry*, 128, 1103-1107.

199. Shaw S. and Liber C. S. (1983), Plasma amino acids in the alcoholic: nutritional aspects, *Alcoholism: Clinical and Experimental Research*, 7, 22-27.

200. Sherlock S. and Dooley J., *Disease of the liver and biliary system*, 11th Edition, 2002, Blackwell Publishing Company.

201. Shukla B., Visen P. K. S., Patnaik G. K. and Dhawan B. N. (1992), Reversal of thioacetamide induced cholestasis by picroliv in rodents, *Phytotherapy Research*, 6, 53-55.

202. Smith J. L., Wishnok J. S. and Deen W. M. (1994), Metabolism and excretion of methylamines in rats, *Toxicology and Applied Pharmacology*, 125, 296-308.

203. Spira B. and Raw I. (2000), The effect of thioacetamide on the activity and expression of cytosolic rat liver glutathione-S-transferase, *Molecular and Cellular Biochemistry*, 211, 103-110.

204. Steele W. J. and Busch H. (1966), Increased content of high molecular weight RNA fractions in nuclei and nucleoli of livers of thioacetamide-treated rats, *Biochimica et Biophysica Acta*, 119, 501-509.

205. Stejskal E. O. (1972), Spin-echo measurement of self-diffusion in colloidal systems, *Advances in Molecular Relaxation Processes*, 3, 27-42.

206. Stejskal E. O. and Tanner J. E. (1965), Spin diffusion measurements: Spin echoes in the presence of a time-dependent field gradient, *Journal of Chemical Physics*, 42, 288-292.

207. Stoyanova R. and Brown T. R. (2001), NMR Spectral Quantitation by Principal Component Analysis, *NMR in Biomedicine*, 14, 271-277.

208. Sun F., Hayami S., Ogiri Y. Haruna S., Tanaka K., Yamada Y., Tokumaru S. and Kojo S. (2000), Evaluation of oxidative stress based on lipid hydroperoxide, vitamin C and vitamin E during apoptosis and necrosis caused by thioacetamide in rat liver, *Biochimica et Biophysica Acta*, 1500, 181-185.

209. Tannock G. W. (1999), *Probiotics - a critical view*, Horizon Scientific Press.

210. Tannock G. W. (2001), Molecular assessment of intestinal microflora, *American Journal of Clinical Nutrition*, 73, 410-414.

211. Tate A. R., Foxall P. J. D., Holmes E., Moka D., Spraul M., Nicholson J. K. and Lindon J.C. (2000), Distinction between normal and renal cell carcinoma kidney cortical biopsy samples using pattern recognition of ^{1}H magic angle spinning (MAS) NMR spectra, *NMR in Biomedicine*, 13, 64-71.

212. Tavaloni N., and Boyer J. L. (1980), Relationship between hepatic metabolism of chlorpromazine and cholestatic effects in the isolated the perfused rat liver, *Journal of Pharmacology and Experimental Therapeutics*, 214, 269-274.

213. Teck Y. L., Chon K. L., Salto-Tellez M. and Chung M. C. M. (2004), A proteomic analysis of thioacetamide-induced hepatotoxicity and cirrhosis in rat livers, *Proteomics*, 4, 3960–3974.

214. Timbrell J. A. (1998), Biomarkers of toxicology, *Toxicology*, 129, 1-12

215. Timbrell J. A. (2000), *Principles of Biochemical Toxicology*, 3rd Edition, Taylor and Francis.

216. Timbrell J. A. (2002), *Introduction to Toxicology*, 3rd Edition, Taylor and Francis.

217. Timbrell J. A., Seabra V. and Waterfield C. J. (1995a), The in-vivo and in-vitro protective properties of taurine, *General Pharmacology*, 26, 453-462.

218. Timbrell J. A., Waterfield C. J. and Draper R. P. (1995b), Use of urinary taurine and creatine as biomarkers of organ dysfunction and metabolic perturbations, *Comparative Haematology International*, 5, 112-119.

219. Tjioe S. A., Manian A. A., and O'Neill J. J. (1972), Calcium efflux and respiratory inhibition in brain mitochondria: Effects of chlorpromazine metabolites, *Biochemical and Biophysical Research Communications*, 48, 212-218.

220. Tomlins A. M., Foxall P. J. D., Lindon J. C., Lynch M. J., Spraul M., Everett J. R. and Nicholson J. K. (1998b), High resolution magic angle spinning ^{1}H nuclear magnetic resonance analysis of intact prostatic hyperplastic and tumour tissues, *Analytical Communications*, 35, 113-115.

221. Tomlins A. M., Foxall P. J. D., Lynch M. J., Parkinson J., Everett J. R. and Nicholson J. K. (1998a), High resolution NMR spectroscopic studies on dynamic biochemical processes in incubated human seminal fluid samples, *Biochimica et Biophysica Acta - General Subjects*, 1379, 367-380.

222. Traficante L.J., Sakalis G., Siekierski J., Rotrosen J., and Gershon S. (1979), Rapid in vitro sulfoxidation of chlorpromazine by human blood: Inhibition by an endogenous plasma protein factor, *Life Sciences*, 24, 337-346.

223. Trennery P. N. and Waring R. H. (1983), Early changes in thioacetamide-induced liver damage, *Toxicology Letters*, 19, 299-307.

224. Underhaug A. 2001, Chlorpromazine: Stimulatory effects on human blood platelet activation and intercalation in monolayers and liposomes of glycerophospholipids, *Thesis for the degree of CANDIDATA SCIENTIARUM*, Department of Biochemistry and Molecular Biology, University of Bergen.

225. Vadi H. V. and Neal R. A. (1981), Microsomal activation of thioacetamide-S-oxide to a metabolite(s) that covalently binds to calf thymus DNA and other polynucleotides, *Chemico-Biological Interactions*, 35, 25-38.

226. Van Der Greef J., Tas A. C., Bouwman J., Ten Noever De Brauw M. C. and Schreurs W. H. P. (1983), Evaluation of field-desorption and fast atom-bombartment mass spectrometric profiles by pattern recognition techniques, *Analytica Chimica Acta*, 150, 45-52.

227. Van Heckel P. and Van Hufel S. (2001), NMR spectroscopy quantitation, *NMR in Biomedicine*, 14, 223.

228. Virtanen P. and Lassila V. (1986), Influence of thioacetamide-provoked liver injury on female rat blood and alveolar bone under stress, *Acta Anatomica*, 127. 285-289.

229. Wang Y., Bollard M. E., Keun H., Antti H., Beckonert O., Ebbels T. M., Lindon J. C., Holmes E., Tang H. and Nicholson J. K. (2003), Spectral editing and pattern recognition methods applied to high-resolution magic-angle spinning ^{1}H nuclear magnetic resonance spectroscopy of liver tissues, *Analytical Biochemistry*, 323, 26-32.

230. Waterfield C. J., Asker D. S. and Timbrell J. A. (1997), Triglycerides disposition in isolated hepatocytes after treatment with hydrazine, *Chemico-Biological Interactions*, 107, 157-172.

231. Waterfield C. J., Mesquita M., Parnham P. and Timbrell J. A. (1994), Cytoprotective effects of taurine in isolated rat hepatocytes, *Toxicology In Vitro*, 8, 573-575.

232. Waterfield C. J., Turton J. A., Scales M. D. C. and Timbrell J. A. (1991), Taurine, a possible urinary marker for liver damage: a study of taurine excretion in carbon tetrachloride-treated rats, *Archives of Toxicology*, 65, 548-555.

233. Waterfield C. J., Turton J. A., Scales M. D. C. and Timbrell J. A. (1993a), Investigation into the effects of various hepatotoxic compounds on urinary and liver taurine levels in rats, *Archives of Toxicology*, 67, 244-254.

234. Waterfield C. J., Turton J. A., Scales M. D. C. and Timbrell J. A. (1993b), Effects of various non-hepatotoxic compounds on urinary and liver taurine levels in rats, *Archives of Toxicology*, 67, 538-546.

235. Waterfield C. J., Turton J. A., Scales M. D. C. and Timbrell J. A. (1993c), The correlation between urinary and liver taurine levels and between pre-dose urinary taurine and liver damage, *Toxicology* 77, 1-5.

236. Waterfield C. J., Turton J. A., Scales M. D. C. and Timbrell J. A. (1993d), Reduction of liver taurine in rats by β-alanine treatment increases carbon tetrachloride toxicity. *Toxicology*, 77, 7-20.

237. Waterfield C. J., Mesquita M., Parnham P. and Timbrell J. A. (1993e), Taurine protects against the cytotoxicity of hydrazine, 1, 4-naphthoquinone and carbon tetrachloride in isolated rat heptocytes, *Biochemical Pharmacology*, 46, 589-595.

238. Waterfield C. J., Westmoreland C., Asker D. S., Murdock J. C., George E. and Timbrell J. A. (1998), Ethionine toxicity in vitro: the correlation of data from rat hepatocyte suspensions and monolayers with in vivo observations, *Archives of Toxicology*, 72, 588-596.

239. Waters N. J., Garrod S., Farrant R. D., Haselden J. N., Connor S. C., Conelly J., Lindon J. C., Holmes E. and Nicholson J. K. (2000), High-resolution magic angle spinning ^{1}H NMR spectroscopy of intact liver and kidney: Optimization of sample preparation procedures and biochemical stability of tissue during spectral acquisition, *Analytical Biochemistry*, 282, 16-23.

240. Waters N. J., Holmes E., Waterfield C. J., Farrant R. D. and Nicholson J. K. (2002), NMR and pattern recognition studies on liver extracts and intact livers from rats treated with α-naphthylisothiocyanate, *Biochemical Pharmacology*, 64, 67-77.

241. Waters N. J., Holmes E., Williams A., Waterfield C. J., Farrant R. D. and Nicholson J. K. (2001), NMR and pattern recognition studies on the time-related metabolic effects of α-

Naphthylisothiocyanate on liver, urine, and plasma in the rat: An integrative Metabonomic approach, *Chemical Research Toxicology*, 14, 1401-1412.

242. Waters N. J., Waterfield C. J., Farrant R. D., Holmes E. and Nicholson J. K. (2005), Metabonomic deconvolution of embedded toxicity: Application to thioacetamide hepato- and nephrotoxicity, *Chemical Research Toxicology*, 18, 639-654.
243. Wold S. (1978), Cross-validatory estimation of the number of components in factor and principal components models, *Technometrics*, 20, 397-405.
244. Wold S. (1987), Principal component analysis, *Chemometrics and Intelligent Laboratory Systems*, 2, 37-52.
245. Wold S., Johansson E., Jellum E., Bjornson I., and Nesbakken R. (1981), Application of SIMCA multivariate data analysis to the classification of gas chromatography profiles of human brain tissues, *Analytica Chimica Acta*, 133, 251-259.
246. Wold S., Kettaneh N., Friden H. and Holmberg A. (1998), Modelling and diagnostics of batch processes and analogous kinetic experiments, *Chemometrics and Intelligent Laboratory Systems*, 44, 331-340.
247. Wu D., Chen A. and Johnson Jr. C. S. (1995), An improved diffusion-ordered spectroscopy experiment incorporating bipolar-gradient pulses, *Journal of Magnetic Resonance, Series A.*, 115, 260-264.
248. Wu J. T., Wu L. H. and Knight J. A. (1986), Stability of NADPH: Effect of various factors on the kinetics of degradation, *Clinical Chemistry*, 32, 314-319.
249. Xu J., Bjursell M. K., Himrod J., Deng S., Carmichael L. K., Chaing H. C., Hooper L. V. and Gordon J. I. (2003), A genomic view of the human-Bacteroides thetaiotaomicron symbiosis, *Science*, 299, 2074-2076.
250. Yagi K., Nagatsu T., and Ozawa T. (1956), Inhibitory action of chlorpromazine on the oxidation of D-Amino-Acid in the diencephalon of the brain, *Nature*, 177, 891-892.
251. Yagi K., Ozawa T., and Nagatsu T. (1960), Mechanism of inhibition of D-Amino Acid Oxidase, *Biochimica Et Biophysica Acta*, 43, 310-317.
252. Yeung P. K. F., Hubbard J. W., Korchinski E. D. and Midha K. K. (1993), Pharmacokinetics of chlorpromazine and key metabolites, *European Journal of Clinical Pharmacology*, 45, 563-569.
253. Zhang A. Q., Mitchell S. C. and Smith R. L. (1999), Dietary precursors of trimethylamine in man: A pilot study, *Food and Chemical Toxicology*, 37, 515-520.
254. Zborek, Malusecka, Krzyyoska-Gruca, Wysocka and Krawczyk (2002), Immunohistochemical studies on the expression patter of molecular chaperones HSC70 and

HSP25 and cell cycle-related proteins cycling D1 and PCNA in rat liver after Thioacetamide intoxication, *Histochemical and Cellular Biology,* 118, 311-319.

255. Zethof T. J., Van der Heyden J. A., Tolboom J. T. and Olivier B. (1994), Stress-induced hyperthermia in mice: A methodological study, *Physiological Behaviour*, 55, 109-15.
256. Ziegler D. M. (1990), Flavin-containing monooxygenases: enzymes adadpted for multisubstrate specificity, *Trends in Pharmacological Sciences*, 11, 321-324.
257. Ziegler D. M. (1993), Recent studies on the structure and function of multi-substrate flavin-containing monooxygenases, *Annual Review in Pharmacology and Toxicology*, 33, 179-199.
258. Zitting A. and Heinonen T. (1980), Decrease of reduced glutathione in isolated rat hepatocytes caused by acrolein, acrylonitrile and the thermal degradation products of styrene copolymers, *Toxicology*, 17, 333-341.

Appendices

Appendix I. Experimental Materials and Suppliers.

Material	**Supplier**	**Address**
D_2O NaCl Na_2HPO_4 NaH_2PO_4 NaOH TSP	Sigma-Aldrich	Fancy Lane Poole Dorset BH17 7BR UK

Appendix II. Phosphate Buffer Solution.

Preparation of 0.1M Sodium Phosphate Buffer (pH 7.4) for ^{1}H NMR Urinalysis

Stock Solution A: 0.2M NaH_2PO_4 (aq)

4.80g of monosodium dihydrogen phosphate monohydrate ($NaH_2PO_4.H_2O$) into 200ml of deionised water.

Stock Solution B: 0.2M Na_2HPO_4 (aq)

5.68g of disodium monohydrogen phosphate heptahydrate ($Na_2HPO_4.7H_2O$) into 200ml of deionised water.

Buffer Solution Preparation

Prepare a 0.2M stock solution A of NaH_2PO_4 in H_2O

Prepare a 0.2M stock solution B of Na_2HPO_4 in H_2O

Mix 19ml of stock solution A (0.2M NaH_2PO_4) with 81ml of stock solution B (0.2M Na_2HPO_4)

The pH was measured and adjusted to pH 7.4 by the drop wise addition of either solution A (if too basic) or solution B (if too acidic). The final volume was made up to 200ml with deionised water.

Preparation of the TSP/D_2O solution

Take 0.0948 g of TSP and make up to 50ml with D_2O in a volumetric flask

TSP = 3-trimethylsilyl-(2,2,3,3-$^2H_4$)-1-propionate.

Appendix III. Deuterosaline Solution.

Preparation of Deuterosaline Solution

6.3g of Sodium Chloride (NaCl) into 63ml of deionised water and 7ml D_2O.

This resulted in a 9:1 ratio of H_2O to D_2O.

The overall product was 0.9% NaCl (w/v)